UNIVERSITY OF LIVERPOOL

Porous materials for the uptake of ammonia

Thesis submitted in accordance with the requirements of the University of Liverpool for the degree of Doctor in Philosophy by:

Oliver Thomas Wilcox

September 2015

Abstract

This work presents the synthesis and characterisation of water-stable metal-organic frameworks and conjugated microporous polymers for use as ammonia sorbents.

An aluminium porphyrin-based metal-organic framework (Al-PMOF) is shown to adsorb large quantities of both hydrochloric and formic acids; 6.1 molecules of HCl and 6.4 molecules of HCOOH are adsorbed per porphyrin linker. The MOF shows remarkable stability towards these reactive guests, even allowing cycling of acid loading despite vigorous removal conditions of 170^{o}C at 10^{-5} bar. Ammonia uptake by these acid-loaded materials, assessed using dynamic micro-breakthrough experiments, is exceptional; Brønsted acid-Brønsted base interactions are exploited which yield vastly increased performance over traditional BPL activated carbon as well as the unloaded framework. Performance is further enhanced by the presence of moisture in the ammonia flow, simulating environmental conditions.

An indium porphyrin-based MOF is characterised revealing a material isostructural to Al-PMOF, with a larger unit cell and the presence of In(III)OH bound within its porphyrin core. The material is shown to perform well as an ammonia sorbent, outperforming BPL activated carbon and Al-PMOF. The MOF is unstable to the loading of formic and hydrochloric acids. The material's potential for CO_2 and CH_4 uptake is assessed, which compares very favourably with other MOFs.

An isostructural vanadium porphyrin-based MOF exhibits good ammonia uptake, outperforming its aluminium and indium analogues, and far surpassing BPL activated carbon. The material is seen to be entirely unstable to HCl loading, yet

stable to formic acid loading, which yields a corresponding increase in ammonia uptake in comparison with the unloaded material.

The zirconium based MOF UiO-66 is functionalised with increasing numbers of amino groups. The addition of a single -NH_2 group per linker resulted in a large increase in ammonia uptake. The addition of a second -NH_2 group per linker results in performance intermediate between the unfunctionalised material and its mono-amino analogue, highlighting the important balance between porosity and functionality. The addition of moisture to the ammonia flow revealed competitive uptake of water in the case of the aminated MOFs. The materials are shown to be stable to HCl loading with the resulting crystalline materials yielding excellent improvements in ammonia uptake, exhibiting up to 9 times the performance over the non-loaded material.

The conjugated microporous polymer CMP-1 is functionalised with both one and two carboxylic acid moieties per monomer. An increase in ammonia uptake by the mono-acid over the unfunctionalised material is seen, however the di-acid polymer shows less ammonia uptake than even the unfunctionalised CMP-1. Isotherms using N_2, H_2O and MeOH reveal the likelihood of interesting hydrogen bonding effects which result in a closed di-acid polymer structure, inaccessible to ammonia at 298 K. The presence of moisture is seen to disrupt the hydrogen bonding of the network sufficiently to reveal increased performance of the di-acid in comparison with the CMP analogues as well as BPL activated carbon.

Acknowledgments

Firstly, I would like to thank my supervisor, Professor Matt Rosseinsky for his advice and support and for offering opportunity to undertake my PhD within his group. I would also like to thank Martin Smith and Corinne Stone for their continued input and support and for facilitating such an enjoyable and valuable collaboration with Dstl. Many thanks to Jane Remmer for all her help.

I would like to thank Alex Fateeva for showing me the ropes in the lab, and I offer particular thanks to Alex Katsoulidis for being a fantastic mentor and friend throughout his time here, offering invaluable advice, discussion and so much wonderful food. I am extremely grateful to my friends, particularly Darren, Borbala, Dani, Tim, Noemie, Tom, Jibs, Zoe and Harry for making my time here so much fun.

Thanks to Liam for everything, and finally my parents have provided so much encouragement and support that I can't begin to thank them enough.

Contents

Supporting publications

Acid loaded porphyrin-based metal–organic framework for ammonia uptake

O. T. Wilcox, A. Fateeva, A. P. Katsoulidis, M. W. Smith, C. A. Stone and M. J. Rosseinsky, *Chem. Commun.*, 2015, **51**, 14989-14991.

1 Introduction

1.1 General introduction

Porous materials are defined as solids containing pores.[1] Porous materials are of considerable interest to the scientific community as a result of their accessibility to molecules, atoms and ions not only at the external particle surface but throughout the bulk of the material.[2] These materials have been applied to industrial processes for decades, and continue to contribute to developments in gas storage, gas and liquid separations, catalysis, sensing, ion exchange and drug delivery, to name a few.

Porous materials can be made from solely organic constituents (such as activated carbons, porous organic polymers and covalent organic frameworks), inorganic constituents (such as zeolites and silica[3,4]) and hybrid inorganic-organic materials (such as metal-organic frameworks and polysilsesquioxanes[5]).

Porous materials can be conveniently categorised by their pore size according to the International Union of Pure and Applied Chemistry (IUPAC) as shown below:[6]

i. Materials with pores not exceeding around 2 nm are known as microporous.
ii. Materials with pores greater than around 2 nm but not exceeding 50 nm are known as mesoporous.
iii. Materials with pores greater than around 50 nm are referred to as macroporous.

1.1.1 Zeolites

Zeolites are porous, crystalline aluminosilicates based framework structures of corner sharing SiO_4 and AlO_4 tetrahedra with the general formula $M_{x/z}[xAlO_2.nSiO_2].qH_2O$, where M^{z+} is an exchangeable cation, $[xAlO_2.nSiO_2]$ is the anionic framework and qH_2O is the sorbate phase.[7] The amount of Al within zeolites can vary, with Si/Al = 1 to ∞, with zeolites consisting entirely of silica being polymorphs of SiO_2.[8] The presence of Al^{3+} results in an overall negative charge within the framework, compensated for by the M^{z+} cations; the varied and exchangeable nature of these cations gives rise to the diverse properties and applications of zeolites.[8,9]

The existence of natural zeolites has been known for centuries, however work by Barrer in the 1930's and 40's inspired the industrial scale synthesis of these materials.[8,9] In 1954, synthetic zeolites were first commercialised by Union Carbide for application in separation and purification, and since have been used in numerous areas of industry; these include catalysis, such as Fischer-Tropsch catalysis and catalytic cracking, water purification, including the removal of radioactive contaminants in nuclear wastewater, gas separation, detergents, heating and refrigeration.[10,11,12]

1.1.2 Activated carbon

Activated carbon is an amorphous porous material that can be produced from various carbonaceous matter including wood, coal, nut shells and coconut husk. Two main methods of producing activated carbons exist: thermal activation and chemical activation. Thermal activation involves heating the raw material to high temperatures

and gasification using an oxidising agent (usually steam). Chemical activation involves heating the raw material with chemicals such as phosphoric acid, $ZnCl_2$ and alkaline hydroxides. Varying the raw material and activation method can have significant impacts on the resulting pore size and surface chemistry, and impregnation with metals salts, acids and amines can further differentiate activated carbons. As such, many types of activated carbon exist, with broad application in areas such as gas storage and separation, catalysis, water purification and toxic gas uptake.[13,14]

1.1.3 Porous organic polymers and covalent organic frameworks

Covalent organic frameworks (COFs) are crystalline porous materials consisting of many covalently bonded organic monomers generally comprising light elements such as carbon, hydrogen, oxygen, nitrogen and boron. First discovered in 2005 using condensation reactions of phenyldiboronic acid ($C_6H_4(B(OH)_2)_2$) and hexahydroxytriphenylene ($C_{18}H_6(OH)_6$),[15] COFs exhibit well-defined 2D or 3D structures whereby the molecular length of the building units govern their pore size;[16] COFs with pore widths of 9 to 42 Å are known.[15,17] In addition to the use of boroxines, linking groups formed of triazines, imines, and hydrazones have been exploited in COF synthesis.[18-20]

In contrast with crystalline COFs, amorphous porous organic polymers are much more diverse; generally, the monomers are more varied and the reactions for their synthesis are more abundant.[21] Typical classes of amorphous porous organic polymers include polymers of intrinsic microporosity (PIMs), hypercrosslinked polymers (HCPs), porous aromatic frameworks (PAFs) and conjugated microporous polymers (CMPs).

PIMs are made using condensation reactions to form rigid, contorted macromolecules which pack inefficiently, resulting in an open pore structure.[22,23] Conversely, HCPs contain many rigid covalent crosslinks, formed using non-crosslinked or lightly-crosslinked polymers and promoting further crosslinking to produce highly porous structures.[24] PAFs are another example of amorphous porous polymers, reported first in 2009. They are generally formed with aromatic monomers using Yamamoto-type Ullmann cross-coupling reactions, which can result in materials with much higher surface areas than PIMs, HCPs and CMPs.[25]

CMPs can be considered a sub-class of HCPs comprising of extended 3D π-conjugated networks.[26] First discovered by Cooper and co-workers,[27] there have since been many examples of CMPs using a broad variety of monomer units, examples shown in Figure 1.1, as well as a large diversity in synthetic routes including Suzuki cross-coupling, Sonogashira-Hagihara reactions, Yamamoto reactions, oxidative coupling, Schiff-base reactions, cyclotrimerization, phenazine ring fusion reactions and Friedel–Crafts arylation.[28] Examples of the potential application of these materials in areas such as gas adsorption, separation, heterogeneous catalysis and sensing is of significant interest, as discussed later.

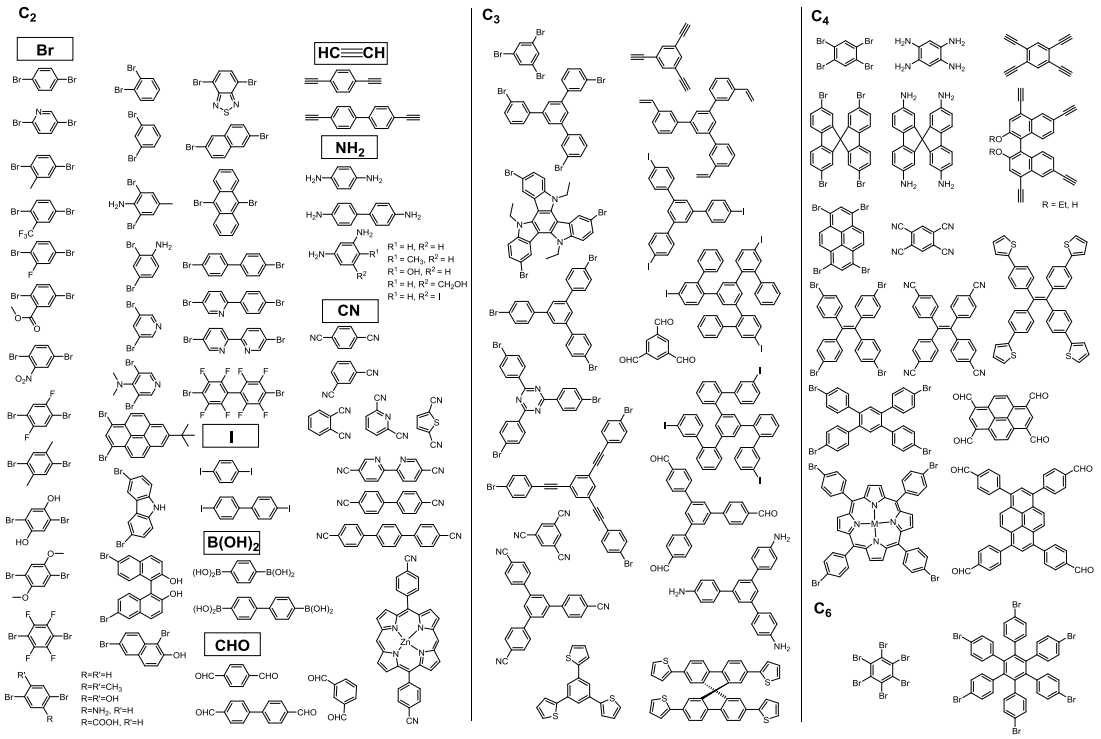

Figure 1.1

Examples of the broad variety of monomers used in the synthesis of CMPs. Figure redrawn based on original from reference 28.

1.1.4 Metal-organic frameworks

Metal-organic frameworks (MOFs) are crystalline porous materials which consist of metal cations, or metal-oxy clusters, connected by organic linker molecules. The huge variety of organic linkers, metals and structural motifs offer countless combinations, with over 20,000 examples reported. These porous solids display remarkable properties, with BET surface areas reported in excess of 7000 m^2/g, and proposed theoretical limits of over 14,000 m^2/g.[29] A hugely important feature of MOFs is the ability to design their pores, such that their size, chemical functionality and even flexibility can be tailored through careful choice of metals, ligands and reaction conditions.

The first permanently porous MOFs, as evidenced by reversible isotherms were reported in the late 1990's by the research groups of S. Kitagawa and O. M. Yaghi.[7,30] In 1997 Kitagawa and co-workers produced MOFs with Co, Ni, and Zn as metal nodes in combination with 4,4'-bipyridine linkers, resulting in crystalline frameworks of $([M_2 (4,4'\text{-bipy})_3(NO_3)_4]\cdot H_2O)_n$ (M = Co, Ni, Zn). The MOF structure existed as interpenetrated double sheets leaving small voids for guest uptake. The Co material was seen to exhibit reversible uptake of CH_4 in the range of 1-36 atm at 298 K. Adsorption of N_2 and O_2 was also measured.[7]

In 1998 Yaghi and co-workers reported MOF-2, Zn(BDC)(DMF)(H_2O), which was synthesised using zinc nitrate tetrahydrate and benzene dicarboxylic acid (BDC) in DMF. The resulting structure consisted of BDC ligands coordinated to two square pyramidal Zn^{2+} ions forming a known square paddlewheel $Zn_2(O_2CR)_4L_2$ cluster (L=axial ligand). The network structure was 2D, with the layers held together by hydrogen-bonding interactions between axial water ligands of one layer and carboxylate oxygens of the adjacent layer. The framework was seen to be stable to activation conditions of 140 ^oC, 5 x 10^{-5} Torr for 16 h, resulting in a dehydrated, evacuated material which exhibited reversible N_2 and CO_2 isotherms. The removal of water was thought to cause the formation of zinc-carboxylate bonds between the 2D layers.

These breakthroughs led to a huge progression in the synthesis of MOFs, particularly carboxylate based, initially exploiting square paddlewheel clusters and other known metal-oxy clusters, however quickly promoting the quest for novel metal-oxy clusters.[31] Many clusters have been discovered since, which serve as secondary building units (SBUs) in MOFs.[32]

Amongst the most significant features of MOF chemistry is the concept of isoreticular synthesis. This principle refers to the ability to replace either the organic or inorganic building unit with topologically similar building units.[33] This allows the increase of pore volume by employing longer linkers, or the changing of surface chemistry by employing functionalised linkers and varying the metal cations. The replacement often requires variation in synthesis conditions. An example of early isoreticular synthesis is typified by the IRMOF (isoreticular MOF) series of materials, developed by Yaghi and co-workers. The IRMOF series arose from MOF-5, also known as IRMOF-1, which consists of Zn_4O clusters connected by benzene dicarboxylate (BDC) linkers resulting in a cubic structure. By using alternate dicarboxylate linkers, a series of isostructural materials with varying pore size and functionality were produced.

MOF-5, first reported in 1999, is one of the most highly cited MOFs, likely as a result of pioneering findings in reversible hydrogen adsorption,[35-37] thermal stability[38,39] and luminescent properties.[40] However, whilst thermally stable to approximately 300^{o}C, the material has been shown to be unstable to water and decomposes quickly in humid air.[41] Thermal and chemical stability are of interest to researchers as many applications including gas storage, catalysis and sensing rely on these properties.

Some representative MOFs which exhibit high chemical and thermal stability are the UiO-66, MIL-100, MIL-101 and MIL-53 families of materials. UiO-66 compounds are based on $Zr_6O_4(OH)_4$ clusters which are bridged up to twelve times to adjacent SBUs (Figure 1.2). The high stability has been credited to strength of the Zr−O bonds, and also due the ability of the Zr_6 cluster to rearrange reversibly upon

dehydroxylation or rehydration, without disturbing the connecting dicarboxylate linkers. UiO-66 decomposes at temperatures in excess of 500 °C.[42,43] A wide variety of linkers have been used to bridge the $Zr_6O_4(OH)_4$ SBUs resulting in materials with a multitude of pore sizes and functionalities with broad application.[44]

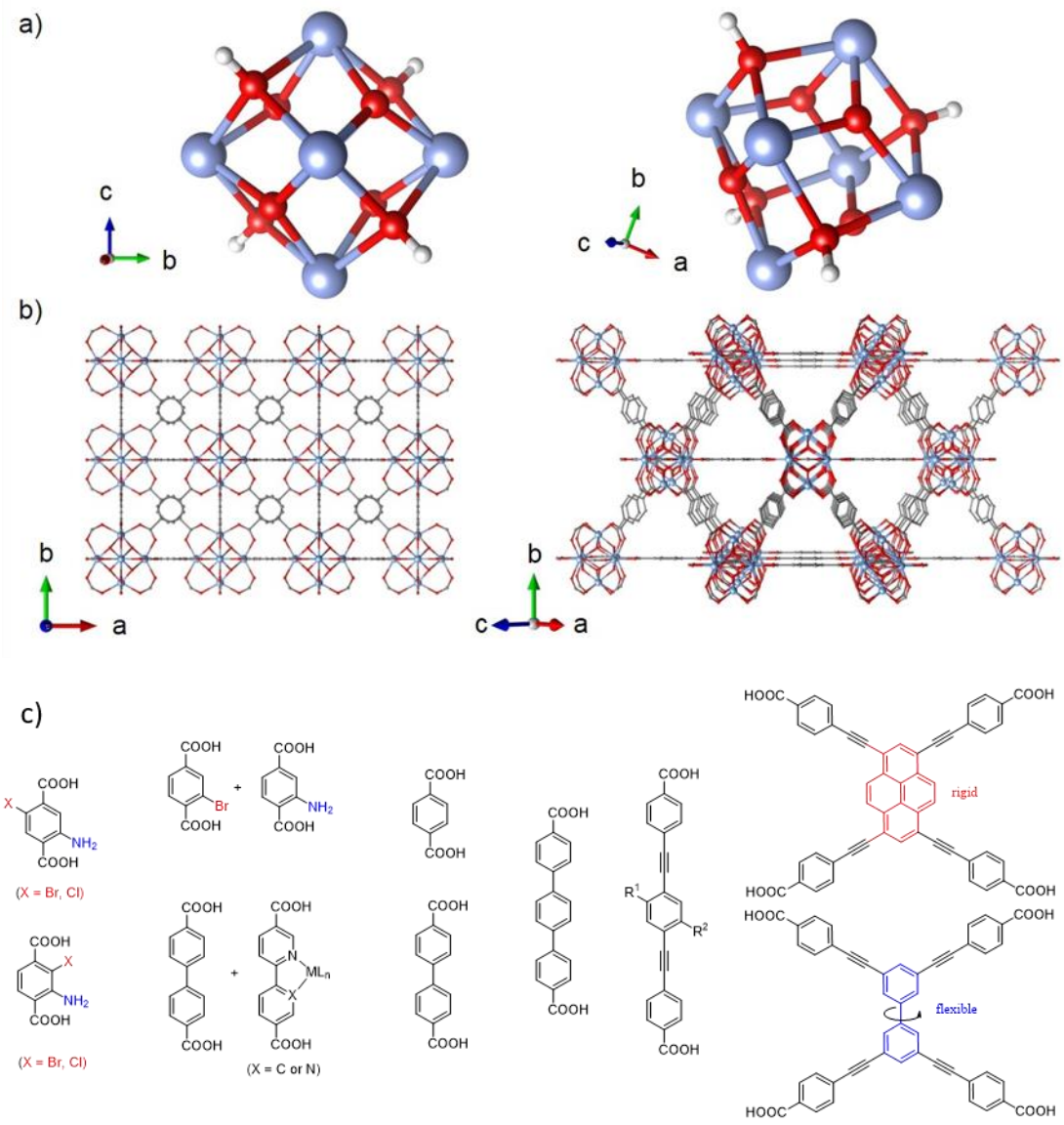

Figure 1.2

a) UiO-66 SBU; zirconium (blue), oxygen (red), carbon (grey), hydrogen (white) b) Crystal structure of UiO-66 c) A selection of the numerous carboxylate linkers used in combination with the $Zr_6O_4(OH)_4$ SBU. CIF can be found on the open-access Crystallography Open Database at http://www.crystallography.net/cod/

The MIL-53 materials are a well-studied group of MOFs that generally exhibit high stability, particularly in the case of Al-MIL-53 and Cr-MIL-53.[46-48] Consisting of infinite chains of $M(OH)_2$ octahedra (with M being Fe^{3+}, Al^{3+}, Ga^{3+}, Cr^{3+}, In^{3+} or Sc^{3+}) and terephthalate ligands, these materials are well known for their interesting breathing behaviour in the presence of guests.[49,50] Breathing is a reversible phenomenon whereby the pores of the MOF contract upon certain guest uptake, such as water and carbon dioxide. In the case of Al-MIL-53 differences in cell volume of up to 40% have been observed.[51]

Another series of MIL materials, MIL-100 and MIL-101, use trimeric Cr_3O SBUs and 1,3,5-benzenetricarboxylic acid (BTC) and 1,4-benzenedicarboxylic acid (BDC), respectively to form frameworks with extremely large pores, in the range of 25-34 Å. The structures are based on supertetrahedra consisting of $Cr_3O(H_2O)_2(OH)$ corners linked either by BTC on the faces or BDC along the edges of the supertetrahedra.[52,53] Showing high thermal and chemical stability, these materials have shown potential in areas such as gas storage and catalysis. [52-54] MIL-100 can also been synthesised using Fe, Sc, Al, Mn and V and MIL-101 with Al and Fe, with a variety of linkers.[55-57]

By using the principle of isoreticular synthesis, together with the ever-expanding library of organic linkers[58] and SBUs[32] the discovery of new structures and tuning of existing, well-studied materials continues at an exponential rate.[59]

1.2 Applications of porous materials

1.2.1 Gas storage

1.2.1.1 Hydrogen storage

Hydrogen possesses high energy density (by weight), environmentally clean combustion products and is naturally abundant; for these reasons it is considered as one of the best alternatives to fossil fuels.[60] However, its volumetric energy density under ambient conditions is extremely low, which presents the need for lightweight porous materials that can store hydrogen, ideally at near ambient conditions,[61] in densities comparable to or greater than that of liquid hydrogen. Other necessary characteristics include low desorption temperature, reversibility, stability to cycling and low cost.[62]

Some of the first MOFs studied for hydrogen storage were the zinc based MOFs MOF-5, IRMOF-6, and IRMOF-8 by Rosi et al.[35] Despite the hundreds of MOFs studied for hydrogen storage since,[62] MOF-5 remains amongst the best known cryogenic hydrogen storage materials with uptake of 10.0 wt% at 100 bar and 77 K.[60,63]

It has been observed that the incorporation coordinatively unsaturated metal sites can improve hydrogen uptake performance by increasing the interaction with hydrogen molecules. This strategy was used by Long and co-workers to achieve high hydrogen heats of adsorption of 9.5– 10.1 kJ mol^{-1} in MOFs containing exposed Mg^{2+} or Mn^{2+} metal centres.[64-66]

Examples of some of the highest hydrogen uptakes known for MOFs are seen for the zinc based MOF-200 and the copper based NU-100. With BET surface areas of 4530 m^2/g (MOF-200) and 6143 m^2/g (NU-100), the materials were seen to adsorb 14.0 wt% at 80 bar and 14.09 wt% at 70 bar respectively at 77 K.[67,68]

Cooper and co-workers reported the use of the HCMP-1 and HCMP-2 polymer networks for use in hydrogen uptake (shown in Figure 1.3). The materials showed adsorption of 0.96 wt% and 1.17 wt% at 77 K and 1.13 bar.[27] Further work by Li et al using HCMP-1 showed that it exhibits moderate uptake of 1.6 wt% at 77 K at 1 bar, however lithium doping improved this value significantly, reaching a hydrogen uptake of 6.1 wt% at Li-CMP loadings of 0.5 wt%. Beyond this value, increased lithium loading is seen to decrease H_2 uptake. [69]

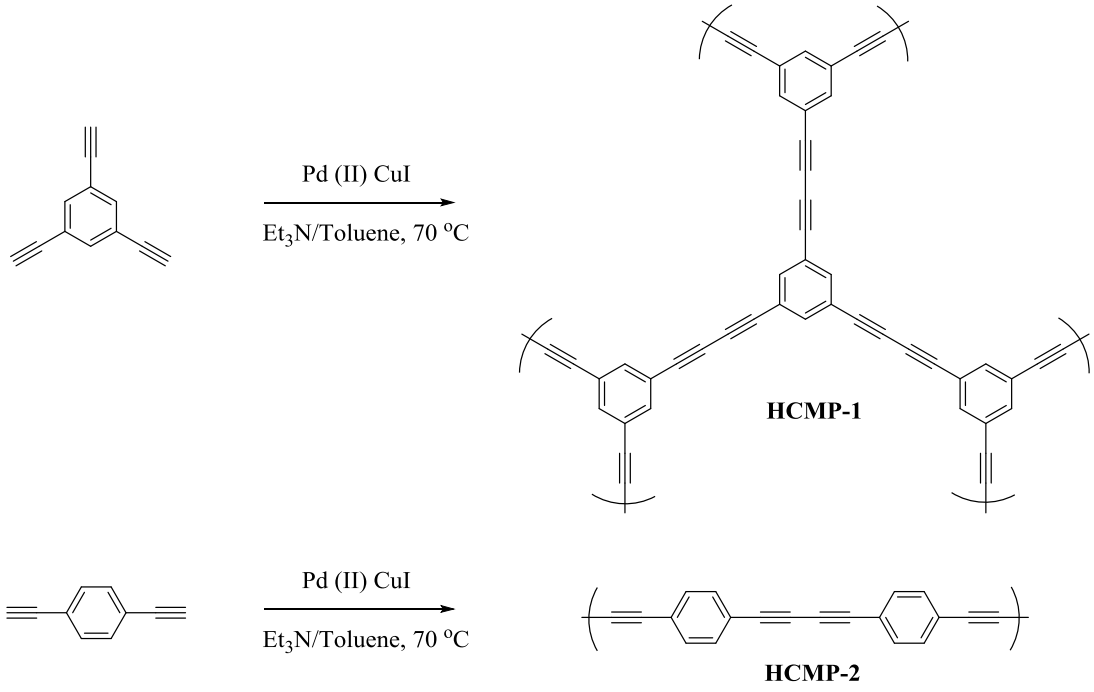

Figure 1.3

Synthesis and structure of HCMP-1 and HCMP-2. Figure redrawn based on original from reference 27.

1.2.1.2 Methane storage

Natural gas, comprising mostly of methane, is employed as a feedstock for syngas in many countries. It is typically stored under high pressures of around 207 bar, which involves expensive multi-stage compression.[60] An appealing alternative is to adsorb the gas onto porous materials at lower pressures.[70] Methane storage capacities of MOFs depend largely on high overall porosity, as demonstrated by its total pore volume and/or BET surface area.[71,72] In addition, it is seen that small pores are often important in the uptake of methane, such as those in PCN-14. PCN-14 exhibits an extremely high volumetric methane capacity of 230 v/v (15 wt% based on the PCN-14 crystal density of 0.871 g/cm^3) at 35 bar and 298 K, outperforming the U.S. Department of Energy (DOE) volumetric storage target of 180 v/v. High heats of adsorption of around 30 kJ/mol are also demonstrated,[71] resulting in a promising material for methane storage.

Coordinatively unsaturated metal sites have also been shown as desirable for methane storage, particularly at lower pressures. For example, in the case of MOF-74 the metal sites offer primary binding sites for methane, with total capacity of up to 230 v/v (13.7 wt% based on a crystal density of 1.195 g/cm^3) in the case Ni-MOF-74 at 298 K, 35 bar.[73] It is noted by He et al. that the effect of various functionalities on methane uptake is still unclear, requiring further study.[71]

The CMP COP-1 exhibits methane uptake of 2.9 wt% at 298 K, 18 bar, yet, as seen with H_2 uptake experiments, the materials performance increases following lithium ion loading, with uptake of 3.9 wt% for Li@COP-1.[74] Compared with MOFs, this uptake capacity is still relatively low.

1.2.1.3 Carbon dioxide capture

Approximately 60 % of global warming effects are linked to carbon dioxide emission.[75] As such, sequestration of carbon dioxide from the flue gas of fossil fuel burning power plants is considered important in the mitigation of global warming. The relatively low partial pressures of CO_2 in flue gas streams presents a challenge for solid sorbents, as they will generally require high performance at these pressures (~0.1 bar), and also high selectivity.[76]

Mg-MOF-74 exhibits one of the highest uptakes of CO_2 measured at 0.15 bar and 303 K, adsorbing 20.6 wt%. It also exhibits high selectivity over both CH_4 and N_2 making this MOF an excellent candidate for carbon dioxide binding from flue gas streams.[75,77] Cr-MIL-100, first reported by Férey et al. in 2004, has a large Langmuir surface area (around 3100 m^2/g) and possesses high chemical/hydrothermal stability.[78] It possesses one of the highest heats of adsorption known for CO_2 at 62 kJ/mol. Uptake is seen to be relatively high at elevated pressures, adsorbing 44.2 wt%, at 50 bar and 304 K. Some of the highest CO_2 uptakes known for MOFs are exhibited by the zinc based frameworks MOF-200 (BET surface area of 4530 m^2/g) and MOF-210 (BET surface area of 6240 m^2/g), both of which adsorb 73.9 wt%, at 50 bar and 298 K.[79-81]

Cooper and co-workers have reported a series of CMPs, shown in Figure 1.4, for CO_2 uptake that utilize varying functionalities such as carboxylic acids, amines, hydroxyls and methyls.[82] It was observed that absolute surface area and pore volume did not solely define CO_2 uptake at 298 K and 1 bar, and at this temperature and pressure CMP-1 exhibits the highest uptake (5.2 wt%), followed by CMP-1-$(OH)_2$

(4.7 wt%) despite the latter having higher surface area. CMP-1–$(CH_3)_2$ exhibited the lowest uptake (4.136 wt%).

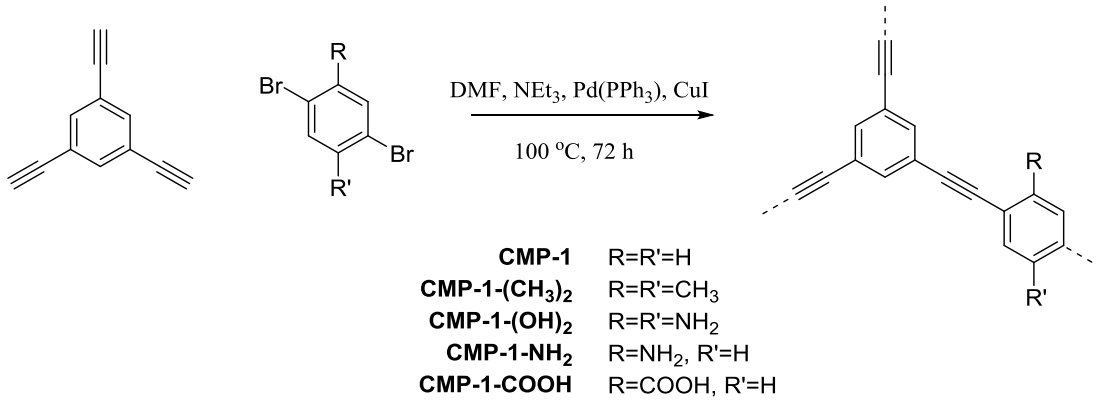

Figure 1.4

Synthesis of functionalised CMPs. Figure redrawn based on original from reference 82.

1.2.2 Catalysis

With the various types of active sites available in MOFs, which include coordinatively unsaturated metal sites metalloligands, functional organic sites, along with the ability to embed metal nanoparticles in the pores, MOFs offer an interesting platform for heterogeneous catalysis.[83] The ability to easily separate and reuse the heterogeneous catalyst is an attractive feature of these materials, particularly in large scale reactions, and the extremely tuneable nature of MOFs allows innumerable possibilities in pore size, functionality and reactivity. Figure 1.5 shows the various methods of incorporating catalytic sites into MOFs.

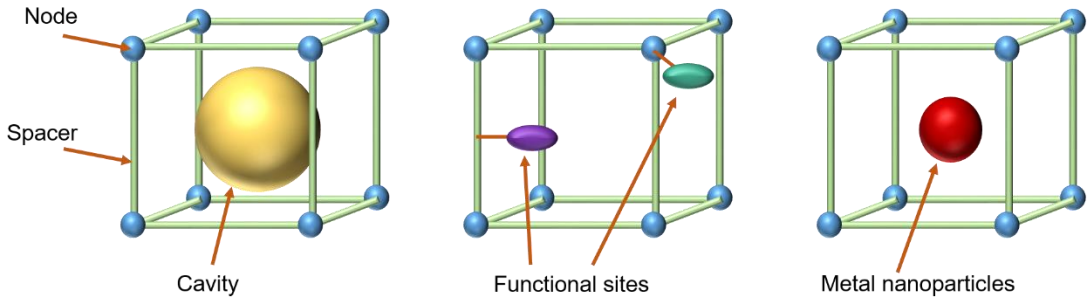

Figure 1.5

Schematic showing from left to right the potential catalytic sites in MOFs, postsynthetic modification methods, and metal nanoparticles embedded in the pores. Figure redrawn based on original from reference 83.

Corma and co-workers examined the catalytic activity of $Pd(2\text{-pymo})_2$, a palladium based MOF, for its use in catalysing Suzuki cross-coupling reactions, alcohol oxidation, and olefin hydrogenation.[84] It was seen to catalyse the reaction between phenylboronic acid and 4-bromoanisole with high conversion (85 %) and selectivity (99 %), after 5 h at 150 ^{o}C. The MOF was separated and reused, showing minimal loss in catalytic activity and selectivity. Cinnamyl alcohol was oxidised with Pd-MOF as the catalyst, 100 % conversion was achieved using air at atmospheric pressure in 20 h, with a selectivity of 74 % to cinnamylaldehyde, which is comparable to palladium-catalysed oxidations of allylic alcohols.[84,85] The conversion of 1-octene to octane was assessed, revealing total conversion under H_2 (2 atm) after 40 min.

Haruta and co-workers developed an effective method for inserting gold nanoparticles into a variety of MOFs.[86] The procedure involved grinding in air the volatile organogold complex, $Me_2Au(acac)$, with the MOF of interest, which introduced it into the MOF's pores. Treating the resulting solid with a stream of 10

vol% H_2 in N_2 at 120 ^oC for 2 hours afforded the gold inserted MOF. These gold cluster containing MOFs could then be used as catalysts for a variety of aerobic oxidation reactions of alcohols. It was observed that product selectivity could be altered depending on the selection of the MOF.

CMPs can be synthesised using monomers containing catalytic sites functionalities, or alternatively catalysts can be incorporated post-synthesis.[28] A CMP known as FeP-CMP, reported by Chen et al., uses iron inserted porphyrin monomers to provide catalytic activity in the oxidation of sulphide, with high conversion of up to 97%. FeP–CMP was seen to be active with a broad scope of substrates, including alkyl, aromatic and cyclic sulphides.[87]

Palkovits et al. reported the post-synthetic insertion of a triazine-based CMP with platinum, resulting in the material Pt-CTF (CTF=conjugated s-triazine-based framework). This material was tested for the oxidation of methane to methanol and was seen to exhibit catalytic activity comparable to that of the homogeneous analogue.

1.2.3 Sensing

The potential of MOFs in sensing applications is substantial because of their previously mentioned attributes such as high surface area and porosity, flexibility, structural diversity as well as their highly tuneable nature. As with any sensor, the use of MOFs in sensing relies upon detectable changes, such as electrical, photophysical, or mechanical, in response to physical or chemical stimuli.

In 2007 Lu et al. reported a tungsten and copper based MOF which showed remarkable solvatochromic behaviour in the presence of various solvents of ranging

polarity.[88] The solvents tested were acetonitrile, water, methanol, dimethylformamide, acetone, ethanol and chloroform. It was observed that with the increasing polarity of the solvent, the adsorption bands were shifted to lower wavelength. It was noted that such good solvent dependence indicates that the MOF may offer efficient sensing for these solvents.

Luminescent MOFs have been used for sensing various volatile organic chemicals and small molecules including H_2S, H_2O, CO_2.[89] The silver functionalised Tb-amp MOF (amp = adenosine monophosphate) exhibits a response to hydrogen sulphide by fluorescence quenching as a result of Ag_2S formation. [90] The photoluminescence of the MOF $MV[Mn_2Cu_3(mpba)_3(H_2O)_3]\cdot 20\ H_2O$ is seen to increase with increased water loading. Furthermore, its emission is also seen to shift upon exposure to carbon dioxide.[91]

Examples of sensing with CMPs are less common than those with MOFs. However, the first example was reported by Liu et al., whereby TCB–CMP, a carbazole based CMP shown in Figure 1.6, was seen to display fluorescence enhancement when exposed to electron-rich arene vapours, such as 2,4-dinitrotoluene, 2-nitrotoluene, nitrobenzene, and 1,4-benzoquinone. However, when exposed to electron-deficient arene vapours, such as chlorobenzene, mesitylene, benzene and toluene, significant fluorescence quenching was observed.[92]

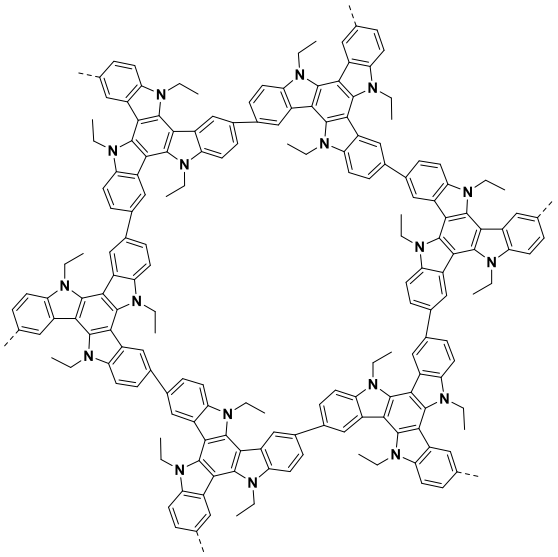

Figure 1.6

Carbazole-based CMP used as a chemical sensor for arenes. Figure redrawn based on original from reference 92.

1.3 Porous materials for the uptake of ammonia

Ammonia is a colourless gas readily identifiable by its pungent, suffocating odour. It is among the most extensively produced chemicals, with global production estimated at 147 million tons in 2006.[93] It is mostly used in the production of fertiliser, but other uses include the production of nitric acid, explosives, commercial cleaning products pharmaceuticals and as a refrigerant.[94-96] It has been classified as a high hazard toxic industrial chemical (TIC) that can be lethal, with exposure symptoms including nose and throat irritation, convulsive coughing, severe eye irritation, and respiratory spasms.[96] EU-OSHA have set long term (8 h) and short term (15 min) exposure limits of 25 ppm and 35 ppm, respectively.[97]

Effective uptake of ammonia is important regarding both the protection of the environment and to personnel at risk of being exposed. Current filters generally

employ activated carbon impregnated with metal salts such as zinc, silver, copper, and molybdenum, as well as triethylenediamine (TEDA), which is effective in trapping a broad range of TICs;[95,98-101] however more recent materials such as MOFs and POPs are seen to offer significant improvement in ammonia uptake. Potential improvements to activated carbons are thought to be largely limited by lack of adequate control over the pore size and pore functionality as a result of the highly amorphous nature of the carbon network.[99]

This section aims to present a comprehensive review of the literature examining MOFs and porous organic polymers as sorbents for ammonia.

1.3.1 MOFs

1.3.1.1 Ammonia uptake

In 2008, Britt et al. provided an important first step in the study of the dynamic adsorption of harmful gases in MOFs.[99] A selection of well-known MOFs (MOF-5, IRMOF-3, MOF-177, IRMOF-62, MOF-199 and MOF-74) were tested using kinetic breakthrough measurements as sorbents for ammonia, as well as sulphur dioxide, chlorine, tetrahydrothiophene, benzene, dichloromethane, ethylene oxide, and carbon monoxide, in dry (0% RH) conditions.

It was observed that the MOFs outperformed BPL activated carbon in the ammonia breakthrough experiments, with particularly high performance noted for IRMOF-3, MOF-74, and MOF-199 (Cu-BTC) with capacities of 6.2, 5.7 and 5.1 mmol g^{-1}, respectively under an ammonia concentration of 0.99%. It was noted that IRMOF-3 performed almost 18 times better than MOF-5, which has the same structure but

without an amino functionality, and was hypothesised that the addition of amino functionality provides a favourable hydrogen bonding site for ammonia. The high capacities of MOF-74 and MOF-199 were attributed to the coordinatively unsaturated sites (zinc and copper, respectively) within the frameworks that act as Lewis acids, and thus offer reactivity towards the Lewis basic ammonia. MOF-5, MOF-177 and IRMOF-62, containing no free coordinatively unsaturated sites or functional groups, were seen to have relatively poor dynamic ammonia capacities. It should be noted that the instability with respect to moisture of most of the MOFs tested is well known.[63, 104]

In 2009 Peterson et al. assessed the ammonia adsorption capacity of Cu-BTC (MOF-199) using breakthrough measurements under flows of dry (0% RH) and humid (80% RH) ammonia at a concentration of 1438 ppm (1000 mg/m^3).[105] The MOF was shown to exhibit high ammonia uptake, showing 6.6 mmol g^{-1} and 8.9 mmol g^{-1} in dry and humid conditions respectively, however MAS NMR, PXRD and N_2 isotherms showed that this was due to reaction with the framework as opposed to traditional adsorption. It was seen that the MOF reacted with ammonia to form a diammine−copper(II) complex under dry conditions and $Cu(OH)_2$ and $(NH_4)_3BTC$ were formed under humid conditions. Unsurprisingly, the formation of such compounds was at the cost of the structure and porosity of the framework. The decomposition of Cu-BTC as a result of ammonia exposure was first reported by Schlichte et al.[106]

MOF-74, originally discovered by Rosi and co-workers,[107] can be synthesised using a variety of metals which all produce the same topology;[108-110] thus the coordinatively unsaturated sites which form infinite 1D chains within the MOF can

be altered without changing its structure. The framework was used in 2011 by Glover et al. to study the effect of metal type on the uptake of toxic gases, whereby analogous materials constructed using zinc, copper, nickel and magnesium were subjected to both dry and humid flows of ammonia, cyanogen chloride, and sulphur dioxide.[111]

BET surface areas calculated from nitrogen isotherms at 77K showed that there were considerable differences between the synthesised materials, with Mg, Co, Ni and Zn-MOF-74 showing surface areas of 1206, 835, 599 and 496 m^2/g. Dry (0% RH) ammonia capacities of 7.6, 6.7, 2.3 and 3.7 mmol g^{-1} were measured for the Mg, Co, Ni and Zn MOFs, respectively, under ammonia flows of 1438 ppm (1000 mg/m^3). It is not certain whether the large differences in ammonia uptake were a result of the different metals or due to the variation in surface area. It is also noted that the surface areas of the MOFs used in this study are consistently lower than other reported values.[110] Interestingly, when these MOFs were measured under a humid (80% RH) flow of ammonia it was seen that the capacity was considerably lower than for the dry runs, with loadings of 4.3, 2.8, 1.9, and 1.7 mmol g^{-1} for the Co, Zn, Ni, and Mg analogues, respectively. It was proposed that binding of water to the coordinatively unsaturated sites in the MOFs competed with the binding of ammonia.

Spanopoulos et al. functionalised DUT-6 with –OH groups and measured ammonia isotherms of the material and non-functionalised DUT-6.[112] It was seen that the addition of hydroxy groups increased the equilibrium uptake of ammonia at 298 K and 1 bar from 12.0 to 16.4 mmol g^{-1}. A considerable difference at low pressures of ammonia was noted, with DUT-6 adsorbing only 0.8 mmol g^{-1} at 0.76 Torr in

comparison with DUT-6-OH, which adsorbed 4.7 mmol g^{-1}, once again suggesting functional groups capable of hydrogen bonding can have a favourable effect on the uptake of ammonia.

In 2011, Morris et al. synthesised UiO-66-NH_2 and then postsynthetically modified it to form a mixture of hemiaminal and aziridine functionalised UiO-66. Ammonia isotherms were measured which showed reversible ammonia uptake, with the hemiaminal functionalised UiO-66 adsorbing 5.5 mmol g^{-1} at 1 bar and 298 K and the aziridine functionalised UiO-66 adsorbing 7.9 mmol g^{-1} (1 bar, 298 K). The materials were shown to maintain their crystallinity following the sorption experiments.

In 2010, Lieder et al. studied the adsorption of ammonia on MIL-53 using ^{1}H MAS NMR. It was seen that the signal associated with the bridging hydroxyl group in the $Al(O_4)OH$ chains shifted from 2.3 ppm to 5.3 ppm upon ammonia adsorption, and an additional peak appeared at 0.4 ppm; this peak was attributed to non-interacting ammonia, which was comparable to chemical shifts measured for ammonia in the gas phase (0.3-0.8 ppm).[113,114] It was proposed that the presence of two ammonia peaks at 0.4 and 5.23 ppm indicated that the exchange of adsorbate molecules from the adsorbed to the free state is slow relative to their resonance frequencies.

A systematic study on the stability of a wide variety of MOFs against ammonia was conducted by Kajiwara et al. in 2014.[115] MOFs were evaluated using PXRD before and after exposure to ammonia up to 350 ^{o}C. The authors proposed three general trends in MOFs which showed ammonia stability: 1) MOFs which contained both oxophilic metal cations and linkers which bound via oxygen donors were highly

stable against ammonia; 2) MOFs containing inert (determined by water exchange rate constants for solvated cations) metal cations such as Al^{3+} and Cr^{3+} are more stable than those with labile cations such as Cu^{2+} and In^{3+}; 3) MOFs containing a neutral nitrogen donor linker were unstable against ammonia, whereas MOFs with anionic nitrogen donors were unaffected by ammonia.

Van Humbeck et al. reported ammonia isotherms of three MOFs containing functionality targeting ammonia uptake: UiO-66-NH_2, UiO-66-NH_3Cl and Fe-MIL-101-SO_3H were shown to have maximum uptakes of approximately 10.7, 12.0 and 17.9 mmol g^{-1} at 298 K and 1 bar. The addition of Brønsted acid functional groups was seen to provide large increases in ammonia uptake, which led to decoration of PAF-1 like polymer materials with Brønsted acid functionality, discussed in section 1.3.2.

Peterson et al. studied the effect of pelletisation, using high pressure pressing, on the ammonia breakthrough performance of UiO-66-NH_2.[116] Ammonia uptake was measured on a non-pressed sample, as well as samples pressed under 5000, 10000, 25000 and 100000 psi, which were subsequently ground into powders. Ammonia breakthrough testing of the as-made material revealed that it yielded highest ammonia uptake of the materials, with loadings of 3.3 mmol g^{-1}. Pressed samples showed a clear trend, with ammonia uptake decreasing with increasing pelletisation pressure. The increased pelletisation pressure also resulted in decreased surface areas and pore volumes of the materials, as measured by nitrogen at 77 K. Thus, the decrease in ammonia uptake of the pelletised materials was attributed to them having less available accessible pore volume and thus less accessible active sites for ammonia sorption.

Recently, in 2015 Jasuja et al. evaluated a range of MOFs as sorbents for ammonia by performing ammonia breakthrough experiments in both dry and humid conditions (0% RH and 80% RH) with ammonia concentration of 1438 ppm (1000 mg/m^3). The MOFs and their uptakes are shown in Table 1.1. Interestingly the MOFs containing the acidic groups, SO_3H and COOH exhibited relatively underwhelming performance (uptake <3 mmol/g) in comparison to materials containing functionalities expected to hydrogen bond with influent ammonia (UiO-66-OH and UiO-66-NH_2 showed higher capacities of ~5.7 and ~3.6 mmol/g, respectively). This was explained by suggesting that the acidic groups in question were bulky relative to the pores of the MOF resulting in such decreased pore volume as to hinder any appreciable ammonia uptake. Furthermore, decreased uptake in humid conditions is often observed in comparison with dry conditions, which is unusual. This is attributed to functionalisation causing water to fill the pores more extensively than for the non-functionalised material, leaving less space for ammonia. In the case of ZnBTTB the high uptake in dry and humid conditions was attributed to the poor stability of the material, resulting in ammonia chemically reacting with the material.

Table 1.1 MOFs examined for ammonia uptake by Jasuja et al.[117]

MOF	**Functional group**	**Dry ammonia uptake (mmol/g)**	**Humid ammonia uptake (mmol/g)**
ZnBTTB	$(–COOH)_2$	4.59	20.26
DMOF-A		0.48	1.18
DMOF-TM2		0.15	4.57
UiO-66		1.79	2.75

UiO-66-NH_2	(–NH_2)	3.56	3.01
UiO-66-NO_2	(–NO_2)	1.98	1.6
UiO-66-OH	(–OH)	5.69	2.77
UiO-66-$(OH)_2$	(–$OH)_2$	2.29	2.16
UiO-66-SO_3H	(–SO_3H)	2.24	1.45
UiO-66-$(COOH)_2$	(–$COOH)_2$	2.83	1.83

1.3.1.2 Computational studies of ammonia uptake

Snurr and co-workers performed grand canonical Monte Carlo (GCMC) simulations in order to predict ammonia adsorption isotherms and heats of adsorption in functionalised MIL-47, IRMOF-1, IRMOF-10, and IRMOF-16.[118] Four different functional groups were used (–OH, –Cl, –C=O, and –COOH), attached to the aromatic linkers of the MOFs, and it was seen that their incorporation could greatly enhance the adsorption of ammonia. Specifically, at low pressure the increase in uptake correlated with the binding strength of ammonia to the functional groups. Furthermore, smaller pore sizes and increased density of functionality aided ammonia uptake at low pressures.

Snurr and co-workers later performed density functional theory (DFT) calculations GCMC simulations to study the binding energies of ammonia and water with a large variety of functional groups found in MOFs.[119] Differences in the binding energy of water and ammonia to the various functionalities was calculated, indicating whether ammonia may be adsorbed preferentially over water (Table 1.2). The computational methods revealed that ammonia binds most strongly with metal carboxylate groups,

however in these cases the difference between the binding energy of ammonia and that of water varied significantly.

Table 1.2 Calculated lowest binding energies (kJ/mol) of ammonia and water on naphthalene and 21 functional groups; the right column indicates the difference between the lowest binding energies of ammonia and water, thus a positive value indicates that the binding of ammonia is stronger than the binding of water. All data from reference[119].

Functional group	**NH_3**	**H_2O**	**lowest binding energy of H_2O − lowest binding energy of NH_3**
R−COOCu	−161.2	−97.8	63.4
R−COOAg	−84.9	−51.5	33.4
R−HSO_4	−65.9	−46.9	19
R−COOLi	−81.1	−70.2	10.9
R−OOH	−37.2	−27.7	9.5
R−SO_3H	−52.1	−42.7	9.4
R−OP=$O(OH)_2$	−54.2	−44.9	9.3
R−P=$O(OH)_2$	−50.8	−42.7	8.1
R−OH	−34.3	−26.5	7.8
R−COOH	−41.8	−37.2	4.6
R−Cl	−11.2	−11.9	−0.7
R−NCO	−15.6	−16.8	−1.2
R−NO_3	−14.7	−16.7	−2.0
R−F	−12.9	−15.2	−2.3
R−NH2	−18.8	−21.2	−2.4
R (Napthalene)	−8.2	−10.7	−2.5
R−COONa	−62.3	−65.0	−2.7
R−CH_2−F	−13.9	−19.5	−5.6
R−C(=O)−H	−16.4	−23.3	−6.9
Carbonyl	−16.1	−23.4	−7.3
R−CH_2−NH_2	−18.3	−28.1	−9.8
R−COOK	−48.0	−61.8	−13.8

In 2010, DFT calculations and GCMC simulations were used to calculate the binding energies of Cu-BTC with a range of substrates, including ammonia, by Watanabe

and Sholl.[120] It was calculated that ammonia bound to the strongly Lewis acid Cu site, with a binding energy of approximately 0.8 eV, and the binding of a second ammonia molecule to a Cu site resulted in a lower binding energy than the first. Furthermore, it was calculated that for ammonia to be bound to each Cu site in Cu-BTC, low pressures of only 10^{-2} mbar are necessary at 300 K.

Huang et al. in 2013 used REaxFF molecular dynamics simulations to study the adsorption of ammonia and water on Cu-BTC.[121] It was observed that the Cu-BTC framework partially collapses upon adsorption of just one ammonia molecule per copper site, however the Cu-Cu dimer remained stable under the investigated conditions (301, 318 and 348 K). The molecule distribution of mixtures of water and ammonia on Cu-BTC at 301 K were studied; the distribution was recorded over a simulation lasting 200 picoseconds.

It was observed that the small number of water molecules that change from the gas phase indicates that most water molecules do not interact with Cu-BTC and remain as free molecules in the pores of the MOF. However, when the number of water molecules is increase from 24 to 96, the number of adsorbed ammonia molecules is significantly reduced from 86 to 48. This result suggests that despite the lack of chemisorption exhibited by water, the presence of water affects ammonia interaction with the framework and thus reduces the amount of chemisorbed ammonia molecules. It also suggests that the framework has higher selectivity for ammonia than water. Enhanced ammonia uptake in humid conditions due to dissolution of ammonia in the water film in the pores of materials is often seen, however the authors note that, the amount of water present in their calculations is not sufficient to provide such pore coverage.

Supronawicz et al. conducted DFT calculations to determine interaction energies of a variety of small gases, including ammonia, with the Cu-BTC framework.[122] It was seen that the adsorption enthalpy for ammonia was the highest of the materials studied, at -91.5 kJ mol^{-1}, suggesting that ammonia is adsorbed preferentially over water, which was seen to exhibit an interaction energy of -60.9 kJ mol^{-1}.

1.3.1.3 Ammonia uptake in MOF composites

Bandosz and co-workers have conducted ammonia adsorption experiments on MOFs and MOF/graphite oxide composite materials,[123-129] using MOF-5, Cu-BTC and Fe-MIL-100. Dry (0% RH) and humid (70% RH) breakthrough experiments were performed on graphite oxide, MOF-5 and MOF-5/graphite oxide composites (containing 5 wt% graphite oxide). It was seen that the graphite oxide (GO) performed better against ammonia (1000 ppm) than MOF-5, adsorbing 3.29 and 3.59 mmol g^{-1} in dry and humid conditions, respectively, in comparison with 0.35 and 2.50 mmol g^{-1} for MOF-5. The composite material was seen to perform better than MOF-5, but worse than pure GO, exhibiting uptakes of 0.40 and 3.14 mmol g^{-1} in dry and humid conditions.[123] Subsequent work involved increasing the amount of GO in MOF-5 samples to 10, 20 and 55 wt%. Dry ammonia breakthrough experiments were conducted and it was observed that increasing GO content resulted in increased ammonia uptake; however only the 55 wt% MOF-5/GO sample outperformed GO itself, with an uptake 4.8 mmol g^{-1} (in comparison with 3.29 measured mmol g^{-1} for GO).[126] A mechanism of adsorption was proposed which included intercalation between GO layers, adsorption at the GO-MOF-5 interface, and hydrogen bonding to the Zn-O clusters of MOF-5; however it should be noted

that hydrogen bonding of ammonia to the Zn-O clusters of MOF-5 is thought to cause complete destruction of the framework.[130]

Fe-MIL-100/GO and Cu-BTC composites were studied Bandosz and co-workers.[124, 127,128] In the case of Fe-MIL-100/GO, the MOF was deemed a relatively poor candidate for formation of the composites due to its structure, however the materials showed relatively good ammonia uptake in dry conditions with a n ammonia concentration of 1000ppm; the composite containing 4 wt% GO performed best, adsorbing 5.3 mmol g^{-1} ammonia, followed by Fe-MIL-100 which adsorbed 4.3 mmol g^{-1}, interestingly 9 wt% MIL/GO followed with an uptake of 3.55 mmol g^{-1}. In the case of Cu-BTC, a composite material containing 18 wt% GO performed best with an uptake of 8.8 mmol g^{-1} in comparison with the 6.7 mmol g^{-1} that was measured for Cu-BTC. It was noted that ammonia adsorption capacities on the composites were higher than those calculated for simple physical mixtures of the GO and MOF, which suggested there may be a synergetic effect between the MOF and graphite oxide layers. [127,124]

In 2013, Peterson et al. formed composites using $Zr(OH)_4$ and Cu-BTC by pressing various mixtures of the materials under high pressure (5000 psi) and then grinding the resulting pellet. These materials were then subjected to ammonia breakthrough testing in both 0% RH and 80% RH conditions at ammonia concentrations of 1438 ppm.[131] In dry conditions the materials corresponded with hypothetical loadings based on summing the uptake of the components, with pure zirconium hydroxide (100Z) adsorbing the least ammonia (0.9 mmol g^{-1}) and Cu-BTC (100C) adsorbing the most (7.8 mmol g^{-1}). In humid conditions the 100Z material showed decreased performance, which was attributed to the presence of water molecules taken to be

responsible for blocking active sites, in addition to the sheet-like pores of the material which may reduce the dwell time of ammonia within the pore structure.[131] However the 75Z/25C and 50Z/50C composite materials provided increase ammonia uptake in comparison with the dry experiments, and in comparison with the hypothetical loading of the components, which indicates synergistic effects. In particular, 75Z/25C exhibited approximately double ammonia uptake in comparison with the hypothetical uptake. It was proposed that this behaviour was due the moisture allowing ammonia to enter into solution, which allows it to react with the CuBTC MOF substrate more efficiently.[131]

1.3.2 Ammonia uptake in POPs and COFs

In 2010 Doonan et al. examined the use of COF-10, a crystalline covalent organic framework, as an ammonia sorbent.[132] Ammonia isotherms were conducted at 298 K and 1 bar which revealed total capacity of 15 mmol g^{-1}, outperforming Amberlyst 15 (11 mmol g^{-1}), 13X zeolite (9 mmol g^{-1}), and MCM-41 mesoporous silica (7.9 mmol g^{-1}). It should be noted that adsorption of ammonia at lower pressures was considerably lower than the benchmark materials mentioned, at less than 1 mmol g^{-1} at 25 Torr. The Lewis acidic boron groups which make up the structure of the material were attributed to the high uptake of Lewis basic ammonia. It was seen that adsorption and desorption could be cycled several times with only slight loss in overall ammonia uptake despite significant deterioration of pore volume, as measured by nitrogen isotherms at 77K. The decrease in pore volume was attributed to turbostratic disorder, whereby the planes of the COF are no longer aligned due to the ammonia cycling. This was supported by MASNMR data which indicated that connectivity of the framework was not disrupted.

In 2012, Peterson et al. evaluated the porous organic polymer, NU-POP-1 as a sorbent for ammonia, sulphur dioxide, octane and cyanogen chloride.[133] Breakthrough experiments were carried out in 0% RH conditions and 80% RH conditions, under a flow of ammonia with a concentration of 1000 mg/m^3 (1438 ppm), and showed ammonia uptake of 5.56 and 6.17 mmol g^{-1} in dry and humid conditions, respectively. The material was compared to a zinc oxide and triethylenediamine (TEDA) impregnated BPL activated carbon, which exhibited ammonia uptakes of 0.69 and 0.45 mmol g^{-1} in dry and humid conditions, respectively. The good uptake exhibited by NU-POP-1 was explained by the presence of accessible nitrogen and oxygen groups within the polymer network, shown in Figure 1.7 in blue and red respectively, which can act as hydrogen bond acceptors using their available lone pairs, in addition to the highly microporous nature of the material.

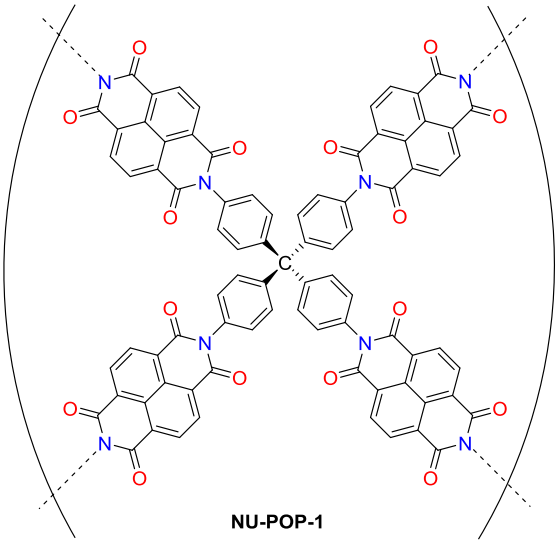

Figure 1.7

NU-POP-1. Available oxygen (red) and nitrogen (blue) can act as hydrogen bond acceptors. Figure redrawn based on original from reference 133.

Weston et al. demonstrated the synthesis of readily metalated catechol-containing porous organic polymers,[134] using a cobalt-catalysed acetylene trimerisation strategy.[135-138] In 2013 it was reported that this material, along with copper and zinc metalated analogues, had been evaluated as sorbents for toxic chemicals, namely ammonia, cyanogen chloride, octane and sulphur dioxide.[139] This was achieved by carrying out breakthrough experiments in both dry and humid conditions. The metalated analogues containing both copper and zinc (13.8 wt% and 16.3 wt%, respectively) resulted in coordinatively unsaturated metal sites throughout the polymer network. It was noted that metalation resulted in significant reduction in pore volume of the materials, dropping from 0.51 cm^3g^{-1} for the non metalated polymer, to 0.20 and 0.28 cm^3g^{-1} for the zinc and copper metalated polymers, respectively. Ammonia uptake in dry conditions, under a flow of 1438 ppm was measured to be 0.70, 1.36 and 2.10 mmol g^{-1} for the non-metalated, zinc inserted and copper inserted polymers, respectively, showing no correlation with pore volumes. All materials were seen to gain increased performance from the presence of water, showing uptakes of 1.31, 3.32 and 4.32 mmol g^{-1} in humid ammonia breakthrough tests. The ammonia uptake exhibited by the non-metalated materials was attributed to the acid catechols interacting with the ammonia, in addition to simple physisorption and pore filling. The Lewis acidity of the zinc and copper was cited as the reason for the increased uptake in the case of the metalated polymers.

In 2014 Humbeck et al. reported the synthesis of porous polymers containing functional groups for the uptake of ammonia.[140] PAF-1 was functionalised with -NH_2, -NH_3Cl, and -SO_3H groups and uptake of ammonia was determined by conducting isotherms at 298 K. At 1 bar uptake of approximately 2.9, 6.0, 11.2 and

12.1 mmol/g was measured for the non-functionalised, -NH_2, -NH_3Cl, and -SO_3H functionalised polymers respectively. Further synthesis of PAF like materials to contain multiple carboxylic acid groups per monomer unit yielded highly interpenetrated structures with a high density of COOH groups which were thought to cooperatively bind ammonia within the polymer network. Increased ammonia uptake was observed with the carboxylic acid containing materials, showing up to approximately 17.7 mmol g^{-1} ammonia uptake at 1 bar and 298 K, depending on the synthetic route. Such high uptake was attributed to cooperative binding of single ammonia molecules between multiple carboxylic acid groups.

1.3.3 Summary and strategy

The performance of the most recent porous materials for the uptake of ammonia has been summarised below in Table 1.3. It is clear that functionality plays an important role in ammonia uptake, with high performing materials utilizing hydrogen bonding, coordinatively unsaturated metal sites and acid-base interactions for gas capture. It is also evident that extremely large surface areas and pore volumes do not seem to be a prerequisite for high performance, with the higher performing materials possessing surface areas typically less than 1600 m^2/g.

Table 1.3 Uptake of ammonia adsorbed before breakthrough by current porous materials

Material	**Ammonia uptake at breakthrough (mmol/g)**	
	Dry (0% RH)	**Humid (80% RH, unless stated otherwise)**
Cu-BTC/GO (18 wt%)[|, 127]	8.8	-
Cu-BTC[*, 131]	7.8	7.7
Mg-MOF-74[‡, 111]	7.6	1.7

Co-MOF-74[‡, 111]	6.7	4.3
Cu-BTC[‖, 127]	6.7	-
Cu-BTC[*, 105]	6.6	8.9
IRMOF-3[†, 99]	6.2	-
Zn-MOF-74[†, 99]	5.7	-
UiO-66-OH[‡, 117]	5.69	2.77
NU-POP-1[*, 133]	5.56	6.17
Fe-MIL-100[‖, 128]	5.30	-
Cu-BTC[†, 99]	5.1	-
MOF-5/graphite oxide (55 wt% GO) [§, 126]	4.81	-
ZnBTTB[‡, 117]	4.59	20.26
$Zr(OH)_4$/ Cu-BTC (50:50)[*, 131]	4.4	5.8
Fe-MIL-100/GO (4 wt%)[‖, 128]	4.30	-
Zn-MOF-74[‡, 111]	3.7	2.8
UiO-66-NH_2[‡, 117]	3.56	3.01
Fe-MIL-100/GO (9 wt%)[‖, 128]	3.55	-
UiO-66-NH_2[*,116]	3.3	-
Graphite oxide[§, 123]	3.29	3.59 (70% RH)
UiO-66-$(COOH)_2$[‡, 117]	2.83	1.83
$Zr(OH)_4$/ Cu-BTC (75:25)[*, 131]	2.4	5.2
Ni-MOF-74[‡,111]	2.3	1.9
UiO-66-$(OH)_2$[‡, 117]	2.29	2.16
UiO-66-SO_3H[‡, 117]	2.24	1.45
MOF-5/graphite oxide (20 wt% GO) [§, 126]	2.23	-
Catechol-containing POP (Zn inserted)[*, 139]	2.10	4.32
UiO-66-NO_2[‡, 117]	1.98	1.6

UiO-66[‡, 117]	1.79	2.75
$Zr(OH)_4$/ Cu-BTC (90:10)[*, 131]	1.4	1.5
Catechol-containing POP (Cu inserted)[*, 139]	1.36	3.32
IRMOF-62[†, 99]	1.35	-
MOF-5/graphite oxide (10 wt% GO) [§, 126]	1.29	-
$Zr(OH)_4$[*, 131]	0.9	0.5
Catechol-containing POP[*, 139]	0.70	1.31
Triethylenediamine impregnated BPL Carbon[*, 133]	0.69	0.45
DMOF-A[‡, 117]	0.48	1.18
MOF-177[†, 99]	0.45	-
MOF-5/graphite oxide (5 wt% GO) [§, 123]	0.4	3.14 (70% RH)
MOF-5[†, 99]	0.35	-
MOF-5[§, 123]	0.35	2.50 (70% RH)
DMOF-TM2[‡, 117]	0.15	4.57
BPL Carbon[†, 99]	0.059	-

[*] Flow rate: 20 mL/min, NH_3 concentration: 1000 mg/m^3 (1438 ppm), amount of sorbent: 55 mm^3, temperature: 20 ^oC

[†] Flow rate: 25 mL/min, NH_3 concentration: 0.99 %, amount of sorbent: 2 cm^3, temperature: 25 ^oC

[‡] Flow rate: 20 mL/min, NH_3 concentration: 1000 mg/m^3 (1438 ppm), amount of sorbent: 50 mm^3, temperature: 20 ^oC

[§] Flow rate: 450 mL/min, NH_3 concentration: 1000 ppm, amount of sorbent: 1.5 cm^3, temperature: N/A

[‖] Flow rate: 225 mL/min, NH_3 concentration: 1000 ppm, amount of sorbent: 1.5 cm^3, temperature: N/A

The uptake of ammonia at 1 bar, 298 K from isotherms for various materials has been summarised in Table 1.4. As seen with lower pressure breakthrough data, high uptake at 1 bar is seen in materials with functional groups which offer hydrogen bonding, coordinatively unsaturated metal sites and acid-base interactions with ammonia. The highest uptake, achieved by Fe-MIL-101-SO_3H combined acidic functionality and a large surface area of around 1900m^2/g. At higher pressures, it appears the importance of greater surface area and pore volume is more pronounced.

Table 1.4 Uptake of ammonia by current porous materials from isotherms at 1 bar, 298K

Material	**Uptake of ammonia at 1 bar, 298 K (mmol/g)**
Fe-MIL-101-SO_3H [140]	17.9
DUT-6-OH [112]	16.4
COF-10 [132]	15
PAF-1-SO_3H [140]	12.1
UiO-66-NH_3Cl [140]	12.0
DUT-6 [112]	12.0
PAF-1-NH_3Cl [140]	11.2
Amberlyst 15 [132]	11
UiO-66-NH_2 [140]	10.7
13X zeolite [132]	9
Aziridine-UiO-66 [141]	7.9
MCM-41 [132]	7.9
PAF-1-NH_2 [140]	6.0
Hemiaminal-UiO-66 [141]	5.5
PAF-1 [140]	2.9

The aims of this project have been focussed on the synthesis and characterisation of water stable MOFs and porous polymers for use as ammonia sorbents, and their evaluation for purpose using dynamic ammonia micro-breakthrough experiments.

Porous materials have been synthesised containing various densities of functional groups targeted at interaction with ammonia by exploiting hydrogen bonding, coordinatively unsaturated metal sites and acid-base interactions, often simultaneously. The results presented in this work demonstrate the highly versatile and tuneable nature of these classes of porous materials concerning application to ammonia uptake.

1.4 References

1. K. Ishizaki, S. Komarneni and M. Nanko, in *Porous Materials*, Springer US, 1998, vol. 4, ch. 1, pp. 1-11.
2. M. E. Davis, *Nature*, 2002, **417**, 813-821.
3. K. K. Unger, *Porous silica, its properties and use as support in column liquid chromatography / K. K. Unger*, Elsevier Scientific Pub. Co. ; distributors for the U.S.A. and Canada, Elsevier/North-Holland, Amsterdam ; New York : New York, 1979.
4. L. E. Cascarini de Torre and E. J. Bottani, in *Colloidal Silica*, CRC Press, 2005, pp. 311-329.
5. D. A. Loy and K. J. Shea, *Chem. Rev.*, 1995, **95**, 1431-1442.
6. D. H. Everett, *Journal*, 1972, **31**, 577.
7. M. Kondo, T. Yoshitomi, H. Matsuzaka, S. Kitagawa and K. Seki, *Angewandte Chemie International Edition in English*, 1997, **36**, 1725-1727.
8. S. M. Auerbach, K. A. Carrado and P. K. Dutta, *Handbook of Zeolite Science and Technology*, CRC Press, 2003.
9. E. M. Flanigen, in *Stud. Surf. Sci. Catal.*, eds. E. M. F. H. van Bekkum and J. C. Jansen, Elsevier, 2001, vol. Volume 58, pp. 13-34.
10. E. M. Flanigen, *Journal*, 1980, **52**, 2191.

11. M. Schoonover and M. Cohn, *Top. Catal.*, 2000, **13**, 367-372.
12. A. Galarneau, F. Di Renzo, F. Fajula and J. Védrine, *Zeolites and Mesoporous Materials at the dawn of the 21st century*, Elsevier, 2001.
13. H. Marsh and F. Rodríguez-Reinoso, in *Activated Carbon*, ed. H. M. Rodríguez-Reinoso, Elsevier Science Ltd, Oxford, 2006, pp. 13-86.
14. J. A. Menéndez-Díaz and I. Martín-Gullón, in *Activated Carbon Surfaces in Environmental Remediation*, ed. J. B. Teresa, Elsevier, 2006, vol. Volume 7, pp. 1-47.
15. A. P. Côté, A. I. Benin, N. W. Ockwig, M. O'Keeffe, A. J. Matzger and O. M. Yaghi, *Science*, 2005, **310**, 1166-1170.
16. S.-Y. Ding and W. Wang, *Chem. Soc. Rev.*, 2013, **42**, 548-568.
17. E. L. Spitler, B. T. Koo, J. L. Novotney, J. W. Colson, F. J. Uribe-Romo, G. D. Gutierrez, P. Clancy and W. R. Dichtel, *J. Am. Chem. Soc.*, 2011, **133**, 19416-19421.
18. P. Kuhn, M. Antonietti and A. Thomas, *Angew. Chem. Int. Ed.*, 2008, **47**, 3450-3453.
19. F. J. Uribe-Romo, J. R. Hunt, H. Furukawa, C. Klöck, M. O'Keeffe and O. M. Yaghi, *J. Am. Chem. Soc.*, 2009, **131**, 4570-4571.
20. F. J. Uribe-Romo, C. J. Doonan, H. Furukawa, K. Oisaki and O. M. Yaghi, *J. Am. Chem. Soc.*, 2011, **133**, 11478-11481.
21. G. Zhu and H. Ren, in *Porous Organic Frameworks*, Springer Berlin Heidelberg, 2015, ch. 2, pp. 13-42.
22. N. B. McKeown and P. M. Budd, *Chem. Soc. Rev.*, 2006, **35**, 675-683.
23. S. Tedds, A. Walton, D. P. Broom and D. Book, *Faraday Discuss.*, 2011, **151**, 75-94.
24. J. Germain, J. M. J. Fréchet and F. Svec, *Small*, 2009, **5**, 1098-1111.
25. T. Ben and S. Qiu, *CrystEngComm*, 2013, **15**, 17-26.
26. R. Dawson, A. I. Cooper and D. J. Adams, *Prog. Polym. Sci.*, 2012, **37**, 530-563.
27. J.-X. Jiang, F. Su, H. Niu, C. D. Wood, N. L. Campbell, Y. Z. Khimyak and A. I. Cooper, *Chem. Commun.*, 2008, **4**, 486-488.

28. Y. Xu, S. Jin, H. Xu, A. Nagai and D. Jiang, *Chem. Soc. Rev.*, 2013, **42**, 8012-8031.
29. O. K. Farha, I. Eryazici, N. C. Jeong, B. G. Hauser, C. E. Wilmer, A. A. Sarjeant, R. Q. Snurr, S. T. Nguyen, A. Ö. Yazaydın and J. T. Hupp, *J. Am. Chem. Soc.*, 2012, **134**, 15016-15021.
30. H. Li, M. Eddaoudi, T. L. Groy and O. M. Yaghi, *J. Am. Chem. Soc.*, 1998, **120**, 8571-8572.
31. M. Eddaoudi and J. F. Eubank, in *Metal-Organic Frameworks*, John Wiley & Sons, Inc., 2010, pp. 37-89.
32. D. J. Tranchemontagne, J. L. Mendoza-Cortes, M. O'Keeffe and O. M. Yaghi, *Chem. Soc. Rev.*, 2009, **38**, 1257-1283.
33. N. Stock, H. Reinsch and L.-H. Schilling, in *Metal Organic Frameworks as Heterogeneous Catalysts*, The Royal Society of Chemistry, 2013, pp. 9-30.
34. M. Eddaoudi, J. Kim, N. Rosi, D. Vodak, J. Wachter, M. O'Keeffe and O. M. Yaghi, *Science*, 2002, **295**, 469-472.
35. N. L. Rosi, J. Eckert, M. Eddaoudi, D. T. Vodak, J. Kim, M. O'Keeffe and O. M. Yaghi, *Science*, 2003, **300**, 1127-1129.
36. J. L. C. Rowsell, A. R. Millward, K. S. Park and O. M. Yaghi, *J. Am. Chem. Soc.*, 2004, **126**, 5666-5667.
37. S. Bordiga, J. G. Vitillo, G. Ricchiardi, L. Regli, D. Cocina, A. Zecchina, B. Arstad, M. Bjørgen, J. Hafizovic and K. P. Lillerud, *The Journal of Physical Chemistry B*, 2005, **109**, 18237-18242.
38. H. Li, M. Eddaoudi, M. O'Keeffe and O. M. Yaghi, *Nature*, 1999, **402**, 276-279.
39. M. Eddaoudi, H. Li and O. M. Yaghi, *J. Am. Chem. Soc.*, 2000, **122**, 1391-1397.
40. S. Bordiga, C. Lamberti, G. Ricchiardi, L. Regli, F. Bonino, A. Damin, K. P. Lillerud, M. Bjorgen and A. Zecchina, *Chem. Commun.*, 2004, 2300-2301.
41. H. Li, W. Shi, K. Zhao, H. Li, Y. Bing and P. Cheng, *Inorg. Chem.*, 2012, **51**, 9200-9207.
42. J. H. Cavka, S. Jakobsen, U. Olsbye, N. Guillou, C. Lamberti, S. Bordiga and K. P. Lillerud, *J. Am. Chem. Soc.*, 2008, **130**, 13850-13851.

43. M. Kandiah, M. H. Nilsen, S. Usseglio, S. Jakobsen, U. Olsbye, M. Tilset, C. Larabi, E. A. Quadrelli, F. Bonino and K. P. Lillerud, *Chem. Mater.*, 2010, **22**, 6632-6640.
44. M. Kim and S. M. Cohen, *CrystEngComm*, 2012, **14**, 4096-4104.
45. S. B. Kalidindi, S. Nayak, M. E. Briggs, S. Jansat, A. P. Katsoulidis, G. J. Miller, J. E. Warren, D. Antypov, F. Corà, B. Slater, M. R. Prestly, C. Martí-Gastaldo and M. J. Rosseinsky, *Angew. Chem. Int. Ed.*, 2015, **54**, 221-226.
46. S. Marx, W. Kleist, J. Huang, M. Maciejewski and A. Baiker, *Dalton Transactions*, 2010, **39**, 3795-3798.
47. N. C. Burtch, H. Jasuja and K. S. Walton, *Chem. Rev.*, 2014, **114**, 10575-10612.
48. X. Qian, B. Yadian, R. Wu, Y. Long, K. Zhou, B. Zhu and Y. Huang, *Int. J. Hydrogen Energy*, 2013, **38**, 16710-16715.
49. T. Loiseau, C. Serre, C. Huguenard, G. Fink, F. Taulelle, M. Henry, T. Bataille and G. Férey, *Chemistry – A European Journal*, 2004, **10**, 1373-1382.
50. C. Serre, F. Millange, C. Thouvenot, M. Nogues, G. Marsolier, D. Louer and G. Ferey, *J. Am. Chem. Soc.*, 2002, **124**, 13519-13526.
51. A. Boutin, F.-X. Coudert, M.-A. Springuel-Huet, A. V. Neimark, G. Férey and A. H. Fuchs, *J. Phys. Chem. C*, 2010, **114**, 22237-22244.
52. M. Latroche, S. Surblé, C. Serre, C. Mellot-Draznieks, P. L. Llewellyn, J.-H. Lee, J.-S. Chang, S. H. Jhung and G. Férey, *Angew. Chem. Int. Ed.*, 2006, **45**, 8227-8231.
53. P. L. Llewellyn, S. Bourrelly, C. Serre, A. Vimont, M. Daturi, L. Hamon, G. De Weireld, J.-S. Chang, D.-Y. Hong, Y. Kyu Hwang, S. Hwa Jhung and G. Férey, *Langmuir*, 2008, **24**, 7245-7250.
54. S. Bhattacharjee, C. Chen and W.-S. Ahn, *RSC Advances*, 2014, **4**, 52500-52525.
55. M. Lammert, S. Bernt, F. Vermoortele, D. E. De Vos and N. Stock, *Inorg. Chem.*, 2013, **52**, 8521-8528.

56. L. Mitchell, P. Williamson, B. Ehrlichová, A. E. Anderson, V. R. Seymour, S. E. Ashbrook, N. Acerbi, L. M. Daniels, R. I. Walton, M. L. Clarke and P. A. Wright, *Chemistry – A European Journal*, 2014, **20**, 17185-17197.
57. P. Llewellyn, G. Maurin and J. Rouquerol, in *Adsorption by Powders and Porous Solids (Second Edition)*, ed. F. R. R. S. W. S. L. Maurin, Academic Press, Oxford, 2014, pp. 565-610.
58. W. Lu, Z. Wei, Z.-Y. Gu, T.-F. Liu, J. Park, J. Park, J. Tian, M. Zhang, Q. Zhang, T. Gentle Iii, M. Bosch and H.-C. Zhou, *Chem. Soc. Rev.*, 2014, **43**, 5561-5593.
59. S. Horike and S. Kitagawa, in *Metal-Organic Frameworks*, Wiley-VCH Verlag GmbH & Co. KGaA, 2011, pp. 1-21.
60. K. M. Radha, L. Jian, A. F. Carlos, K. N. Satish, T. Praveen and B. P. Mcgrail, in *Industrial Catalysis and Separations*, Apple Academic Press, 2014, pp. 61-103.
61. L. Wang, J. A. J. Lachawiec and R. T. Yang, *RSC Advances*, 2013, **3**, 23935-23952.
62. H. W. Langmi, J. Ren, B. North, M. Mathe and D. Bessarabov, *Electrochim. Acta*, 2014, **128**, 368-392.
63. S. S. Kaye, A. Dailly, O. M. Yaghi and J. R. Long, *J. Am. Chem. Soc.*, 2007, **129**, 14176-14177.
64. M. Dincă and J. R. Long, *J. Am. Chem. Soc.*, 2005, **127**, 9376-9377.
65. M. Dincă, A. F. Yu and J. R. Long, *J. Am. Chem. Soc.*, 2006, **128**, 8904-8913.
66. M. Dincă, A. Dailly, Y. Liu, C. M. Brown, D. A. Neumann and J. R. Long, *J. Am. Chem. Soc.*, 2006, **128**, 16876-16883.
67. H. Furukawa, N. Ko, Y. B. Go, N. Aratani, S. B. Choi, E. Choi, A. O. Yazaydin, R. Q. Snurr, M. O'Keeffe, J. Kim and O. M. Yaghi, *Science*, 2010, **329**, 424-428.
68. O. K. Farha, A. Özgür Yazaydın, I. Eryazici, C. D. Malliakas, B. G. Hauser, M. G. Kanatzidis, S. T. Nguyen, R. Q. Snurr and J. T. Hupp, *Nat Chem*, 2010, **2**, 944-948.

69. A. Li, R.-F. Lu, Y. Wang, X. Wang, K.-L. Han and W.-Q. Deng, *Angew. Chem. Int. Ed.*, 2010, **49**, 3330-3333.
70. T. Düren, L. Sarkisov, O. M. Yaghi and R. Q. Snurr, *Langmuir*, 2004, **20**, 2683-2689.
71. Y. He, W. Zhou, G. Qian and B. Chen, *Chem. Soc. Rev.*, 2014, **43**, 5657-5678.
72. H. Wu, J. M. Simmons, Y. Liu, C. M. Brown, X.-S. Wang, S. Ma, V. K. Peterson, P. D. Southon, C. J. Kepert, H.-C. Zhou, T. Yildirim and W. Zhou, *Chemistry – A European Journal*, 2010, **16**, 5205-5214.
73. J. A. Mason, M. Veenstra and J. R. Long, *Chem. Sci.*, 2014, **5**, 32-51.
74. Z. Xiang, D. Cao, W. Wang, W. Yang, B. Han and J. Lu, *J. Phys. Chem. C*, 2012, **116**, 5974-5980.
75. R. Sabouni, H. Kazemian and S. Rohani, *Environ Sci Pollut Res*, 2014, **21**, 5427-5449.
76. J. Liu, P. K. Thallapally, B. P. McGrail, D. R. Brown and J. Liu, *Chem. Soc. Rev.*, 2012, **41**, 2308-2322.
77. D. Britt, H. Furukawa, B. Wang, T. G. Glover and O. M. Yaghi, *Proc. Natl. Acad. Sci. U.S.A.*, 2009, **106**, 20637-20640.
78. G. Férey, C. Serre, C. Mellot-Draznieks, F. Millange, S. Surblé, J. Dutour and I. Margiolaki, *Angew. Chem. Int. Ed.*, 2004, **43**, 6296-6301.
79. H. Furukawa, N. Ko, Y. B. Go, N. Aratani, S. B. Choi, E. Choi, A. Ö. Yazaydin, R. Q. Snurr, M. O'Keeffe, J. Kim and O. M. Yaghi, *Science*, 2010.
80. A. Ö. Yazaydın, R. Q. Snurr, T.-H. Park, K. Koh, J. Liu, M. D. LeVan, A. I. Benin, P. Jakubczak, M. Lanuza, D. B. Galloway, J. J. Low and R. R. Willis, *J. Am. Chem. Soc.*, 2009, **131**, 18198-18199.
81. A. R. Millward and O. M. Yaghi, *J. Am. Chem. Soc.*, 2005, **127**, 17998-17999.
82. R. Dawson, D. J. Adams and A. I. Cooper, *Chem. Sci.*, 2011, **2**, 1173-1177.
83. J. Liu, L. Chen, H. Cui, J. Zhang, L. Zhang and C.-Y. Su, *Chem. Soc. Rev.*, 2014, **43**, 6011-6061.
84. F. X. Llabrés i Xamena, A. Abad, A. Corma and H. Garcia, *J. Catal.*, 2007, **250**, 294-298.

85. A. Abad, C. Almela, A. Corma and H. Garcia, *Chem. Commun.*, 2006, 3178-3180.
86. T. Ishida, M. Nagaoka, T. Akita and M. Haruta, *Chemistry – A European Journal*, 2008, **14**, 8456-8460.
87. L. Chen, Y. Yang and D. Jiang, *J. Am. Chem. Soc.*, 2010, **132**, 9138-9143.
88. Z.-Z. Lu, R. Zhang, Y.-Z. Li, Z.-J. Guo and H.-G. Zheng, *J. Am. Chem. Soc.*, 2011, **133**, 4172-4174.
89. Z. Hu, B. J. Deibert and J. Li, *Chem. Soc. Rev.*, 2014, **43**, 5815-5840.
90. B. Liu and Y. Chen, *Anal. Chem.*, 2013, **85**, 11020-11025.
91. J. Ferrando-Soria, H. Khajavi, P. Serra-Crespo, J. Gascon, F. Kapteijn, M. Julve, F. Lloret, J. Pasán, C. Ruiz-Pérez, Y. Journaux and E. Pardo, *Adv. Mater.*, 2012, **24**, 5625-5629.
92. X. Liu, Y. Xu and D. Jiang, *J. Am. Chem. Soc.*, 2012, **134**, 8738-8741.
93. O. Deutschmann, H. Knözinger, K. Kochloefl and T. Turek, *Ullmann's Encyclopedia of Industrial Chemistry*, Wiley-VCH Verlag GmbH & Co. KGaA, 2011.
94. N. P. Cheremisinoff and P. Rosenfeld, *Handbook of Pollution Prevention and Cleaner Production Vol. 3: Best Practices in the Agrochemical Industry, 1st Edition*, Elsevier, 2010.
95. J. B. DeCoste and G. W. Peterson, *Chem. Rev.*, 2014, **114**, 5695-5727.
96. F. Hincal and P. Erkekoğlu, *FABAD J. Pharm. Sci.*, 2006, **31**, 220-229.
97. EH40/2005 Workplace exposure limits: Containing the list of workplace exposure limits for use with the Control of Substances Hazardous to Health Regulations 2002 (as amended) Environmental Hygiene guidance Note EH40 (Second edition) http://www.hse.gov.uk/pUbns/priced/eh40.pdf).
98. G. W. Peterson, C. J. Karwacki, W. B. Feaver and J. A. Rossin, *Industrial & Engineering Chemistry Research*, 2008, **47**, 185-191.
99. D. Britt, D. Tranchemontagne and O. M. Yaghi, *Proc. Natl. Acad. Sci. U.S.A.*, 2008, **105**, 11623-11627.
100. C. Petit, C. Karwacki, G. Peterson and T. J. Bandosz, *J. Phys. Chem. C*, 2007, **111**, 12705-12714.
101. G. Odell Wood, *Carbon*, 1992, **30**, 593-599.

102. Y. Li and R. T. Yang, *Langmuir*, 2007, **23**, 12937-12944.
103. F. Gul-E-Noor, B. Jee, A. Poppl, M. Hartmann, D. Himsl and M. Bertmer, *PCCP*, 2011, **13**, 7783-7788.
104. P. Guo, D. Dutta, A. G. Wong-Foy, D. W. Gidley and A. J. Matzger, *J. Am. Chem. Soc.*, 2015, **137**, 2651-2657.
105. G. W. Peterson, G. W. Wagner, A. Balboa, J. Mahle, T. Sewell and C. J. Karwacki, *J. Phys. Chem. C*, 2009, **113**, 13906-13917.
106. K. Schlichte, T. Kratzke and S. Kaskel, *Microporous Mesoporous Mater.*, 2004, **73**, 81-88.
107. N. L. Rosi, J. Kim, M. Eddaoudi, B. Chen, M. O'Keeffe and O. M. Yaghi, *J. Am. Chem. Soc.*, 2005, **127**, 1504-1518.
108. P. D. C. Dietzel, Y. Morita, R. Blom and H. Fjellvåg, *Angew. Chem. Int. Ed.*, 2005, **44**, 6354-6358.
109. P. D. C. Dietzel, B. Panella, M. Hirscher, R. Blom and H. Fjellvag, *Chem. Commun.*, 2006, 959-961.
110. S. R. Caskey, A. G. Wong-Foy and A. J. Matzger, *J. Am. Chem. Soc.*, 2008, **130**, 10870-10871.
111. T. G. Glover, G. W. Peterson, B. J. Schindler, D. Britt and O. Yaghi, *Chem. Eng. Sci.*, 2011, **66**, 163-170.
112. I. Spanopoulos, P. Xydias, C. D. Malliakas and P. N. Trikalitis, *Inorg. Chem.*, 2013, **52**, 855-862.
113. W. P. J. H. Jacobs, J. W. de Haan, L. J. M. van de Ven and R. A. van Santen, *The Journal of Physical Chemistry*, 1993, **97**, 10394-10402.
114. R. K. Harris and B. E. Mann, *NMR and the Periodic Table*, Academic Press, 1978.
115. T. Kajiwara, M. Higuchi, D. Watanabe, H. Higashimura, T. Yamada and H. Kitagawa, *Chemistry – A European Journal*, 2014, **20**, 15611-15617.
116. G. W. Peterson, J. B. DeCoste, T. G. Glover, Y. Huang, H. Jasuja and K. S. Walton, *Microporous Mesoporous Mater.*, 2013, **179**, 48-53.
117. H. Jasuja, G. W. Peterson, J. B. Decoste, M. A. Browe and K. S. Walton, *Chem. Eng. Sci.*, 2015, **124**, 118-124.
118. D. Yu, P. Ghosh and R. Q. Snurr, *Dalton Transactions*, 2012, **41**, 3962-3973.

119. K. C. Kim, D. Yu and R. Q. Snurr, *Langmuir*, 2013, **29**, 1446-1456.
120. T. Watanabe and D. S. Sholl, *J. Chem. Phys*, 2010, **133**, 094509.
121. L. Huang, T. Bandosz, K. L. Joshi, A. C. T. van Duin and K. E. Gubbins, *J. Chem. Phys*, 2013, **138**, 034102.
122. B. Supronowicz, A. Mavrandonakis and T. Heine, *J. Phys. Chem. C*, 2013, **117**, 14570-14578.
123. C. Petit and T. J. Bandosz, *J. Mater. Chem.*, 2009, **19**, 6521-6528.
124. C. Petit, B. Mendoza, D. O'Donnell and T. J. Bandosz, *Langmuir*, 2011, **27**, 10234-10242.
125. C. Petit and T. J. Bandosz, *Dalton Transactions*, 2012, **41**, 4027-4035.
126. C. Petit and T. J. Bandosz, *Adv. Funct. Mater.*, 2010, **20**, 111-118.
127. C. Petit, B. Mendoza and T. J. Bandosz, *Langmuir*, 2010, **26**, 15302-15309.
128. C. Petit and T. J. Bandosz, *Adv. Funct. Mater.*, 2011, **21**, 2108-2117.
129. C. Petit, L. Huang, J. Jagiello, J. Kenvin, K. E. Gubbins and T. J. Bandosz, *Langmuir*, 2011, **27**, 13043-13051.
130. D. Saha and S. Deng, *J. Colloid Interface Sci.*, 2010, **348**, 615-620.
131. G. W. Peterson, J. A. Rossin, J. B. DeCoste, K. L. Killops, M. Browe, E. Valdes and P. Jones, *Industrial & Engineering Chemistry Research*, 2013, **52**, 5462-5469.
132. C. J. Doonan, D. J. Tranchemontagne, T. G. Glover, J. R. Hunt and O. M. Yaghi, *Nat Chem*, 2010, **2**, 235-238.
133. G. Peterson, O. Farha, B. Schindler, P. Jones, J. Mahle and J. Hupp, *J. Porous Mater.*, 2012, **19**, 261-266.
134. M. H. Weston, O. K. Farha, B. G. Hauser, J. T. Hupp and S. T. Nguyen, *Chem. Mater.*, 2012, **24**, 1292-1296.
135. Z. Xie, C. Wang, K. E. deKrafft and W. Lin, *J. Am. Chem. Soc.*, 2011, **133**, 2056-2059.
136. L. Ma, M. M. Wanderley and W. Lin, *ACS Catal.*, 2011, **1**, 691-697.
137. S. Yuan, B. Dorney, D. White, S. Kirklin, P. Zapol, L. Yu and D.-J. Liu, *Chem. Commun.*, 2010, **46**, 4547-4549.
138. S. Yuan, S. Kirklin, B. Dorney, D.-J. Liu and L. Yu, *Macromolecules*, 2009, **42**, 1554-1559.

139. M. H. Weston, G. W. Peterson, M. A. Browe, P. Jones, O. K. Farha, J. T. Hupp and S. T. Nguyen, *Chem. Commun.*, 2013, **49**, 2995-2997.

140. J. F. Van Humbeck, T. M. McDonald, X. Jing, B. M. Wiers, G. Zhu and J. R. Long, *J. Am. Chem. Soc.*, 2014, **136**, 2432-2440.

141. W. Morris, C. J. Doonan and O. M. Yaghi, *Inorg. Chem.*, 2011, **50**, 6853-6855.

2 Experimental methods

2.1 Introduction

This chapter reviews the synthetic techniques, characterisation methods and related theory used for the synthesis and analysis of materials discussed in this thesis. Characterisation was achieved using powder X-ray diffraction (PXRD), gas sorption isotherms, thermo-gravimetric analysis (TGA), CHN elemental analysis, scanning electron microscopy (SEM), ion chromatography, UV-visible spectroscopy and micro-breakthrough testing.

2.2 Hydrothermal/solvothermal synthesis

There are examples of some well-known MOFs that can be synthesised at room temperature by direct precipitation, including MOF-5, MOF-74, MOF-177, HKUST-1 and ZIF-8.[1-3] Generally, however, the synthesis of MOFs requires elevated temperatures, pressures and extended reaction times.[4] Solvothermal synthesis is used extensively in this thesis as a means of producing metal-organic frameworks. It is a reaction method in which reactants and solvents are placed in a PTFE liner, which is then sealed in a stainless steel autoclave reactor. The autoclave can then be heated up to temperatures of around 250 ^{o}C if necessary, typically far beyond the boiling point points of organic solvents. Furthermore, the pressure within the sealed reactor increases markedly with temperature, depending also on the fill level of the liner, allowing reactions to be carried out above atmospheric pressure. Hydrothermal synthesis is analogous, but with the use of water as the solvent. Reactions are carried

out by heating the autoclaves in an oven, using specific heating rates, dwell times, and cooling rates.

2.3 TGA

Thermo-gravimetric analysis is a technique which involves precise measurement of the mass of a sample as a function of time and temperature in a known atmosphere. During heating, changes in mass are observed which can be associated with a variety of effects. In porous materials, such as those studied in this thesis, mass loss is often observed due to removal of adsorbed solvents (for instance those used in synthesis or washing procedures). Often porous materials adsorb atmospheric moisture, the mass of which can be attained from TGA experiments. The technique is also used for observing the point of thermal decomposition of a material, which in MOFs and porous polymers is often accompanied by a large mass loss due to the combustion of organics. This can be useful in determining activation procedures. Furthermore, when considering materials containing both organic and inorganic components, such as MOFs, metal content can be accurately determined by comparing the ratio between the remaining residue (often a metal-oxide) and the mass of the desolvated compound.

In this thesis, TGA was carried out using a TA instruments Q500 Thermogravimetric Analyzer. In a typical experiment, 5-10 mg of ground sample was placed a platinum pan. The material was then heated to 650 ^{o}C at a rate of 10^{o}C/min under a 50 mL/min flow of air, and following heating allowed to cool under the same flow.

2.4 Gas sorption

Adsorption processes can typically be categorized as chemical adsorption or physical adsorption, with the difference depending on the strength of the interaction. Chemical adsorption, also called chemisorption, is typified by high heats of adsorption, comparable to chemical bonds, whereby the adsorbate interacts strongly with functional groups on the adsorbent surface. As such chemisorption is irreversible and is restricted to single layer adsorption.[5]

Physical adsorption, or physisorption, exhibits contrary behavior; it is a general phenomenon which is characterized by low heats of adsorption, and occurs when any adsorbate gas comes into contact with a surface as a result of van der Waals interactions. It can result in surface coverage beyond one layer of adsorbate; pores can often be completely filled. As a result of the weak interaction demonstrated by physisorption, the process is fully reversible allowing the study of both adsorption process and desorption processes. As such physisorption is generally used for determining surface areas, pore volume and pore size distributions of porous materials.[5]

2.4.1 Adsorption isotherms

There are six main types of sorption isotherms, as shown in Figure 2.1.[6] Type I isotherms, often called Langmuir isotherms, are characteristic of microporous materials. The distinguishing feature of Type I isotherms is the horizontal plateau which extends to high relative pressures. The value of gas adsorbed at the plateau can be used to calculate the pore volume of the adsorbent by assuming that pores are filled with the adsorbate in the liquid state. Pore volume is then given by multiplying

the volume of gas adsorbed by the ratio of the density of the adsorbate in the gas and liquid phase (for which nitrogen at 77 K has a value of 0.0015):

$$V_p = V_a\left(\frac{d_g}{d_l}\right)$$

Equation 2.9: Where $\boldsymbol{V_p}$ = Pore volume (cm^3/g), $\boldsymbol{V_a}$ = volume of gas adsorbed (cm^3/g, STP), $\boldsymbol{d_g}$ = density of adsorbate in gas phase, $\boldsymbol{d_l}$ = density of adsorbate in liquid phase

The Type II isotherm is usually seen for non-porous or macroporous adsorbents, and represents unrestricted monolayer-multilayer adsorption. The 'knee' of the isotherm, point B, is the point at which monolayer coverage is complete and multilayer adsorption can begin.

Type III isotherms are relatively uncommon, typified by being convex to the p/p_0 axis. Type III isotherms are indicative of weak adsorbate-adsorbent interactions relative to the of adsorbate-adsorbate interactions. This type of isotherm is generally obtained from non-porous or macroporous adsorbents. [7]

The Type IV isotherm is characteristic of materials with mesoporosity, typified by its hysteresis loop and limiting uptake at high p/p_0. The initial part is similar to the Type II isotherm and is similarly attributed to monolayer-multilayer adsorption.

The Type V isotherm is related to the Type III isotherm in that it is mostly convex to the p/p_0 axis, thus the adsorbent-adsorbate interaction is thought to be weak relative to the adsorbate-adsorbate interaction. This type is generally obtained from microporous or mesoporous adsorbents.[7]

The Type VI isotherms are indicated by their stepwise adsorption branches. This is a result of stepwise layer formation on a uniform, non-porous surface. The step height indicates the monolayer capacity for each adsorbed layer.

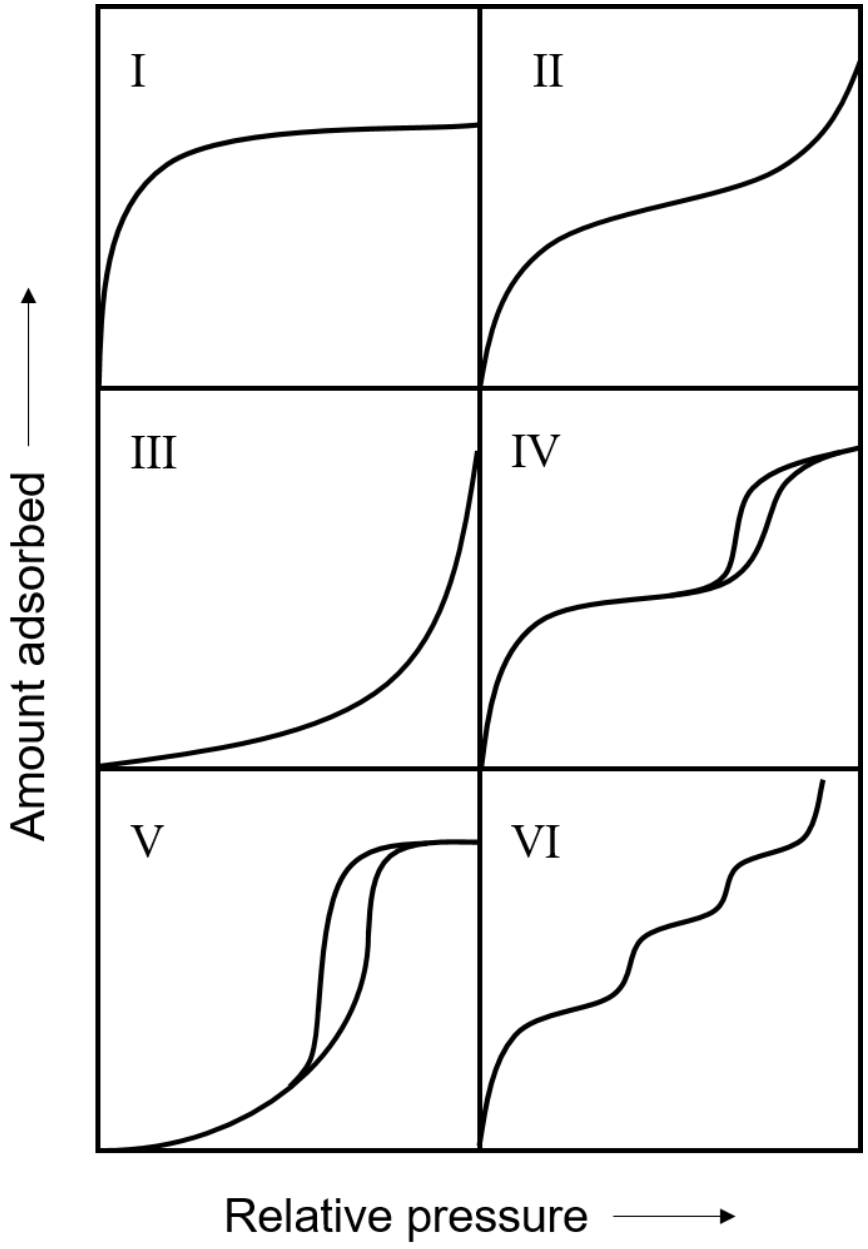

Figure 2.4

Main types of gas physisorption isotherms

2.4.2 Adsorption models

2.4.2.1 Langmuir adsorption model

In 1916 Irving Langmuir proposed a model for adsorption onto surfaces.[8] The Langmuir theory of adsorption makes several assumptions[9]:

1. The surface contains a fixed number of adsorption sites
2. The adsorption sites are all energetically equivalent
3. There can only be one adsorbate molecule per site (monolayer formation)
4. There exist no adsorbate-adsorbate interactions, as they assumed to be negligible adsorbate-adsorbent interactions

The Langmuir equation can be expressed in linear terms as follows:

$$\frac{P}{V} = \frac{1}{bV_{\mathrm{m}}} + \frac{P}{V_{\mathrm{m}}}$$

Equation 2.10: Where $\boldsymbol{P}$ is the equilibrium gas pressure, $\boldsymbol{V}$ is the volume at equilibrium of adsorbate adsorbed per unit mass of adsorbent (at pressure $\boldsymbol{P}$), $\boldsymbol{V_{\mathrm{m}}}$ is the volume adsorbate for complete monolayer coverage and $\boldsymbol{b}$ is the Langmuir parameter.

The Langmuir equation has been seen to describe Type I isotherms and chemisorption isotherms, however in general it fails to describe physisorption and isotherms beyond Type II. The calculation of surface areas by the Langmuir adsorption model is still often quoted in the literature, however due to its limitations, particularly regarding its consideration of only monolayer formation, BET surface area is the more widely accepted method.

2.4.2.2 BET adsorption model

In 1938 Brunauer, Emmett and Teller published a theory which extends the Langmuir model to multilayer adsorption. As an extension of the theory, BET theory inherits the assumptions made by the Langmuir theory, applying it to each adsorption layer. According to the BET model, molecules adsorbed onto a surface can act as adsorption sites for subsequent molecules. There can be unlimited layers, and the layers do not need to be filled before subsequent layers can form. As such adsorption on a surface is not uniform, it is instead made up of random stacks of molecules.[10] It is also assumed that the evaporation and condensation properties of second layer and above are the same as those of the adsorbate in the liquid state. The BET equation is shown below:

$$\frac{p}{v(p_0 - p)} = \frac{c-1}{v_m c}\frac{p}{p_0} + \frac{1}{v_m c}$$

Equation 2.11: BET equation where $\boldsymbol{p}$ is the equilibrium pressure, $\boldsymbol{p_0}$ is the saturation pressure, $\boldsymbol{v}$ is the volume of gas adsorbed at equilibrium, $\boldsymbol{v_m}$ is the volume of gas adsorbed in a monolayer, $\boldsymbol{c}$ is a constant.

Plotting $\frac{p}{v(p_0-p)}$ against$\frac{p}{p_0}$, gives a linear plot at low pressures, the gradient of which is equal to $\frac{c-1}{v_m c}$ and the intercept is equal to $\frac{1}{v_m c}$. Thus, the value of v_m can be calculated from the slope and the intercept, and the surface area of the material, *S*, in m^2/g can calculated using:

$$S = \frac{v_m N \sigma}{Vm}$$

Equation 2.12: Where $\boldsymbol{v_m}$ = monolayer volume, $\boldsymbol{N}$ = Avagadro's number, $\boldsymbol{\sigma}$ = cross sectional area of one adsorbate molecule, $\boldsymbol{V}$ =molar volume of gas, $\boldsymbol{m}$ = adsorbent mass

Brunauer, Emmett and Teller found that plots of $\frac{p}{v(p_0-p)}$ against $\frac{p}{p_0}$ gave linear plots in the pressure range p/p_0 = 0.05 - 0.3. However in microporous materials the linear range can be difficult to locate due to the difficulty in separating the processes of monolayer and multilayer adsorption and micropore filling particularly in high surface area materials.[11] Three general and useful criteria have been proposed by Rouquerol et al. to overcome this difficulty:[12] firstly the BET constant c should be positive; secondly the BET equation should be applied to the range where a plot of $v(1 - p/p_0)$ against p/p_0 continuously increases; thirdly the range should include a p/p_0 value which corresponds to the monolayer capacity, v_m. Generally, the range at which the BET equation showed linearity for the microporous materials studied in this thesis, and also coincided with the three criteria above was at $p/p_0 < 0.1$.

There have been several modifications to the BET theory to address some of its assumptions and limitations,[13-16] but the BET method remains the standard procedure for determining the surface areas of porous materials. This is likely because, despite its simplifications, it nevertheless appears to provide a reasonable estimate of monolayer capacity, particularly in the case of N_2 at 77 K, and also because it is relatively easy to apply.[17] It is noted however that the BET surface area should not be treated as a realistic value for the surface area of a material, but as an apparent surface area useful for comparing porous materials.[11]

2.4.3 Isosteric heat of adsorption

The isosteric heat of adsorption is defined as the difference between the molar enthalpy of adsorbate in the gas phase and its molar enthalpy in the adsorbed phase. This value can be calculated from isotherms measured for the same material at multiple temperatures. This can be achieved by first fitting a virial equation,[18] below, to the adsorption branches of the isotherm in order to determine the virial coefficients (a_i and b_i).

$$lnP = lnN + \frac{1}{T}\sum_{i=0}^{n_1} a_i N^i + \sum_{i=0}^{n_2} b_i N^i$$

Equation 2.13: Virial equation where $\boldsymbol{P}$ = pressure (Torr), $\boldsymbol{N}$ = amount of gas adsorbed (mmol/g), $\boldsymbol{T}$ = temperature (K), $\boldsymbol{a_i}$ and $\boldsymbol{b_i}$ = virial coefficients.

The isosteric heat of adsorption at zero coverage, Q_{st}, can then be determined using Equation 2.6:

$$Q_{st} = -R\sum_{i=0}^{n} a_i N^i$$

Equation 2.14: Where R is the gas constant

Typically, in this work heats of adsorption were calculated using isotherms measured at 283, 293 and 303 K.

2.4.4 Sorption measurements

For this work, gas sorption isotherms were measured using multiple instruments; a Micromeritics ASAP 2020, a Micromeritics TriStar II and a Micromeritics 3Flex. Samples were degassed under vacuum and at a temperature specific to the material.

High pressure sorption isotherms were carried out using an Intelligent Gravimetric Analyser (IGA) from Hiden. Samples were degassed at 80^{o}C under vacuum (10^{-5} mbar).

Water and methanol vapour isotherms were measured by M. W. Smith at Defence Science and Technology Laboratory, Porton Down using a DVS Advantage, made by Surface Measurement Systems Ltd. Typically samples of 10-30mg were measured at 298 K, following outgassing using a flow of dry N_2.

2.5 Powder X-Ray Diffraction

2.5.1 Crystalline solids

Powder X-ray diffraction has been used throughout this thesis in order to characterise the crystalline materials produced. A crystalline solid is a material whose constituent atoms are arranged in an ordered manner, which can be described as a repeating structural motif in a three-dimensional unit cell. This unit cell can be defined using a parallelepiped with edges *a, b* and *c* and angles *α, β* and *γ.* The three-dimensional stacking of the unit cell produces the crystal structure (Figure 2.1).

The crystal structure may be classified as one of seven crystal systems as shown in Table 2.1. The seven crystal systems can be combined with lattice centring to give

the 14 Bravais lattices. There are five possible types of centring: primitive (P), body centred (I), face-centred (F), side centred (A, B, C) and rhombohedral (R). The Bravais lattice, when combined with the unit cell gives the translational symmetry of the lattice. Further, when the Bravais lattice is combined with all possible symmetry operations for a unit cell, the 230 space groups are revealed. [19]

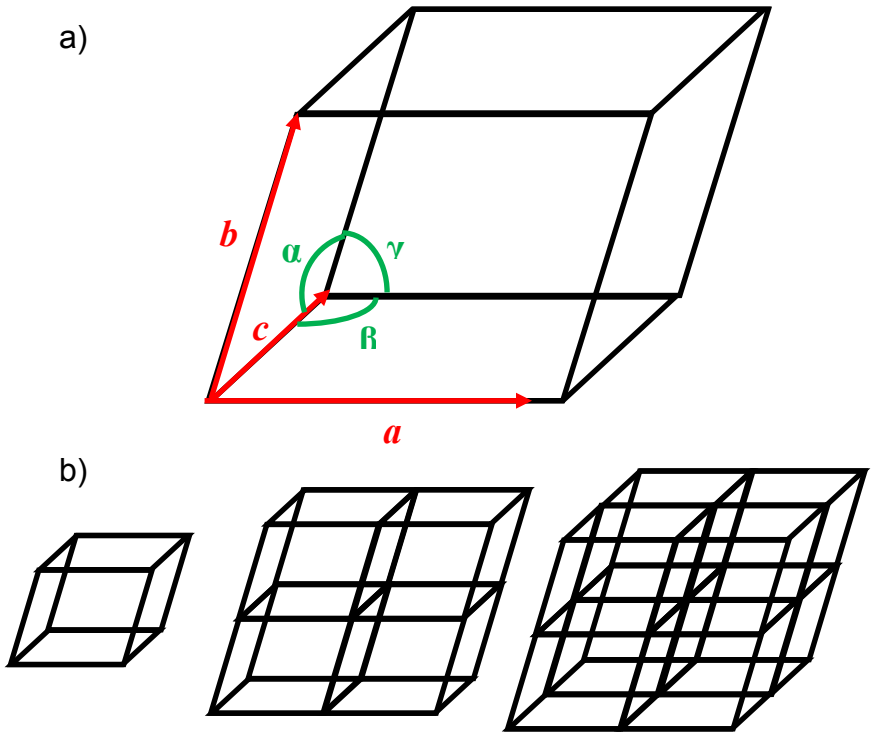

Figure 2.1

a) Unit cell with cell lengths *a*, *b* and *c*, and cell angles α, β and γ b) From left to right: unit cell, expansion in 2 dimensions, expansion in 3 dimensions

Table 2.1 The seven crystal systems with their unit cell parameters

Crystal system	Cell edge	Cell angle	Minimum symmetry elements
Triclinic	$a \neq b \neq c$	$\alpha \neq \beta \neq \gamma \neq 90°$	None
Monoclinic	$a \neq b \neq c$	$\alpha = \gamma = 90°, \beta \neq 90°$	One C2 axis or mirror plane
Orthorhombic	$a \neq b \neq c$	$\alpha = \beta = \gamma = 90°$	Three C2 axes or mirror planes
Tetragonal	$a = b \neq c$	$\alpha = \beta = \gamma = 90°$	One C4 axis
Hexagonal	$a = b \neq c$	$\alpha = \beta = 90°, \gamma = 120°$	One C6 axis
Trigonal	$a = b = c$	$\alpha = \beta = \gamma \neq 90°$	One C3 axis
Cubic	$a = b = c$	$\alpha = \beta = \gamma = 90°$	Four C3 axes

2.5.2 X-ray diffraction

As X-rays pass through a material they cause vibrations of the electrons of the atoms composing the material, due to the oscillating electric field of the incident electromagnetic radiation. Secondary radiation is emitted, the wavelength of which is synchronous with that of the incident radiation. This is known as elastic scattering, whereby there is no change in energy between the incident and scattered X-rays, and is the foremost type of scattering exploited in X-ray crystallography.[20] When an X-ray beam encounters an atom, each electron is capable of coherent scattering. The mass of the nucleus is much larger than that of electron, as such the oscillation of the nucleus caused by X-ray radiation is effectively negligible. Hence, when considering the ability of an atom to scatter X-rays, we typically consider only electrons associated with the atom.[21]

If many atoms are together, as in a crystal, then the scattered X-rays from all of the atoms can interfere. The coherent waves can interfere in a constructive manner, resulting in diffracted X-ray beams in specific directions. The directions of the diffracted X-ray beams are determined by the wavelength of the incident radiation and also the make-up of crystalline material itself.[22] W. H. Bragg and W. L. Bragg developed a theory that relates the wavelength of incident X-rays to the spacing of atomic planes within a crystal. Miller indices (*h*, *k* and *l*) can be used to describe these planes, which intersect the unit cell at $\frac{a}{h}$, $\frac{b}{k}$ and $\frac{c}{l}$, examples of which are shown in Figure 2.2.

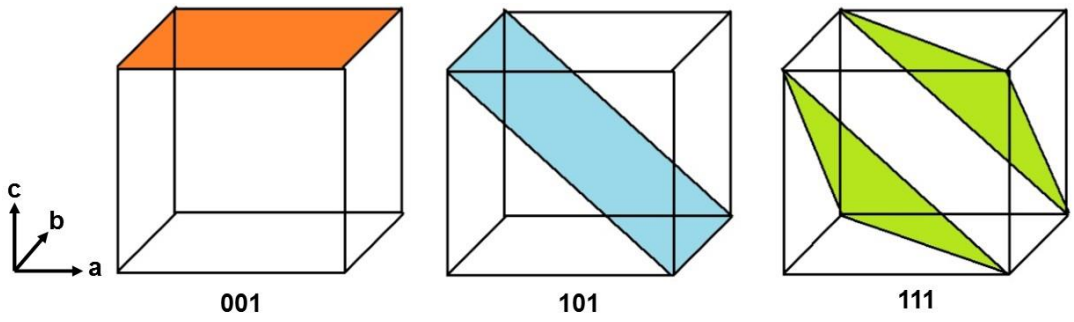

Figure 2.2

Illustration of a unit cell with lattice planes described by Miller indices.

Figure 2.3 can be used to explain Bragg's law. Two beams with the same wavelength and phase are diffracted off two different atomic planes within a crystalline material. Beam 2 is seen to travel further than beam 1, by a distance of AB + BC. AB and BC are equal and can be determined to have a value of dsinθ. As such the additional path length of beam 2 over beam 1 is 2dsinθ. Constructive interference will occur when the additional path length, 2dsinθ, is equal to an integer of the wavelength of the incident radiation. This is Bragg's law, Equation 2.1.

By varying the angle of incidence (θ), using a specific wavelength of radiation (λ), reflections (constructive interference) can be observed at specific values of θ, relating to the spacing between atomic planes (d). Indexing is the process of assigning Miller indices to these reflections, allowing the unit cell parameters and the crystal system to be determined.

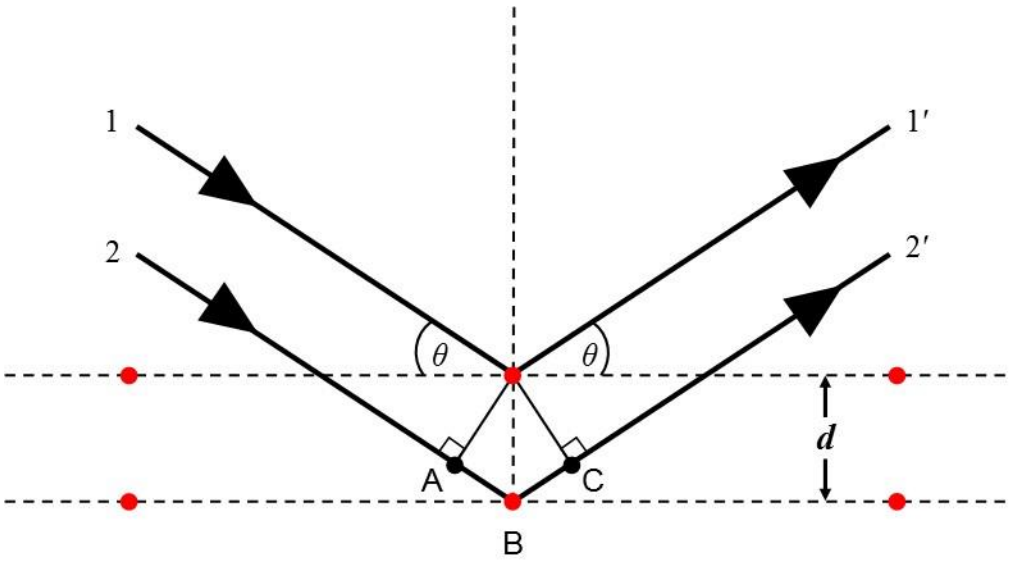

Figure 2.3

Schematic illustrating Bragg's Law; diffraction of monochromatic X-rays by atomic planes of a crystal.

$$n\lambda = 2dsin\theta$$

Equation 2.4: Bragg's law $\boldsymbol{\lambda}$ = wavelength of incident radiation, $\boldsymbol{n}$ = an integer, $\boldsymbol{d}$ = distance between atomic planes, $\boldsymbol{\theta}$ = angle between the incident beam and the atomic plane

2.5.2.1 Rietveld method

As mentioned, powder X-ray diffraction has been used throughout this thesis as a method for the characterisation of crystalline materials. It can be used to quickly identify the phase purity of materials by comparing patterns directly to patterns from various databases (such as PDF of JCPDS) or to those simulated using single crystal data from databases such as CSD.[23] Using the Rietveld method structural information can be extracted from powder X-ray diffraction data also.

The Rietveld refinement technique that we use today is based on a general method for whole pattern fitting of diffraction patterns, suggested by Hugo M. Rietveld in the late 1960's.[19] The principle of the Rietveld method is that all relevant structural and instrumental parameters are refined by fitting a calculated pattern to the experimental data. Assuming a chemically sensible model, and suitable background and peak shape functions, a good fit between the observed data and calculated profile generally means that the model can be considered correct. A key aspect of the Rietveld method is obtaining a starting model that is reasonably close to the actual crystal structure of the material.

The method uses the value of intensity, y_i, at each of the measured 2θ values. The best fit is the best least squares fit to all of the y_i values simultaneously according to the equation below:[24]

$$S = \sum_i w_i \, (y_i(obs) - \, y_i(calc))^2$$

Equation 2.5: Where $\boldsymbol{w_i}$ is the weighting factor, $\boldsymbol{y_i(obs)}$ is the observed intensity, and $\boldsymbol{y_i(calc)}$ is the calculated intensity. The yi(calc) values result from the intensity contributions from the structure factors $F_{(hkl)}$, Lorentz-Polarization factor and preferred orientation.[24]

In a Rietveld refinement, the least squares calculation contains many parameters to refine, often too many to refine at once, therefore refinements are broken up into stages. Generally basic parameters are refined first, including zero shift, peak profile, background and lattice parameters. Depending on the quality of the starting model, it can be beneficial to use a structureless refinement, such as a Pawley[25] fitting (which treats peak intensities a free variables) to obtain these parameters. This can provide a good starting point for a Rietveld refinement.

Structural parameters, i.e. fractional coordinates, thermal parameters and site occupancies can then be refined, taking care between each iteration to assess the chemical and physical meaning of the refined parameters, and the fit of the calculated pattern to the observed data. This can be achieved by visual inspection of the calculated plot in comparison with the observed data (a difference plot, *(obs)-(calc)*, is useful) and also by statistical means, making use of R-values. R-values are calculated from differences between the observed and calculated data. R_{wp}, the weighted profile R-value is defined as:

$$R_{wp} = \frac{\sqrt{\sum_i w_i (y_i\,(obs) - y_i(calc))^2}}{\sqrt{\sum_i w_i (y_i\,(obs)^2}}$$

Equation 2.6: weighted profile R-value

The theoretical limit attainable for R_{wp}, known as the expected R-value, or R_{exp} is given by:

$$R_{exp} = \frac{\sqrt{n-m}}{\sqrt{\sum_i w_i (y_i\,(obs)^2}}$$

Equation 2.7: expected R-value where n = number of steps (discrete measured 2θ values), m = number of refined parameters

The 'goodness of fit', or χ, can be calculated from R_{wp} and R_{exp} as shown below in Equation 2.8 and thus a value for χ^2:

$$\chi^2 = \left(\frac{R_{wp}}{R_{exp}}\right)^2$$

Equation 2.8

It should be noted that a $\chi^2 < 1$ should not be achievable, as R_{wp} should not be greater than R_{exp}. A value of of $\chi^2 < 1$ is generally indicative of overestimated standard uncertainties, or too many parameters in the refinement.[26]

2.5.2.2 Data collection

During this work, X-ray powder diffraction data was collected at room temperature on the following instruments:

Panalytical X'Pert Pro diffractometer using Co *Kα* radiation, using a monochromator which allowed *Kα* radiation of λ = 1.7890 Å operating in reflection mode.

STOE Stadi-P diffractometer using Cu Kα radiation, using a monochromator which allowed $K\alpha$ radiation of λ = 1.54056 Å, operating in transmission mode using 0.7mm borosilicate glass capillaries.

Panalytical X'Pert Pro diffractometer using Cu $K\alpha$ radiation, using a monochromator which allowed $K\alpha$ radiation of λ = 1.54056 Å, operating in transmission mode.

2.6 UV-visible spectroscopy

UV/visible spectroscopy involves the absorption of light in the visible and ultraviolet regions (light with wavelength of around 200 – 800 nm) as a result of electronic transitions in a material. UV-vis can provide useful information regarding the local structure of an atom or functional group in a material.

UV/vis reflectance spectra were collected for ground samples in quartz holders at room temperature on a Perkin–Elmer Lambda 650S UV/vis spectrometer equipped with a Labsphere integrating sphere, using $BaSO_4$ as the standard for 100% reflectance.

2.7 SEM/EDX

Scanning electron microscopy uses a beam of electrons to scan a sample in order to provide high magnification and resolution imaging of a sample surface, allowing sample topology to be explored in much greater detail than possible by optical microscopy. This is due to the fact that electrons have a much shorter wavelength in comparison to visible light (approximately 10^{-12} m and 10^{-7} m for electrons and visible light, respectively). Resolution is determined by wavelength according to Equation 2.1, which explains the higher resolution when using electrons.

$$d = \frac{0.61 \times \lambda}{n \sin \alpha}$$

Equation 2.15: Rayleigh criterion where $\boldsymbol{d}$ = theoretical resolution, $\boldsymbol{\lambda}$ = wavelength, $\boldsymbol{n}$ = is the refractive index of the viewing medium and $\boldsymbol{\alpha}$ = is the half-angle of the illumination cone

A scanning electron microscope produces an image by detecting both backscattered electrons and secondary electrons emitted from a sample's surface as a result of excitation by the primary electron beam.[27]

The principle of energy-dispersive X-ray spectroscopy (EDX) is that when the primary electron beam interacts with the sample, electrons can be ejected from an inner shell of the atoms. A higher energy electron falls into this shell, causing the emission of an X-ray with energy equivalent to the difference in energy of the two electrons. Thus, the energy, and hence the wavelength of the emitted X-ray(s) are unique to each element. By detecting these X-rays and using their relative intensities allows for the elements in the sample be quantified.

SEM images and EDX spectra were obtained by A. Katsoulidis using a Hitachi S-4800 scanning electron microscope. Typically, sample preparation involved placing a small amount of sample onto an adhesive carbon tab attached to an aluminium SEM sample holder. The sample and holder were then coated in a thin layer of gold, approximately 5-10 nm, using a sputter coater to aid sample conductivity.

2.8 Micro-breakthrough

Micro-breakthrough experiments were carried out using a custom micro-breakthrough rig at the Defence Science and Technology Laboratory, Porton Down. Breakthrough testing was performed by M. W. Smith and by J. Jackson

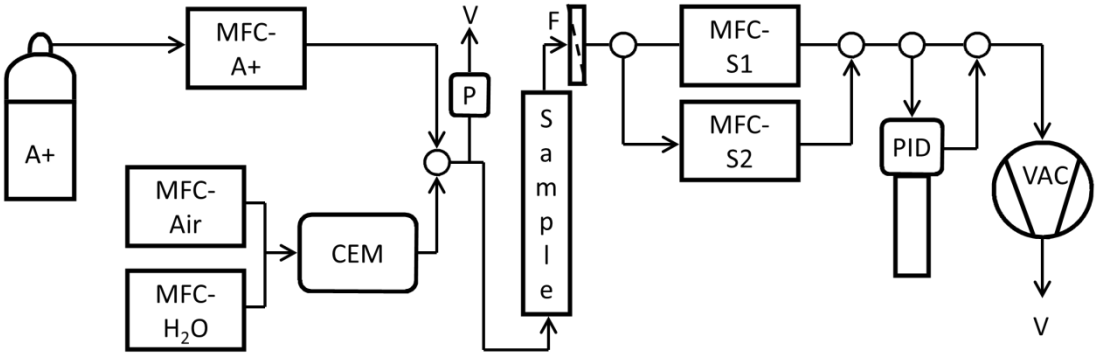

A+	Agent gas
MFC	Mass flow controller
MFC S1	Low sample flow mass flow controller
MFC S2	High sample flow mass flow controller
CEM	Controlled evaporator mixer
P	Relative humidity and temperature probe
F	PTFE dust filter
VAC	Diaphragm vacuum pump
PID	Photo-ionisation detector
V	Vent to fume cupboard
O	Tube junction

Figure 2.5

Schematic of micro-breakthrough rig

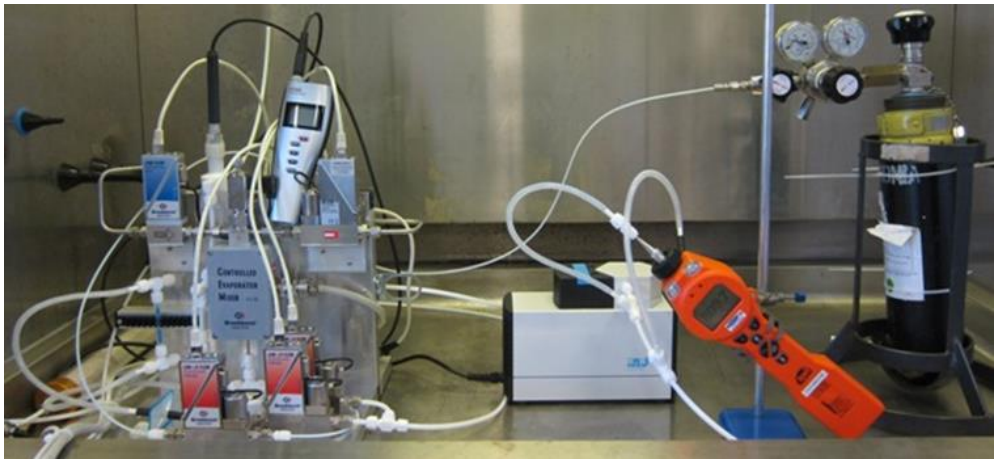

Figure 2.6

The micro-breakthrough rig

Breakthrough experiments were carried out by loosely packing a 4 mm internal diameter glass tube with 30 mg of adsorbent and plugging both ends with glass wool. Assisted by a vacuum pump at the end of the flow line, mass-flow controllers regulated a flow of ammonia and air through a Bronkhorst Controlled Evaporation and Mixing system to produce a gas flow with a concentration of 500 ppm and a flow rate of 30 mL/min (unless otherwise stated). A photo-ionisation detector (PID) was attached to the line after the sample tube in order to monitor the concentration of ammonia. Before each run, a flow of dry air was passed through the sample until the concentrations measured by the PID was in accordance background levels of around 10 ppm.

Breakthrough was generally defined as the time at which, after the flow of ammonia is initiated, sample concentration as measured by the photo-ionisation detector exceeds 20 ppm. In rare cases, the detectors measured background levels in excess of

20 ppm. In such cases breakthrough is measured at the sharp increase in detected concentration beyond background levels.

Due to the internal volume of the breakthrough rig, there occurs a brief delay between addition of ammonia to the flow and it reaching the sample. Using blank samples, this delay was measured as approximately 2 minutes at 30 ml/min. This is accounted for when calculating ammonia uptake, but is included when quoting breakthrough times.

It was observed during testing that breakthrough curves did not always level out at 500 ppm, as detected by the PID. This was noted for various samples in various conditions and is a result the PID sampling downstream, between the vacuum pump and the mass flow controller which controls the flow through the sample. This part of the line is at a slight negative pressure, which causes the response of the PID to drop from the true value.

The amount of ammonia at breakthrough was calculated by using the ideal gas law (Equation 2.1) to convert the concentration of the flow into mol/m^3. Using the flow rate of 30 mL/min, and the breakthrough time, the uptake of ammonia, in moles, can be calculated.

$$n = \frac{PV}{RT}$$

Equation 2.16: Ideal gas law

Amount of ammonia at saturation was calculated by first normalising the data so that effluent concentration was 500 ppm. Using OriginPro 9.0 graphical software[28], the breakthrough curve could be integrated to give the area beneath. This area could then be used to calculate the area shown in blue in Figure 2.1, which corresponds to the remaining ammonia adsorbed between breakthrough and saturation.

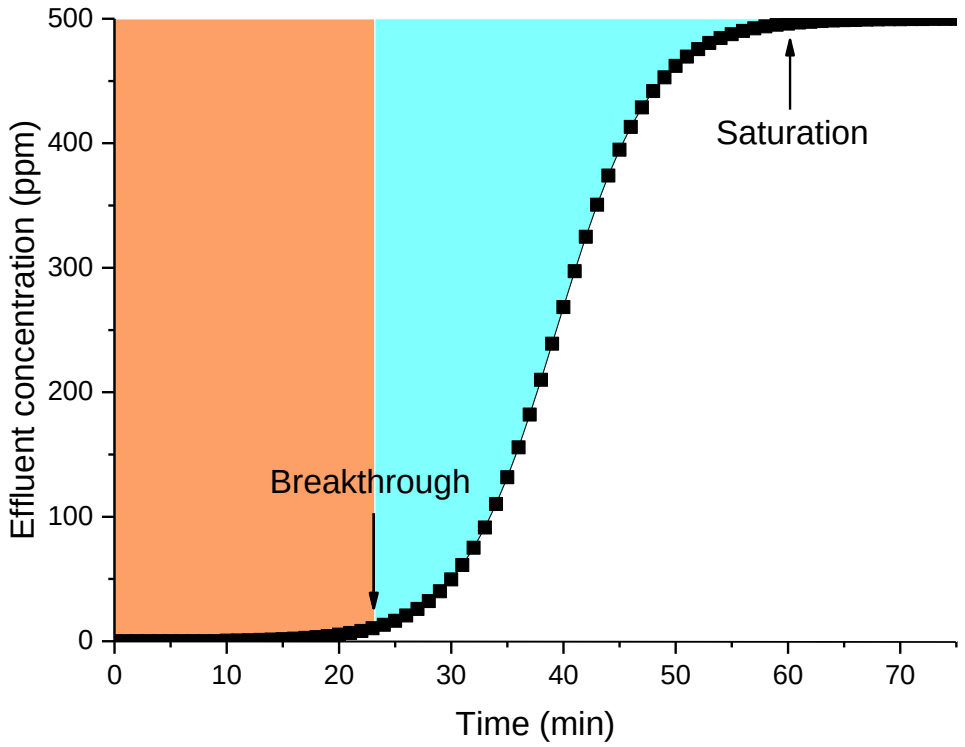

Figure 2.7

Idealised breakthrough curve. The area in orange corresponds to ammonia uptake observed at breakthrough. The area in blue corresponds to the ammonia uptake between breakthrough and saturation.

In the literature, it is often seen that a normalised breakthrough time is given whereby the breakthrough time of the material is divided by the mass of the material used in the experiment. This is presumably so that materials can be compared easily with one another regardless of test conditions. However, there are limitations with

this idea. There are numerous other variables within a test rig including flow rate, influent concentration, sample tube dimensions, sample packing density, ambient temperature, etc. all of which will significantly influence the data. Different groups will use different test rig conditions, therefore normalising data by mass will offer little in terms of a method of comparison. Furthermore, within a single research group where the test rig conditions are kept consistent across experiments, the mass of the sample is also expected to be kept constant, thus normalisation is unnecessary. It is thought that that the use of a standard material (for instance BPL carbon) as a benchmark provides a more practical method of comparison. As such all materials have been tested under the same conditions as the standard BPL carbon.

2.9 Elemental microanalysis

CHN elemental analysis is a technique for finding the relative amounts of carbon hydrogen and nitrogen in a sample. This is achieved by accurately weighing a small amount of sample, around 2 mg, in a tin capsule. The sample and capsule are heated to around 1000^{o}C in the presence of oxygen which causes an exothermic reaction between the oxygen and the tin, which raises the temperature to around 1800^{o}C for a short time. At this temperature, both the organic and inorganic components of the sample are vaporised and combust to form CO_2, H_2, H_2O and nitrogen oxides which can be separated in a GC column and detected using a thermal conductivity sensor (TCD).[29] Elemental analysis was performed using a Thermo EA1112 Flash CHNS-O Analyzer at the University of Liverpool.

2.10 References

1 L. Huang, H. Wang, J. Chen, Z. Wang, J. Sun, D. Zhao and Y. Yan, *Microporous and Mesoporous Materials*, 2003, **58**, 105.

2 D. J. Tranchemontagne, J. R. Hunt and O. M. Yaghi, *Tetrahedron*, 2008, **64**, 8553.

3 J. Cravillon, S. Münzer, S.-J. Lohmeier, A. Feldhoff, K. Huber and M. Wiebcke, *Chemistry of Materials*, 2009, **21**, 1410.

4 N. Stock and S. Biswas, *Chemical Reviews*, 2012, **112**, 933.

5 S. Lowell, J. Shields, M. Thomas and M. Thommes, in *Characterization of Porous Solids and Powders: Surface Area, Pore Size and Density*, Springer Netherlands, 2004, pp. 5-10.

6 K. S. W. Sing, in *Pure and Applied Chemistry*, 1985, p. 603.

7 R. C. Bansal and M. Goyal, *Activated Carbon Adsorption*, CRC Press, 2005.

8 I. Langmuir, *Journal of the American Chemical Society*, 1916, **38**, 2221.

9 J. U. Keller and R. Staudt, *Gas Adsorption Equilibria*, Springer, 2005.

10 F. Rouquerol, J. Rouquerol and K. Sing, in *Adsorption by Powders and Porous Solids*, eds. F. Rouquerol, J. Rouquerol and K. Sing, Academic Press, London, 1999, pp. 1-26.

11 M. Thommes, K. Kaneko, V. Neimark Alexander, P. Olivier James, F. Rodriguez-Reinoso, J. Rouquerol and S. W. Sing Kenneth, in *Pure and Applied Chemistry*, 2015.

12 J. Rouquerol, P. Llewellyn and F. Rouquerol, in *Studies in Surface Science and Catalysis*, eds. F. R.-R. J. R. P.L. Llewellyn and N. Seaton, Elsevier, 2007, pp. 49-56.

13 G. Pickett, *Journal of the American Chemical Society*, 1945, **67**, 1958.

14 R. B. Anderson, *Journal of the American Chemical Society*, 1946, **68**, 686.

15 R. M. Barrer, N. Mackenzie and D. Macleod, *Journal of the Chemical Society (Resumed)*, 1952, 1736.

16 S. Brunauer, J. Skalny and E. E. Bodor, *Journal of Colloid and Interface Science*, 1969, **30**, 546.

17 J. Fraissard, *Physical Adsorption: Experiment, Theory and Applications*, Springer, 1997.

18 L. Czepirski and J. JagieŁŁo, *Chemical Engineering Science*, 1989, **44**, 797.

19 V. K. Pecharsky and P. Y. Zavalij, *Fundamentals of Powder Diffraction and Structural Characterization of Materials*, Springer, 2008.

20 N. Kasai and M. Kakudo, *X-Ray Diffraction by Macromolecules*, Springer, 2005.

21 Y. Waseda, E. Matsubara and K. Shinoda, *X-Ray Diffraction Crystallography*, Springer, 2011.

22 C. Suryanarayana and M. G. Norton, *X-Ray Diffraction: A Practical Approach*, Springer, 1998.

23 F. Allen, *Acta Crystallographica Section B*, 2002, **58**, 380.

24 G. Will, *Powder Diffraction: The Rietveld Method and the Two Stage Method to Determine and Refine Crystal Structures from Powder Diffraction Data*, Springer, 2006.

25 G. Pawley, *Journal of Applied Crystallography*, 1981, **14**, 357.

26 B. H. Toby, *Powder Diffraction*, 2006, **21**, 67.

27 W. Zhou, R. Apkarian, Z. Wang and D. Joy, in *Scanning Microscopy for Nanotechnology*, eds. W. Zhou and Z. Wang, Springer New York, 2007.

28 N. Origin (OriginLab, MA).

29 R. Levens, *More Modern Chemical Techniques*, RSC Publishing, 2001.

3 Initial testing and the effect of functionality

3.1 Introduction

This chapter presents initial ammonia breakthrough testing of several water-stable porous materials, studied previously within the group for a wide array of applications. The materials studied range from non-functionalised and marginally functionalised materials, to those synthesised with functionality targeted toward ammonia. The metal organic frameworks Ce(HTCPB) and Zn-Carnosine, the conjugated microporous polymers, CMP-1, CMP-1-COOH and CMP-1-$(COOH)_2$ and the porous organic polymer CC3 were benchmarked against BPL carbon using ammonia breakthrough experiments. The conclusions drawn from the results presented in this chapter help direct the work discussed in chapters 4,5 and 6.

3.2 Ce-(HTCPB)

Ce-(HTCPB) is a flexible metal-organic framework consisting of chains of cerium dimers linked by 1,2,4,5-Tetrakis-(4-carboxyphenyl)-benzene linker units. This material was discovered and studied within the group for selective adsorption of para-xylene over meta-xylene.[1] Shown to be stable to water from reversible water isotherms, this material was considered as an initial candidate for ammonia breakthrough testing. The material was synthesized by Catherine Perkins according the conditions in reference[1], exhibiting a surface area of 379 m^2/g as determined by CO_2 isotherms at 195K. Figure 3.1 shows the crystal structure of this material, it is noted that this material lacks any obvious functionality for interaction with ammonia.

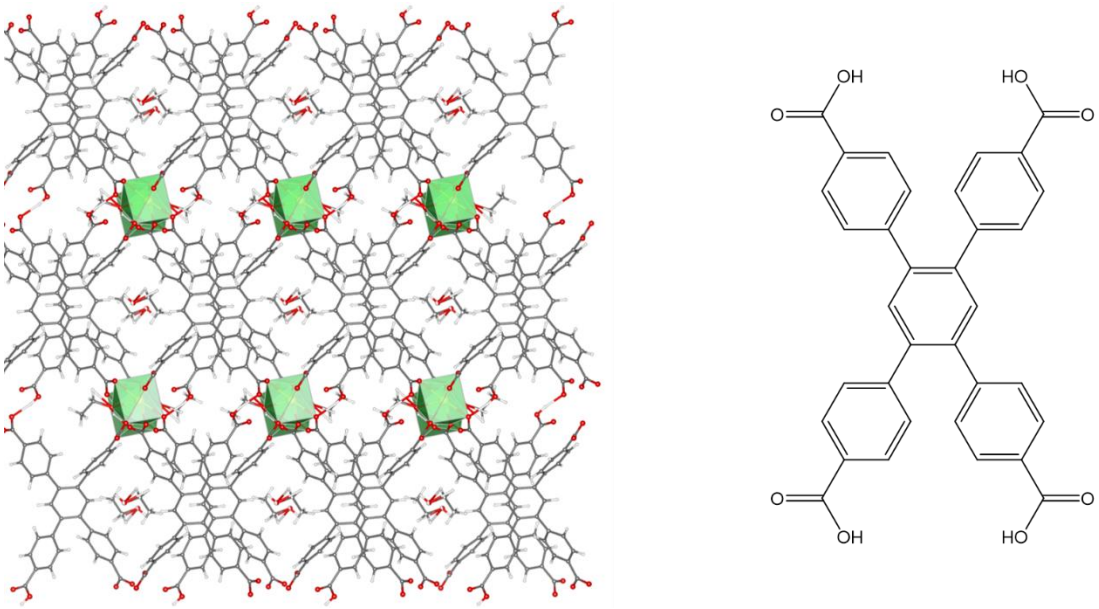

Figure 3.1

Crystal structure (left) of Ce-(HTCPB) viewed along [100], showing ethanol within the 1D channels. H_4TCPB linker is shown on the right.

Dry (0% relative humidity) ammonia was used in order to assess the potential of Ce-(HTCPB) as a sorbent of ammonia. The results, presented in Figure 3.2, show that ammonia was detected above 20 ppm after only 2.2 minutes of testing, performing worse in comparison with the benchmark BPL activated carbon, which itself breaks through after approximately 3.5 minutes. This material is seen to have almost no capacity for ammonia under breakthrough conditions, with only 2.5 $x10^{-4}$ mmol adsorbed at breakthrough. Like BPL carbon, this material contains little functionality that would interact with ammonia, relying on physisorption alone for ammonia uptake. Ce-HTCPB has low surface area of 379 m^2/g in comparison with around 1000 m^2/g for BPL activated carbon,[2, 3] which is the likely cause of the reduced performance.

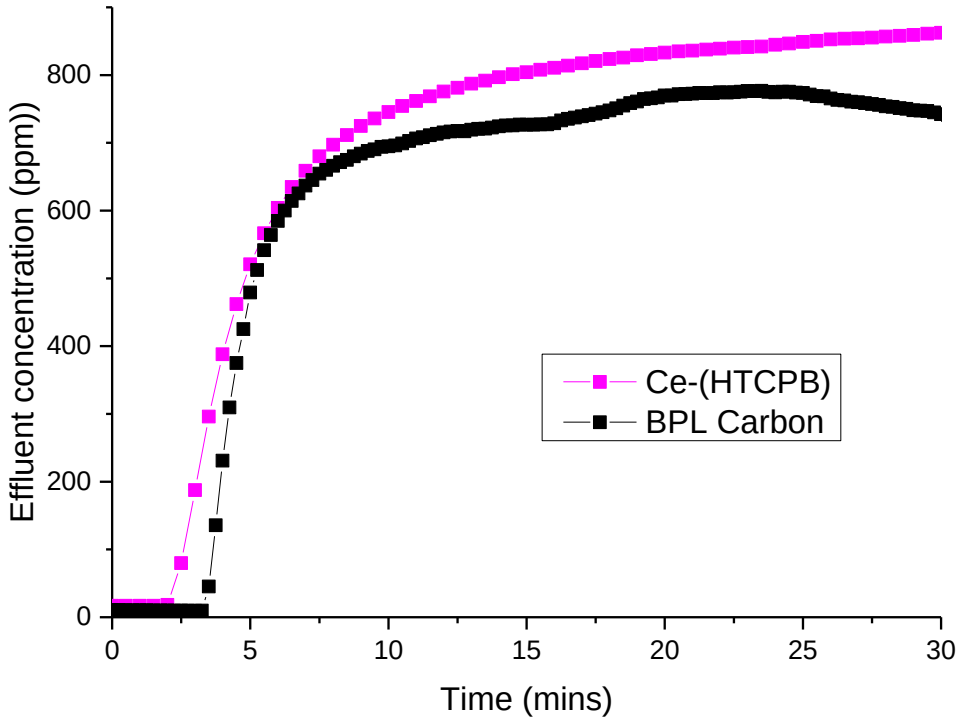

Figure 3.2

Ammonia breakthrough curve of Ce-(HTCPB) (purple), in a 0% RH flow of ammonia at 1000 ppm. BPL activated carbon (black) is shown for comparison.

3.3 CC3

Porous organic cages are a relatively new class of porous material, molecules with permanent voids inside a rigid structure demonstrated by Cooper *et al.* in 2009.[4] Unlike MOFs and porous polymers, these porous materials consist of discrete molecules with intrinsic porosity within the cavity of each cage. In addition to the porosity as a result of the void, porosity can also result from inefficient packing between cage molecules.[4] CC3 is an example of a porous organic cage molecule formed by a cycloimination reaction between benzene-1,3,5-tricarboxaldehyde and

cyclohexanediamine (Figure 3.3).[4] This material had previously been studied for the separation of chiral molecules and rare gases.[5]

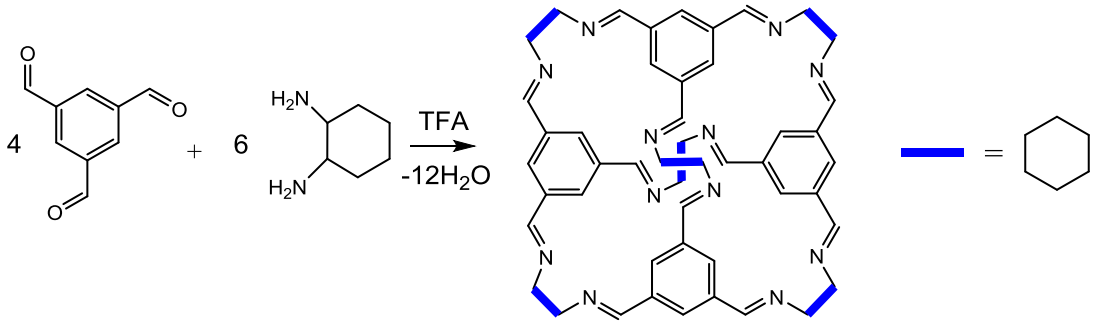

Figure 3.3

Reaction scheme for the synthesis of CC3, whereby four benzene-1,3,5-tricarboxaldehyde molecules are reacted with six cyclohexanediamine molecules

These materials are based on imines which can often decompose in the presence of water, and it is thought that water can cause such materials to become amorphous, or cause them to transition into non-porous polymorphs.[6, 7] However, among the porous cages, CC3 was shown to be surprisingly stable to water vapour, submersion in water, and even boiling in water, and was show to adsorb up to 12.5 molecules of water per cage at 95% relative humidity. CC3 has a reported surface area of 624 m^2/g as probed by N_2 at 77 K. As a result of its water stability and porosity this material was considered an interesting candidate for initial ammonia breakthrough testing. CC3 was synthesised by Tom Hasell using the procedure outlined in reference[4].

The results of the ammonia breakthrough experiment on CC3 are shown below in Figure 3.4. Ammonia breakthrough was detected after only 3.5 minutes of testing,

performing on par with the benchmark BPL activated carbon. The amount of ammonia adsorbed at breakthrough is calculated to be 1.8 x 10^{-3} mmol. The imine functionality might have been expected to provide good hydrogen bond acceptor sites for ammonia to interact, however evidently the interactions are not sufficient to adsorb significant amounts of ammonia. Further, it is possible that water may already be adsorbed onto CC3 from the atmosphere, which could compete with the influent ammonia.

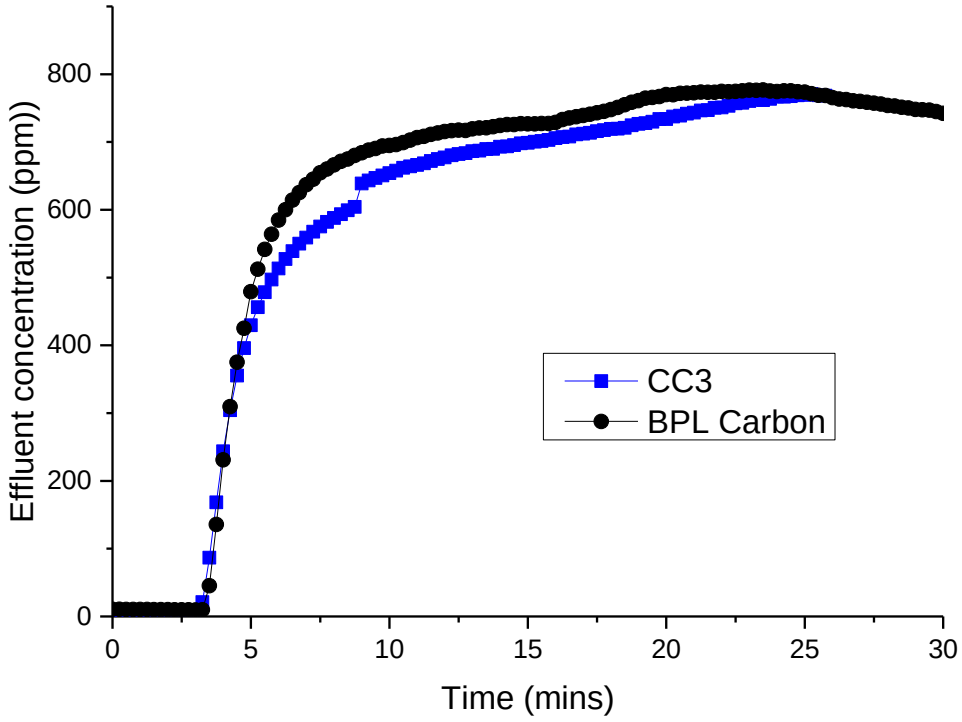

Figure 3.4

Ammonia breakthrough curve of CC3 (blue), in a 0% RH flow of ammonia at 1000 ppm. BPL activated carbon (black) is shown for comparison.

3.4 Zn-Carnosine

Zn-carnosine is a metal-organic framework synthesised from $Zn(NO_3)_2$ and carnosine, a natural dipeptide with the structure beta-alanyl-L-histidine.[8] The MOF

exhibits one-dimensional channels and a BET surface area of 448 m^2/g calculated from CO_2 isotherms at 195 K. The structure of the material is shown in Figure 3.5, whereby the Zn^{2+} cations are coordinated to four carnosine ligands, and each carnosine ligand is coordinated to four separate Zn^{2+} ions through the two nitrogen atoms of the imidazole ring, the C-terminal histidine carboxylate group, the N-terminal alanine amine group. This MOF was shown to be stable to water by stirring in water for 3-days.

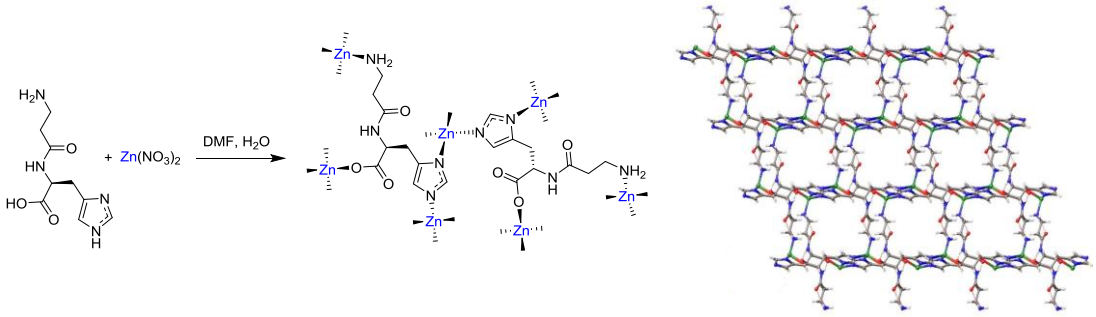

Figure 3.5

Reaction scheme showing the formation of Zn-Carnosine from $Zn(NO_3)_2$ and carnosine, showing the connectivity (left) and the crystal structure of the desolvated material (right).

The carnosine linker unit appeared to offer multiple hydrogen bonding sites for interaction with ammonia, both as donor and acceptor. As a result, and due to its stability toward water, Zn-Carnosine was tested as an ammonia sorbent under a dry flow of ammonia. The results are shown in Figure 3.6. Breakthrough was detected after approximately 9 minutes of dry ammonia flow, outperforming the benchmark BPL activated carbon, adsorbing 8.6 x 10^{-3} mmol ammonia at breakthrough. Despite a moderate surface area of 448 m^2/g, around half that of BPL carbon, it appears the additional functionality offered by the carnosine linker units provided significant

interaction with the influent ammonia, affording almost a 3-fold increase in performance in comparison with the benchmark material.

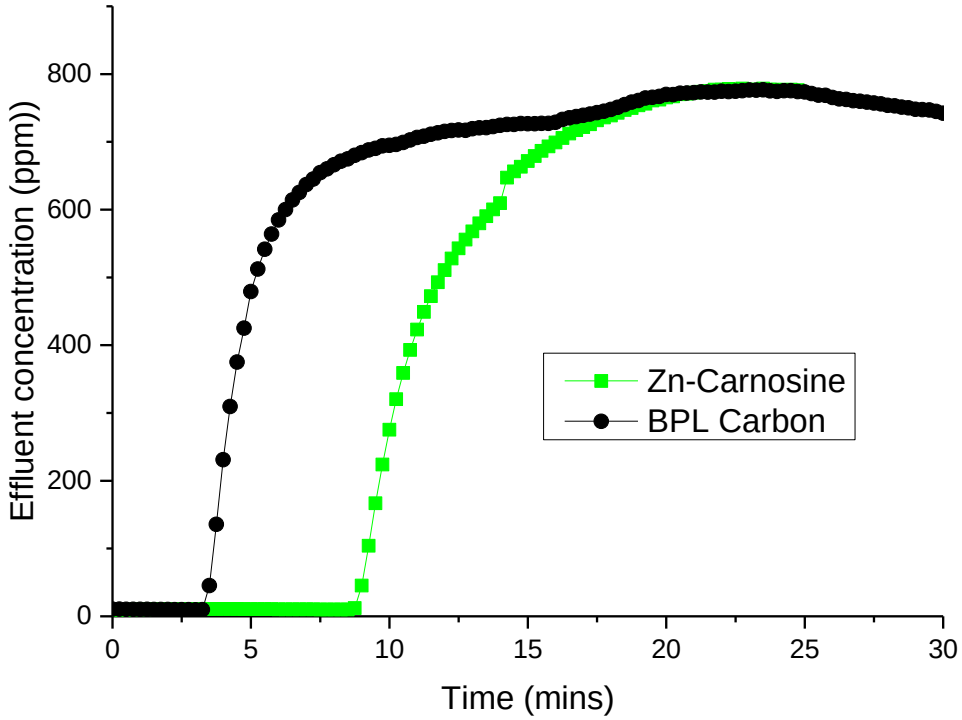

Figure 3.6

Ammonia breakthrough curve of Zn-Carnosine (green), in a 0% RH flow of ammonia at 1000 ppm. BPL activated carbon (black) is shown for comparison.

3.5 Conjugated microporous polymers

The potential of microporous polymer networks for use in areas such as gas storage, separation, sensing and catalysis has been widely studied,[9,10,11] however there are comparatively few examples of their use as sorbents for toxic industrial chemicals.[12] Alongside high surface area and physicochemical stability, an attractive feature of microporous polymer networks is the ability to easily customise the chemical functionality within the pores, providing an interesting platform for targeted sorption of TICs. Hence it was sought to provide an adsorbent surface appropriate for

interaction with ammonia by synthesising a series of conjugated microporous polymer (CMP) networks functionalised to varying degrees with carboxylic acid moieties. It was hypothesised that the carboxylic acids should participate in favourable Bronsted acid/base interactions with ammonia, increasing ammonia uptake with increased density of acid groups. Herein the capacity of three CMP materials (CMP-1, CMP-1-COOH and CMP-1-$(COOH)_2$) as ammonia sorbents are reported.

3.5.1 Synthesis

The series of CMPs were synthesised and characterised by T. Ratvijitvech. according to methods based on those previously described in the literature[13].

In a typical synthesis 1,3,5-triethynylbenzene (150 mg, 1.0 mmol), the dibromo aromatic monomer (1.0 mmol), triethylamine (1.5 mL) and DMF (1.5 mL) were mixed under nitrogen in a 2-necked round bottomed flask (150 mL) on a Radleys carousel reactor, and the reaction mixture heated to 100 °C. Tetrakis(triphenylphosphine)palladium(0) (50 mg, 0.04 mmol) and copper(I) iodide (15 mg, 0.08 mmol) were added in a DMF slurry (1.0 mL), and the reaction mixture was stirred for 72 h. The resulting precipitate was collected by filtration, washed with hot DMF and a Soxhlet extraction was performed using methanol for 18 h. The product was dried in a vacuum oven at 60 °C for 18 hours.

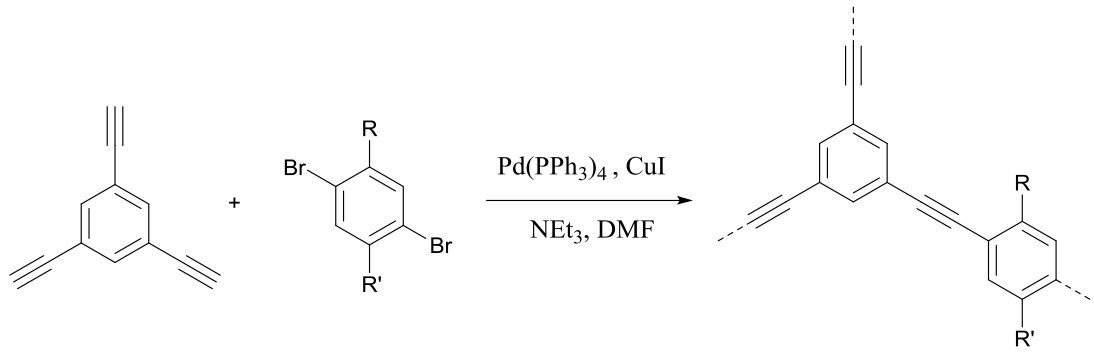

Figure 3.7

Reaction scheme for the synthesis of CMP-1, CMP-1-COOH and CMP-1-$(COOH)_2$

Table 3.1 Functional groups in CMP-1, CMP-1-COOH and CMP-1-$(COOH)_2$

CMP	**R**	**R′**
CMP-1	H	H
CMP-1-COOH	COOH	H
CMP-1-$(COOH)_2$	COOH	COOH

3.5.2 Dry ammonia breakthrough

Initially, breakthrough experiments were performed using a dry ammonia stream. The results are presented in Figure 3.8. Ammonia was detected above 20 ppm after 4.5 minutes of testing, performing less well than the 7 minutes displayed by the benchmark BPL activated carbon. The amount of ammonia adsorbed at breakthrough is calculated to be 3.1 x 10^{-3} mmol, a loading of only 0.17 wt%. At saturation, taken at 25 minutes, CMP-1 has adsorbed 5.3 x 10^{-3} mmol ammonia, or a loading of 0.30 wt%. Despite its relatively high surface area, this non-functionalised CMP-1

performs particularly poorly as an ammonia sorbent, likely as a result of its lack of any reactive/attractive functionality towards ammonia.

The addition of a carboxylic acid moiety throughout the polymer network, resulting in CMP-1-COOH, provides a significant boost in performance in comparison to both the CMP-1 polymer and BPL carbon. It can be seen from Figure 3.8 that ammonia breakthrough occurred after 12 minutes of testing, equivalent to uptake of 7.4×10^{-3} mmol, or 0.42 wt%. Furthermore, at saturation, taken at 60 minutes, CMP-1-COOH has adsorbed 0.014 mmol ammonia and a value of 0.82 wt% has been calculated. The increase in performance observed in comparison with CMP-1 is attributed to the favourable acid/base interactions between the COOH and NH_3.

In the case of CMP-1-$(COOH)_2$ a largely unexpected result was observed. The addition of a second carboxylic acid moiety causes a considerable decrease in ammonia breakthrough time, with ammonia detected after 3.5 minutes, equating to only 2.1×10^{-3} mmol of ammonia, or 0.12 wt%. At saturation, taken at 30 minutes, CMP-1-$(COOH)_2$ has adsorbed 4.2×10^{-3} mmol ammonia and a value of 0.24 wt% has been calculated. It might be expected that doubling the number of COOH groups would have a favourable effect on ammonia breakthrough performance, considering the result observed for CMP-1-COOH, allowing for up to twice the number of acid/base interactions. However, this considerably lower breakthrough time implies that the majority of the COOH groups are not accessible to the influent NH_3. This is consistent with the extremely low surface area calculated from the N_2 isotherm.

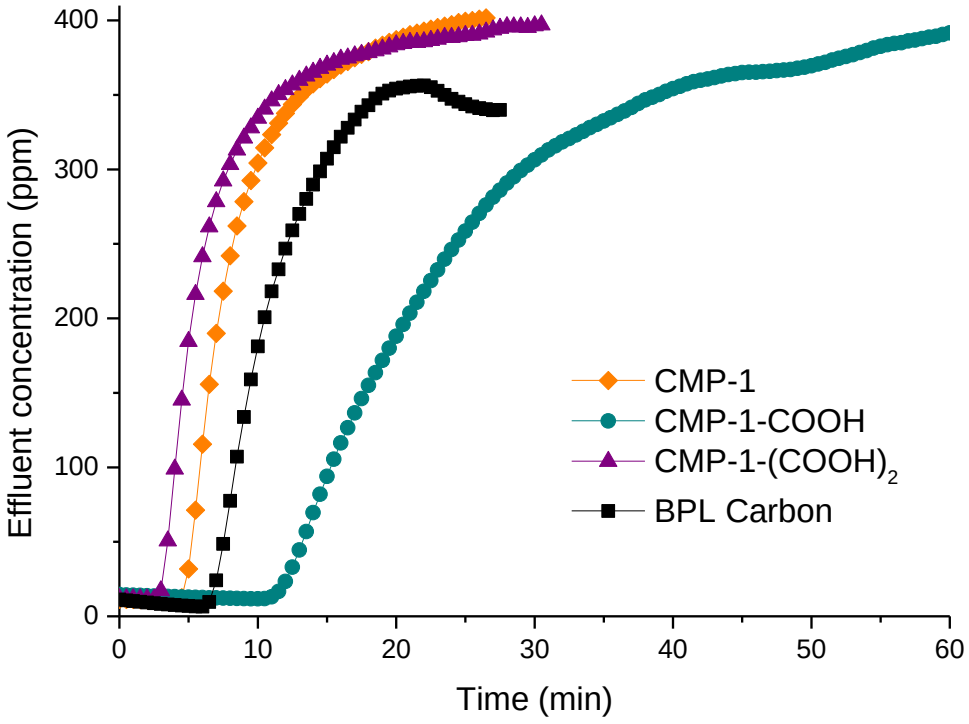

Figure 3.8

Ammonia breakthrough curve of CMP-1 (orange), CMP-1-COOH (cyan) and CMP-1-$(COOH)_2$ (purple) in a 0% RH flow of ammonia. BPL activated carbon (black) is shown for comparison.

3.5.3 **Humid breakthrough**

Following dry breakthrough measurements, the materials were assessed as ammonia sorbents in a humid ammonia stream. Measuring breakthrough times using an 80% relative humidity stream demonstrates a significantly different trend to that shown in dry conditions.

Firstly, CMP-1 shows a slight improvement in humid conditions over dry conditions, with ammonia breakthrough occurring after 7 minutes. The ammonia adsorbed at the point of breakthrough is be calculated to be 4.3 x 10^{-3} mmol (0.24 wt%). It was

hypothesised that due to the hydrophobic nature of the polymer, CMP-1 does not adsorb water particularly well, and as such, the benefit attributed to the high solubility of ammonia in any water film created in the pores[14] is likely small. It can be seen also that, as in dry conditions, CMP-1 is outperformed by BPL carbon.

CMP-1-COOH shows a large improvement in ammonia uptake in humid conditions in comparison with dry conditions. As evidenced by Figure 3.9, ammonia is detected after 19.5 minutes, an uptake of 0.012 mmol ammonia, a loading of 0.68 wt%. With almost twice the breakthrough time of the dry ammonia run, the CMP-1-COOH material also outperforms activated BPL carbon.

The CMP-1-$(COOH)_2$ shows particularly interesting behaviour when testing ammonia breakthrough in a humid flow. Ammonia is detected after 27.5 minutes, outperforming the other CMP materials, and the benchmark BPL activated carbon, adsorbing 0.96 wt% ammonia, or 0.017 mmol at the point of breakthrough. It is shown that with water present, breakthrough times ascend with increasing acid functionality. In order to help explain these effects, water isotherms at 298 K were performed.

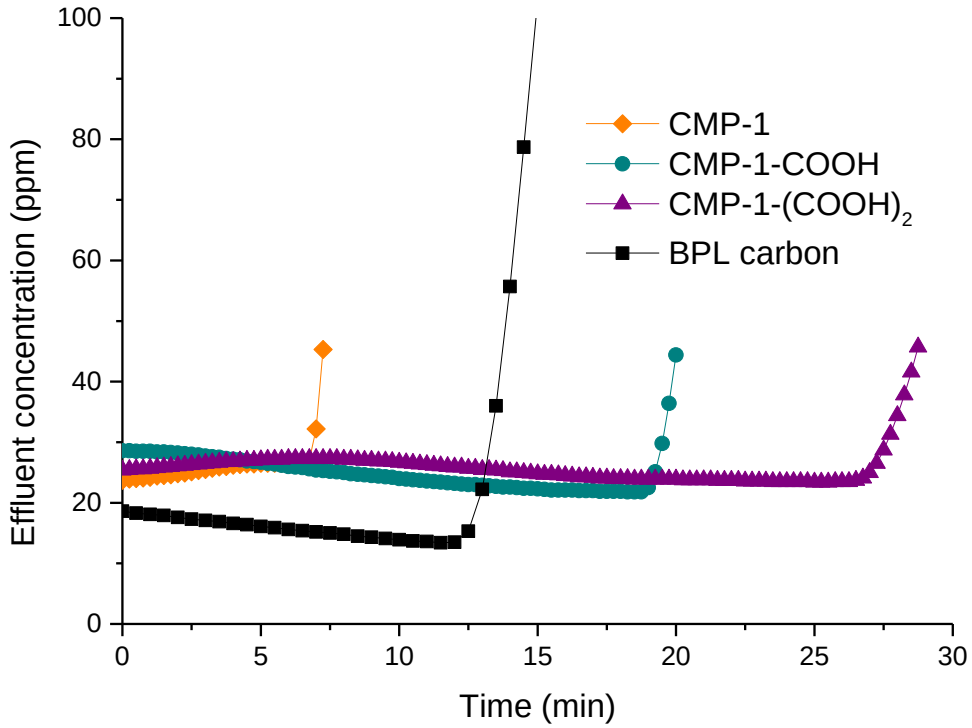

Figure 3.9

Ammonia breakthrough curve of CMP-1 (orange), CMP-1-COOH (cyan) and CMP-1-$(COOH)_2$ (purple) in an 80% RH flow of ammonia. BPL activated carbon (black) is shown for comparison.

Table 3.2 Breakthrough times and ammonia uptake of CMPs in dry and humid flows

Material	**RH (%)**	**Breakthrough time (min)**	**NH_3 uptake at breakthrough (wt %)**
CMP-1	0	4.5	0.17
	80	7	0.24
CMP-1-COOH	0	12	0.42
	80	19.5	0.68
CMP-1-$(COOH)_2$	0	3.5	0.12
	80	27.5	0.96
BPL carbon	0	7	0.24
	80	13	0.45

3.5.4 Sorption isotherms

Water isotherms are useful for probing both the polarity and the porosity of sorbents. Generally, the water uptake at low humidities is dominated by interactions with polar functional groups on the surface, whereas overall capacity often dictates water uptake at higher relative humidities.

Water isotherms measured at 298 K (Figure 3.10) demonstrate that CMP-1 shows Type III isotherm behaviour, generally obtained with non-porous materials when the interaction between adsorbent and adsorbate is weak. Indeed, CMP-1 is seen to be essentially non-porous to water at relative humidities between 0% and 70%, unsurprising considering the hydrophobic nature of the polymer surface. From 70% RH modest water uptake occurs up to a maximum value of 13.8 wt% at 95% RH.

In the case of CMP-1-COOH we see generally Type V behaviour. At low loading, where the behaviour is solely controlled by molecule to surface interactions, we see a significant increase in water uptake in comparison with CMP-1. We attribute this to the increased polarity of the surface, thanks to the presence of the COOH groups. It is thought that water molecules are adsorbed on the polar COOH sites on the surface initially, with clusters of water growing around these sites due to strong adsorbent-adsorbent interactions (H-bonding between adsorbed H_2O). The CMP-1-COOH material shows greater uptake at all relative humidities that CMP-1.

The water isotherm of CMP-1-$(COOH)_2$ shows an interesting trend. Again, a Type V isotherm, the polymer shows the highest uptake of the three materials at lower pressure, consistent with the higher density of polar acidic sites on the surface. Water

uptake by CMP-1-$(COOH)_2$ remains higher than CMP-1-COOH until after 80 % RH, beyond which uptake begins to tail off, likely as a result of decreased overall capacity in comparison with CMP-1-COOH.

Perhaps the most striking is difference between the isotherms measured using water and those using nitrogen as a probe. Where CMP-1-$(COOH)_2$ shows minimal nitrogen uptake, the same material adsorbs 21.8 wt% of water. It is hypothesised that the large number of carboxylic acid groups within the polymer could result in significant internal hydrogen bonding, resulting in decreased pore volume, as observed by the low uptake seen from N_2 isotherms. It is proposed that the porosity towards water is a result of its ability to disrupt this hydrogen bonding, in effect "opening" the polymer. This would help explain the ammonia breakthrough results attained for CMP-1-$(COOH)_2$, whereby the presence of H_2O sufficiently disrupts the hydrogen bonding structure present within CMP-1-$(COOH)_2$ to such an extent that ammonia can more easily penetrate the framework and interact with the larger number of the COOH species present within the polymer network. Furthermore, it is proposed that a swelling phenomenon may also occur upon water adsorption, as evidenced by the hysteresis loops at low pressure,[15] which may be beneficial for ammonia uptake.

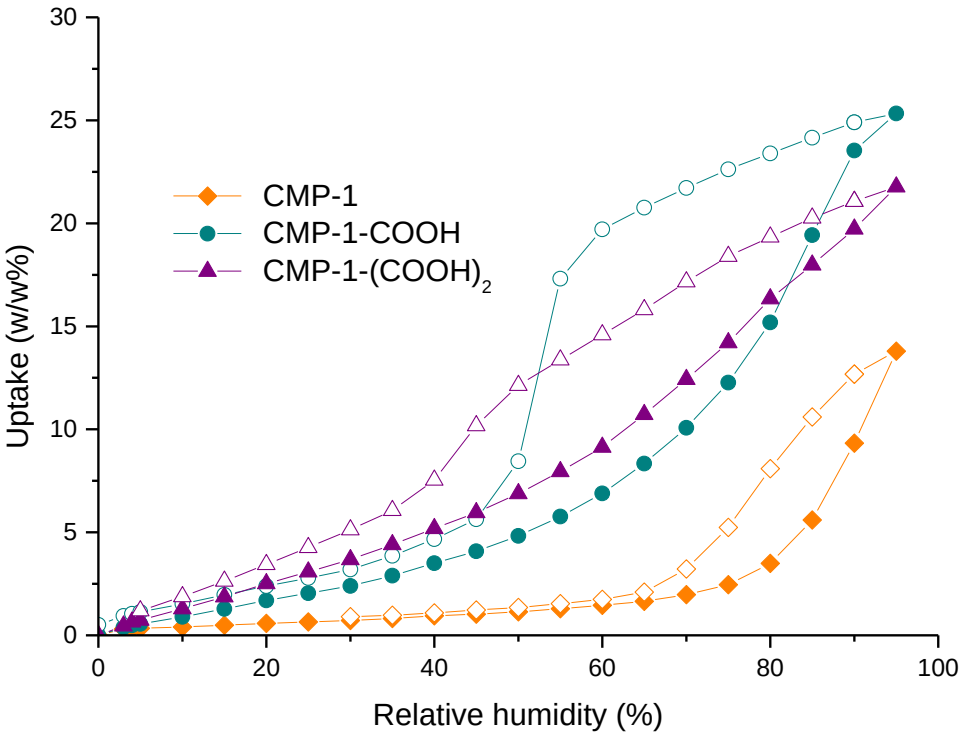

Figure 3.10

Water isotherms conducted at 298 K of CMP-1 (orange), CMP-1-COOH (cyan) and CMP-1-$(COOH)_2$ (purple) from 0% RH to 95% RH. Closed circles show the adsorption branch, open circles show the desorption branch.

Figure 3.11 illustrates that the surface area and pore volume drop significantly with the introduction of carboxylic acid moieties, with CMP-1-$(COOH)_2$ demonstrating almost no porosity to N_2 at 77 K. It is likely that this trend is a result of increased density of hydrogen bonding interactions between the COOH species, causing a relatively contracted polymer network.

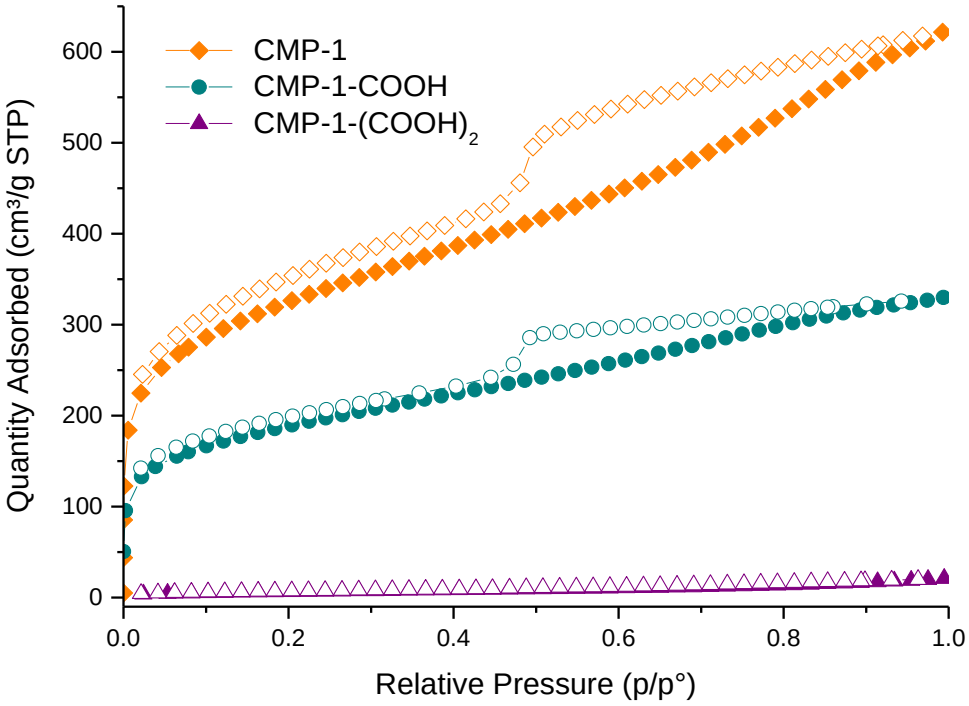

Figure 3.11

Nitrogen isotherms conducted at 77K of CMP-1 (orange), CMP-1-COOH (cyan) and CMP-1-$(COOH)_2$ (purple), Closed circles show the adsorption branch, open circles show the desorption branch.

Methanol isotherms performed on the CMP series show a clear trend in uptake, as shown in Figure 3.12. It is evident that uptake is determined by overall capacity of the polymer, with CMP-1 showing highest uptake both at high and low pressures, with a maximum capacity of 46.6 wt% at 95 % relative humidity. CMP-1-COOH shows intermediate uptake adsorbing up to 33.7 wt% at 95 % relative humidity. Finally, CMP-1-$(COOH)_2$ shows the lowest uptake of the series with a total methanol uptake of 27.8 wt %. It is supposed that the possession of a hydrophobic methyl group allows for the high uptake seen by the CMP-1 material, whereas the -OH functionality is clearly capable of disrupting the hydrogen bonding of the CMP-1-$(COOH)_2$. The slightly larger kinetic diameter of methanol (3.8 Å)[16] over nitrogen

(3.6 Å)[17] further suggests that the –OH functionality is necessary for pore access. As seen with water isotherms, the hysteresis at lower pressure may indicate polymer swelling upon methanol uptake.

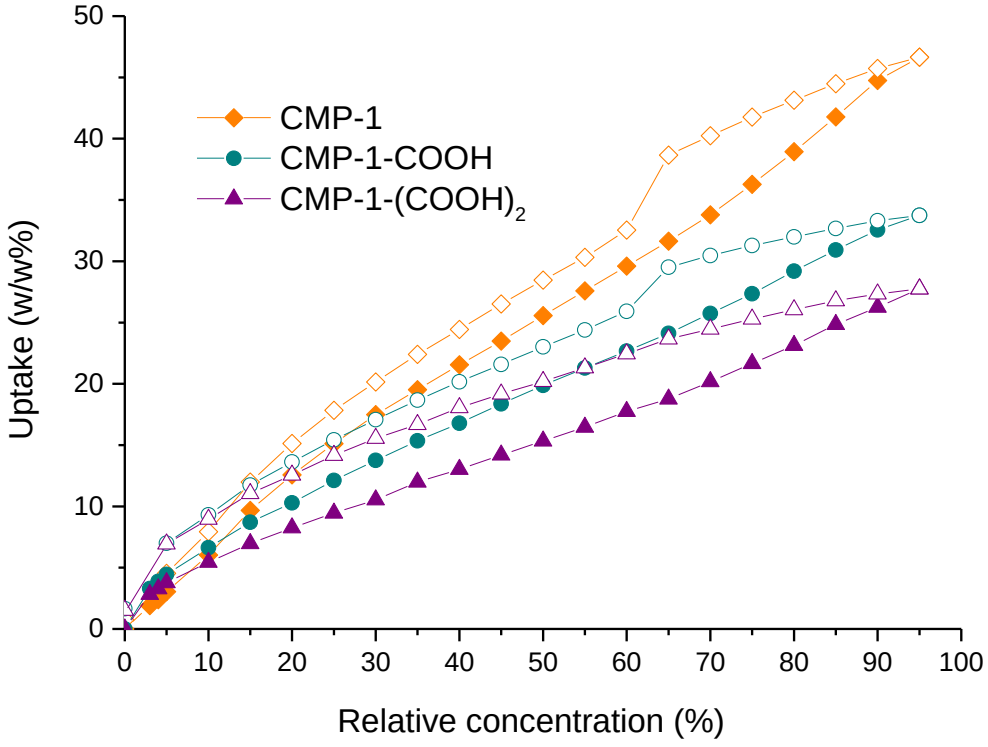

Figure 3.12

Methanol isotherms conducted at 298 K of CMP-1 (orange), CMP-1-COOH (cyan) and CMP-1-$(COOH)_2$ (purple) from 0% relative concentration to 95% relative concentration. Closed circles show the adsorption branch, open circles show the desorption branch.

3.6 Conclusion

Initial ammonia breakthrough testing of water-stable porous materials has been performed. Non-functionalised materials such as Ce-(HTCPB) and CMP-1 perform worse than BPL activated carbon, seemingly relying on physisorption alone for

ammonia uptake. As such the higher surface area of BPL carbon can account for its superior performance.

The study of the porous organic cage CC3, with its imine functionality, did not show any increased in performance over BPL carbon. Though suffering slightly decreased surface area, it is apparent that the presence of imines did not cause significant interaction with ammonia. It is possible that this was a result of competing hydrogen bonded water, adsorbed from the atmosphere.

Zn-Carnosine, containing beta-alanyl-L-histidine dipeptide linkers, exhibits almost a three-fold increase in performance over BPL carbon despite its lesser surface area, which can be attributed to the varied functionality of the linker units, offering opportunities for hydrogen bonding with ammonia.

In the case of CMP-1, the addition of one –COOH moiety per aromatic monomer caused an increase in ammonia uptake, however the addition of a second resulted in a material that showed almost no affinity for ammonia. Studies using polar solvents indicated that this was a result of dense hydrogen bonding within the polymer which ammonia could not sufficiently disrupt at 298 K. It was observed that the presence of water was necessary in order for the di-acid polymer to exhibit its full potential for ammonia uptake, with the material far outperforming the non-functionalised and mono-acid analogues in humid ammonia breakthrough experiments.

It can be concluded that careful selection of functionality is necessary for significant ammonia uptake in porous materials, in agreement with the current literature, with non-functionalised materials performing poorly, and suitably functionalised materials considerably outperforming BPL activated carbon.

3.7 References

1. J. E. Warren, C. G. Perkins, K. E. Jelfs, P. Boldrin, P. A. Chater, G. J. Miller, T. D. Manning, M. E. Briggs, K. C. Stylianou, J. B. Claridge and M. J. Rosseinsky, *Angew. Chem. Int. Ed.*, 2014, **53**, 4592-4596.
2. W. Feng, E. Borguet and R. D. Vidic, *Carbon*, 2006, **44**, 2990-2997.
3. M. Jaroniec, in *Access in Nanoporous Materials*, eds. T. J. Pinnavaia and M. F. Thorpe, Springer US, Boston, MA, 2002, DOI: 10.1007/0-306-47066-7_17, p. 263.
4. T. Tozawa, J. T. A. Jones, S. I. Swamy, S. Jiang, D. J. Adams, S. Shakespeare, R. Clowes, D. Bradshaw, T. Hasell, S. Y. Chong, C. Tang, S. Thompson, J. Parker, A. Trewin, J. Bacsa, A. M. Z. Slawin, A. Steiner and A. I. Cooper, *Nat Mater*, 2009, **8**, 973-978.
5. L. Chen, P. S. Reiss, S. Y. Chong, D. Holden, K. E. Jelfs, T. Hasell, M. A. Little, A. Kewley, M. E. Briggs, A. Stephenson, K. M. Thomas, J. A. Armstrong, J. Bell, J. Busto, R. Noel, J. Liu, D. M. Strachan, P. K. Thallapally and A. I. Cooper, *Nat Mater*, 2014, **13**, 954-960.
6. J. T. A. Jones, D. Holden, T. Mitra, T. Hasell, D. J. Adams, K. E. Jelfs, A. Trewin, D. J. Willock, G. M. Day, J. Bacsa, A. Steiner and A. I. Cooper, *Angew. Chem. Int. Ed.*, 2011, **50**, 749-753.
7. T. Hasell, M. Schmidtmann, C. A. Stone, M. W. Smith and A. I. Cooper, *Chem. Commun.*, 2012, **48**, 4689-4691.
8. A. P. Katsoulidis, K. S. Park, D. Antypov, C. Martí-Gastaldo, G. J. Miller, J. E. Warren, C. M. Robertson, F. Blanc, G. R. Darling, N. G. Berry, J. A. Purton, D. J. Adams and M. J. Rosseinsky, *Angewandte Chemie (International Ed. in English)*, 2014, **53**, 193-198.
9. R. Dawson, A. I. Cooper and D. J. Adams, *Prog. Polym. Sci.*, 2012, **37**, 530-563.
10. A. Laybourn, R. Dawson, R. Clowes, T. Hasell, A. I. Cooper, Y. Z. Khimyak and D. J. Adams, *Polymer Chemistry*, 2014, **5**, 6325-6333.
11. Y. Xu, S. Jin, H. Xu, A. Nagai and D. Jiang, *Chem. Soc. Rev.*, 2013, **42**, 8012-8031.

12. J. F. Van Humbeck, T. M. McDonald, X. Jing, B. M. Wiers, G. Zhu and J. R. Long, *J. Am. Chem. Soc.*, 2014, **136**, 2432-2440.
13. R. Dawson, A. Laybourn, Y. Z. Khimyak, D. J. Adams and A. I. Cooper, *Macromolecules*, 2010, **43**, 8524-8530.
14. C. Petit, B. Mendoza and T. J. Bandosz, *Langmuir*, 2010, **26**, 15302-15309.
15. W. Jens and T. Arne, in *Nanoporous Materials*, CRC Press, 2013, pp. 1-42.
16. T. Bein, K. Brown, G. C. Frye and C. J. Brinker, *J. Am. Chem. Soc.*, 1989, **111**, 7640-7641.
17. E. Albrecht, G. Baum, T. Bellunato, A. Bressan, S. Dalla Torre, C. D'Ambrosio, M. Davenport, M. Dragicevic, S. Duarte Pinto, P. Fauland, S. Ilie, G. Lenzen, P. Pagano, D. Piedigrossi, F. Tessarotto and O. Ullaland, *Nuclear Instruments and Methods in Physics Research Section A: Accelerators, Spectrometers, Detectors and Associated Equipment*, 2003, **510**, 262-272.

4 Aluminium porphyrin metal-organic framework

4.1 Introduction

The use of MOFs as sorbents for toxic industrial chemicals (TICs) is receiving growing attention in the scientific community, with materials often outperforming activated carbon, the current work-horse materials employed in industrial and military filters.[1,2,3] It has been presented in the literature that by tailoring the chemical environment within the pores of MOFs with particular regard to the chemical functionality of the TIC of interest, much higher uptake can be achieved. In the particular case of ammonia, the majority of examples either make use of coordinatively unsaturated metal sites within the framework to form coordinate bonds with ammonia,[4,5,6,7] or employ specific organic linkers that interact with ammonia via intermolecular forces such as hydrogen bonding.[7,8,9] Examples of MOFs that exploit Brønsted acidic sites within the framework are far fewer.[10,11] In this chapter, the ability of a highly stable porphyrin based MOF to maintain its structure after loading with hydrochloric or formic acid is shown, and subsequently its utility as a reservoir of acid to uptake ammonia in both dry and humid conditions.

Prior work within the group by Fateeva et al. resulted in the discovery of the compound $Al_2(OH)_2(H_2TCPP)(H_2O)_{1.8}$.[12] This metal organic framework, displayed in Figure 4.1, utilizes *meso*-tetra(4-carboxyphenyl) porphyrin, a linker comprising of four benzoate groups around a porphyrin core. Each linker is coordinated to eight different aluminium centres via its eight carboxylate oxygen atoms. Infinite axial chains of corner sharing octahedra with the formula $Al(OH)O_4$ are formed, whereby four carboxylate oxygen atoms from four different porphyrin linkers are coordinated

to Al^{3+} in the equatorial plane, and OH^- axially bridges adjacent Al^{3+} centres. These $Al(OH)O_4$ chains are a common motif in aluminium-carboxylate MOFs.[13,14]

$Al_2(OH)_2(H_2TCPP)(H_2O)_{1.8}$, referred to herein as Al-PMOF, was studied by Fateeva et al. with regard to its structural properties and its ability to perform visible light driven hydrogen generation from water.[12] It was found to be a particularly robust framework, stable in aqueous solutions (pH 5-8) and thermally stable up to 350^oC. The material was also seen to be highly porous, exhibiting three-dimensional porosity and a surface area of 1400 m^2/g. These properties in addition to its apparent functionality, suggested that Al-PMOF may perform well as a TIC sorbent.

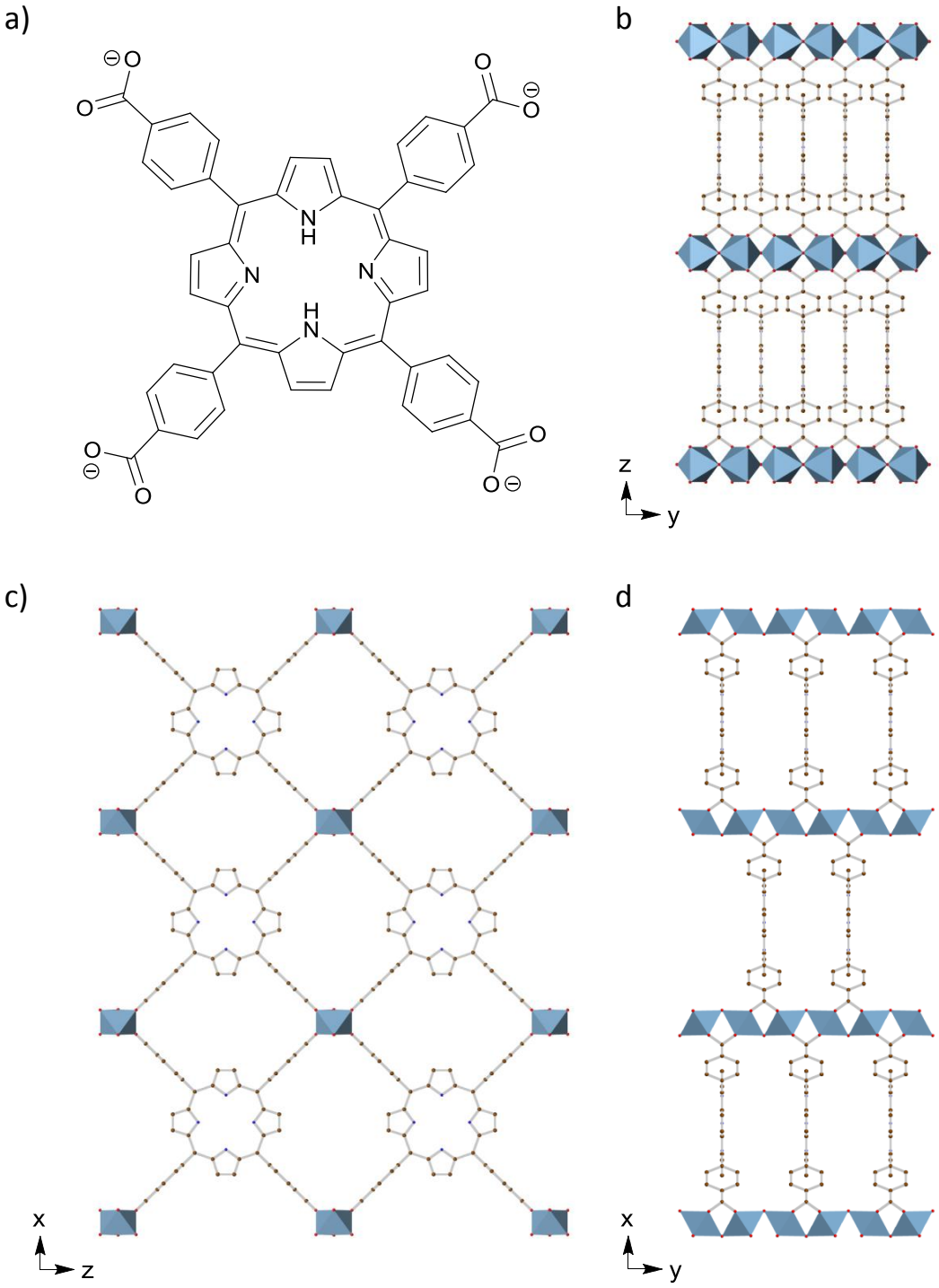

Figure 4.1

a) TCPP porphyrin linker in Al-PMOF; b-d) Crystal structure of Al-PMOF viewed along the x, y and z directions respectively displaying the three-dimensional porosity

It was hypothesised that the functionality present Al-PMOF may provide favourable hydrogen bonding interactions with NH_3. The porphyrin core of the linker is capable of hydrogen bonding [15,16] and its position in the channels of the MOF are readily accessible to NH_3. Further, the bridging hydroxyls between Al^{3+} provide an additional two possible hydrogen bonding sites per repeat unit (Figure 4.2).

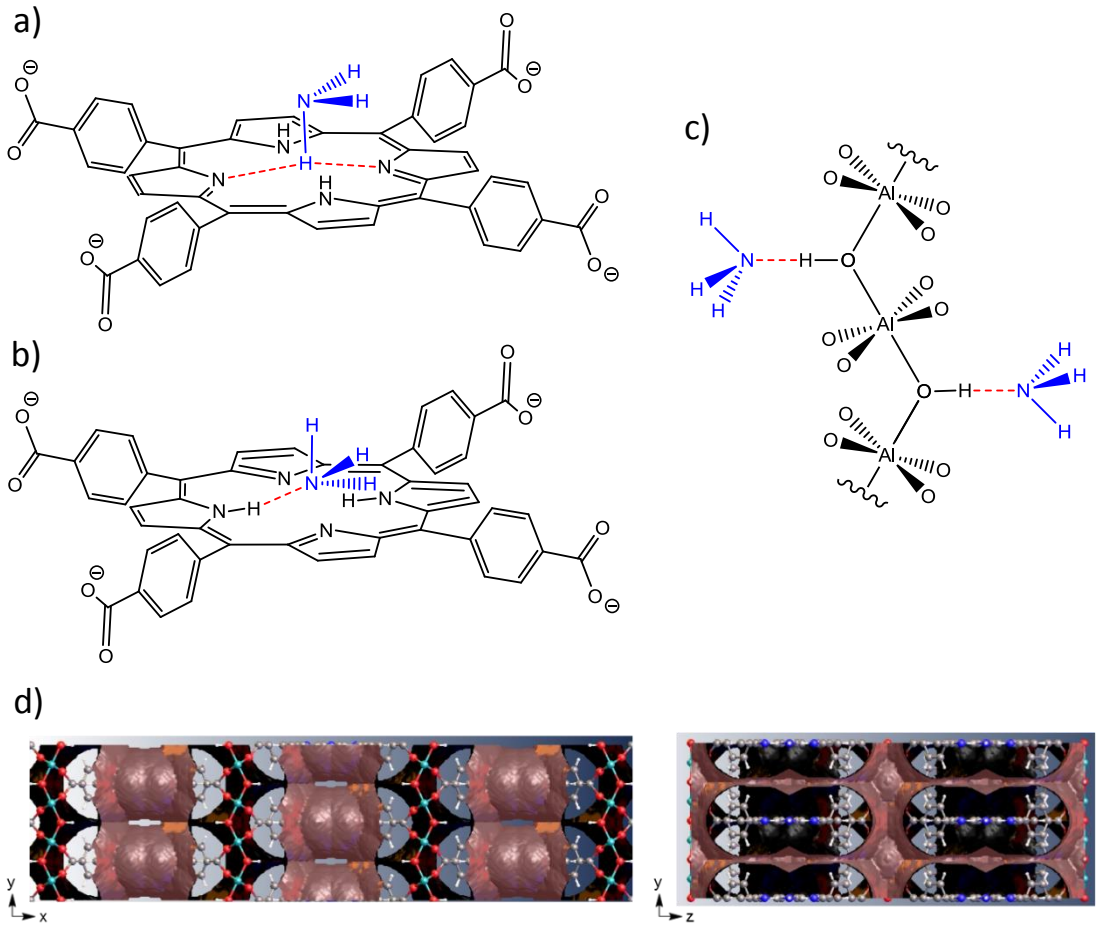

Figure 4.2

Hypothesised hydrogen bonding of ammonia with Al-PMOF where the porphyrin linker acts as a hydrogen bond acceptor (a) and donor (b); c) shows ammonia hydrogen bonding to bridging hydroxyl groups in the $Al(OH)O_4$ chain. d) Pore structure of Al-PMOF showing accessibility of the MOF to NH_3 (1.6 Å probe radius).

4.2 Experimental

Synthetic methods for the synthesis of compounds discussed in this chapter are given in this section.

4.2.1 Synthesis

5,10,15,20-tetrakis(4-carboxyphenyl) was ordered from TCI UK, all other chemicals are from Sigma-Aldrich. All were used without further purification.

Al-PMOF (1)

An aqueous stock solution of $AlCl_3$ was made by dissolving $AlCl_3 \bullet 6H_2O$ (875mg, 3.63 mmol) in 25 mL deionised water. 5,10,15,20-tetrakis(4-carboxyphenyl) porphyrin (300 mg 0.379 mmol) was added to a 125 mL Teflon liner, followed by 24 mL deionised water. $AlCl_3$ stock solution (5.14 mL, 0.75 mmol) was then introduced to the Teflon liner. The suspension was stirred for 5 minutes at room temperature before being sealed in a stainless steel autoclave and heated up to 180°C at a rate of 10°C per minute, for 16 h. The solution was allowed to cool with a cooling rate 2°C per minute. The mixture was transferred to a 50 mL centrifuge tube, using DMF (10 mL) to wash the Teflon liner, causing a colour change from dark green to purple. The solid was recovered by centrifugation, washing 10 times with DMF (10 × 30 mL) and once with THF (1 × 30 mL) in order to remove the unreacted porphyrin. After drying at room temperature, 70 mg of material was obtained as a purple solid. The material was then activated at 170^{o}C under vacuum (3 x 10^{-2} mbar, 16 h) to remove any guest molecules. Following reintroduction to air, atmospheric moisture is adsorbed affording the final product (50mg) with formula

$Al_2(OH)_2(H_2TCPP)(H_2O)_{1.8}$. Elemental microanalysis; calculated: C 63.55, H 3.51, N 6.18; experimental: C 63.72, H 3.05, N 6.05

Al-PMOF-HCl (2)

Activated (170^{o}C, 10^{-2} mbar) Al-PMOF (50mg) was inserted into a lidless 20mL glass vial, which was then inserted into a jar containing conc. hydrochloric acid (12 M, 5 mL). The jar was sealed and left standing for 16 h. The bright green solid was then removed and exposed to flowing N_2 for 1 h to remove any excess HCl.

Al-PMOF-Formic (3)

Activated Al-PMOF (50mg) was inserted into a lidless 20mL glass vial, which was then inserted into a jar containing conc. formic acid (23.6 M, 5 mL). The jar was sealed and left standing for 16 h. The dark green solid was then removed and exposed to flowing N_2 for 1 h to remove any excess formic acid.

Acid insertion method

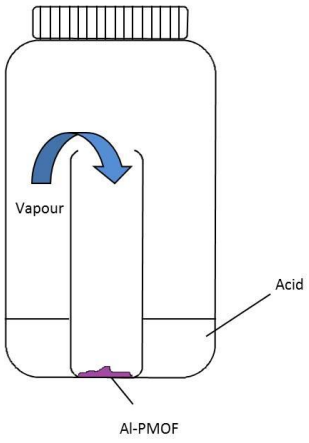

Figure 4.3

Method for acid insertion. Open vial containing Al-PMOF is sealed in a glass jar containing either conc. hydrochloric or formic acid, allowing the MOF to adsorb the acid vapour.

M-Al-PMOFs

Metalated Al-PMOF was synthesised based on a published method.[12] 50 mg of the activated Al-PMOF (170 °C under vacuum, (3 x 10^{-2} mbar, 16 h) was added to 5 mL of 0.04 M solution of metal acetate in DMF. The mixture was allowed to react at 100°C for 48 hours. The resulting solid was recovered by centrifugation and then repeatedly washed and centrifuged in DMF, water (3 times) and finally THF. The material was then activated at 170^{o}C under vacuum (3 x 10^{-2} mbar, 16 h) to remove any guest molecules. EDX confirmed insertion rate of approximately 82% and 90% for Co and Zn inserted materials, respectively, and surface area of approximately 1200m^2/g was calculated from 5-point BET measurements.

4.2.2 Scale up attempts

The initial method for Al-PMOF synthesis followed the procedure outlined by Fateeva *et al.*[12] whereby 100 mg (0.126 mmol) of 5,10,15,20-tetrakis(4-carboxyphenyl) porphyrin and 60 mg (0.25 mmol) of AlCl3·6H2O were added into 10 mL of deionised water. The suspension was stirred for 10 minutes at room temperature and then transferred into a 40 mL Teflon lined autoclave and heated at 180°C for 16 hours. The solution was allowed to cool with a cooling rate 1.5°C per minute. The solid was recovered by centrifugation, washed 3 times with DMF (3 × 80 mL) and once with acetone (1 × 80 mL) in order to remove the unreacted porphyrin. This method typically produced 25-30mg porphyrin material.

In attempt to increase the yield, firstly the reaction concentration was increased. 1.5, 2 and 3 times the initial amounts of porphyrin and aluminium chloride were reacted, which unfortunately afforded in no increase in yield. DMF was then used as solvent instead of water which resulted in a much higher yield, typically 100 mg of product

per 100 mg of porphyrin, over a 3-fold increase in yield. In addition, using DMF as solvent produced material that could be filtered instead of centrifuged, greatly decreasing the time required for washing the material following the reaction. However, PXRD analysis showed the crystallinity of the product to be considerably decreased (Figure 4.4). Further analysis using a 5-point BET measurement showed surface area to be somewhat decreased, at 1000 m^2/g in comparison with 1400 m^2/g for the water-based synthesis.

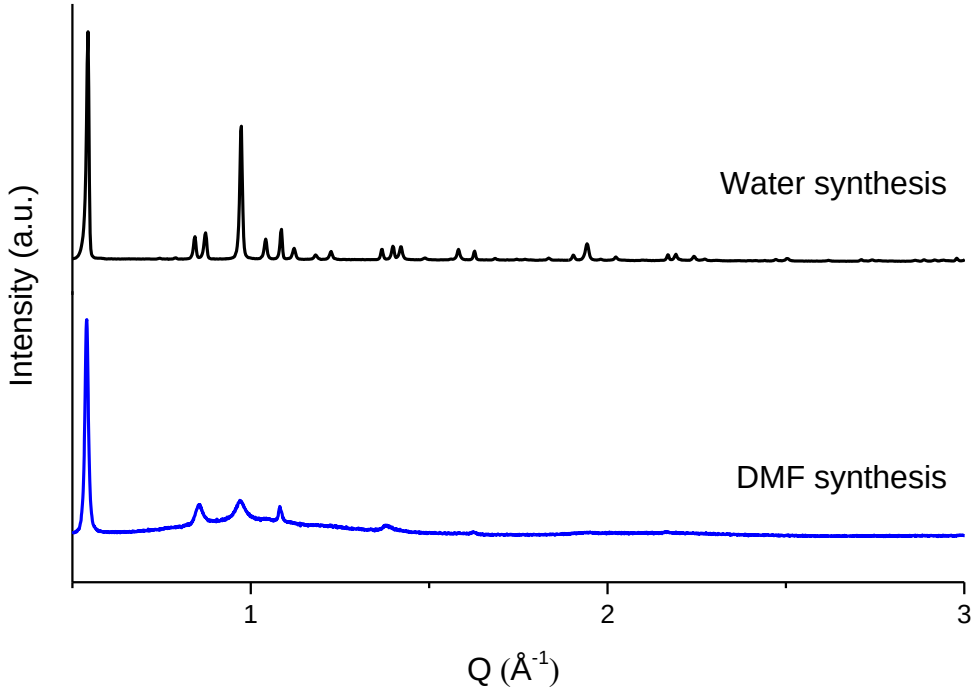

Figure 4.4

PXRD patterns comparing the water based and DMF methods of synthesising Al-PMOF with formic acid

Due to the ease of synthesis and increased yield of the DMF-based synthesis, attempts at increasing the crystallinity of the DMF-made material were attempted by

exploiting a process known as Ostwald ripening. Ostwald ripening is a thermodynamically driven process whereby over a long period, small crystals dissolve and then redeposit onto larger crystals, as a result of surface particles being less stable than interior particles.[17] DMF made Al-PMOF was heated in water in sealed hydrothermal vessels at selected temperatures for between 1 and 7 days, and examined by PXRD to determine if any increase in crystallinity had occurred, as shown in Table 4.1. Unfortunately, heating at 150 ^{o}C, 180 ^{o}C and 210 ^{o}C for between 1 and 3 days afforded no increase crystallinity of the material. At each temperature, after 7 days the MOF had decomposed and no solid material could be retrieved.

Table 4.1 Outcome of Ostwald ripening experiments as measured by PXRD

Experiment	**Temperature (^{o}C)**	**Time (days)**	**Outcome**
1	150	1	No improvement
2	150	3	No improvement
3	150	7	Decomposed
4	180	1	No improvement
5	180	3	No improvement
6	180	7	Decomposed
7	210	1	No improvement
8	210	3	No improvement
9	210	7	Decomposed

It was decided that scale-up would be attempted using larger reaction vessels, maintaining the ratio of reactants and solvent as described in the original synthesis,[12] but increasing them 3-fold to match the 3-fold larger reaction vessels. This resulted in an approximate doubling of MOF produced from each reaction vessel, at the cost

of using 3 times the starting material. Though less economical in raw materials, this method was decided more convenient for the continued synthesis of the material.

4.3 Al-PMOF

4.3.1 Dry ammonia breakthrough

Initially, a dry (0% relative humidity) flow of ammonia was chosen in order to assess the potential of Al-PMOF as a sorbent of ammonia. The results are presented in Figure 4.5. Ammonia was detected above 20ppm after 14 minutes of testing, comparing favourably to the benchmark BPL activated carbon, which itself breaks through after approximately 7 minutes. The amount of ammonia adsorbed at breakthrough is calculated to be 9.3×10^{-3} mmol which gives an NH_3:porphyrin ratio of approximately 0.28:1 in the MOF. At saturation, taken at 32 minutes, Al-PMOF has adsorbed 0.012 mmol NH_3 which equates to a 0.35:1 NH_3:porphyrin ratio. It is evident that neither at breakthrough, nor at saturation does the ammonia fully utilize the three possible binding sites. This may be a result of competitive binding of H_2O at these sites, or perhaps due to the kinetics of adsorption.

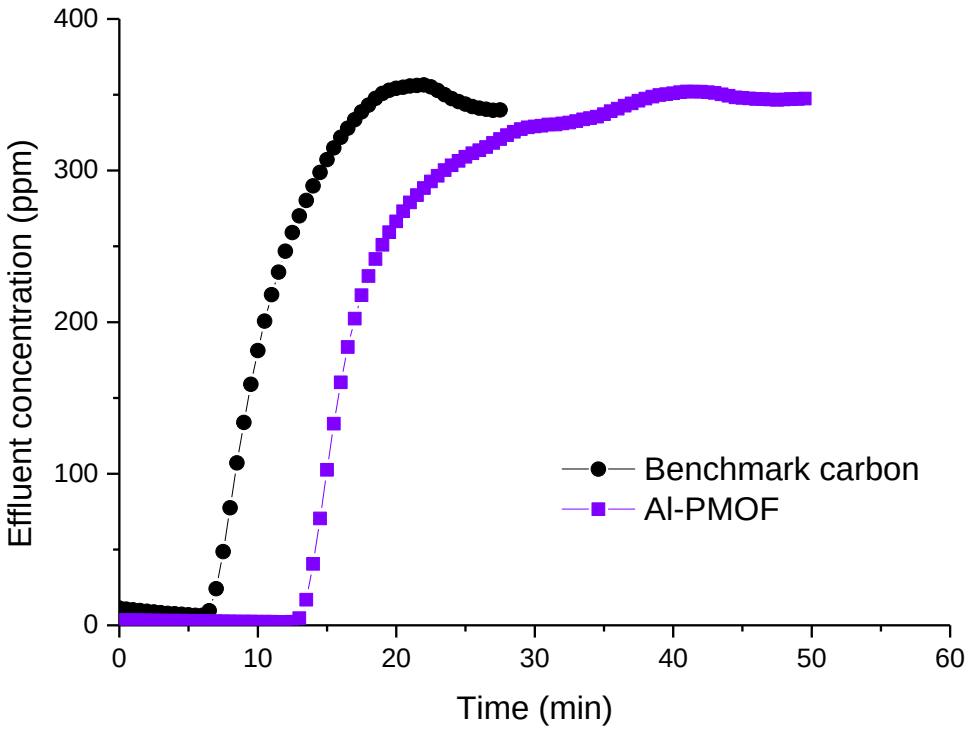

Figure 4.5

Ammonia breakthrough curve of Al-PMOF (purple) in a 0% RH flow of ammonia. BPL activated carbon (black) is shown for comparison.

4.3.2 Humid breakthrough

Humid breakthrough testing was performed on samples in order to assess their performance as ammonia sorbents in an environment closer to real-world conditions. The humid (80% RH) ammonia breakthrough curves are displayed in Figure 4.6. Ammonia was detected above the 20ppm breakthrough limit after 26 minutes, once again comparing well to the benchmark BPL activated carbon result of 13 minutes. 0.016 mmol of ammonia is calculated to have been adsorbed at breakthrough, giving an NH_3:porphyrin ratio of approximately 0.50:1 in the MOF. At saturation, taken at 42 minutes, Al-PMOF has adsorbed 0.019 mmol NH_3 which equates to a 0.59:1 NH_3:porphyrin ratio.

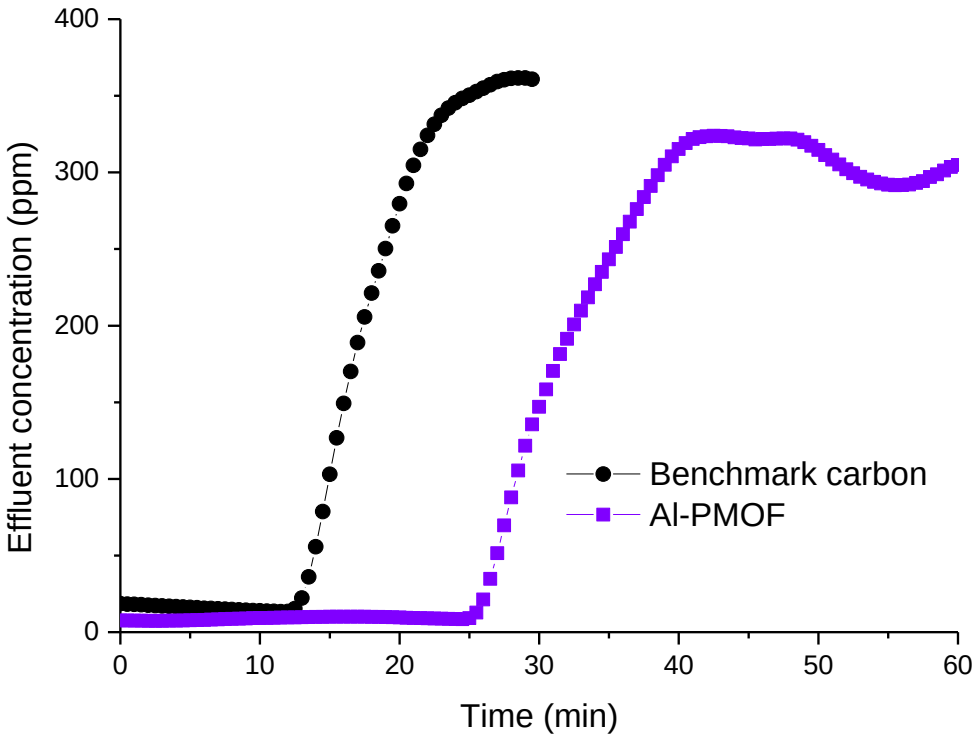

Figure 4.6

Ammonia breakthrough curve of Al-PMOF (purple) in an 80% RH flow of ammonia. BPL activated carbon (black) is shown for comparison.

A common feature of porous materials is to perform better in humid ammonia breakthrough tests than dry tests, attributed to the high solubility of ammonia in the water film created in the pores of the sorbent.[18] Water isotherms were conducted on Al-PMOF to help understand the effect of water in the during humid ammonia breakthrough tests. The results are shown in Figure 4.7.

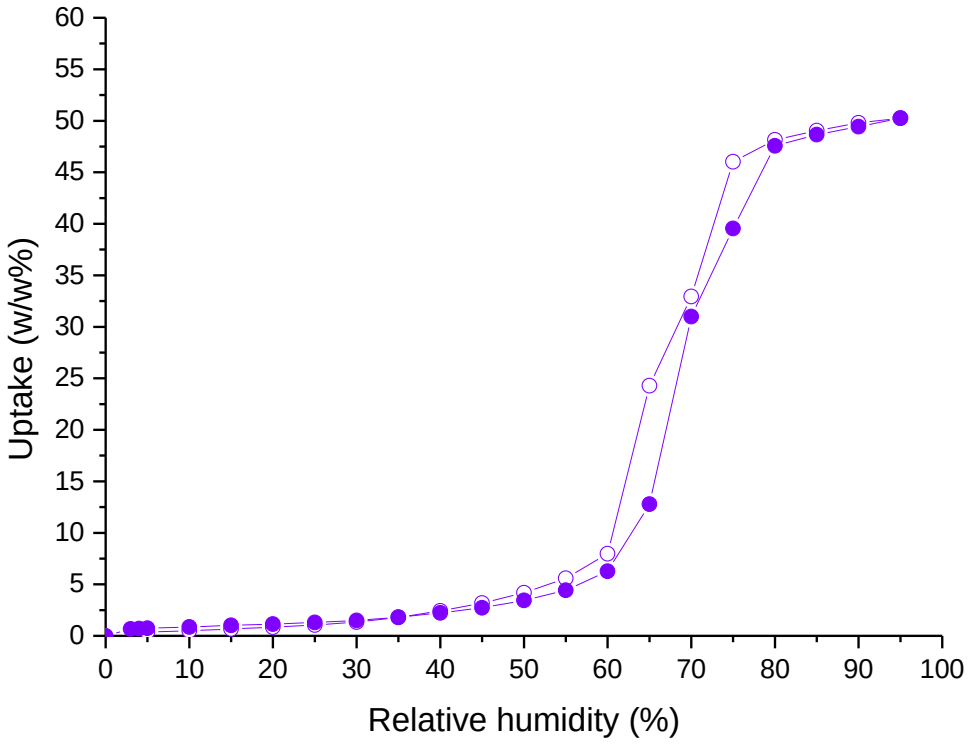

Figure 4.7

Water isotherm at 298 K of Al-PMOF from 0% RH to 95% RH. Closed circles show the adsorption branch, open circles show the desorption branch.

The water adsorption isotherm of Al-PMOF exhibits a sigmoidal shape, belonging to the Type V family per the IUPAC classification.[19] A very low water uptake is observed between RH of 0% and 60%, with sudden micropore filling between 60% and 80% RH, and a final plateau up to 95% RH. These Type V isotherms are very well studied for water vapour uptake on microporous activated carbons,[20] and have also been observed in MOFs.[21] This type of isotherm is typical of when adsorbate-adsorbate interactions are stronger than adsorbent-adsorbate interactions, which is expected in this material due to the hydrophobic character of the material. At low loading, the behaviour is solely controlled by molecule to surface (vertical) interactions. Water molecules are adsorbed on polar sites on the surface initially. The

primary adsorption sites here are believed to be the porphyrinic nitrogens and the OH^- bridging functional groups on the surface, which strongly interact with the polar water molecules. With increasing relative humidity, clusters of water molecules are thought to form around these favourable sites, by association via hydrogen bonding. The clusters rapidly grow with increasing relative humidity until they merge together and the pore filling has occurred. This rapid cluster growth is seen in the isotherm at the typical inflection point associated with Type V isotherms.[22,23]

4.4 Metal insertion

An advantage of Al-PMOF with its porphyrin linker is the ability to metalate the porphyrin core. As discussed in chapter 1, it has been observed in the literature that coordinatively unsaturated metal sites have been seen to have a positive impact on ammonia uptake and breakthrough times as a result of their interaction with ammonia. As such, post-synthetic modification of Al-PMOF was achieved using $Co(OAc)_2$ and $Zn(OAc)_2$ in DMF to insert Co^{2+} and Zn^{2+} into the porphyrin core, as shown in Figure 4.8 (synthetic details in section 3.2). Loadings of 82% and 90% were achieved for Co and Zn, respectively, as determined by EDX.

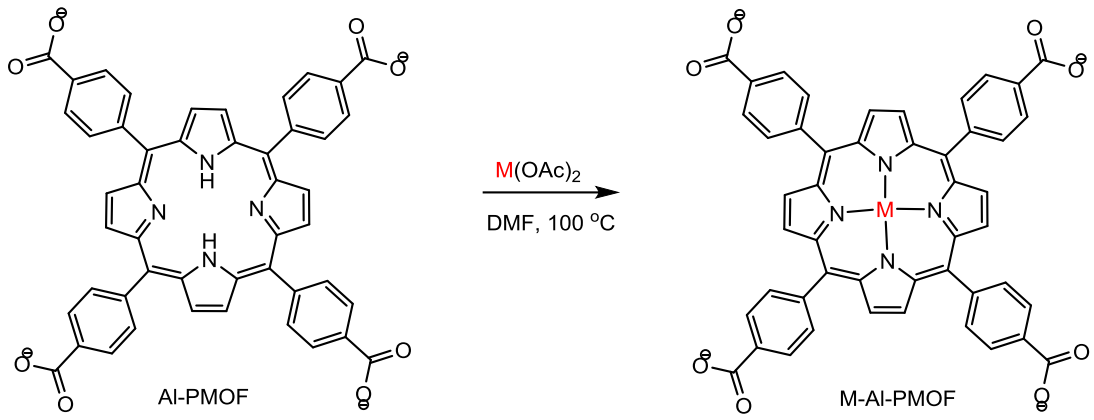

Figure 4.8

Reaction scheme showing the metalation of Al-PMOF using metal acetate

Both Co-Al-PMOF and Zn-Al-PMOF were assessed as sorbents for ammonia by conducting dry ammonia breakthrough runs. The results are displayed in Figure 4.9. The loading of metals into the parent Al-PMOF porphyrin cores has had a significant positive impact on breakthrough times in comparison with BPL carbon. Breakthrough of ammonia occurred after 14 minutes for the cobalt inserted material, and 23.5 minutes for the zinc inserted material under ammonia flows of 1000 ppm (outperforming Al-PMOF, which achieved a breakthrough time of 14 mins under ammonia flows of 500 ppm). The amount of ammonia adsorbed at breakthrough is calculated to be 0.017 mmol and 0.029 mmol for the cobalt and zinc inserted materials respectively comparing well to 9.3×10^{-3} mmol for the Al-PMOF.

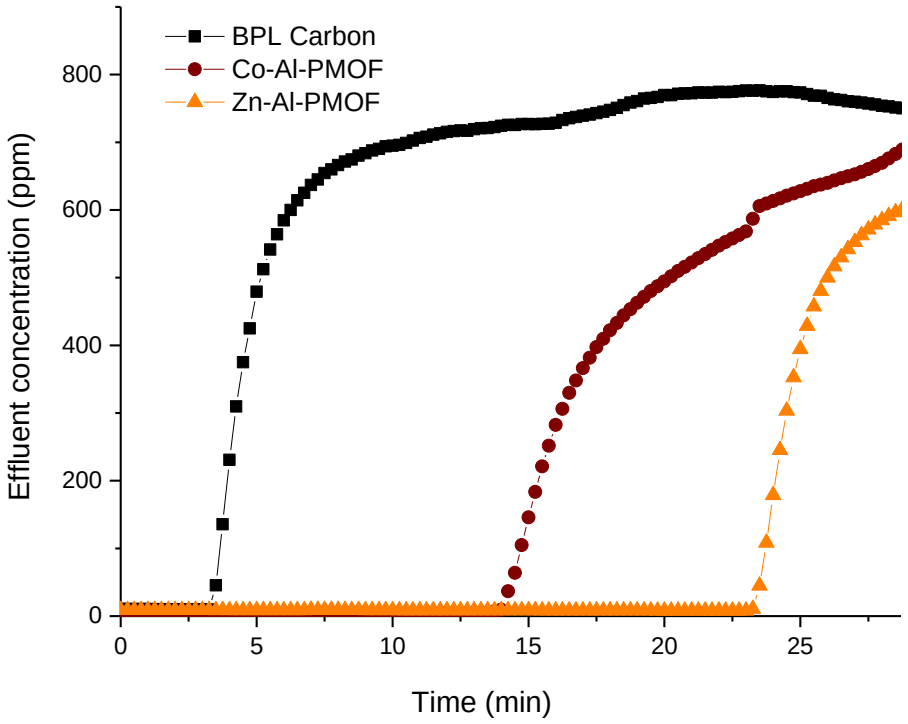

Figure 4.9

Ammonia breakthrough curves for Co-Al-PMOF and Zn-Al-PMOF using a 0% RH flow of ammonia at a concentration of 1000 ppm. BPL activated carbon (black) is shown for comparison.

In addition to the slightly higher loading achieved for Zn-Al-PMOF, the Lewis acidity of Zn^{2+} is greater than that of Co^{2+}, as determined by ammonia binding constants[24], which can account for the difference seen in performance. In addition, it was assumed that as a result of its higher Lewis acidity, Zn-Al-PMOF may also absorb more atmospheric moisture than Co-Al-PMOF, which may aid ammonia uptake to some extent. Water isotherms were subsequently performed on these materials to determine this.

The water isotherms (Figure 4.10) show Type V behaviour for both metalated materials, similar to the parent MOF. The initial part of a Type V water isotherm is

determined by surface chemistry,[25,26] which indicates that the zinc loaded MOF has higher affinity for water than the cobalt loaded MOF and the free base MOF, which was expected based on the Lewis acidity of Zn^{2+}. At higher relative humidity, overall surface area of Al-PMOF dominates (1400 m^2/g, in comparison with 1200 m^2/g for both Zn-Al-PMOF and Co-Al-PMOF). Zn-Al-PMOF has higher overall uptake than Co-Al-PMOF likely as a result of its higher affinity for water.

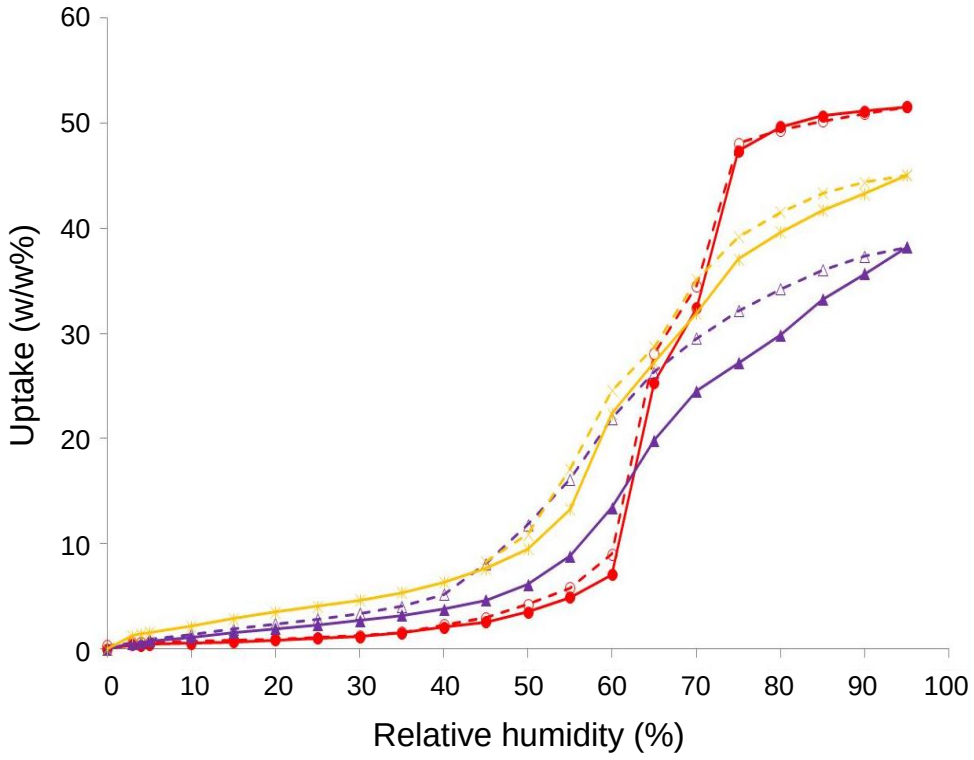

Figure 4.10

Water isotherms at 298 K of Zn-Al-PMOF (yellow), and Co-Al-PMOF (purple) from 0% RH to 95% RH. Al-PMOF (red) shown for comparison.

4.5 HCl loaded Al-PMOF

Work by Fateeva led to the discovery that the porphyrin linker of the Al-PMOF could be protonated with HCl using a vapour insertion method, (discussed in more detail in section 3.2). It was expected that such a material might prove beneficial for the uptake of ammonia.

4.5.1 Characterisation

Following exposure to HCl vapour, a clear colour change from purple to green is observed. This colour change can be attributed to protonation of the porphyrinic nitrogen atoms [27]. Using this vapour method is necessary for acid loading as aqueous solutions were seen to decompose the MOF.

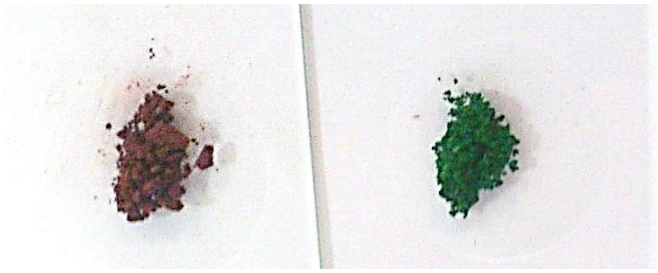

Figure 4.11

Image showing Al-PMOF (left) and Al-PMOF-HCl (right)

Porphyrins tend to show characteristic absorption spectra as a result of their conjugated π systems; typically, there is an intense absorption peak around 400 nm called the Soret band in addition to several weaker absorption peaks at longer wavelengths called Q-bands.[28] The Q bands result from excitation of the porphyrin

from its ground state to the first excited state, whereas the Soret band is due to excitation of the porphyrin from its ground state to its second excited state. A typical porphyrin absorption spectrum is shown in Figure 4.12. Depending on the conditions, the UV−visible spectra of some porphyrins can show split and/or broadened Soret bands, along with greater red-shifts. These spectra are characteristic of hyperporphyrins, which are defined as porphyrins which exhibit prominent additional absorption bands above 320 nm which are not attributed to porphyrin π−π* transitions.[29, 30] Such spectra have been reported in metal porphyrin charge transfer transitions[31], when porphyrins are subjected to acidic[32-38] or basic[39-41] conditions, or with oxidation of porphyrins with electron-rich phenyl substituents[42].

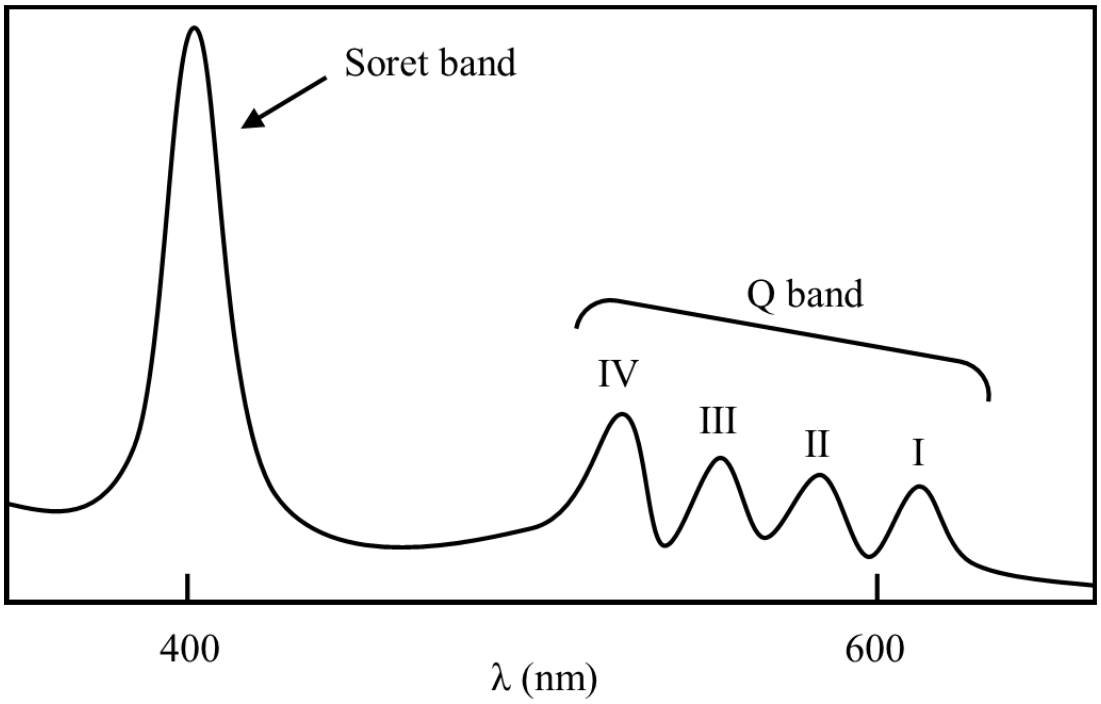

Figure 4.12

A typical porphyrin absorption spectrum

Typically, when the porphyrin is protonated there is a characteristic red shift of the Soret band and a reduction of Q bands from four to two, owing to increased symmetry (and increased degeneracy).[43,44] UV-visible spectra showing the protonation of TCPP (the porphyrin used in Al-PMOF) by HCl and TFA are presented in reference 38, Figure 2.[38] Both a red-shift and splitting of the Soret band are observed, as well as the collapse of the four Q bands and the emergence of Q bands at higher wavelength.

UV-visible spectroscopy carried out on Al-PMOF reveals a lower intensity Soret band than observed for typical molecular porphyrins at 423 nm, and Q-bands at 506 nm, 535 nm, 587 nm and 643 nm (Figure 4.13). Upon exposure to HCl, the Soret band is red-shifted from 423 nm to 477 nm, with possible splitting. The collapse of Q-bands from the parent MOF is apparent, suggesting protonation of the porphyrin.

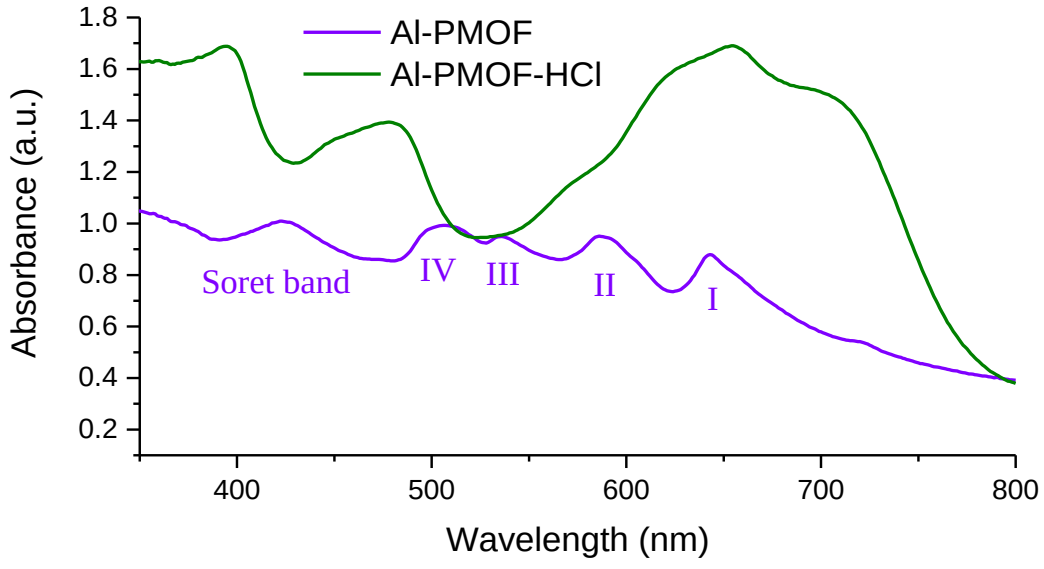

Figure 4.13

UV-Visible absorption spectra of Al-PMOF (purple) and Al-PMOF-HCl (green)

However, within the broad band which arises approximately > 600nm it may be possible to discern more than the two peaks which would be expected from the fully diprotonated porphyrin. It seems possible that the porphyrin may be in part monoprotonated, showing similarities to monoprotonated porphyrin spectra in the literature[30, 45]. The UV-visible spectra of monoprotonated tetraphenylporphyrin can be seen in reference 45, Figure 2.

Thermo-gravimetric analysis and ion chromatography were used to determine the HCl content of the acid loaded material. TGA (Figure 4.14) shows a guest weight loss of 37.0% attributed to HCl and water. Ion chromatography shows a chloride content of 16.7%. Thus, combining the data gives a composition of 63.0% MOF, 16.7% HCl and 20.3% water by weight. It can then be calculated that the Al-PMOF-HCl has a composition of $Al_2(OH)_2(H_2TCPP)(HCl)_{6.5}(H_2O)_{15.3}$. It is noted that desolvated Al-PMOF adsorbs only 1.8 H_2O molecules per porphyrin from the atmosphere in ambient conditions, likely due to the hydrophobic nature of the porphyrin linker. A considerable increase in water adsorption as a result of the acid loading process is seen, presumably due to the polar nature of the acid groups within the pores creating a much more hydrophilic environment.

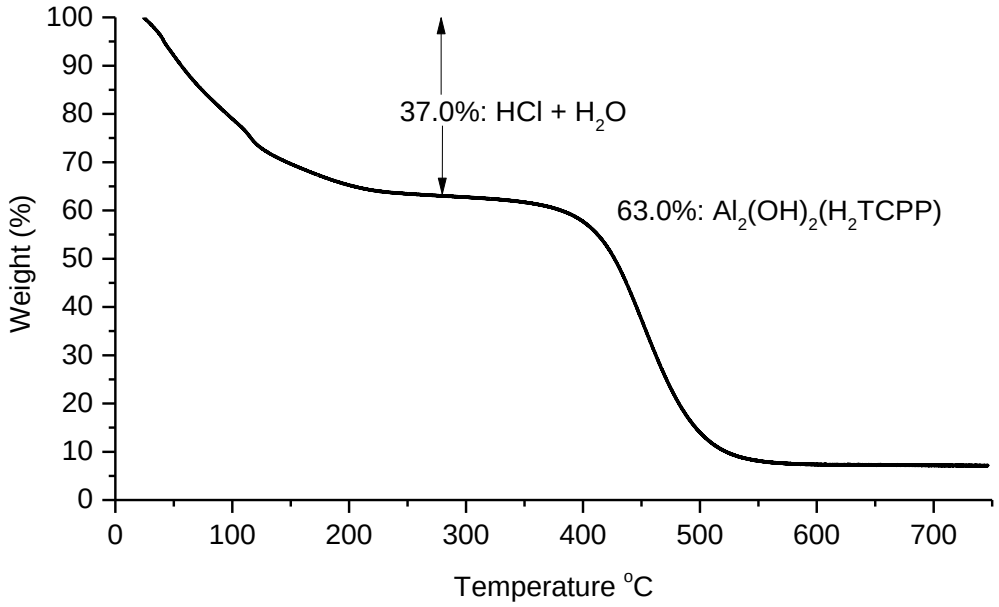

Figure 4.14

TGA trace of Al-PMOF-HCl showing the guest weight loss of 37.0%

In order to compare the experimentally found loadings with maximum possible loadings, calculations were performed using Olex² Crystallography Software[46] to determine the total accessible volume of the MOF to HCl and H_2O. This was achieved by using the kinetic diameter of HCl and H_2O (3.20 Å and 2.65 Å respectively)[47] to model the probe as a sphere, then calculating voids from the Al-PMOF CIF that are large enough to contain this sphere. By using the liquid density of the guest, the maximum loading of the guest can be calculated. The results are summarised in Table 4.2. From these calculations, based on the composition $Al_2(OH)_2(H_2TCPP)(HCl)_{6.5}(H_2O)_{15.3}$, 78% of the pore volume is occupied by HCl and H_2O.

Table 4.2 Experimental guest loading of HCl and H_2O in comparison with calculated maximum loading for Al-PMOF

Adsorbate	Calculated accessible volume ($Å^3$ per unit cell)	Maximum loading (guests per porphyrin)	Experimental loading (guests per porphyrin)
HCl	1577.1	19.23	6.5
H_2O	2011.0	33.61	15.3

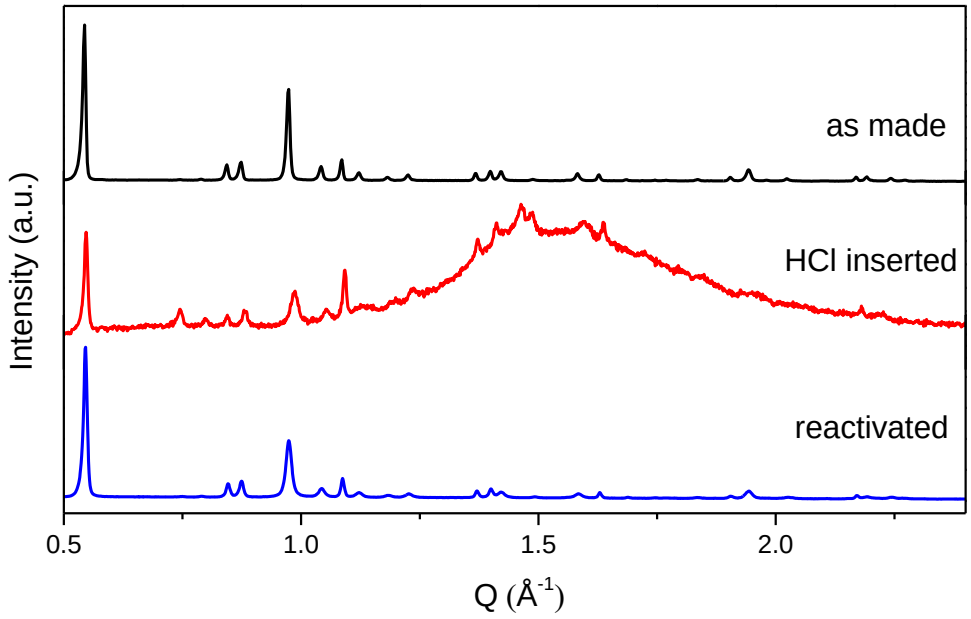

Figure 4.15

PXRD pattern of Al-PMOF (black) Al-PMOF-HCl (red) and Al-PMOF following the removal of HCl at 170°C at 10^{-2} mbar.

Powder X-ray diffraction also reveals a significant difference between the parent MOF and the HCl loaded material. A significant decrease in crystallinity is observed in addition to the appearance of a large amorphous hump in the 20 to 35° 2θ region. This hump is most likely a result of the short range order exhibited by HCl and H_2O

within the pores of the framework. It is a remarkable property of this material however, that upon re-activation at 170^{o}C at 10^{-2} mbar, the guest HCl and H_2O can be removed from the framework leaving the original framework largely intact. Powder x-ray diffraction (Figure 4.15) shows that the original crystallinity is largely restored, and the amorphous hump is no longer present.

Indexing Al-PMOF-HCl to *Cmmm* was initially attempted, however additional reflections were observed. Thus, it was necessary to use a lower symmetry space group (*Pmmm*) which allowed all peaks to index (Figure 4.16), with lattice parameters shown in Table 4.3.

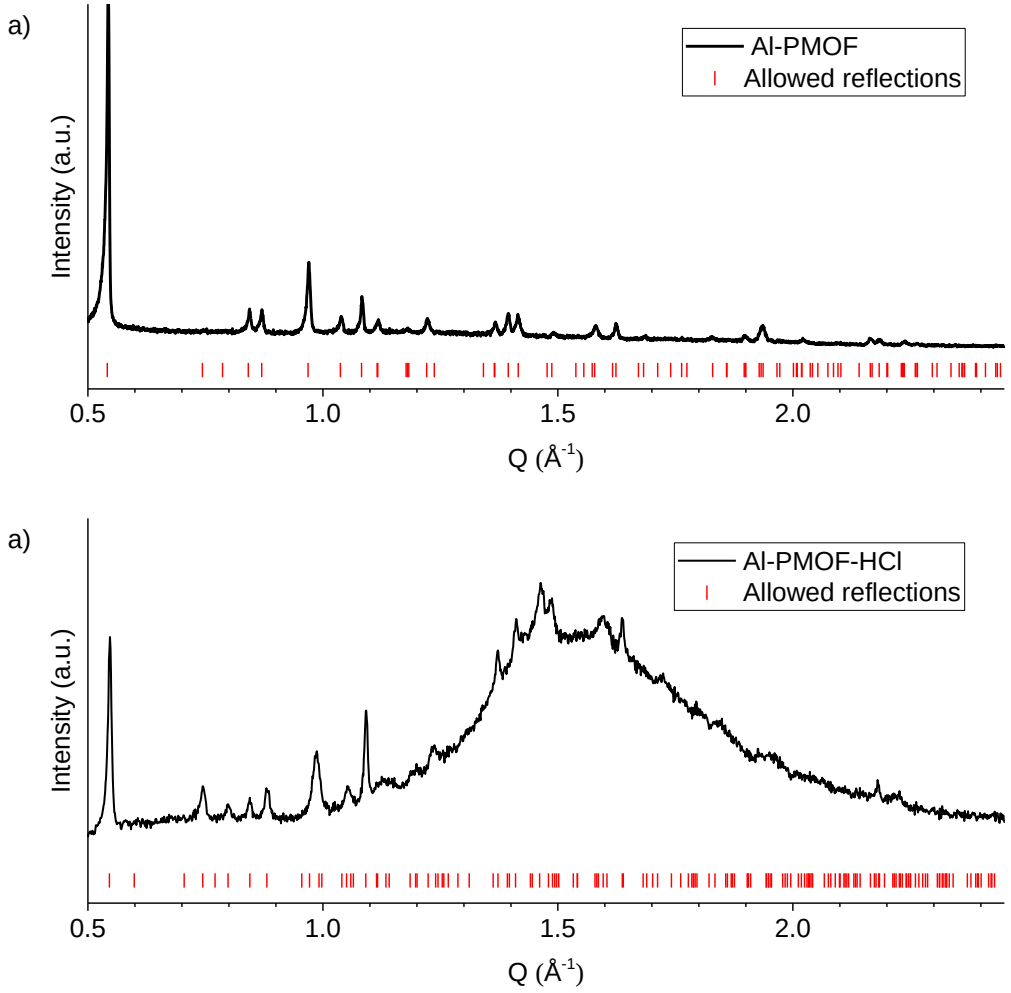

Figure 4.16

PXRD patterns of Al-PMOF prior to (a) and after (b) HCl loading, showing the allowed reflections (red ticks) according to the space group and lattice parameters in Table 4.3

Table 4.3 Lattice parameters of Al-PMOF (*Cmmm*) and Al-PMOF-HCl (*Pmmm*)

MOF	**Lattice Parameters (Å)**		
	a	*b*	*c*
Al-PMOF	31.96(1)	6.627(2)	16.901(6)
Al-PMOF-HCl	31.484(6)	6.460(1)	16.881(5)

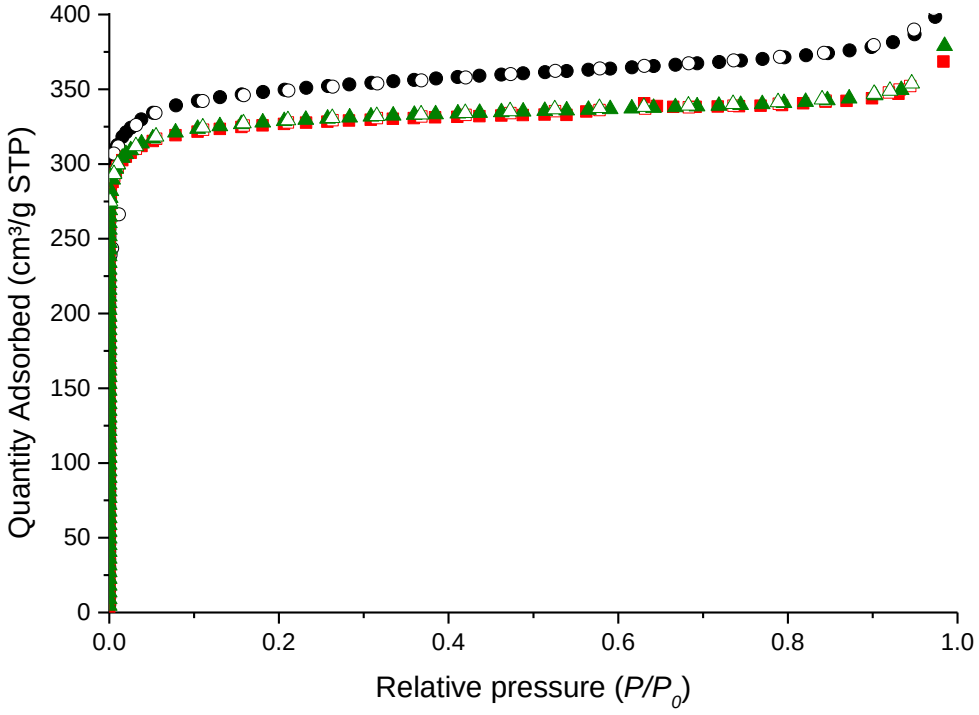

Figure 4.17

Nitrogen isotherms at 77K after cycling hydrochloric acid uptake and removal at 170 ^{o}C, 10^{-2} mbar. Fresh, activated Al-PMOF is shown in black circles; the first and third cycles are shown in red squares and green triangles, respectively. Adsorption and desorption is denoted by filled and empty symbols

The porosity of the material was assessed following removal of HCl (170^{o}C, 10^{-2} mbar) by conducting nitrogen isotherms at 77 K. This revealed a small decrease of approximately 8% in accessible pore volume compared to the parent material. Two further cycles of acid loading and activation were performed on the sample, which interestingly this caused no further loss of porosity as seen in Figure 4.17. The stability of this MOF toward such a highly reactive guest species is extremely surprising.

4.5.2 Dry ammonia breakthrough

Al-PMOF-HCl was assessed as a sorbent for ammonia initially by conducting dry ammonia breakthrough runs. The results are displayed in Figure 4.18. It is plain that the loading of HCl into the parent Al-PMOF framework has substantial effect on the breakthrough time. Breakthrough of ammonia was observed after 133.5 minutes of testing, in comparison to the 14 minutes exhibited by the free base MOF – over 9.5 fold increase in performance. The amount of ammonia adsorbed at breakthrough is calculated to be 0.088 mmol which gives an ammonia:porphyrin ratio of approximately 3.8:1 in the MOF. This material exhibits a much less sharp ascent to saturation than both the BPL activated carbon and the parent Al-PMOF indicating that not all adsorption sites have been occupied at the point of breakthrough, yet those remaining are likely more difficult for the ammonia to access resulting in an overall decrease in reaction kinetics. Unfortunately, due to the length of the measurement, saturation was not reached, however the maximum measured value shows an overall uptake of 0.14 mmol ammonia, equating to 6.6:1 ammonia:porphyrin, and a conservative estimate using a linear projection indicates an ammonia:porphyrin ratio in excess of 6.9:1.

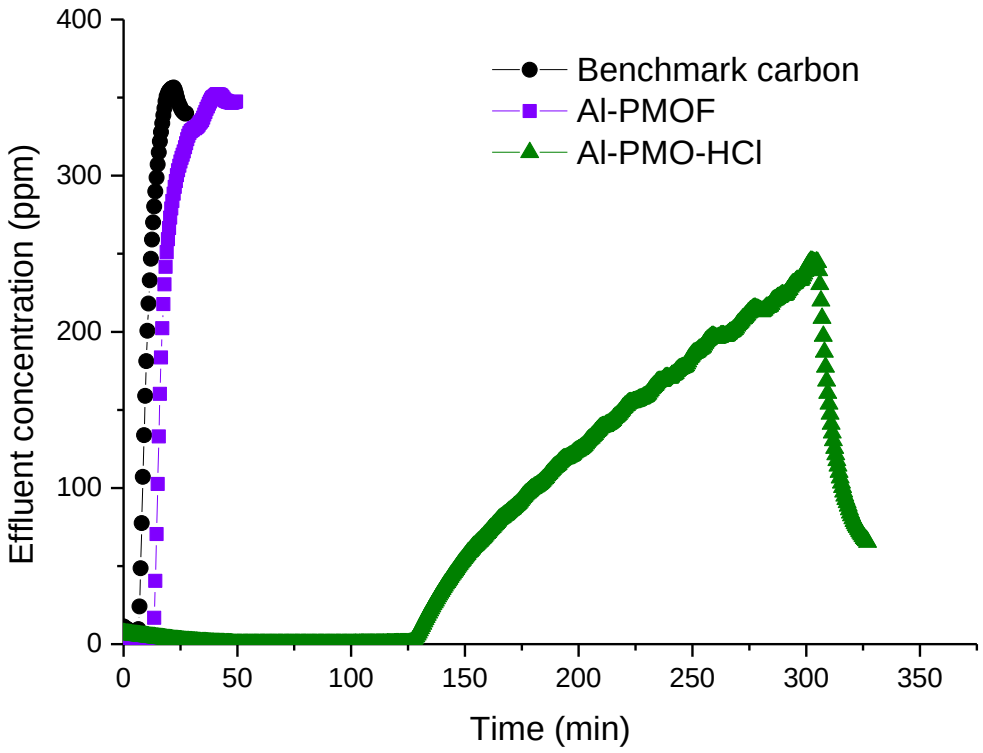

Figure 4.18

Ammonia breakthrough curve for Al-PMOF-HCl using a 0% RH flow of ammonia. Al-PMOF and BPL activated carbon are shown for comparison

Considering the ratio of HCl to basic porphyrinic nitrogen in this material is 6.5:2, and that the PXRD pattern suggests disordered HCl within the material, it is hypothesised that there is HCl within the pores of the MOF that is not bound to the basic nitrogens of the porphyrin, able to freely interact with the effluent ammonia. Indeed, powder X-ray diffraction was performed on the Al-PMOF-HCl following ammonia breakthrough (Figure 4.19) showing highly crystalline peaks that were not present in either the free-base material, or in the HCl loaded material. Peak search and phase identification were performed in Panalytical Highscore Plus using the ICDD PDF2 database gave a positive match for a cubic (Pm-3m) phase of NH_4Cl. This suggests that the interaction between the HCl loaded MOF and the ammonia is

a simple acid-base reaction. Furthermore, the presence of peaks attributed to the parent phase are still visible, however a considerable loss of crystallinity is observed in comparison with the parent material.

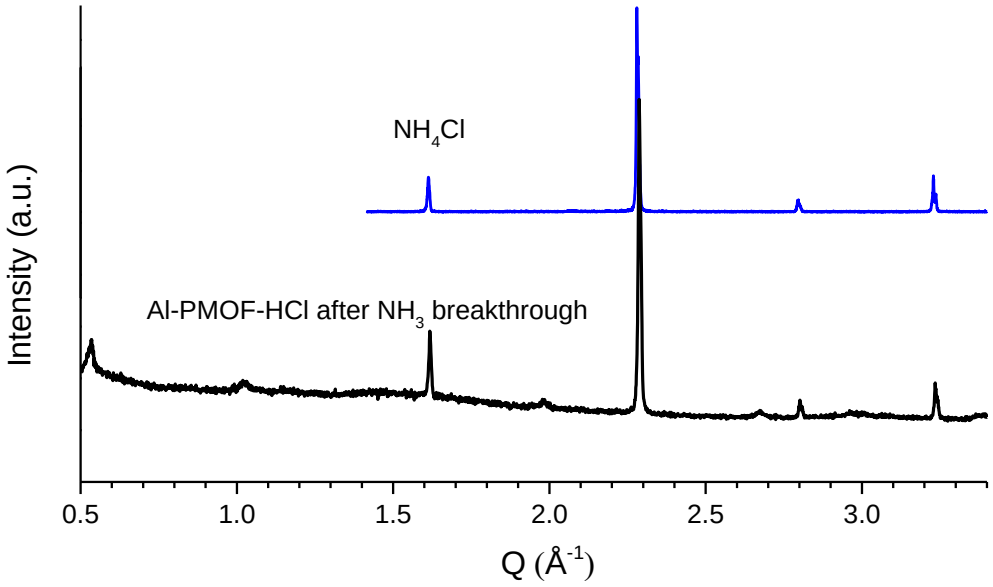

Figure 4.19

PXRD pattern of Al-PMOF-HCl following dry ammonia breakthrough (black) showing the formation of ammonium chloride. PXRD pattern of ammonia chloride (blue) is shown for comparison.

The sharp, well-defined peaks of ammonium chloride from PXRD suggests that the ammonium chloride has not formed inside the channels of the MOF, as crystallites with such small dimensions in the channels would exhibit extremely broad peaks. As such it appears ammonium chloride must form outside of the MOF. Thus, a mechanism for ammonium chloride formation is proposed whereby HCl and ammonia react exterior to the MOF crystallites (Figure 4.20), with the Al-PMOF acting as a stable acid reservoir.

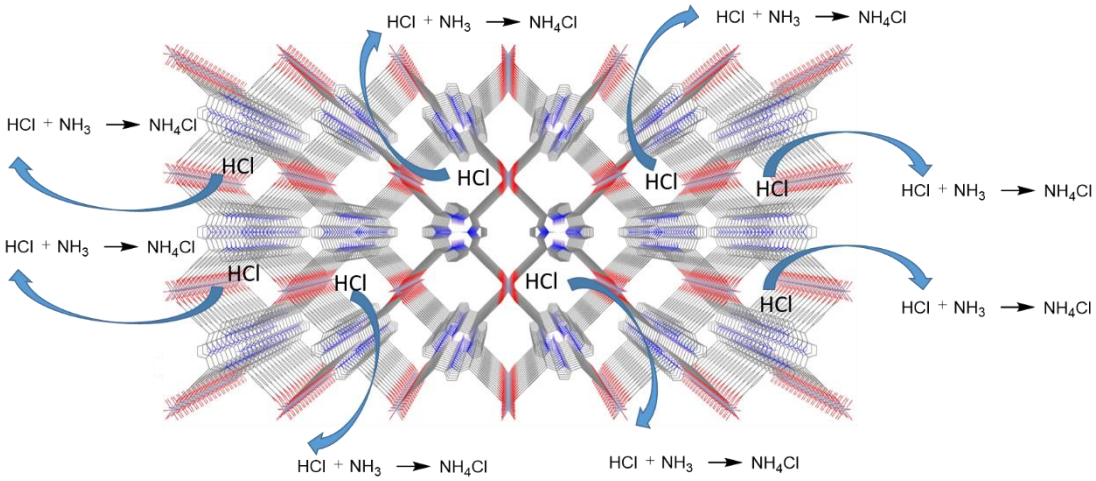

Figure 4.20

Schematic showing the proposed reaction mechanism between Al-PMOF-HCl and NH_3

SEM images were taken in an attempt to observe any ammonium chloride (Figure 4.21). Visually there was no material appearing distinctively different to the parent material, and EDX analysis revealed no evidence of ammonium chloride in the sample, and this was attributed to the volatility of ammonium chloride in the reduced pressure of the SEM.[48] It was noted that particles appeared comparable both before and after ammonia exposure.

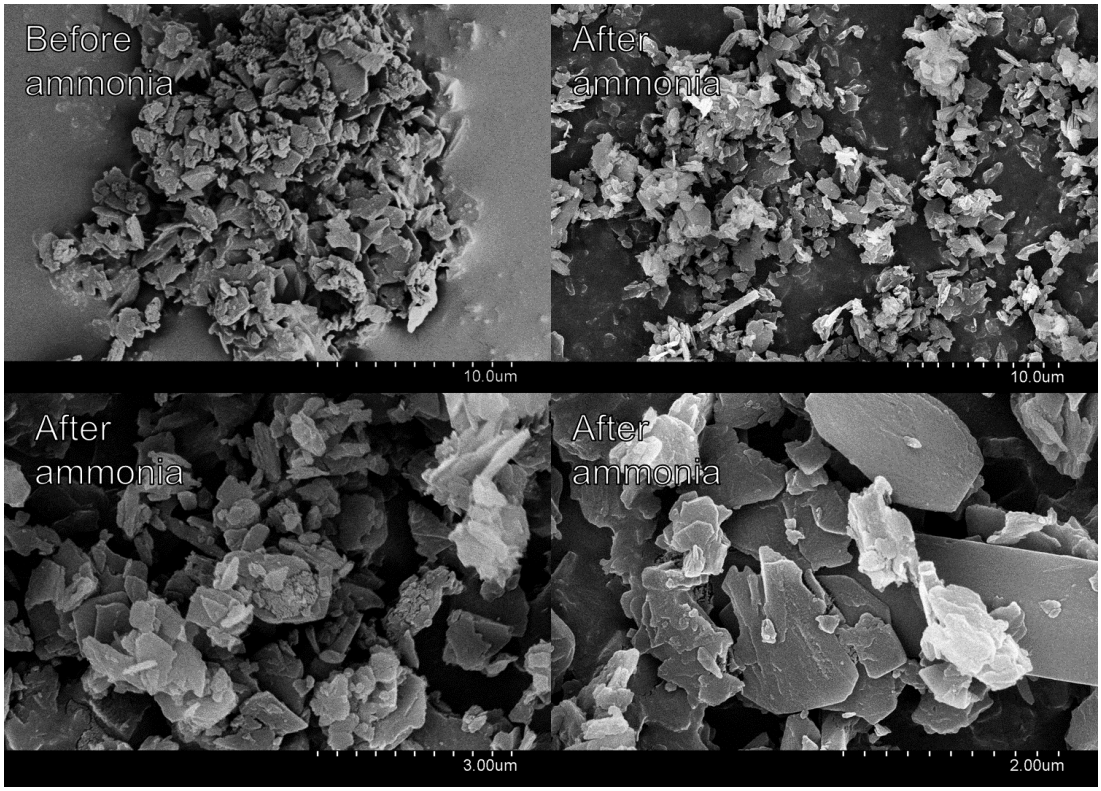

Figure 4.21

SEM images showing Al-PMOF-HCl after ammonia uptake

4.5.3 Stability to humid flows

Based on the excellent breakthrough times observed using a dry flow of ammonia, it was considered that humid ammonia breakthrough experiments should be undertaken. Prior to this, the integrity of the material under a humid stream was assessed. The stability of Al-PMOF-HCl to water was explored by exposing the material to high humidity nitrogen flow (95% RH) for 5 hours followed by exposure to a dry (0% RH) nitrogen flow for 5 hours, repeating this cycle a further three times. Water uptake was measured gravimetrically throughout. The results are shown in Figure 4.22.

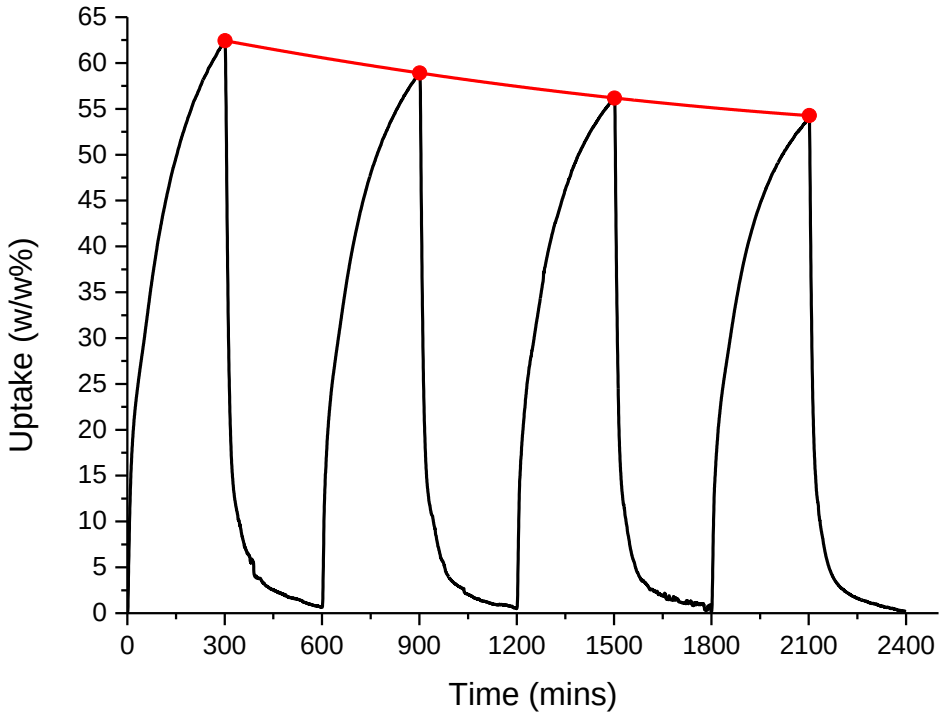

Figure 4.22

Gravimetric trace of Al-PMOF-HCl throughout four cycles of exposure to 95% RH nitrogen flow for 5 hours followed by exposure to 0% RH nitrogen flow for 5 hours.

It was observed that Al-PMOF-HCl adsorbs 62.4 w/w% on the initial cycle, followed by 58.9 w/w% on the second cycle, 56.2 w/w% on the third cycle and 54.3 w/w% on the fourth cycle. The decrease in water uptake after cycling suggests there is some decrease in pore volume upon lengthy exposure to high humidity conditions, likely a result of the presence of enough water to solubilise HCl in the pores causing partial hydrolysis of the carboxylate-metal bond. However it is clear that the material shows surprising stability to water over extended periods, with the majority of the pore volume remaining.

4.5.4 Humid ammonia breakthrough

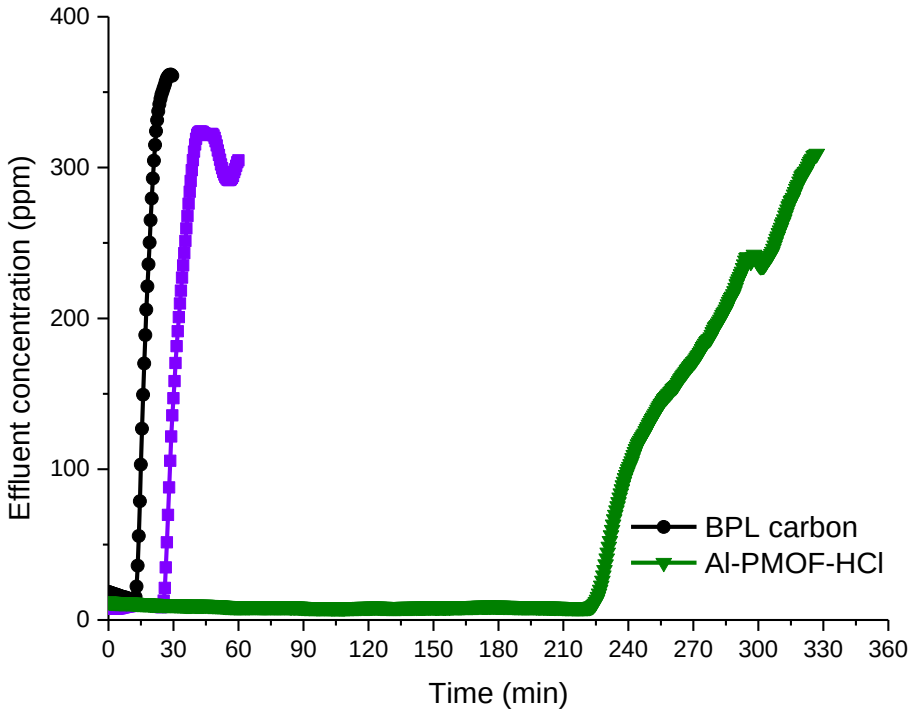

Figure 4.23

Ammonia breakthrough curve for Al-PMOF-HCl using an 80% RH flow of ammonia. Al-PMOF and BPL activated carbon are shown for comparison.

Humid ammonia breakthrough experiments were performed on Al-PMOF-HCl, these results are displayed in Figure 4.23. As expected the humid ammonia flow results in a significantly higher breakthrough time in comparison with the same material in a dry flow, with breakthrough of ammonia occurring after 226 minutes. Thus, the addition of HCl offers a 9-fold increase in performance over the free base material. The amount of ammonia adsorbed at breakthrough is calculated to be 0.15 mmol equating to an ammonia:porphyrin ratio of 6.4:1. As with the dry

breakthrough results, the material is once again seen to exhibit a more gradual ascent to saturation, indicating slower kinetics. The maximum measured value shows an overall uptake of 0.17 mmol ammonia, equating to 7.8:1 ammonia:porphyrin.

The water adsorption isotherm of Al-PMOF-HCl is characteristic of a Type II isotherm per the IUPAC classification.[19] Higher water uptake is seen for Al-PMOF-HCl between 0% and 65% RH in comparison with Al-PMOF, which can be explained by the increased hydrophilicity of the pores due to the presence of considerable amounts of HCl and H_2O already in the material. The steep ascent beginning at around 70% RH is likely due to inter-particle adsorption.

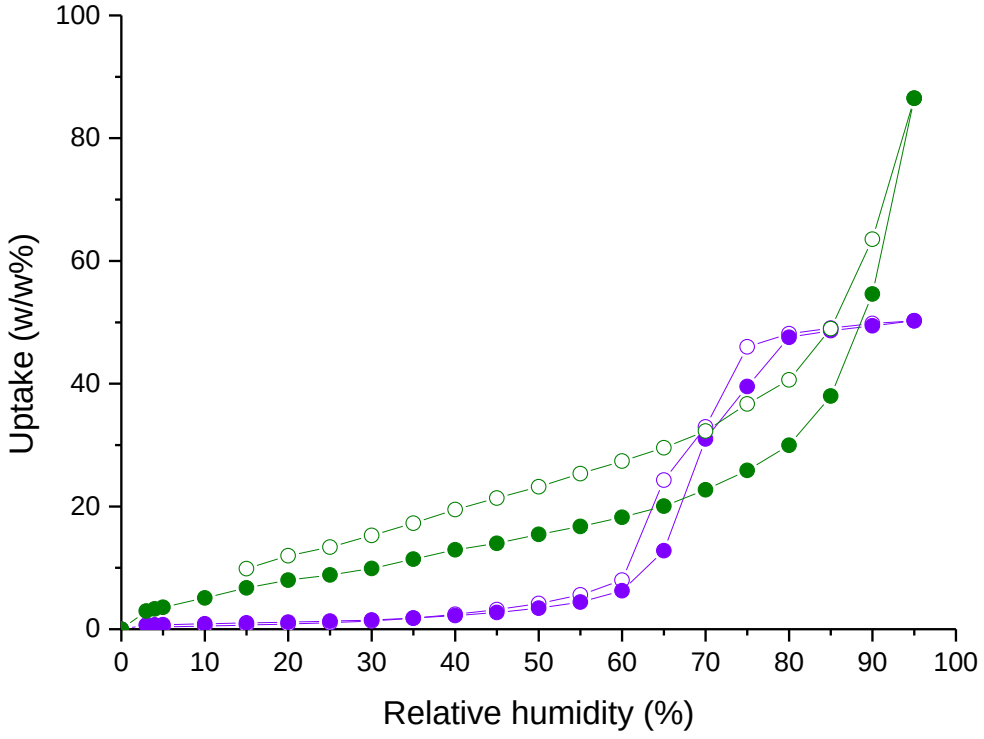

Figure 4.24

Water isotherm at 298 K of Al-PMOF-HCl (green) from 0% RH to 95% RH. Closed circles denote adsorption, open circles denote desorption. Water isotherm at 298 K of Al-PMOF is shown for comparison.

4.5.5 Vacuum treated Al-PMOF-HCl

It is noted for activated carbons that a skewed breakthrough curve that is steeper at the beginning of breakthrough is indicative of heterogeneity of adsorption sites within the pores.[49] It is seen that as the challenge gas moves through the packed bed of sorbent, the forefront of the adsorption wave contacts and occupies the most active adsorption sites leaving the less active ones for subsequently arriving vapours.[49] Furthermore, following uptake of the challenge gas pores may become blocked, resulting in lower accessibility to subsequently arriving vapours and hence overall slower kinetics, as indicated by the shallow gradient of the breakthrough curve. Both the dry and humid breakthrough curves of Al-PMOF-HCl (Figure 4.18 and Figure 4.23) displayed these characteristics. It was postulated that using less HCl within the pores of the MOF may actually provide an increase in performance in terms of breakthrough, at the cost of reducing overall capacity.

This idea was tested by exposing Al-PMOF-HCl to vacuum, however it was discovered that the HCl is bound surprisingly strongly within the framework. Using a turbomolecular vacuum pump it was possible to expose Al-PMOF-HCl to a vacuum of 4×10^{-4} mbar, whereby it was observed that following 14h at room temperature under high vacuum, the green colour associated with the protonation of the porphyrin remained present.

Thermo-gravimetric analysis and ion chromatography were used to determine the HCl content of this vacuum treated Al-PMOF-HCl. TGA (Figure 4.25) shows a guest weight loss of 26.0% attributed to HCl and water. Ion chromatography shows a chloride content of 7.1%, giving a composition of 74.0% MOF, 7.1% HCl and

18.9% water by weight. It can then be calculated that the Al-PMOF-HCl-vac has a composition of $Al_2(OH)_2(H_2TCPP)(HCl)_{2.4}(H_2O)_{12.3}$.

Ammonia breakthrough was performed under dry conditions on Al-PMOF-HCl-vac, ammonia was detected after 55.5 minutes. The amount of ammonia adsorbed at breakthrough is calculated to be 0.034 mmol or approximately 1.3:1 ammonia per porphyrin. These results are compared with Al-PMOF-HCl in Table 4.4. It is seen that the amount of ammonia adsorbed in Al-PMOF-HCl-vac is slightly less than Al-PMOF-HCl per HCl molecule. This indicates that ammonia uptake seems to scale almost linearly with HCl loading, with no relative kinetic breakthrough improvement seen.

Table 4.4 Comparison of NH_3 uptake between Al-PMOF-HCl and Al-PMOF-HCl-vac

Material	HCl per porphyrin	NH_3 per porphyrin	NH_3 per HCl
Al-PMOF-HCl	6.5	3. 8	0.58
Al-PMOF-HCl-vac	2.4	1.3	0.54

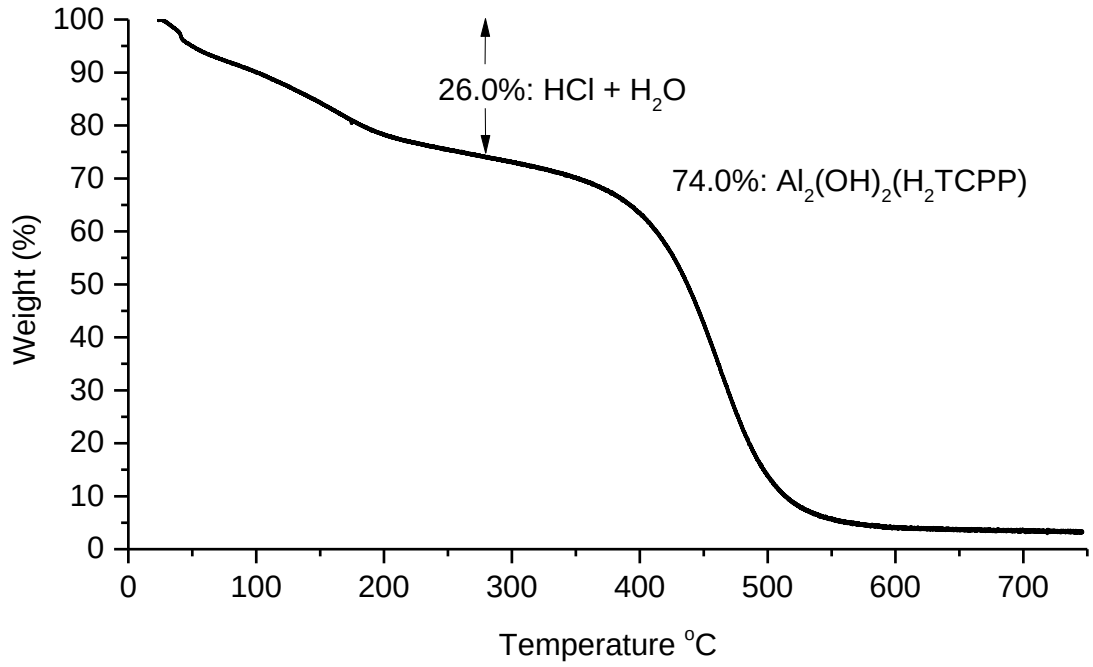

Figure 4.25

TGA trace of Al-PMOF-HCl-vac

Highlighting the affinity of the HCl for the framework, it is noteworthy that the high vacuum could maintained and temperature was increased to 80°C with the bright green colour attributed to porphyrin protonation remaining present. Higher temperatures resulted in the colour fading and returning to its original purple by 140°C at 4 x 10^{-4} mbar.

Based on the ability to treat the Al-PMOF-HCl to 4 x 10^{-4} mbar at room temperature, it was decided that isotherms could be measured on the sample without the risk of pumping HCl through the equipment. As such a N_2 isotherm at 77K was performed on the Al-PMOF-HCl-vac sample (Figure 4.26).

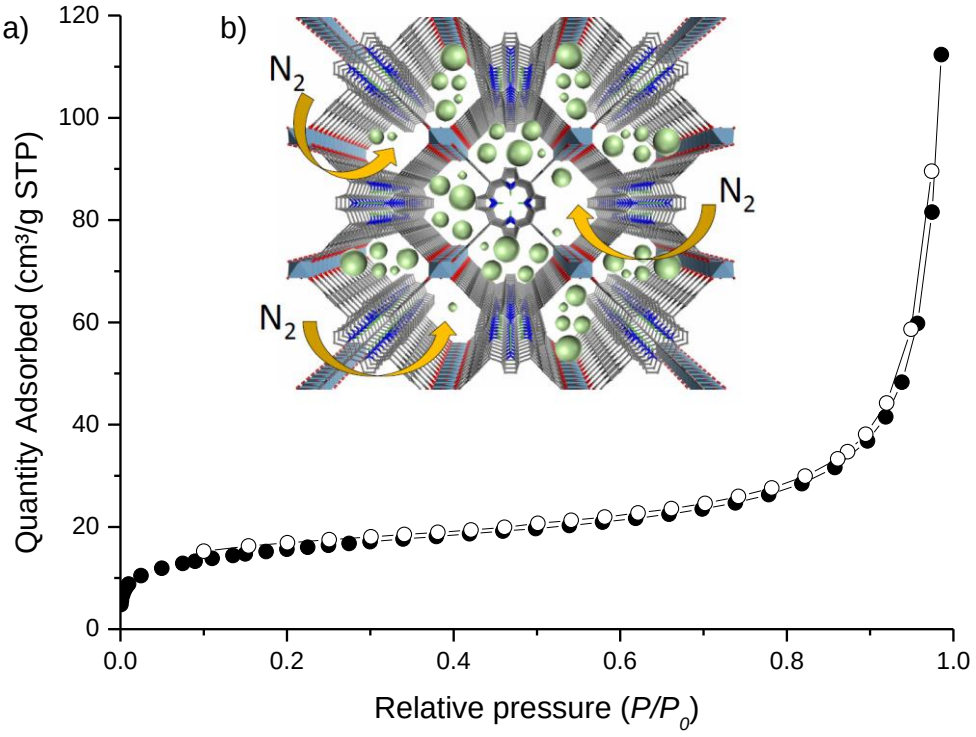

Figure 4.26

a) Nitrogen isotherms at 77 K after exposing Al-PMOF-HCl to vacuum at 10^{-4} mbar. Adsorption and desorption is denoted by filled and empty symbols. b) Schematic showing the accessibility of N_2 to a fraction of the overall pore volume due to guest HCl (green spheres) blocking the pores.

It can be seen that the nitrogen isotherm is a typical Type II isotherm, generally representative of low porosity adsorbents. BET surface is area is calculated from the isotherm to be 55 m^2/g, considerably less than the BET surface area of the parent material, calculated to be 1400m^2/g. It is evident that the presence of HCl blocks the pores of the material to a large extent, causing low porosity to nitrogen at 77K.

Isotherms were performed using CO_2 at 195K to determine whether the material was accessible to a slightly smaller probe (Figure 4.27). As can be seen, there is

significantly greater uptake of CO_2 than N_2, with uptakes of around 60 cm^3/g in comparison with around 17 cm^3/g at 0.2 bar, respectively. This further suggests that pores of the material have been partially blocked by HCl, resulting in less accessible channels that are more accessible to CO_2 due to its smaller kinetic diameter in comparison with N_2 (3.6Å for N_2 3.3Å for CO_2) and also its higher kinetic energy at 195 K in comparison with N_2 at 77 K.

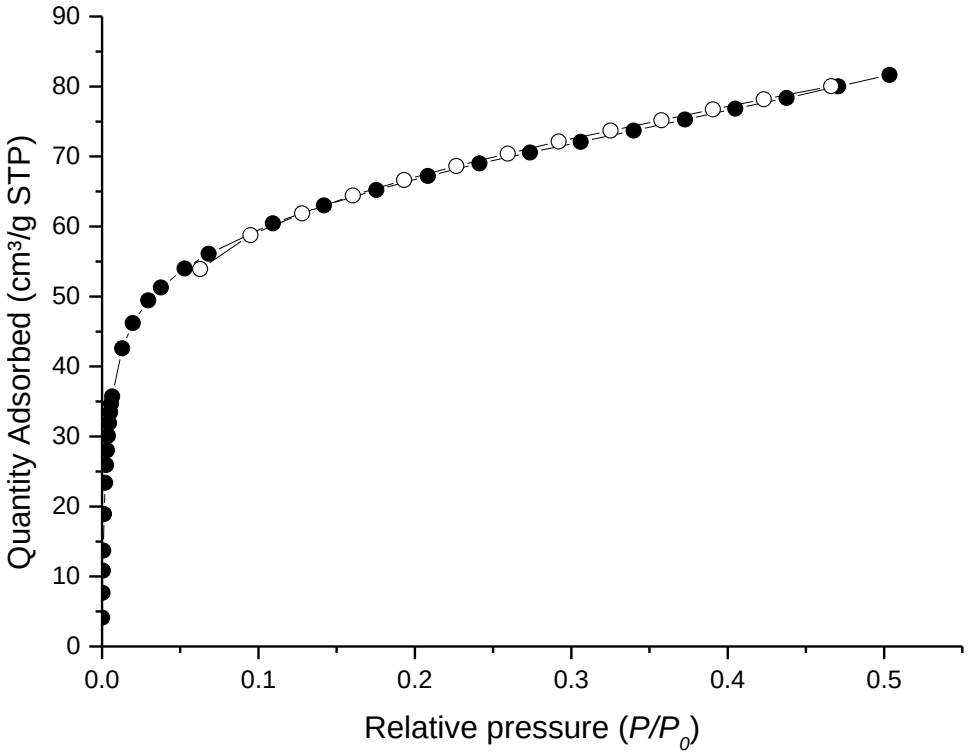

Figure 4.27

CO_2 isotherms at 195K after exposing Al-PMOF-HCl to vacuum at 10^{-4} mbar. Adsorption and desorption is denoted by filled and empty symbols.

4.6 Formic acid loaded MOF

4.6.1 Characterisation

Following the success of HCl insertion into Al-PMOF, other acids were considered for loading. Formic acid seemed a clear choice due to its relatively small size and high volatility. Upon loading, once again a colour change from purple to green associated with porphyrin protonation is observed (Figure 4.28), however it is noted that the colour of the formic acid loaded material (Al-PMOF-FA) is less vibrant green than Al-PMOF-HCl.

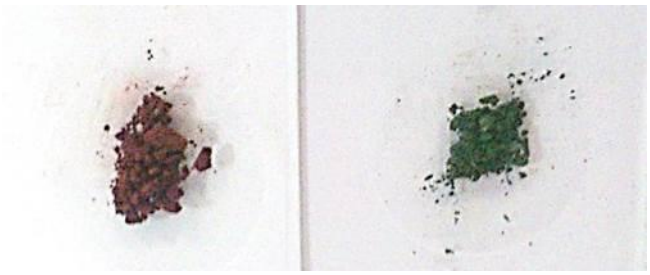

Figure 4.28

Image showing Al-PMOF (left) and Al-PMOF-FA (right)

UV-visible spectroscopy was carried out on Al-PMOF and Al-PMOF-HCl (Figure 4.29) which showed that the Soret band associated with the porphyrin is red shifted from 423 nm to 439 nm consistent with porphyrin protonation, however the four Q-bands are still present, despite shifting closer together. It is stipulated that Al–PMOF-FA is largely in the free-base form due to the presence of the four Q-bands, which indicate the lower symmetry of the non-protonated porphyrin.

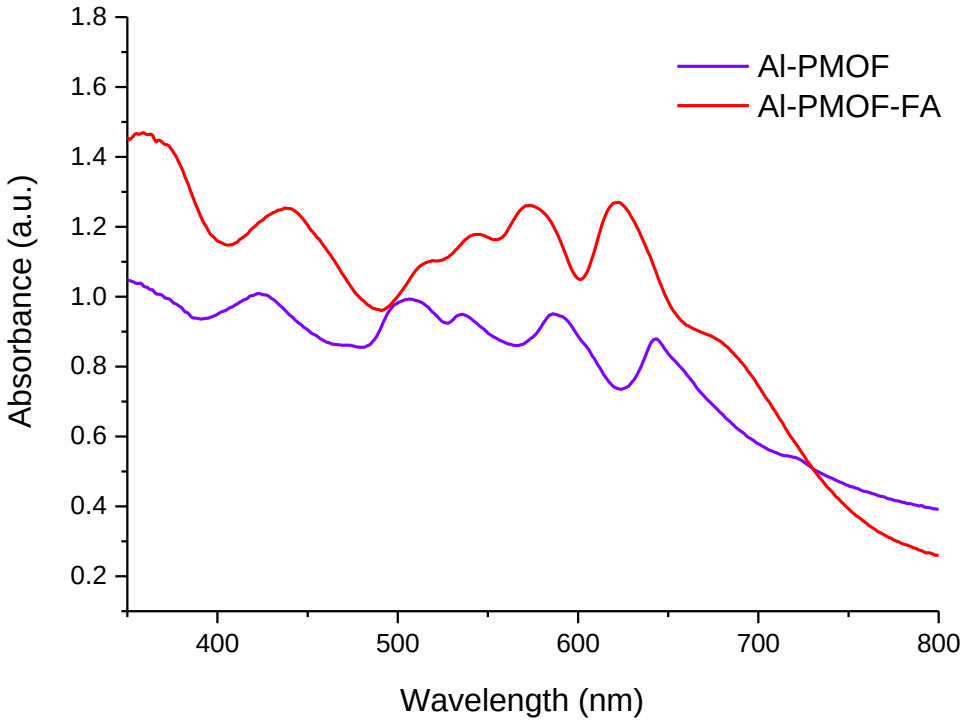

Figure 4.29

UV-Visible absorption spectra of Al-PMOF (purple) and Al-PMOF-FA (red)

As seen in Figure 4.30, PXRD of the formic acid loaded sample revealed that the material remains crystalline upon acid loading with no amorphous component, in contrast with Al-PMOF-HCl. This may indicate that the formic acid arranges in an ordered manner within the framework of Al-PMOF. Conversely it may be that the formic acid is disordered within the framework, yet there is no amorphous hump in the diffraction pattern due to the reduced X-ray scattering power of the constituent atoms of formic acid, thus there is a much weaker impact on the diffraction pattern. It is observed that additional peaks are present in the diffraction pattern, yet all peaks were seen to index to the space group of the parent phase, *Cmmm* (Figure 4.31) with the lattice parameters shown in Table 4.5.

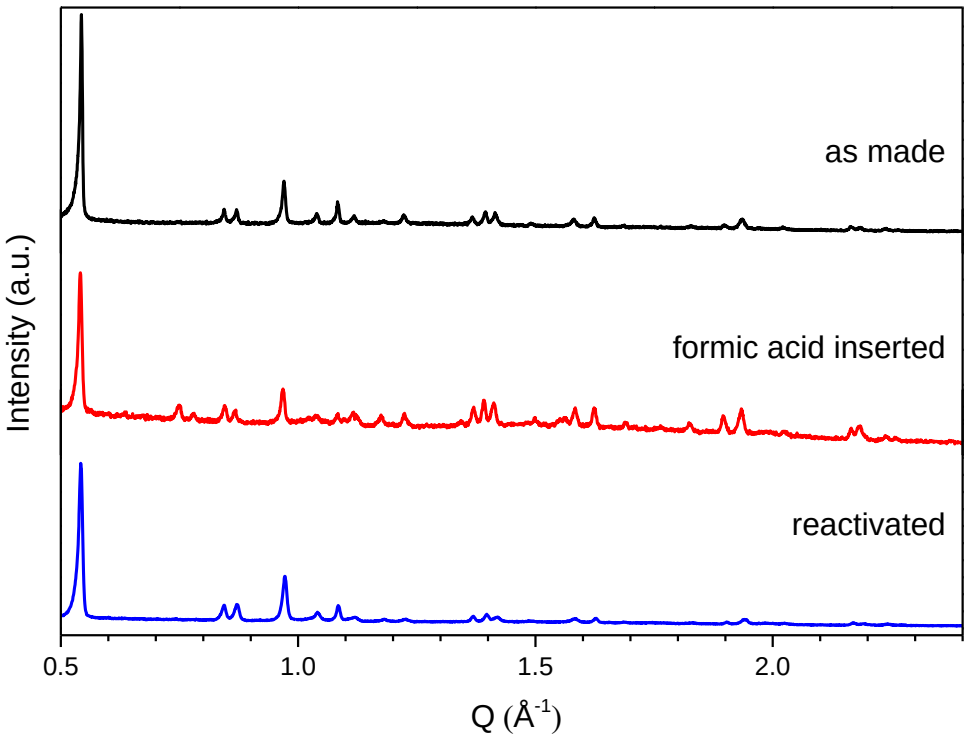

Figure 4.30

PXRD pattern of Al-PMOF (black) Al-PMOF-FA (red) and Al-PMOF following the removal of guests at 170^{o}C at 10^{-2} mbar.

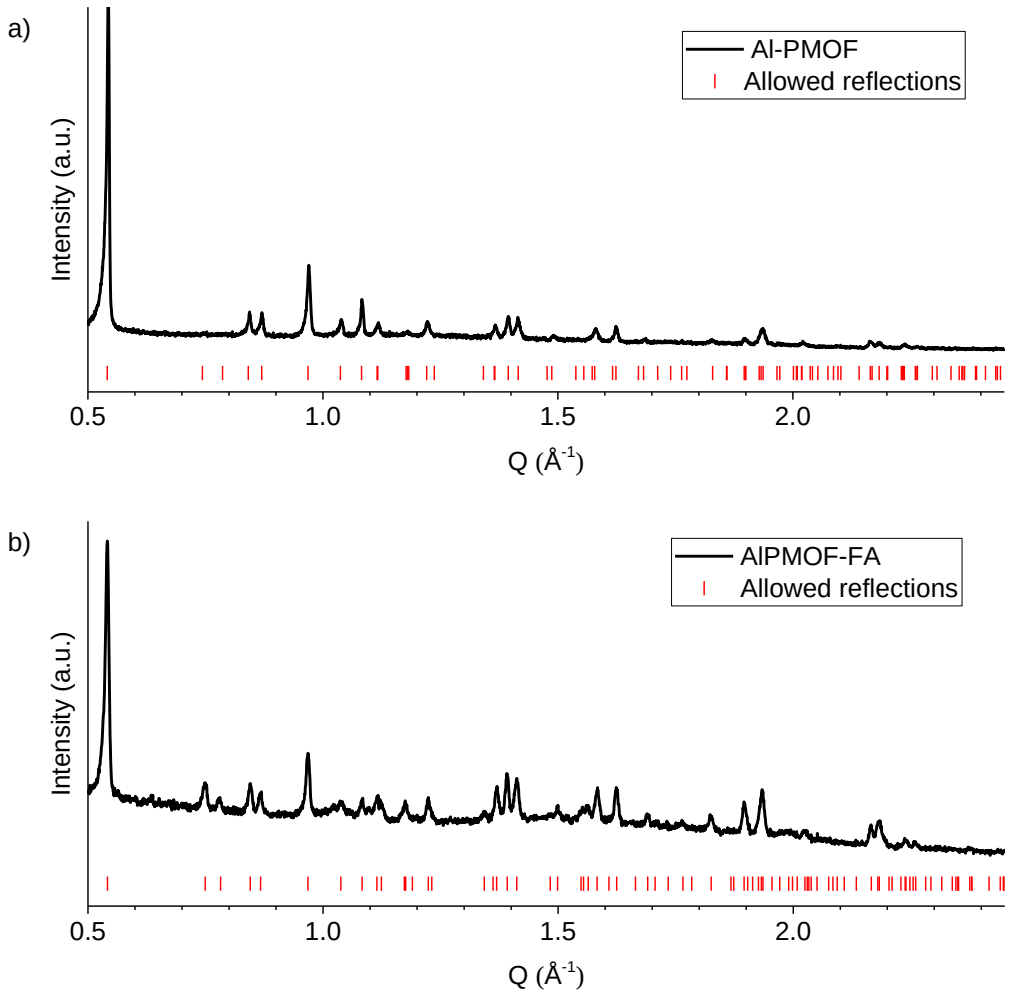

Figure 4.31

PXRD patterns of Al-PMOF prior to (a) and after (b) formic acid loading, showing the allowed reflections (red ticks) in space group *Cmmm* (lattice parameters in Table 4.5)

Table 4.5 Lattice parameters of Al-PMOF (*Cmmm)* and Al-PMOF-FA (*Cmmm)*

MOF	**Lattice Parameters (Å)**		
	a	*b*	*c*
Al-PMOF	31.96(1)	6.627(2)	16.901(6)
Al-PMOF-FA	32.19(2)	6.627(3)	16.77(1)

Interestingly, it can be seen that upon formic acid loading, there is a contraction in the *c* axis and an expansion in the *a* axis; the *b* axis remains the same before and after loading.

It is seen that that upon re-activation at 170^{o}C at 10^{-2} mbar, just like with Al-PMOF-HCl, the guest formic acid and H_2O can be removed from the framework yielding the initial structure as evidenced by the PXRD pattern in Figure 4.30. The PXRD pattern shows that the original crystallinity is largely restored, and the additional peaks present upon formic acid loading are no longer present.

Nitrogen isotherms were conducted in order to assess if any damage occurs to the pore structure of the material following a cycle of formic acid loading and removal (Figure 4.32). It was discovered that following one cycle, a significant decrease in pore volume had occurred, from 0.525 cm^3/g of the free-base material to 0.402 cm^3/g. Following a second cycle of acid loading and removal a further decrease in pore volume to 0.308 cm^3/g was observed. Interestingly, an additional cycle afforded no further loss in pore volume. In comparison to the HCl-loaded MOF, which showed only an 8% loss in pore volume after three cycles, the formic acid loading and activation is seen to be much more detrimental to the pore volume of the material, with an overall decrease of 39% in pore volume.

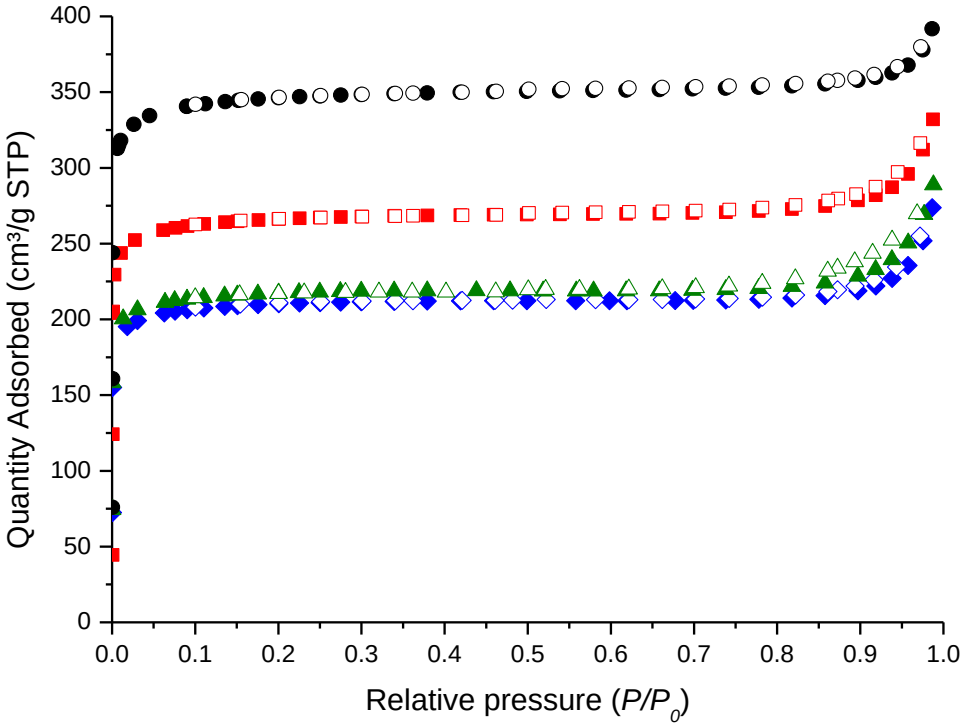

Figure 4.32

Nitrogen isotherms at 77K after cycling formic acid uptake and removal at 170 ^{o}C, 10^{-2} mbar. Fresh, activated Al-PMOF is shown in black circles; the first, second and third cycles are shown in red squares, blue diamonds and green triangles, respectively. Adsorption and desorption is denoted by filled and empty symbols

Thermo-gravimetric analysis and ion chromatography were used to determine the formate content of the acid loaded material. The TGA in Figure 4.33 shows a guest weight loss of 29.6% attributed to formic acid and water. Ion chromatography shows a formate content of 23.2% by weight, giving a composition of 70.4% MOF, 23.2% formic acid and 6.40% water by weight. It can then be calculated that the Al-PMOF-FA has a composition of $Al_2(OH)_2(H_2TCPP)(HCOOH)_{6.4}(H_2O)_{4.0}$. Once again, it is observed that there is an increase in water adsorption from the atmosphere in the formic acid loaded material over the free base material, again attributed to the polar nature of the acid groups within the pores creating a more hydrophilic environment.

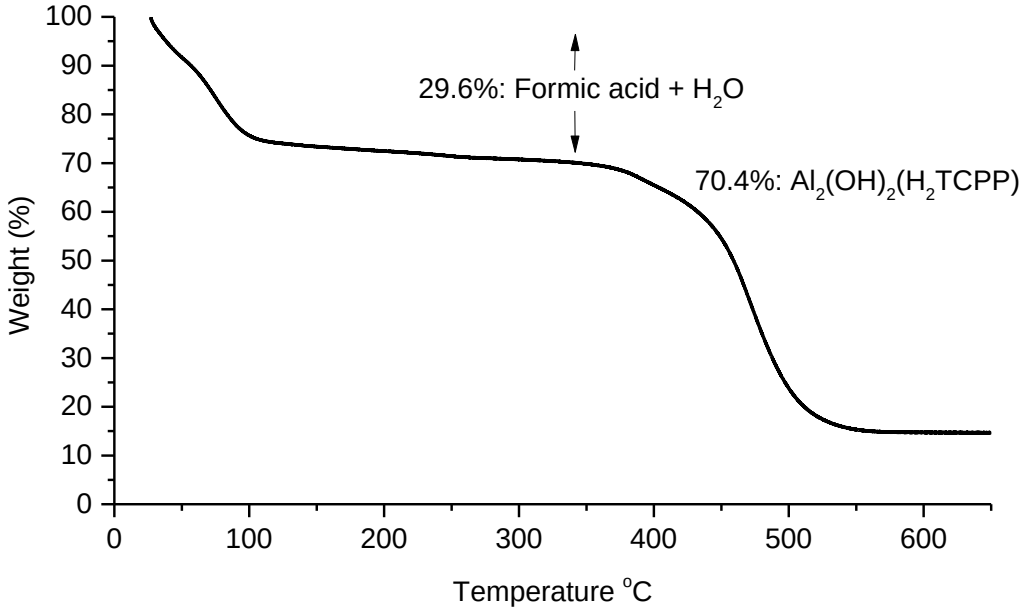

Figure 4.33

TGA trace of Al-PMOF-FA

Experimental loadings and maximum theoretical loadings were compared using Olex² [46] to determine the total accessible volume of the material to HCOOH and H_2O using kinetic diameters of 5.40 Å and 2.65 Å respectively. The results are summarised in Table 4.6 below. From these calculations, based on the composition $Al_2(OH)_2(H_2TCPP)(HCOOH)_{6.4}(H_2O)_{4.0}$, 52% of the pore volume is occupied by HCOOH and H_2O.

Table 4.6 Experimental guest loading of HCOOH and H_2O in comparison with calculated maximum loading for Al-PMOF

Adsorbate	Calculated accessible volume ($Å^3$ per unit cell)	Maximum loading (guests per porphyrin)	Experimental loading (guests per porphyrin)
HCOOH	1299.6	10.37	6.4
H_2O	2011.0	33.61	4.0

4.6.1.1 Liquid loading of formic acid

Interestingly, it was found that Al-PMOF could be loaded with formic acid using a liquid insertion method, detailed in section 4.7. Highlighting the stability of the free base material, the MOF could be stirred in neat formic acid for 1h at room temperature, which yielded comparable results to the vapour loading method. The TGA (Figure 4.34) shows a 30.0% guest weight loss, in comparison to 29.6% when using the vapour loading method. The same additional peaks appear in the PXRD pattern (Figure 4.35) of the liquid loaded material, and crystallinity is comparable.

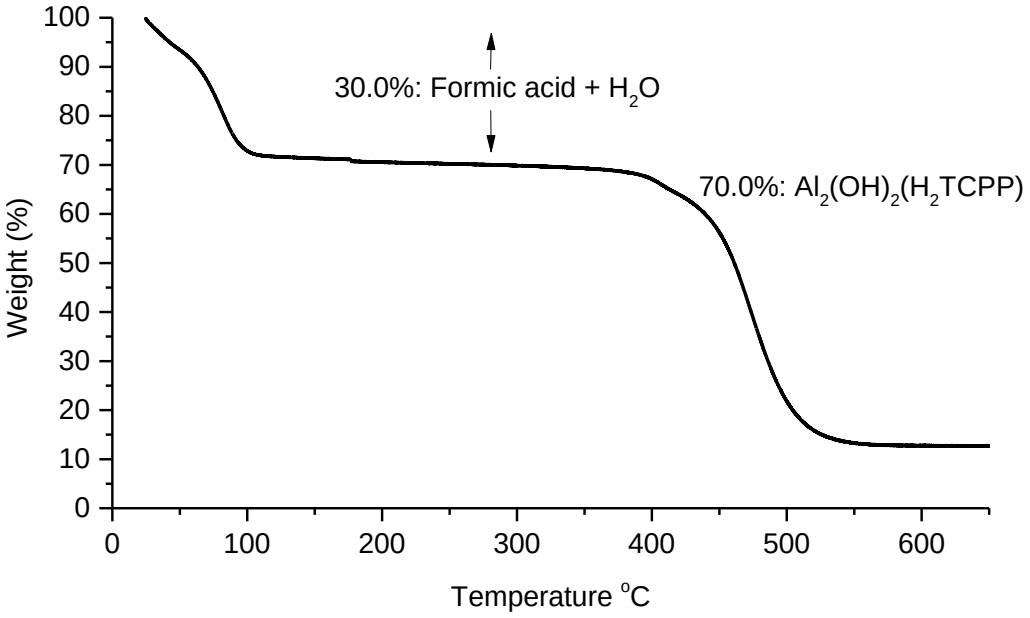

Figure 4.34

TGA trace of Al-PMOF loaded with formic acid using liquid loading

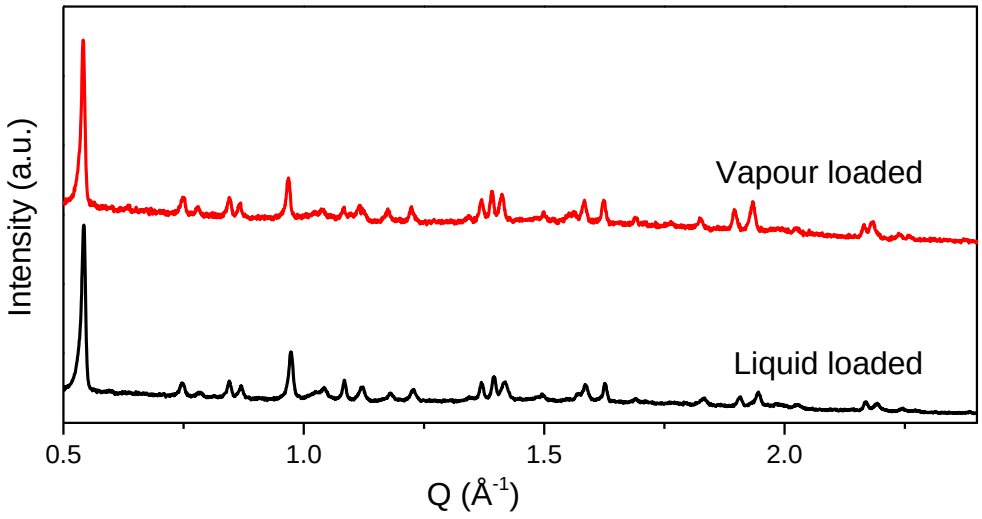

Figure 4.35

PXRD patterns comparing the vapour and liquid methods of loading Al-PMOF with formic acid

4.6.2 Dry ammonia breakthrough

Al-PMOF-FA, synthesised using the vapour insertion method, was assessed as a sorbent for ammonia initially by conducting dry ammonia breakthrough runs. The results are displayed in Figure 4.36. It is clear that the loading of formic acid into the parent Al-PMOF framework has significantly improved breakthrough times. Breakthrough of ammonia after 110 minutes is observed, in comparison to the 14 minutes exhibited by the free base MOF – a 7.9-fold increase in performance. The amount of ammonia adsorbed at breakthrough is calculated to be 0.073 mmol, equating to an ammonia:porphyrin ratio of 3.0:1. This material exhibits a similar breakthrough curve to Al-PMOF-HCl, in that it shows a less steep ascent to saturation than both the BPL activated carbon and the parent Al-PMOF. As mentioned with Al-PMOF-HCl, this can be attributed to the remaining adsorption sites within the material are likely more inaccessible to influent ammonia resulting in overall slower kinetics.

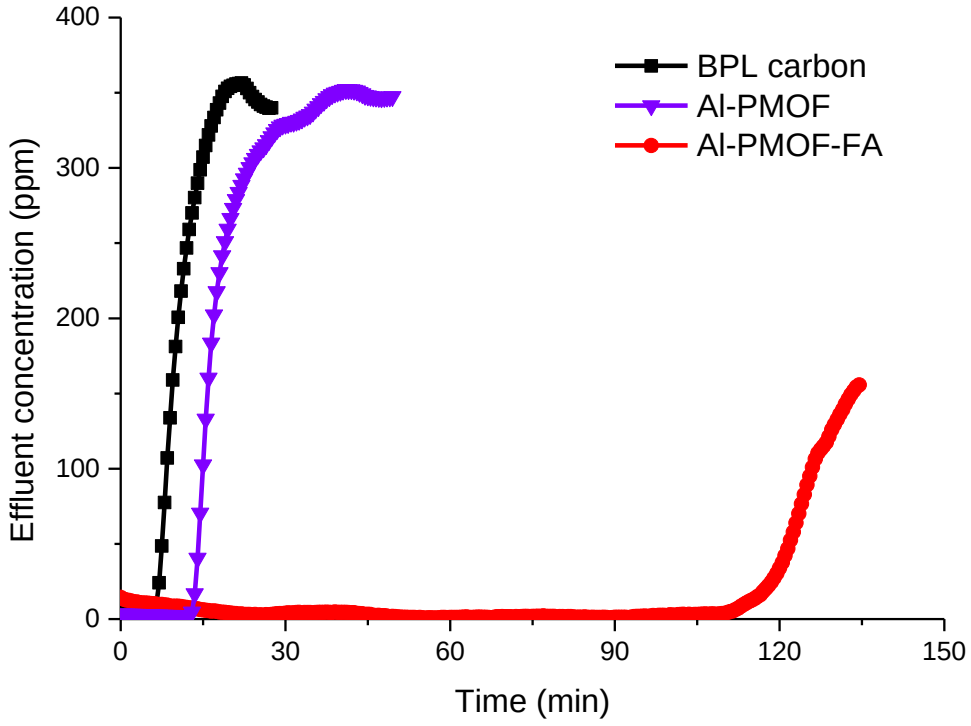

Figure 4.36

Ammonia breakthrough curve for Al-PMOF-FA using a 0% RH flow of ammonia. Al-PMOF (purple) and BPL activated carbon (black) are shown for comparison.

PXRD was performed on the formic loaded MOF after ammonia breakthrough, which revealed a slight loss of crystallinity in comparison with the parent phase (Figure 4.37). The ammonia treated Al-PMOF-FA is still highly crystalline, which differs from results observed with Al-PMOF-HCl after breakthrough. This retained crystallinity is consistent with the reduced X-ray scattering power of the constituent atoms of formate compared with chloride, which would have weaker impact on the diffraction pattern.[50]

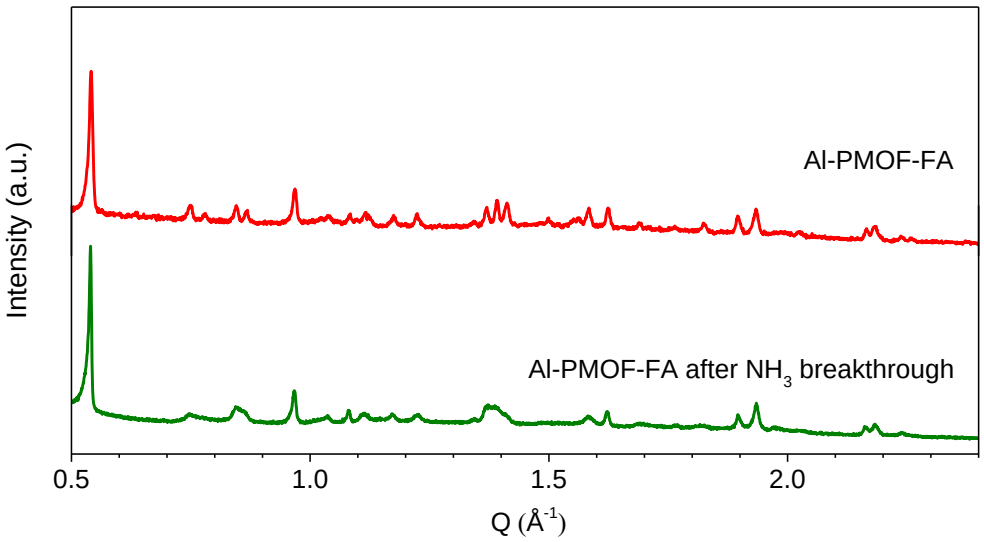

Figure 4.37

PXRD pattern of Al-PMOF-FA following dry ammonia breakthrough (green). PXRD pattern of the as made Al-PMOF-FA (red) shown for comparison.

4.6.3 Humid ammonia breakthrough

Humid ammonia breakthrough experiments were performed on Al-PMOF-FA, the breakthrough curves are shown in Figure 4.38. In agreement with the majority of materials, the humid ammonia flow results in a higher breakthrough time in comparison with the same material in a dry flow, with breakthrough of ammonia occurring after 159 minutes. This is a 6.4 times the performance seen for the free base material. The amount of ammonia adsorbed at breakthrough is calculated to be 0.10 mmol equating to an ammonia:porphyrin ratio of 4.0:1. In concurrence with the dry breakthrough results, the material is seen to exhibit a less steep ascent to saturation. Saturation occurs at 235 minutes, which equates of 0.12 mmol ammonia, or 4.7 ammonia molecules per porphyrin.

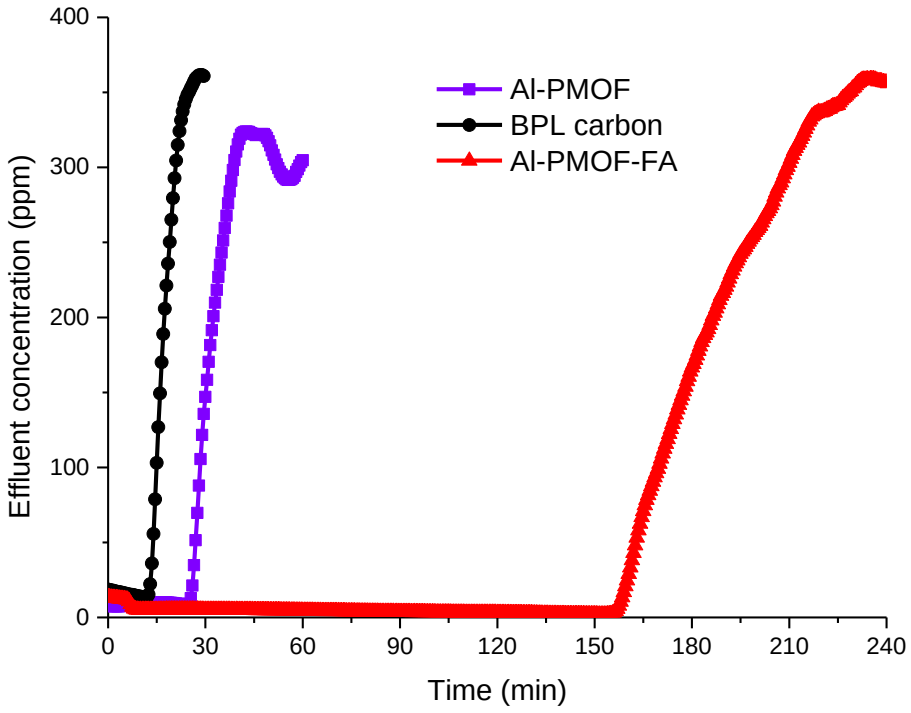

Figure 4.38

Ammonia breakthrough curve for Al-PMOF-FA using an 80% RH flow of ammonia. Al-PMOF (purple) and BPL activated carbon (black) are shown for comparison.

4.7 Conclusion

It has been shown that an aluminium porphyrin-based metal-organic outperforms BPL carbon as a sorbent for ammonia. The porphyrin core of Al-PMOF can be loaded with metals which provide Lewis acidic binding sites for ammonia, showing a corresponding increase in ammonia uptake, in agreement with literature findings. The framework can adsorb large quantities of both hydrochloric and formic acids; 6.1 molecules of HCl and 6.4 molecules of HCOOH can be adsorbed per porphyrin within the MOF. The polar nature of these adsorbates increase the hydrophilicity of the pores resulting in the uptake of 15.3 and 4.0 molecules of water from the atmosphere. The MOF shows remarkable stability towards these reactive guests,

even allowing cycling of acid loading despite vigorous removal conditions of 170^{o}C at 10^{-5} bar. By exploiting Brønsted acid-Brønsted base interactions, micro-breakthrough experiments have shown the utilisation of the high density of acid groups within the pores to afford greatly improved ammonia uptake in comparison to both the parent MOF and activated carbon, the current work-horse material in single use adsorptive protection field. The materials are shown to perform even better under simulated environmental humidity, exhibiting much higher breakthrough times at 80% relative humidity in comparison with 0% relative humidity, with a capacity of up to 7.9 wt% ammonia at breakthrough.

It is thought that materials with similar stability and functionality, but with greater pore volume and surface area (such as PCN-224)[51] would offer interesting further study. Such materials may yield even greater acid uptakes than those reported here, accompanied by a corresponding increase in ammonia uptake.

4.8 References

1. J. B. DeCoste, G. W. Peterson, H. Jasuja, T. G. Glover, Y.-g. Huang and K. S. Walton, *Journal of Materials Chemistry A*, 2013, **1**, 5642-5650.
2. E. Barea, C. Montoro and J. A. R. Navarro, *Chem. Soc. Rev.*, 2014, **43**, 5419-5430.
3. N. A. Khan, Z. Hasan and S. H. Jhung, *J. Hazard. Mater.*, 2013, **244–245**, 444-456.
4. T. G. Glover, G. W. Peterson, B. J. Schindler, D. Britt and O. Yaghi, *Chem. Eng. Sci.*, 2011, **66**, 163-170.
5. T. Watanabe and D. S. Sholl, *J. Chem. Phys*, 2010, **133**, 094509.
6. G. W. Peterson, G. W. Wagner, A. Balboa, J. Mahle, T. Sewell and C. J. Karwacki, *J. Phys. Chem. C*, 2009, **113**, 13906-13917.
7. D. Britt, D. Tranchemontagne and O. M. Yaghi, *Proc. Natl. Acad. Sci. U.S.A.*, 2008, **105**, 11623-11627.
8. D. Saha and S. Deng, *J. Colloid Interface Sci.*, 2010, **348**, 615-620.
9. C. Lieder, S. Opelt, M. Dyballa, H. Henning, E. Klemm and M. Hunger, *J. Phys. Chem. C*, 2010, **114**, 16596-16602.
10. I. Spanopoulos, P. Xydias, C. D. Malliakas and P. N. Trikalitis, *Inorg. Chem.*, 2013, **52**, 855-862.
11. W. Morris, C. J. Doonan and O. M. Yaghi, *Inorg. Chem.*, 2011, **50**, 6853-6855.
12. A. Fateeva, P. A. Chater, C. P. Ireland, A. A. Tahir, Y. Z. Khimyak, P. V. Wiper, J. R. Darwent and M. J. Rosseinsky, *Angew. Chem. Int. Ed.*, 2012, **51**, 7440-7444.
13. G. Ferey, M. Latroche, C. Serre, F. Millange, T. Loiseau and A. Percheron-Guegan, *Chem. Commun.*, 2003, 2976-2977.
14. S. Halis, N. Reimer, A. Klinkebiel, U. Lüning and N. Stock, *Microporous Mesoporous Mater.*, 2015, **216**, 13-19.
15. V. Villari, P. Mineo, E. Scamporrino and N. Micali, *RSC Advances*, 2012, **2**, 12989-12998.
16. K. M. Kadish, K. M. Smith and R. Guilard, *The Porphyrin Handbook*, Academic Press, 2000.

17. K. G. Wang and M. E. Glicksman, in *Materials Processing Handbook*, CRC Press, 2007, pp. 5.1-5.10.
18. C. Petit, B. Mendoza and T. J. Bandosz, *Langmuir*, 2010, **26**, 15302-15309.
19. K. S. W. Sing, *Journal*, 1985, **57**, 603.
20. K. S. W. Sing, in *Adsorption by Powders and Porous Solids (Second Edition)*, ed. F. R. R. S. W. S. L. Maurin, Academic Press, Oxford, 2014, pp. 321-391.
21. J. Canivet, A. Fateeva, Y. Guo, B. Coasne and D. Farrusseng, *Chem. Soc. Rev.*, 2014, **43**, 5594-5617.
22. O. Talu and F. Meunier, *AlChE J.*, 1996, **42**, 809-819.
23. M. M. Dubinin, *Carbon*, 1980, **18**, 355-364.
24. RSC, Royal Society of Chemistry Data Bank Website, http://www.rsc.org/education/teachers/resources/databook/ds_stability_constants.htm).
25. F. Rouquerol, J. Rouquerol and K. Sing, in *Adsorption by Powders and Porous Solids*, eds. F. Rouquerol, J. Rouquerol and K. Sing, Academic Press, London, 1999, pp. 237-285.
26. S. J. Gregg and K. S. W. Sing, *Adsorption, Surface Area, & Porosity, Second Edition*, Academic Press, 1982.
27. M. J. Webb, S. Deroo, C. V. Robinson and N. Bampos, *Chem. Commun.*, 2012, **48**, 9358-9360.
28. C. M. Drain, K. K. S. Singh, R. Guilard and K. S. (Eds.), in *The Handbook of Porphyrin Science with Applications to Chemistry, Physics, Materials Science, Engineering, Biology and Medicine*, eds. C. M. Drain, K. K. S. Singh, R. Guilard and K. S. (Eds.), World Scientific, Singapore 2010, vol. 2.
29. M. Gouterman, in *The Porphyrins*, Academic Press, 1978, pp. 1-165.
30. A. B. Rudine, B. D. DelFatti and C. C. Wamser, *The Journal of Organic Chemistry*, 2013, **78**, 6040-6049.
31. P. Sayer, M. Gouterman and C. R. Connell, *Acc. Chem. Res.*, 1982, **15**, 73-79.
32. P. K. Goldberg, T. J. Pundsack and K. E. Splan, *The Journal of Physical Chemistry A*, 2011, **115**, 10452-10460.

33. E. C. A. Ojadi, H. Linschitz, M. Gouterman, R. I. Walter, J. S. Lindsey, R. W. Wagner, P. R. Droupadi and W. Wang, *The Journal of Physical Chemistry*, 1993, **97**, 13192-13197.
34. R. I. Walter, E. C. A. Ojadi and H. Linschitz, *The Journal of Physical Chemistry*, 1993, **97**, 13308-13312.
35. I. H. Wasbotten, J. Conradie and A. Ghosh, *The Journal of Physical Chemistry B*, 2003, **107**, 3613-3623.
36. J. R. Weinkauf, S. W. Cooper, A. Schweiger and C. C. Wamser, *The Journal of Physical Chemistry A*, 2003, **107**, 3486-3496.
37. S. C. Doan, S. Shanmugham, D. E. Aston and J. L. McHale, *J. Am. Chem. Soc.*, 2005, **127**, 5885-5892.
38. D. L. Akins, H.-R. Zhu and C. Guo, *The Journal of Physical Chemistry*, 1996, **100**, 5420-5425.
39. H. Guo, J. Jiang, Y. Shi, Y. Wang and S. Dong, *Spectrochimica Acta Part A: Molecular and Biomolecular Spectroscopy*, 2007, **67**, 166-171.
40. H. Guo, J. Jiang, Y. Shi, Y. Wang, J. Liu and S. Dong, *The Journal of Physical Chemistry B*, 2004, **108**, 10185-10191.
41. H. Guo, J. Jiang, Y. Shi, Y. Wang, Y. Wang and S. Dong, *The Journal of Physical Chemistry B*, 2006, **110**, 587-594.
42. M. G. Walter and C. C. Wamser, *J. Phys. Chem. C*, 2010, **114**, 7563-7574.
43. X. Huang, K. Nakanishi and N. Berova, *Chirality*, 2000, **12**, 237-255.
44. M. Y. Choi, J. A. Pollard, M. A. Webb and J. L. McHale, *J. Am. Chem. Soc.*, 2003, **125**, 810-820.
45. G. De Luca, A. Romeo, L. M. Scolaro, G. Ricciardi and A. Rosa, *Inorg. Chem.*, 2007, **46**, 5979-5988.
46. O. V. Dolomanov, L. J. Bourhis, R. J. Gildea, J. A. K. Howard and H. Puschmann, *J. Appl. Crystallogr.*, 2009, **42**, 339-341.
47. E. Albrecht, G. Baum, T. Bellunato, A. Bressan, S. Dalla Torre, C. D'Ambrosio, M. Davenport, M. Dragicevic, S. Duarte Pinto, P. Fauland, S. Ilie, G. Lenzen, P. Pagano, D. Piedigrossi, F. Tessarotto and O. Ullaland, *Nuclear Instruments and Methods in Physics Research Section A:*

Accelerators, Spectrometers, Detectors and Associated Equipment, 2003, **510**, 262-272.

48. W. H. Rodebush and J. C. Michalek, *J. Am. Chem. Soc.*, 1929, **51**, 748-759.
49. G. O. Wood, *Carbon*, 2002, **40**, 1883-1890.
50. O. T. Wilcox, A. Fateeva, A. P. Katsoulidis, M. W. Smith, C. A. Stone and M. J. Rosseinsky, *Chem. Commun.*, 2015, **51**, 14989-14991.
51. D. Feng, W.-C. Chung, Z. Wei, Z.-Y. Gu, H.-L. Jiang, Y.-P. Chen, D. J. Darensbourg and H.-C. Zhou, *J. Am. Chem. Soc.*, 2013, **135**, 17105-17110.

5 Indium and vanadium porphyrin metal-organic frameworks

5.1 Introduction

As described in chapter 4, the aluminium porphyrin MOF showed excellent properties as an ammonia sorbent when loaded with acid. It was judged that ammonia uptake performance may be further improved by synthesising isostructural compounds using different metals, yielding materials with different chemistry, larger pores and perhaps greater capacity for acids. In this chapter, two porphyrin based metal organic frameworks are studied, based on indium and vanadium. The synthesis of the indium porphyrin MOF, first discovered by A. Fateeva, is optimised and the resulting material fully characterised. Its stability to, and capacity for, acid loading is evaluated and the materials subjected to micro-breakthrough experiments to test the performance as ammonia sorbents. The vanadium based porphyrin MOF, synthesised according to work by B. Liu, is similarly assessed for acid stability and uptake, and evaluated for its ammonia uptake properties.

5.2 Experimental

In-PMOF

5,10,15,20-tetrakis(4-carboxyphenyl) was ordered from TCI UK, $In(NO_3)_3 \cdot xH_2O$ was purchased from Alfa Aesar. TGA analysis was conducted to confirm that the value of x= 4. All other chemicals are from Sigma-Aldrich. All were used without further purification.

A 30mg/mL stock solution of $In(NO_3)_3 \cdot xH_2O$ in DMF was made in a 100 mL volumetric flask. 5,10,15,20-tetrakis(4-carboxyphenyl) porphyrin (300 mg 0.379 mmol) was added to a 125 mL Teflon liner, followed by 15.85 mL DMF. $In(NO_3)_3$ stock solution (14.15 mL, 1.14 mmol) was then introduced to the Teflon liner. 2.4 mL 1.2 M HCl was then added, and the suspension stirred for 5 minutes at room temperature before being sealed in a stainless steel autoclave and heated up to 160°C at a rate of 10°C per minute, for 16 h. The solution was allowed to cool at a rate of 2 °C per minute. The reaction mixture was then filtered, washing with DMF (3 x 50 mL), then THF (1 x 50 mL). The deep purple solid was left to dry on the filter paper. Once dry, the MOF was transferred into a glass vial and soaked in 20mL THF overnight to exchange any remaining DMF. The MOF was then filtered and washed again with THF (1 x 20 mL). After drying on the filter paper, the material was activated at 80^{o}C under vacuum (3 x 10^{-2} mbar) to remove any guest THF and DMF molecules, providing 200 mg deep purple solid.

V-PMOF

5,10,15,20-tetrakis(4-carboxyphenyl) porphyrin (22mg, 0.028 mmol) was added to a mixture of 2.5 mL DMF and 0.2 mL ethanol in a 5mL glass microwave vial. The mixture was stirred using a magnetic stirrer for 5 minutes. 20 µL (0.085 mmol) vanadium oxytriisopropoxide was then added to the vial and stirred for a further 5 minutes. The vial was gradually heated to 160 ^{o}C over 20 minutes using a CEM Explorer 96 microwave oven, and held at this temperature for 60 minutes, using magnetic stirring throughout. The vial was then left to cool to room temperature. The resulting purple solid was recovered by centrifugation, washing 3 times with DMF (3 × 30 mL) and once with EtOH (1 × 30 mL) in order to remove any starting materials.

The material was subjected to a density separation to remove an additional insoluble impurity product. The solid was placed into a 12 mL glass vial containing 1,2-dibromoethane (10 mL) and after 24 h the layer of purple solid that settled to the top of the 1,2-dibromoethane was decanted off and separated by centrifugation, and washed once with EtOH (1 × 30 mL). The material was then activated at 165^{o}C under vacuum (3 x 10^{-2} mbar) to remove any guest solvent molecules.

Acid Insertion

Acid insertion was performed using the method described for Al-PMOF in the experimental section of chapter 4.

5.3 Indium porphyrin MOF

5.3.1 Scale-up and improvement of activation conditions

Preliminary work by A. Fateeva was conducted in order to find an indium analogue of the Al-PMOF material discussed in the previous chapter. Analogous reaction conditions which produced Al-PMOF were tried initially, yielding material with poor crystallinity. Subsequent trials changing the reaction solvent from H_2O to DMF, along with the addition of small amounts of dilute HCl as a modulator, yielded a crystalline material. The synthesis conditions used by Fateeva are as follows. In a 42mL Teflon reactor, 100mg of porphyrin H_2TCPP was introduced, followed by 5.5mL of DMF and 4.46mL of In nitrate salt solution in DMF (3 eq.). 0.8mL of HCl 1.2mol/L (10 times diluted) was added to the reactants. The mixture was stirred at room temperature for 5 minutes, then the reactor was introduced in a Parr bomb autoclave, and the reaction was heated in an oven at 160°C for 16 hours (heating rate

10°C/min), cooling rate 2°/min. After the reaction, the sample was recovered by filtration, rinsed with DMF and acetone to dry. 70mg of dark purple solid was recovered. The resulting material was characterised using a 5-point BET measurement, activated at 160 ^{o}C under vacuum exhibiting a BET surface area of 900-1000 m^2/g, and by PXRD, which yielded a pattern that indexed to a single phase in the space group *C222*.

Initially, the above conditions and characterisations explored by Fateeva were used to re-synthesise the material for this study, with comparable results. Direct scale-up was attempted, whereby a three times larger reaction vessel was used, and all reactants and solvents were scaled by a factor of three also. This method scaled the yield also, providing typically 200 mg per reaction vessel. Nitrogen isotherms were carried out to assess pore volume and calculate the surface area of the scaled up In-PMOF material (Figure 5.1). The BET surface area was calculated to be 1128 m^2/g with a pore volume of 0.460 cm^3/g. It was noted that the surface area of the indium analogue appeared particularly low in comparison with Al-PMOF (1400 m^2/g).

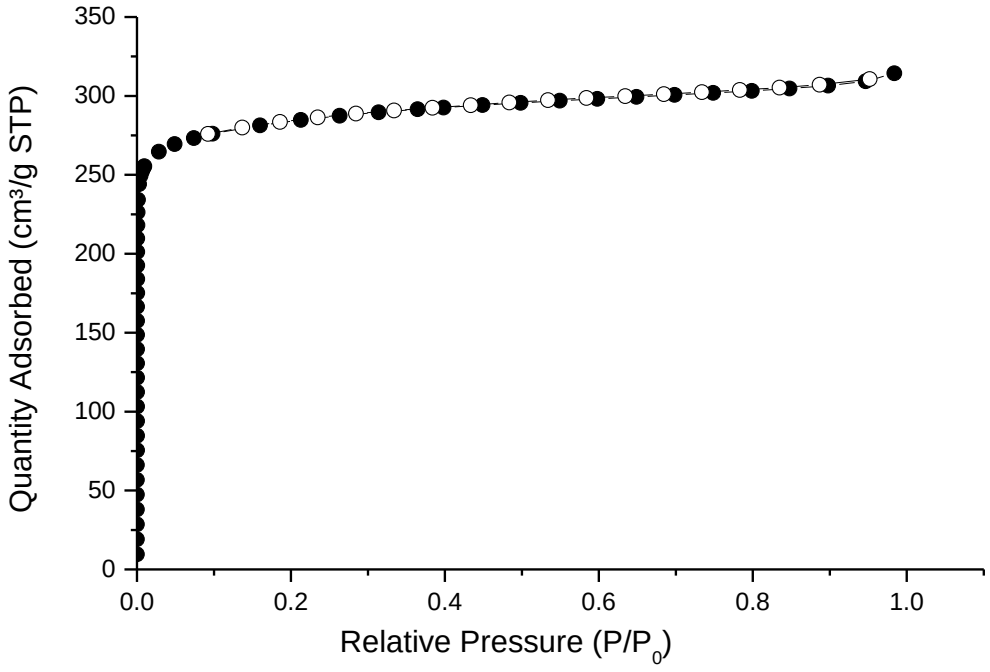

Figure 5.1

Nitrogen isotherms of In-PMOF at 77 K following activation at 160^{o}C

Initially activations at 160 ^{o}C under 10^{-2} mbar were performed, consistent with the activation conditions used by A. Fateeva, which TGA showed was successful in removing any guest molecules from the pores, namely DMF, THF and H_2O. It was thought however that such a high temperature of activation may damage the MOF, resulting in the lower than expected pore volumes that were observed. It was considered that partial pore collapse may be occurring due to the high temperature of activation required for removal of DMF. Experiments were conducted employing solvent exchange in an attempt to reduce activation temperatures. Best results were obtained by performing solvent exchange using THF for 16 h (details in experimental section) whereby it was possible to remove DMF from the pores of the MOF, permitting activation at much lower temperatures. The pore volumes of In-

PMOF following activation at 120 °C, 100 °C, and 80 °C are shown in Figure 5.2. It is evident that increasing the temperature of activation reduces the pore volume of the material. This is most likely due to partial collapse of the framework under high temperatures. It is noted that Al-PMOF does not suffer the same loss of pore volume when activated at higher temperatures, most like due to the much stronger Al-O bond in comparison with the In-O bond.[1] Following successful scale-up and improvements in activation conditions, structural determination then commenced.

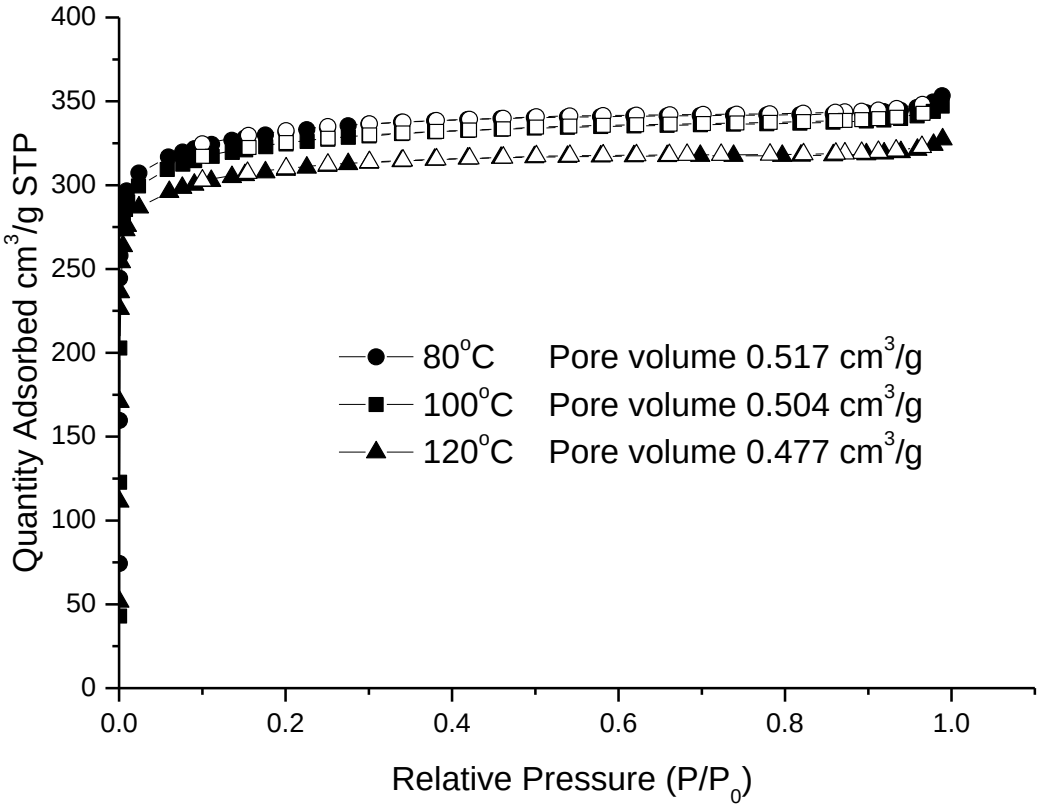

Figure 5.2

Nitrogen isotherms of In-PMOF at 77 K showing the effect of activation temperature on pore volume.

5.3.2 Structural determination

All attempts to produce single crystals of In-PMOF failed. Syntheses produced many crystals which appeared viable under the optical microscope, however were subsequently seen to diffract poorly when conducting single crystal X-ray diffraction, allowing only space group determination. SEM analysis revealed there are two distinct particle morphologies, one consisting of large flat sheets packed closely together in layers to form cuboidal particles, in the range of around 5 -20 μm^3. The second morphology consists of small (<500 nm) flakes packed together to form flower-like structures in the range of around 10 -50 μm^3 (Figure 5.3). It is considered that the 'crystals' selected for SXRD were in fact the cuboid shaped layered particles, which would explain the poor diffraction. EDX analysis confirmed that both morphologies consisted of comparable indium and organic content.

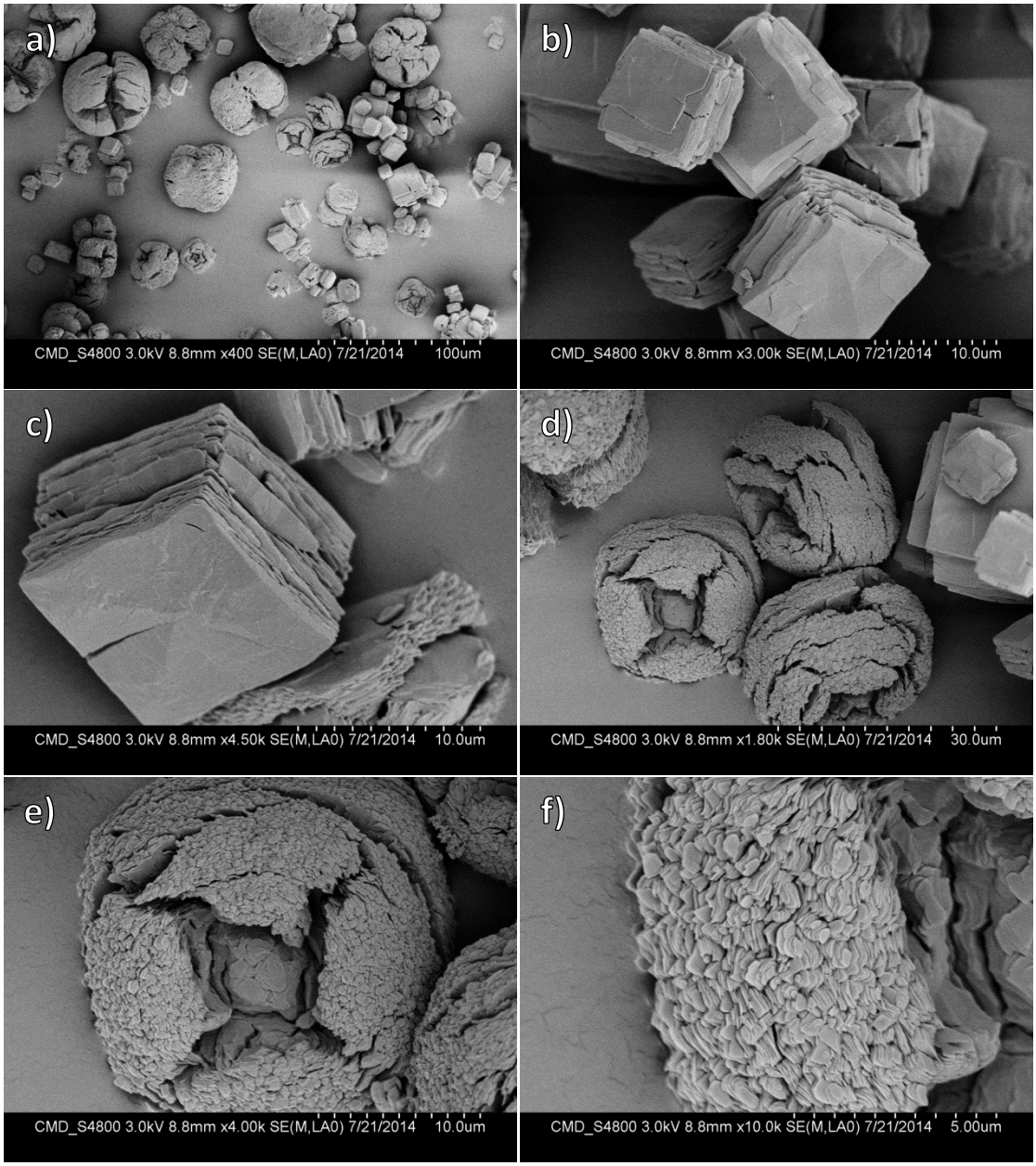

Figure 5.3

SEM images of In-PMOF revealing the two particle morphologies. a) Representative image of the material. b-c) Sheets closely layered to form cuboidal particles. d-f) Flower-like particles consisting of <500 nm sized flakes.

Initially a Pawley fitting, using the computer program Topas Academic[2], was used to fit the PXRD data in the space group *Cmmm*, which showed a good fit to the data with all peaks indexed, shown in Figure 5.4. The lattice parameters were determined to be a=32.659(2) Å b=7.1561(4) Å c=17.1031(11) Å. Table 5.1 compares the lattice parameters determined for In-PMOF with those of Al-PMOF. It is seen that the unit cell of In-PMOF has expanded in all directions.

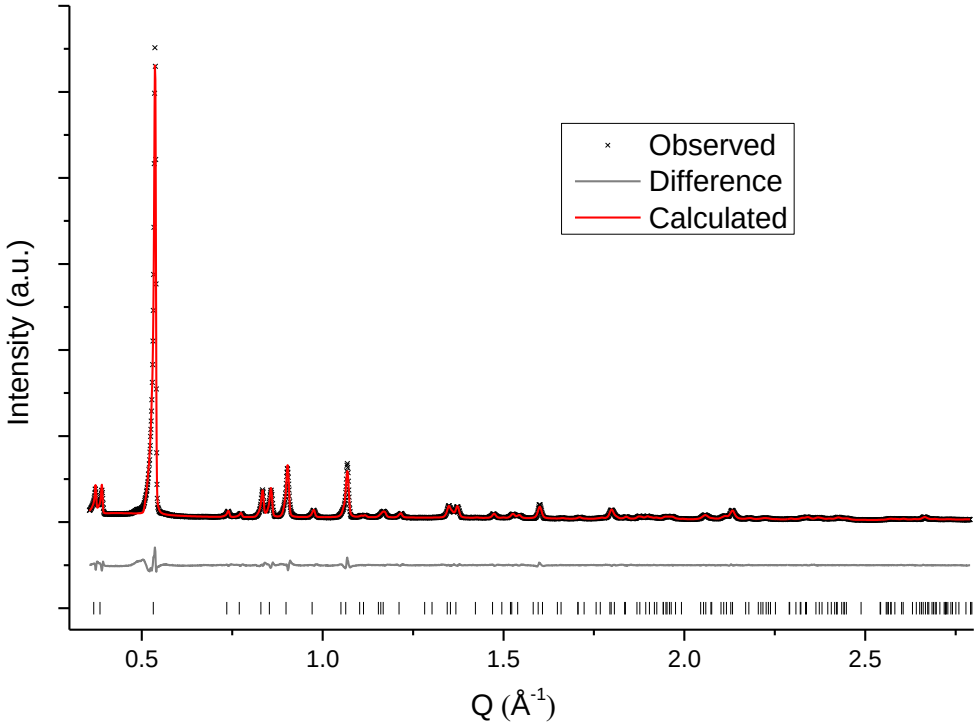

Figure 5.4

Pawley fit of PXRD data for In-PMOF in the Al-PMOF space group, *Cmmm*. Observed pattern (black crosses), calculated pattern (red line) and difference plot (grey line). Bragg peak positions are indicated in black. Refined lattice parameters: a = 32.659(2) Å, b = 7.1561(4) Å, c = 17.103(1) Å, volume = 3997.3(4) Å^3. R_{wp} 7.693, R_{exp} 2.267, χ^2=11.52

Table 5.1 Lattice parameters of Al-PMOF and In-PMOF (*Cmmm*)

MOF	***a* (Å)**	***b* (Å)**	***c* (Å)**	**Cell volume (Å^3)**
Al-PMOF	31.978(3)	6.5812(4)	16.862(2)	3548.7(6)
In-PMOF	32.659(2)	7.1561(4)	17.103(1)	3997.3(4)

Thermo-gravimetric analysis (Figure 5.5) performed on the as made material shows a 26.0% weight loss due to solvent from the reaction and from washing. The material is seen to maintain a steady weight up to 310 ^{o}C, after which thermal decomposition occurs. The activated MOF shows a weight loss of 4.5%, which we attribute to water adsorbed from the atmosphere. Using the weight of the remaining inorganic residue, it is seen that there is considerably more indium than expected based on the MOF being isostructural with Al-PMOF. However, it is generally seen that indium is bound within a porphyrin core of other indium porphyrin MOFs,[3,4] and as such it was supposed that this could be the present case.

To balance the charge of a porphyrin-bound In(III), a counter ion must be present; based on the synthesis conditions this was considered likely to be a chloride or a hydroxide. EDX analysis confirmed the lack of chlorine in the material. As such, a structure was proposed, $(InOH)_2(H_{2-2x}TCPP)[InOH]_x$, where the square brackets indicate the species bound within the porphyrin. The thermo-gravimetric analysis could then be used to determine the ratio of indium:organic as 2.74:1, and hence x = 0.74. The structure $(InOH)_{2.74}(H_{0.52}TCPP)\cdot 3H_2O$ matches well with CHN elemental analysis, shown in below (Table 5.2).

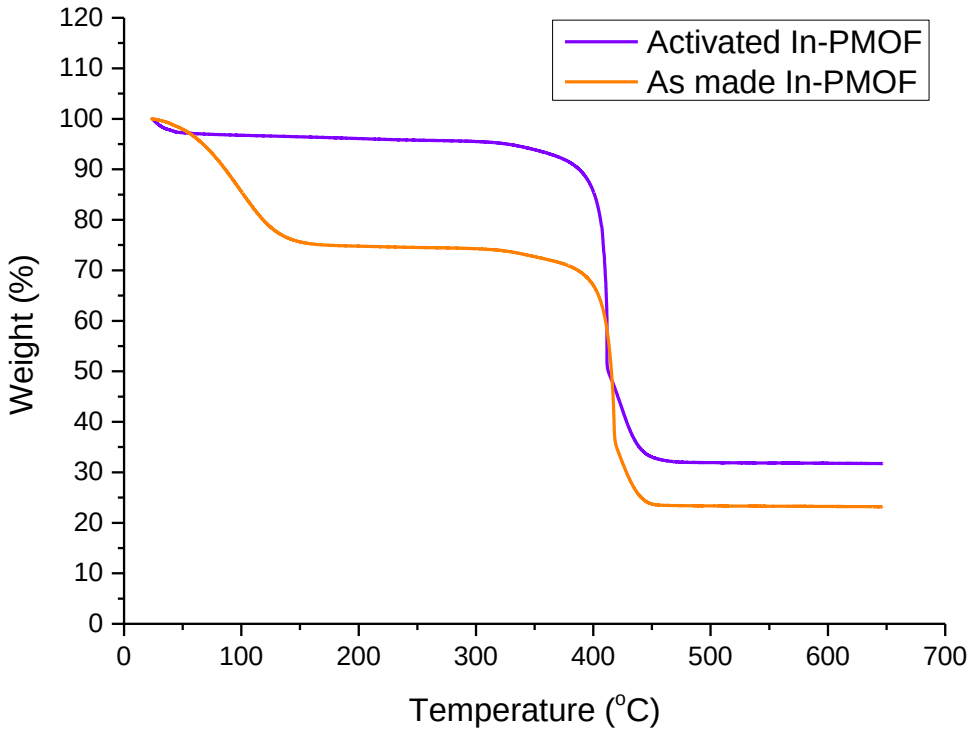

Figure 5.5

TGA traces of as-made and activated In-PMOF

Table 5.2 Elemental analysis of In-PMOF

	Experimental	Theory: $(InOH)_{2.74}(H_{0.52}TCPP)\cdot 3H_2O$
C	48.68	48.02
H	2.48	2.79
N	4.57	4.67

5.3.2.1 Rietveld refinement

Based on the good Pawley fit to the *Cmmm* space group, the sensible lattice parameters of the In-PMOF in comparison with Al-PMOF, and the CHN and TGA data, it was thought likely that the MOF was isostructural to Al-PMOF, but with

InOH bound in the porphyrin core. It was decided to perform a Rietveld refinement to confirm this. Given the presumed similarity to Al-PMOF, its crystal structure could be used as a starting point. As such the porphyrin unit was centred at (0,0,½) on the *ac* plane with a multiplicity of 2, the indium atoms placed on a (¼,¼,0) position with a multiplicity of 4, and the bridging hydroxide oxygen atoms placed on a (0,0,*z*) position with a multiplicity of 4 also, where z = 0.23.

In order to model the porphyrin linker, a semi-rigid body was used throughout the refinement, similar to that used when determining the structure of Al-PMOF.[5] This was done to reduce the complexity and number of refined parameters in the refinement. The semi-rigid body consisted of 8 refinable bond distances, 2 refinable bond angles and one refinable bond rotation, as shown in Figure 5.6. The final semi rigid-body, constructed using a Z-matrix, is shown in Figure 5.7. Though hydrogen atoms were included in the refinement, bond distances were not refined, remaining fixed at 1 Å. The atomic distances of the semi-rigid body and the bridging hydroxide were subjected to simulated annealing, within ±25% of their starting values. Thermo-gravimetric analysis had confirmed the presence of approximately 3 water molecules per porphyrin; the oxygen atoms of these water molecules were included in the final refinement.

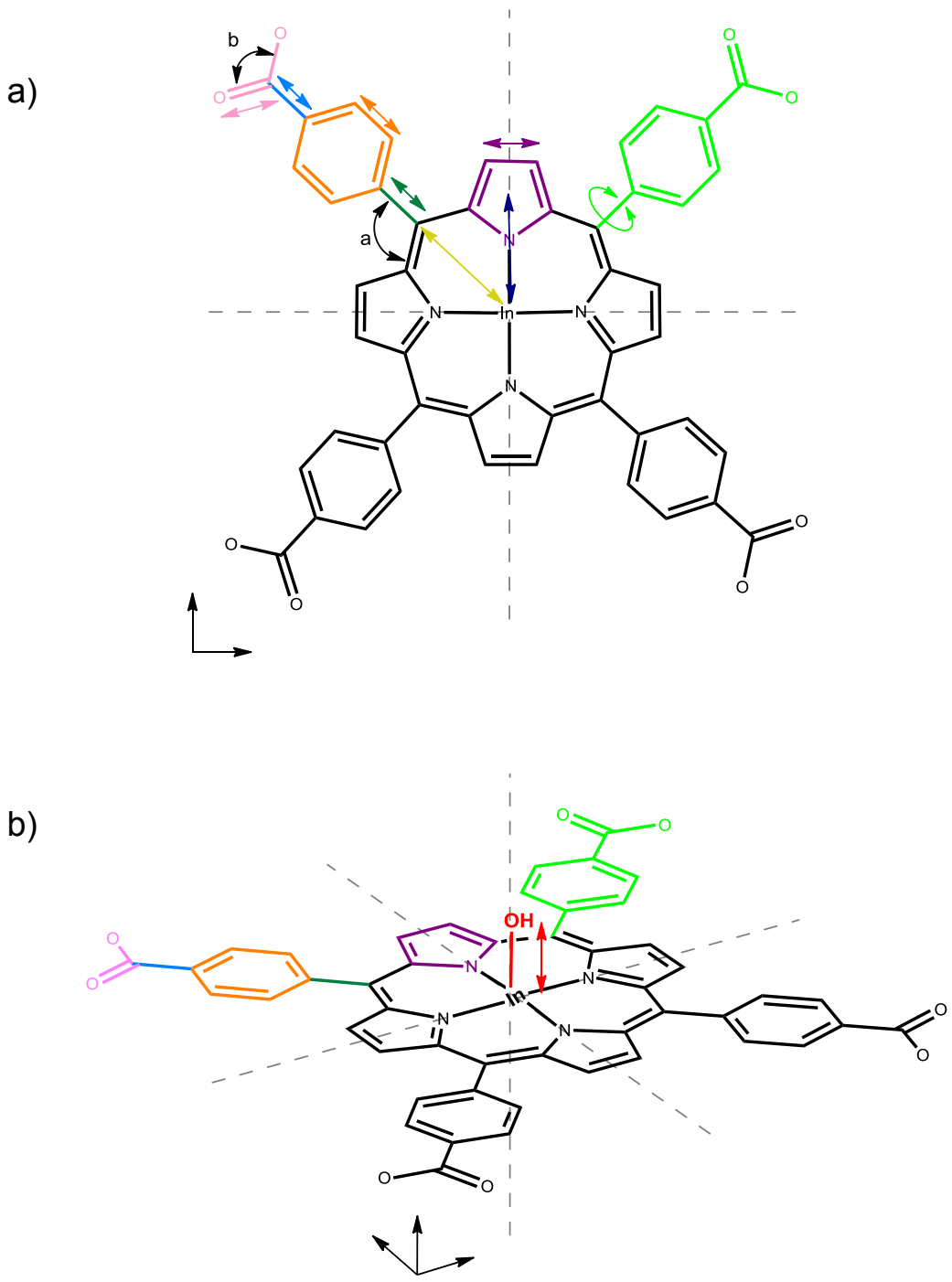

Figure 5.6

Schematic of the semi-rigid body describing the porphyrin linker in the Rietveld refinement. There are eight refined bond distances (shown in various colours), two refined bond angles (shown as black angles a and b) and one refined bond rotation (lime green). a) Schematic represented in 2D showing refined parameters in the plane of the porphyrin b) Schematic represented in 3D showing refined parameters showing refined parameters perpendicular to the plane of the porphyrin. Mirror planes are orthogonal to the grey dotted lines, passing through the central indium.

The final Rietveld refinement was carried out on 54 independent parameters in the *Cmmm* space group, utilising 130 reflections in the range 0.37 $Å^{-1}$ 2.78 $Å^{-1}$ (5 to 40 ^{o} 2θ, d spacing range 17.1 to 2.26 Å). A Chebyshev polynomial with 18 parameters was used to model the background. In order to improve the peak profile fitting, anisotropic strain broadening[6] was refined resulting in a total of 10 profile parameters. Lattice parameters, scale factor and zero-point correction were also refined, along with a single thermal parameter for all atoms except hydrogens.

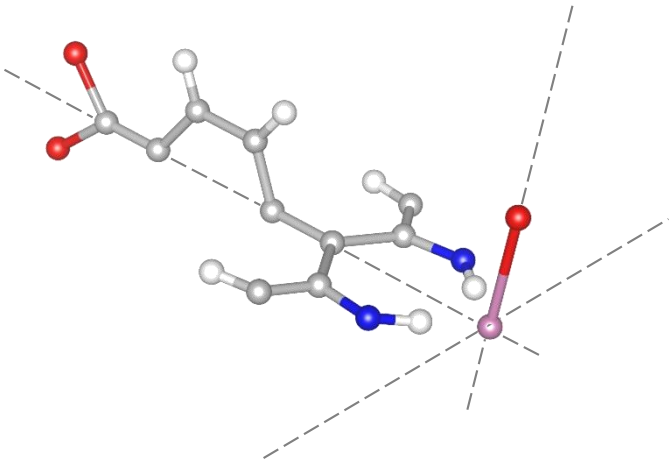

Figure 5.7

The semi-rigid body constructed to describe the porphyrin linker in the Rietveld refinement. Mirror planes are orthogonal to the grey dotted lines, passing through the indium.

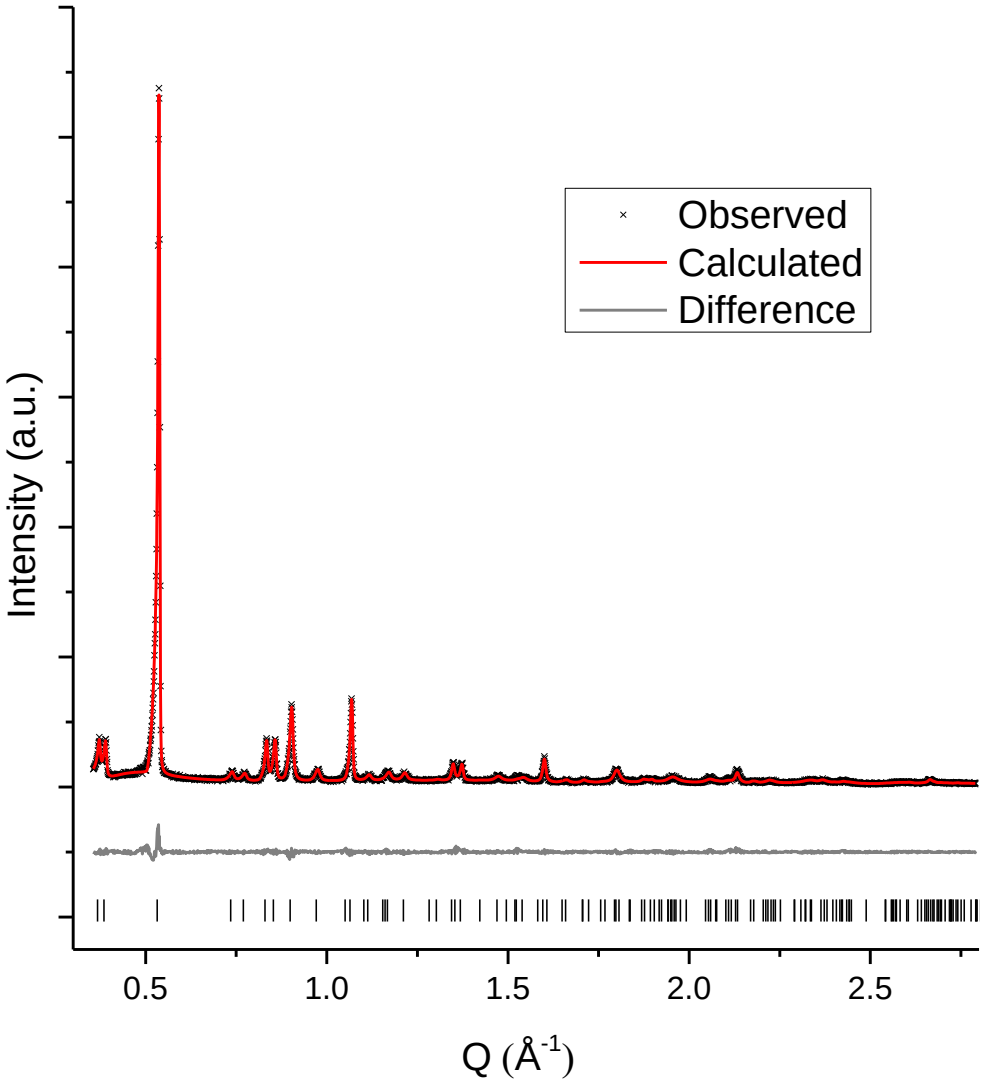

Figure 5.8

Final Rietveld refinement of In-PMOF. Observed pattern (black crosses), calculated pattern (red line) and difference plot (grey line). Bragg peak positions are indicated in black. Refined lattice parameters: a = 32.661(3) Å, b = 7.1564(6) Å, c = 17.1013 (18) Å, volume = 3997.3 (8) $Å^3$. Rwp 9.378, Rexp 2.313, χ^2=16.40, number of independent parameters = 54.

Table 5.3 Atomic parameters for In-PMOF, space group *Cmmm.*

Atom	Wyckoff position	x	y	z	Occupancy	B_{iso} ($Å^2$)
In1	2d	0	0	½	0.74	1.4(5)
In2	4e	¼	¼	0	1	1.4(5)
O2	4g	0.231(3)	½	0	1	1
O3	16r	-0.2189(11)	0.151(5)	0.932(2)	1	1.4(5)
O1	4j	0	0.3353 (1)	½	0.37	1.4(5)
O4	8o	0.06(3)	½	-2.43(7)	0.280(10)	1
O5	4j	0	3.6(7)	½	0.37	1
C1	8o	-0.0788(2)	0	0.6555(4)	1	1.4(5)
C2	8o	-0.03203(2)	0	0.6838(15)	1	1.4(5)
C3	8o	-0.01979(2)	0	0.7557(15)	1	1.4(5)
C4	8o	-0.0962(8)	0	0.5611(2)	1	1.4(5)
C5	8o	-0.1339(8)	0	0.5378(2)	1	1.4(5)
C6	8o	-0.1096(3)	0	0.7164(5)	1	1.4(5)
C7	16r	-0.1246(3)	0.1705(15)	0.7460(6)	1	1.4(5)
C8	16r	-0.1546(5)	0.1705(15)	0.8052(10)	1	1.4(5)
C9	8o	-0.1696(6)	0	0.8348(12)	1	1.4(5)
C10	8o	-0.1973(7)	0	0.8894(13)	1	1.4(5)
N1	4k	0	0	0.6393(15)	1	1.4(5)
N2	4h	-0.0730(8)	0	½	1	1.4(5)
H1	4g	0.201(3)	½	0	1	1
H2	4k	0	0	0.5809(15)	0.26	1
H3	4h	-0.0423(8)	0	½	0.26	1
H4	8o	-0.03779(2)	0	0.8030(15)	1	1
H5	8o	-0.1587(8)	0	0.5721(2)	1	1
H6	16r	-0.1140(3)	0.2915(15)	0.7250(6)	1	1
H7	16r	-0.1653(5)	0.2915(15)	0.8262(10)	1	1

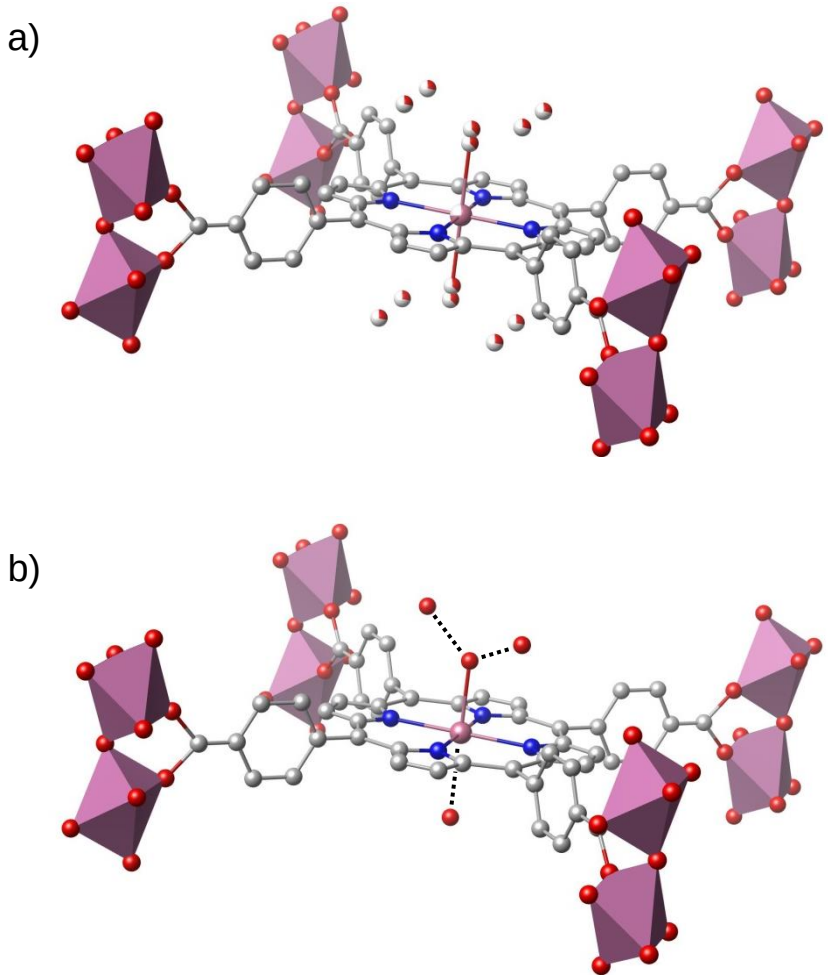

Figure 5.9

a) Structure of In-PMOF showing guest water molecules in the channels. Atom colours are as follows: purple (indium), red (oxygen), grey (carbon) blue (nitrogen). The partially occupied indium site is shown as a part purple and part white sphere and the partially occupied oxygen of hydroxide and water are shown as part red and part white spheres. b) Schematic showing the interactions of guest water in an indium occupied porphyrin in the MOF.

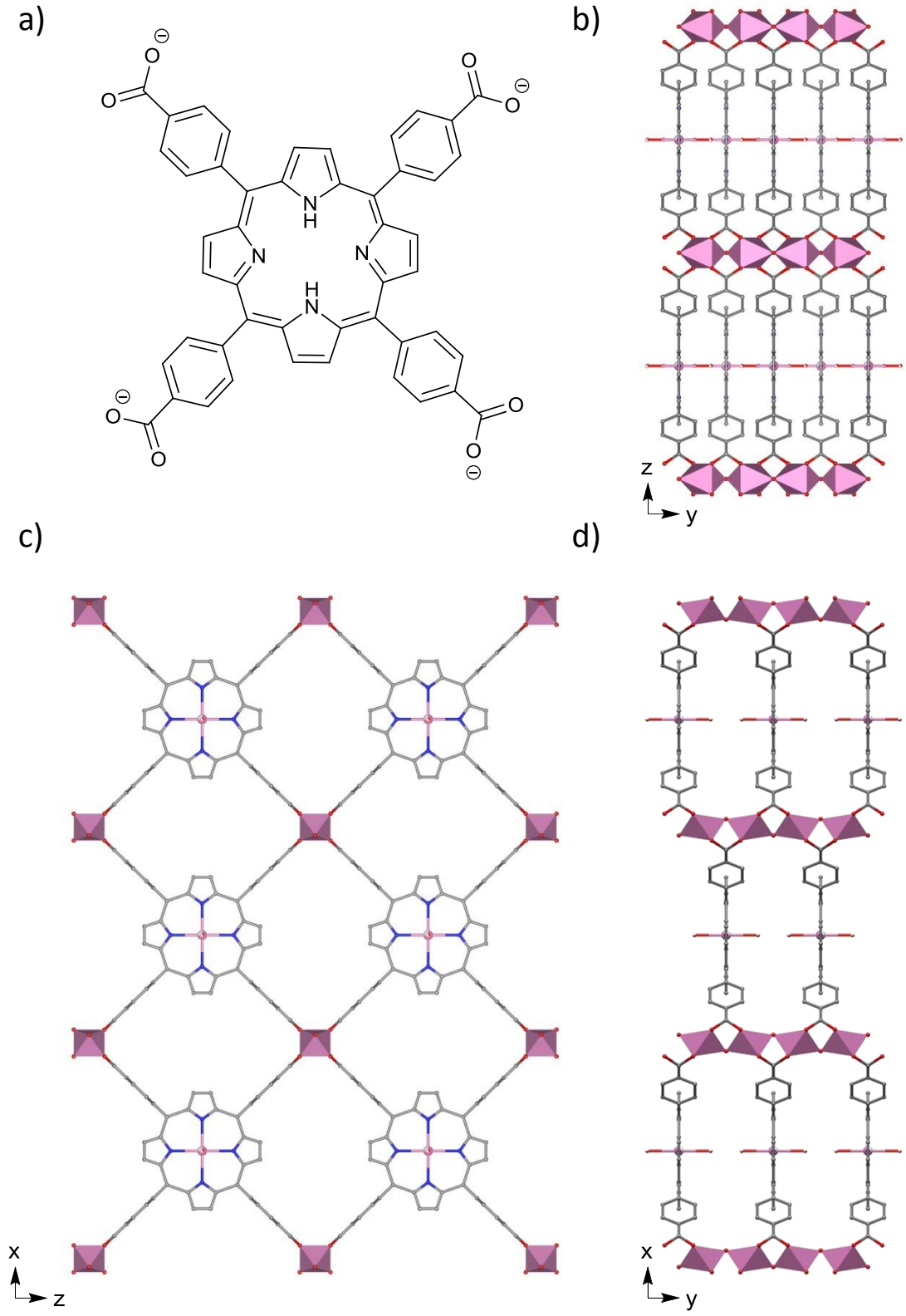

Figure 5.10

a) H_2TCPP porphyrin linker in Al-PMOF; b), c), d) Crystal structure of In-PMOF viewed along the x, y and z directions respectively displaying the three-dimensional porosity.

With the crystal structure determined, it was possible to calculate the accessible pore volume of the material to N_2 using Olex² Crystallography Software[7]. This was achieved by using the kinetic diameter of N_2 (3.6 Å)[8] to model the probe as a sphere, then calculating voids from the In-PMOF CIF that are large enough to contain this sphere. The total pore volume accessible to N_2 was calculated to be 0.589 cm^3/g, which compares well to the experimentally determined value of 0.517 cm^3/g.

5.3.3 Ammonia breakthrough

In-PMOF was assessed as a sorbent for ammonia by conducting dry ammonia breakthrough runs, as shown in Figure 5.11. Breakthrough of ammonia is observed after 33 minutes, in comparison to the 7 minutes exhibited by BPL carbon; a considerable increase in performance. The amount of ammonia adsorbed at breakthrough is calculated to be 0.021 mmol, equating to an ammonia:porphyrin ratio of 0.83:1.

It is noted that the In-PMOF shows much increased uptake in comparison with the free-base Al-MOF. This can be explained by the presence of In-OH in the porphyrin core. The relatively electropositive indium allows for dative bonding by the lone pair of ammonia, and the hydroxide counter-ion provides an additional hydrogen bonding site in the pores.

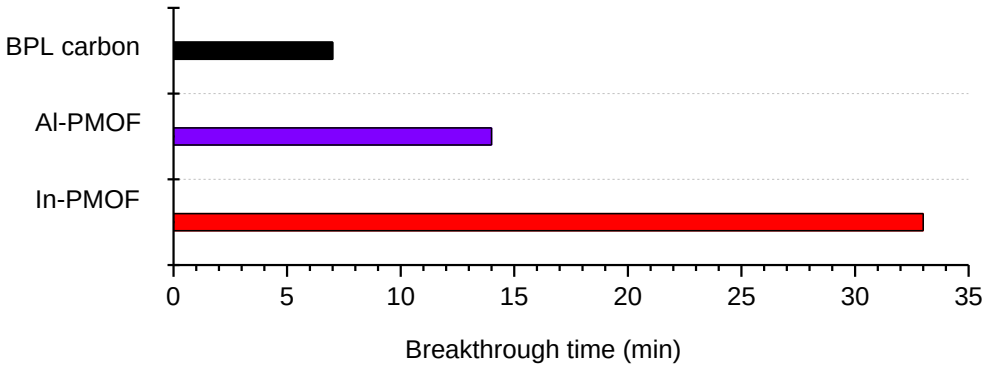

Figure 5.11

Dry (0% RH) breakthrough times for In-PMOF (red). BPL carbon (black) and Al-PMOF (purple) shown for comparison.

5.3.4 Acid insertion

Following the success of acid insertion into Al-PMOF, it was expected that acid insertion into In-PMOF may result in a comparable increase in ammonia breakthrough performance. As such HCl loading was tried using the vapour insertion method that proved successful with Al-PMOF. When analysing the resulting material by PXRD, we observed a significant loss in crystallinity, but most apparent was the loss of the highest intensity peak at 0.54 $Å^{-1}$ (Figure 5.12), suggesting possibly a change in structure, but most likely significant decomposition of the framework. Nevertheless, reactivation of the material was attempted at 120^{o}C under vacuum (10^{-2} mbar) in an effort to remove any HCl and potentially restore crystallinity as seen in the case of Al-PMOF. Unfortunately, after reactivation the crystallinity of material was further reduced (Figure 5.12).

Nitrogen isotherms were performed on the reactivated material in order to determine if any porosity had remained following the acid insertion and removal cycle, as seen with the Al-PMOF. However, the nitrogen isotherm (Figure 5.13) shows a complete

loss of porosity following acid treatment. This, along with the PXRD data, confirms decomposition following a cycle of acid insertion and removal. The reason for the decomposition of In-PMOF when subjected to HCl was thought likely due to breaking of the In-O bond in the $In(OH)O_4$ chains, and hence protonation of the porphyrin carboxylates. This is perhaps not an unsurprising result, however considering the success of the Al-PMOF-HCl material, slightly disappointing.

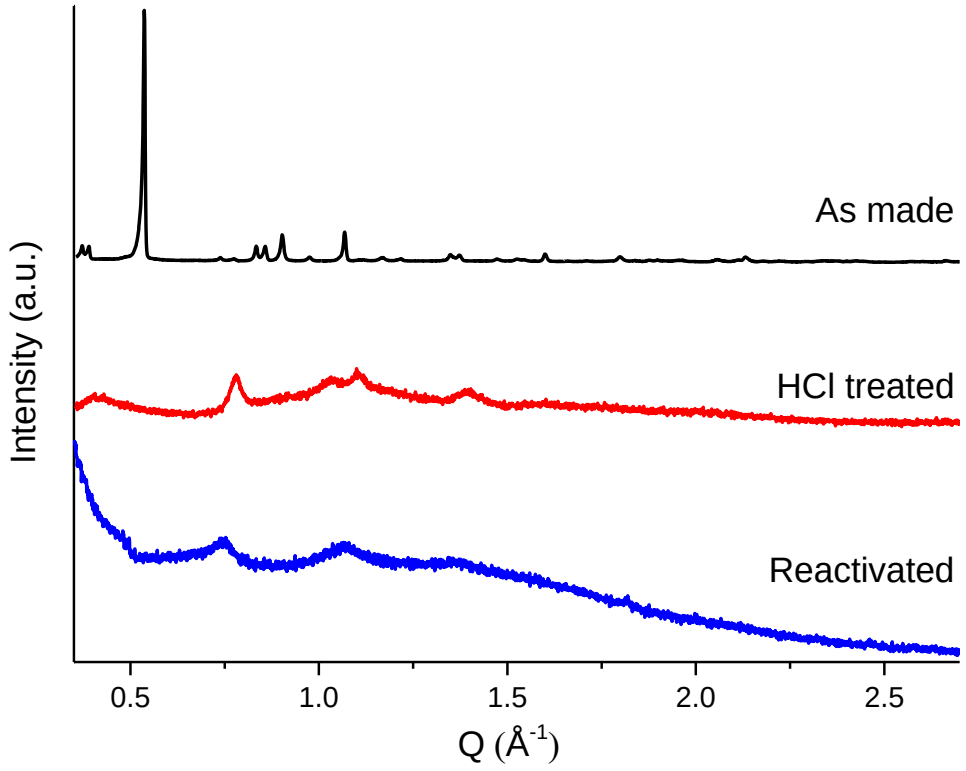

Figure 5.12

PXRD pattern of In-PMOF (black) In-PMOF-HCl (red) and In-PMOF following the removal of HCl at 165°C at 10^{-2} mbar.

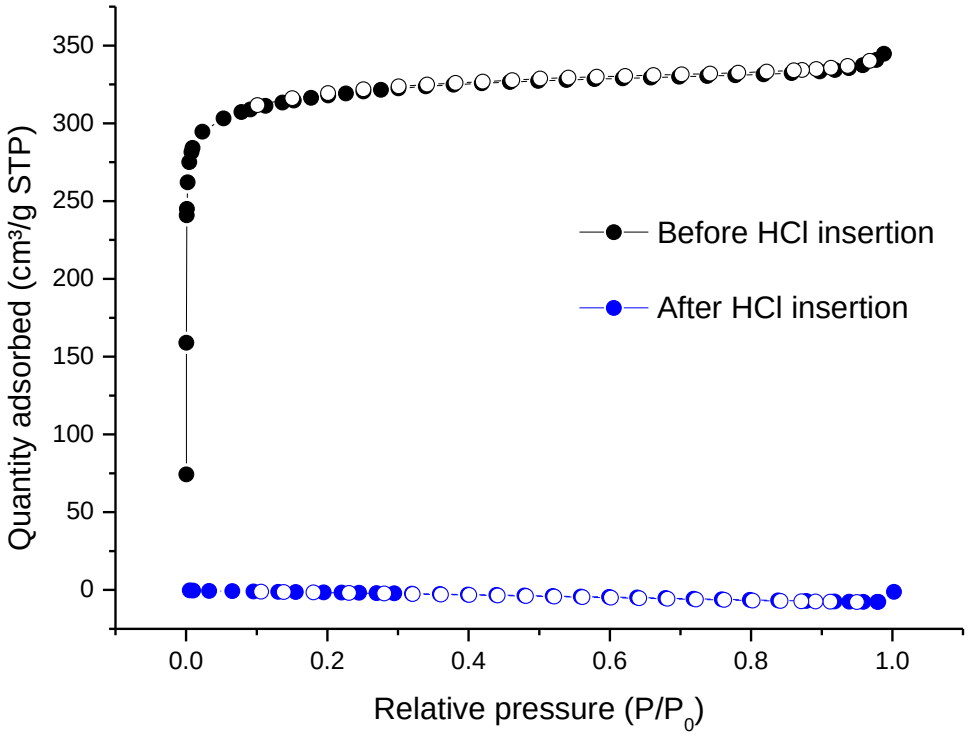

Figure 5.13

Nitrogen isotherms of In-PMOF before and after HCl insertion at 77 K showing the effect of activation temperature on pore volume.

Though clearly decomposition had occurred following activation (120^{o}C, 10^{-2} mbar) of In-PMOF-HCl, it was considered that this may in fact be due to the increased temperature in the presence of HCl, rather than the presence of HCl alone. As such NH_3 breakthrough testing was performed using In-PMOF-HCl to see if there was in fact any improvement over In-PMOF.

It was observed that ammonia breakthrough occurred after 17 minutes for In-PMOF-HCl under a dry ammonia stream, in comparison with the 33 minutes recorded for In-PMOF. It is thus evident that even at room temperature, HCl causes significant decomposition of the framework.

Loading of formic acid into In-PMOF was also attempted, however following activation (120°C, 10^{-2} mbar) it was observed that the framework had clearly decomposed (Figure 5.14).

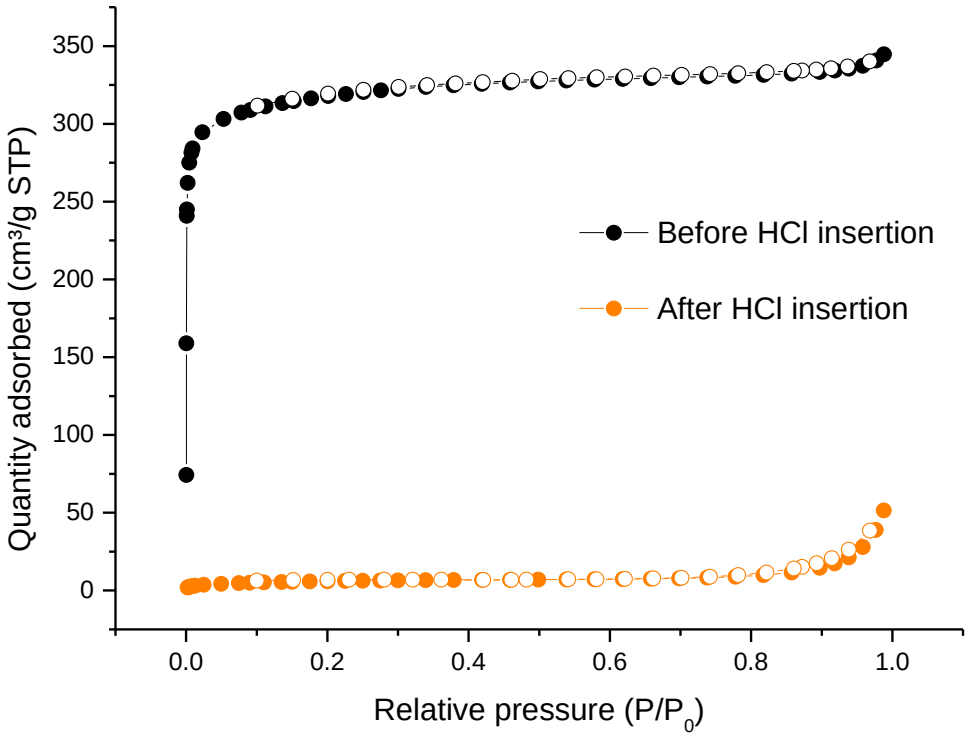

Figure 5.14

Nitrogen isotherms of In-PMOF before and after formic acid insertion at 77 K showing the effect of activation temperature on pore volume.

5.3.5 CO_2 and CH_4 uptake

Due to the respectable surface area and pore volume of the In-PMOF, it was considered viable to conduct carbon dioxide and uptake experiments on this microporous material. Initially low pressure carbon dioxide uptake experiments were performed at 273 K, 283 K, and 293 K (Figure 5.15). The calculation of the isosteric heat of adsorption at zero coverage, Q_{st}, could then be calculated by fitting a virial-type expression to the adsorption branches of the three isotherms. The result, shown

in Figure 5.16, reveals a relatively moderate Q_{st} of 29.3 kJ/mol. The CO_2 uptake at 293K at 1 bar is 17.7 wt%, which compares favourably with the majority of MOFs at the similar temperature and pressures,[9] with well-known materials such as MOF-177, MIL-101(Cr), MOF-5 and NH_2-MIL-53(Al) showing uptakes of 2.6, 4.2, 8.5 and 12 wt% CO_2 respectively at RT and 1 bar.[10-13] In-PMOF is similar to Cu(BTC) in CO_2 uptake (18.3 wt%),[14] however the MOF-74 series, among the best known materials for CO_2 adsorption, shows uptakes of 27.2, 24.9, 23.9 and 19.8 wt% for the Mg, Co, Ni and Zn variants, respectively.[14]

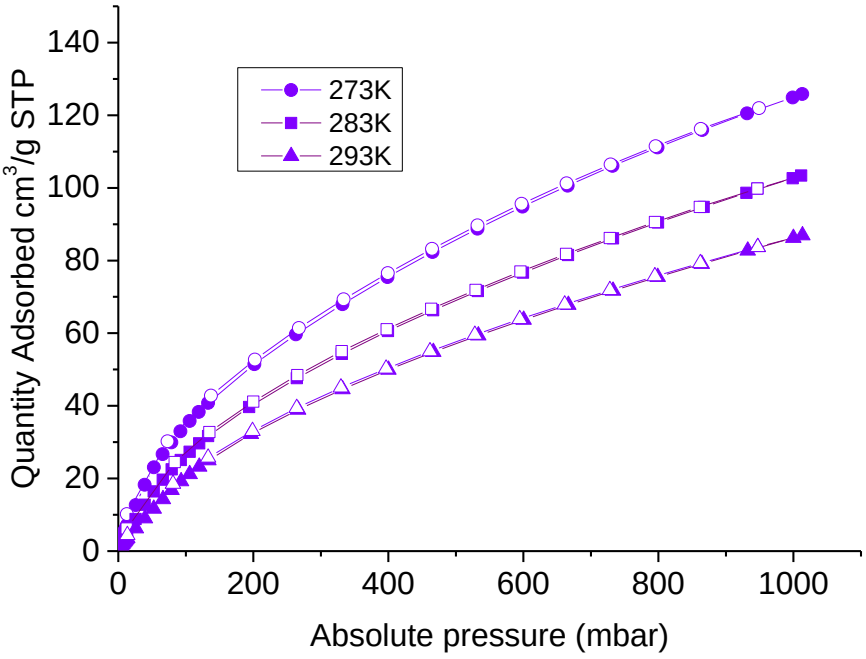

Figure 5.15

CO_2 isotherms carried out on In-PMOF at 273 K, 283K and 293K up to 1 bar. Adsorption and desorption is denoted by closed and open symbols respectively.

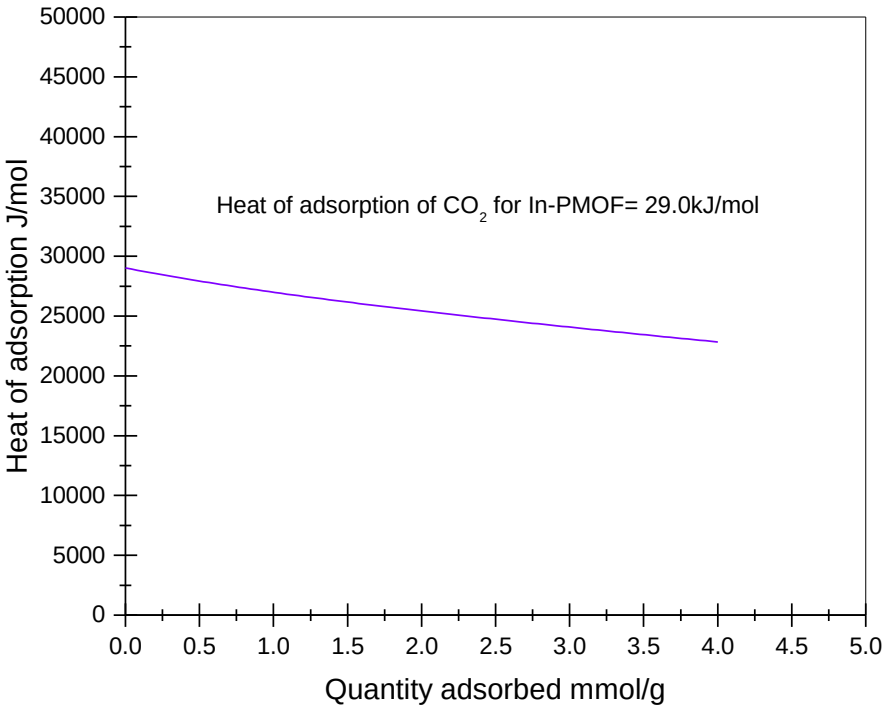

Figure 5.16

Isosteric heats of adsorption of CO_2 for In-PMOF

High pressure (up to 18 bar) CO_2 isotherms were conducted to assess the material's viability for CO_2 capture at 298 K (Figure 5.17). The isotherm is seen to almost reach saturation at 18 bar, adsorbing 268.6 cm^3/g CO_2 (STP), or 52.7 wt%. This compares favourably with other MOFs, even some with much higher surface areas.[9] Well-known materials such as MOF-177 (4500 m^2/g),[15] MIL-101(Cr) (4230 m^2/g),[16] Cu-(BTC) (1270 m^2/g)[17] and NH_2-MIL-53(Al)[18] (~1300 m^2/g) show uptakes of 60.8 wt% (298 K, 50 bar), 56.9 wt% (304 K, 50 bar), 42.8 wt% (313 K, 30 bar) and 30 wt% (303 K, 13 bar), respectively. Highest uptakes are reported for MOF-200 (73.9 wt% at 298 K, 50 bar)[15] and Mg-MOF-74 (68.9 wt% at 278 K, 36 bar).[19]

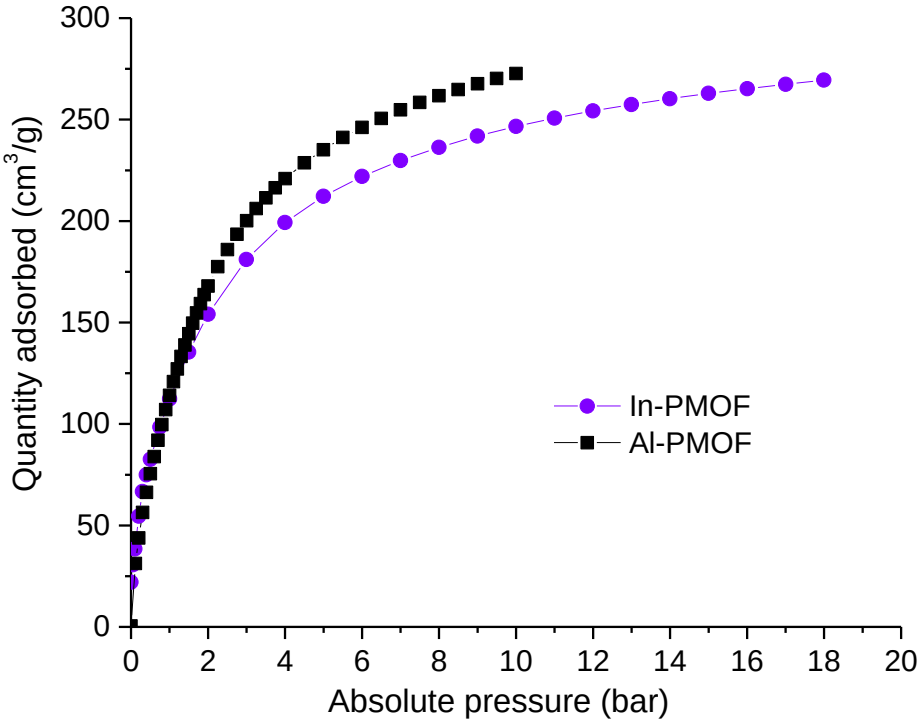

Figure 5.17

High pressure CO_2 adsorption isotherm for In-PMOF (purple circles) carried out at 298 K. High pressure CO_2 adsorption isotherm for Al-PMOF (black squares) shown for comparison. Al-PMOF isotherm carried out by the group of Prof. Mark Thomas, University of Newcastle

Despite larger lattice parameters, it can be seen that In-PMOF adsorbs less CO_2 per unit mass than the isostructural Al-PMOF. Al-PMOF adsorbs 272 cm^3/g CO_2 (STP) at 10 bar in comparison with 246 cm^3/g CO_2 (STP) measured for In-PMOF. The isotherm data for Al-PMOF was fit using a Langmuir model allowing extrapolation giving an approximate maximum uptake of 313 cm^3/g CO_2 (STP), or 61.6 wt%. It is suggested that this is likely in large part due to the presence of In-OH bound in the porphyrin core of In-PMOF, which adds significant mass in comparison with Al-PMOF.

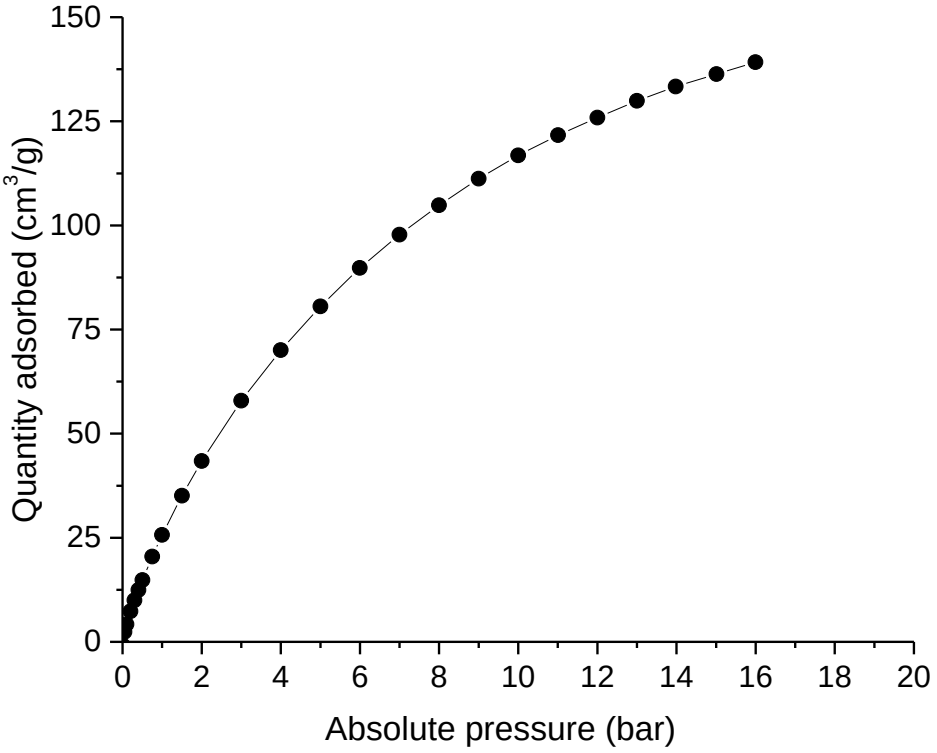

Figure 5.18

High pressure CH_4 adsorption isotherms for In-PMOF carried out at 298 K

High pressure (up to 16 bar) CH_4 adsorption was conducted to evaluate the metal–organic framework for natural gas storage at 298K (Figure 5.18). The isotherm does not quite reach saturation at 16 bar, however the highest measured value shows that 139 cm^3/g of CH_4 (STP) is adsorbed. Even taking into consideration that the material has not reached saturation, this value is still relatively low in comparison with current MOFs, with materials that possess comparable BET surface areas adsorbing around 200 cm^3/g.[20]

Ideal adsorbed solution theory (IAST) was used to calculate the CO_2/CH_4 selectivity at 298K based on the single-component gas adsorption isotherms, using a 1:1 ratio of CO_2/CH_4. The results are shown in Figure 5.19. Selectivity is calculated to be 4.5 at low pressure (0.1 bar) and raises to 6.2 at higher pressure (10 bar). These values are relatively underwhelming in comparison with other MOFs,[21] with materials often exhibiting calculated selectivity in 1:1 mixtures in excess of 30,[21] and materials such as SNU-M10 exhibiting a 1:1 CO_2/CH_4 selectivity of 98 at 298 K.[22]

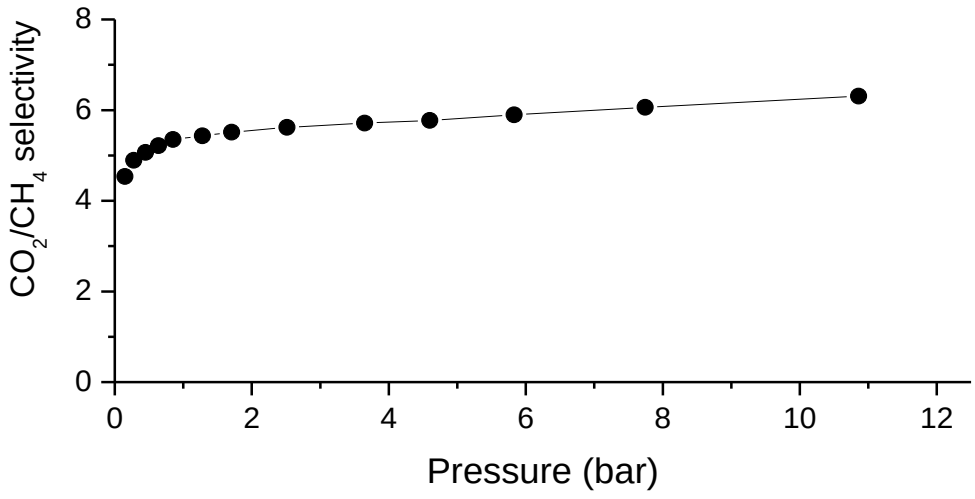

Figure 5.19

CO_2 /CH_4 selectivity of In-PMOF calculated using ideal adsorbed solution theory (IAST)

5.4 Vanadium Porphyrin MOF

Unpublished work within the group led by B. Liu resulted in the discovery of a vanadium porphyrin metal organic framework, isostructural to Al-PMOF and In-PMOF. It was considered of interest to compare this material to Al-PMOF with regard to ammonia breakthrough, and also with regard to its ability to adsorb acids.

Vanadium exists in the 4+ oxidation state in the V-PMOF, as opposed to the 3+ oxidation states of aluminium and indium observed for Al-PMOF and In-PMOF. To balance this additional charge, there is an oxide bridging the vanadium atoms forming the $V(O)_4O$ chain, shown in Figure 5.20.

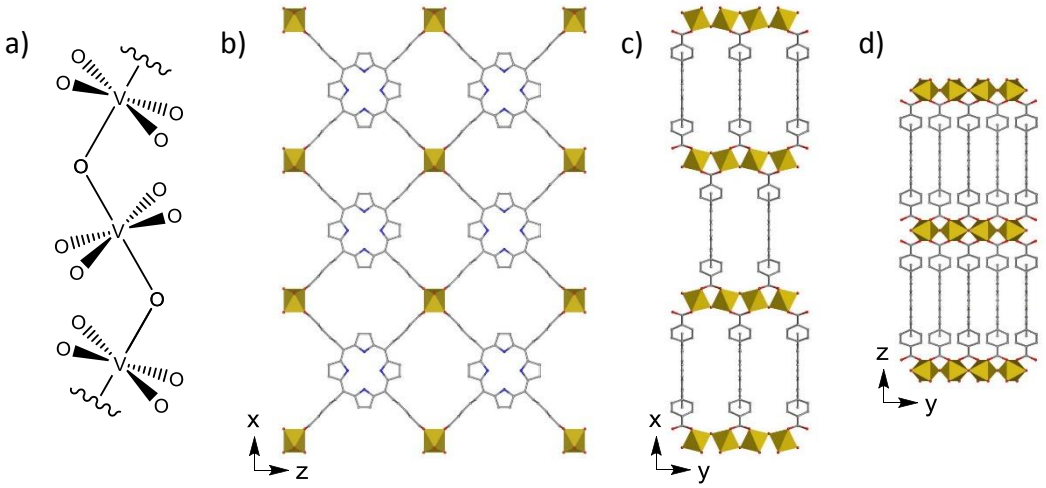

Figure 5.20

V-PMOF structure a) Infinite $V(O)_4$ (μ-O) chains. b-d) Crystal structure of V-PMOF, isostructural to Al-PMOF and In-PMOF showing no vanadium in the porphyrin core

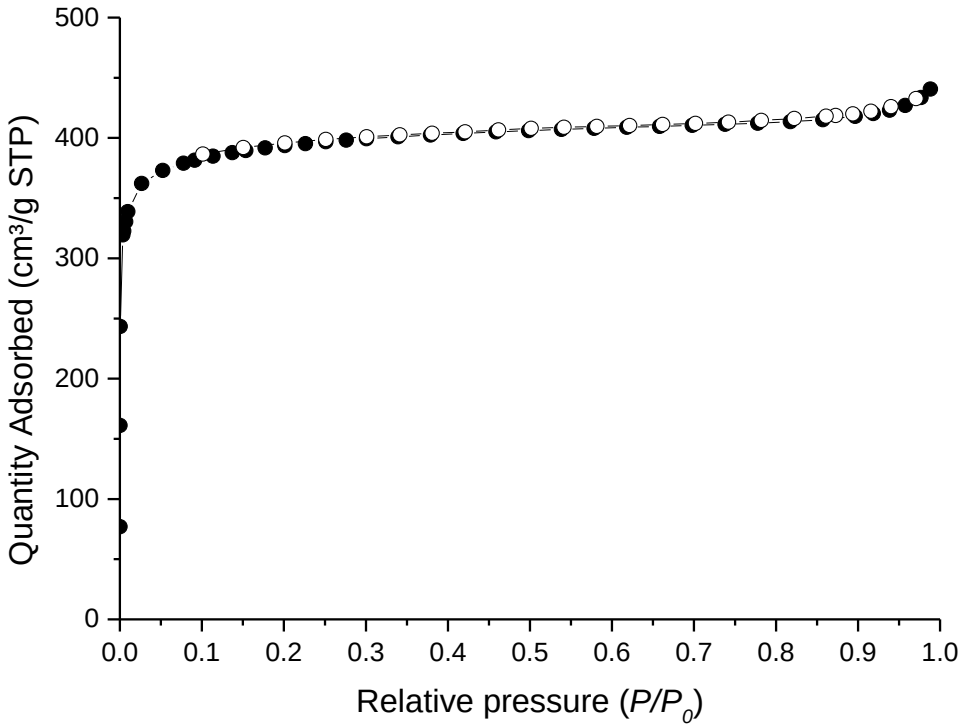

Figure 5.21

Nitrogen isotherms at 77 K of V-PMOF following activation at 165°C, 10^{-2} mbar. Adsorption and desorption is denoted by filled and empty symbols, respectively. BET Surface Area = 1552 ± 6 m²/g

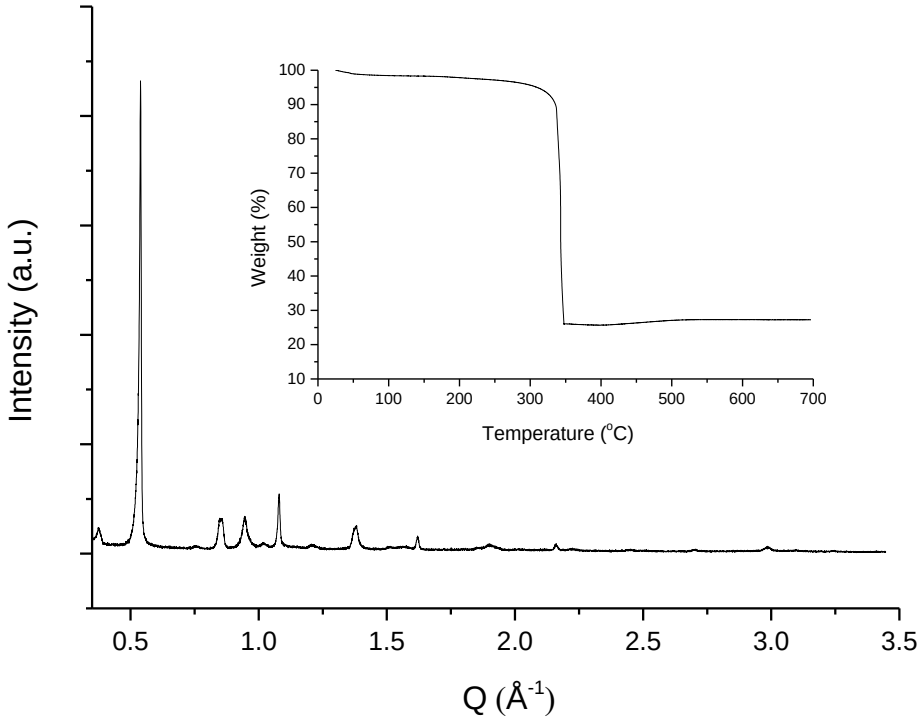

Figure 5.22

PXRD pattern and TGA trace of V-PMOF

5.4.1 Acid insertion

Initially, HCl loading was attempted using the vapour insertion method described for previous materials. PXRD analysis of the resulting material revealed a complete loss in crystallinity, suggesting decomposition of the structure. Nevertheless, reactivation of the material was attempted at 165°C under vacuum (10^{-2} mbar) in an effort to remove any HCl and potentially restore crystallinity as seen in the case of Al-PMOF. Unfortunately, no restoration of crystallinity was observed (Figure 5.23).

Performing a nitrogen isotherm on V-PMOF after HCl removal showed a complete loss in porosity of the material, confirming decomposition of the structure. Based on the similarity of the PXRD patterns upon HCl loading and following reactivation, it

was considered that decomposition was a result of the HCl loading, not due to the activation conditions in the presence of HCl.

It seems that the stability towards acids follows the order Al-PMOF > V-PMOF > In-PMOF, and as such the stability of these metal porphyrin MOFs cannot be explained by M-O bond strength, as the average bond strength follows the order V-O (627 kJ/mol) > Al-O (512 kJ/mol) > In-O (320 kJ/mol).[1] It has been reported that increased oxidation state may result in increased stability in MOFs,[23] but it is seen that oxidation does not play a dominant role here (oxidation states of Al^{III}, V^{IV} and In^{III}). The stability of the M-porphyrin MOFs could be explained by the inertness, determined by rates ligand exchange, of the metal ions which follow the order Al^{III} > V^{IV} > In^{III}.[24-26] These results are also in agreement with the literature findings comparing stability of isostructural M-BDC MOFs, where M = V^{III}, V^{IV}, Al^{III}, Cr^{III}.[26]

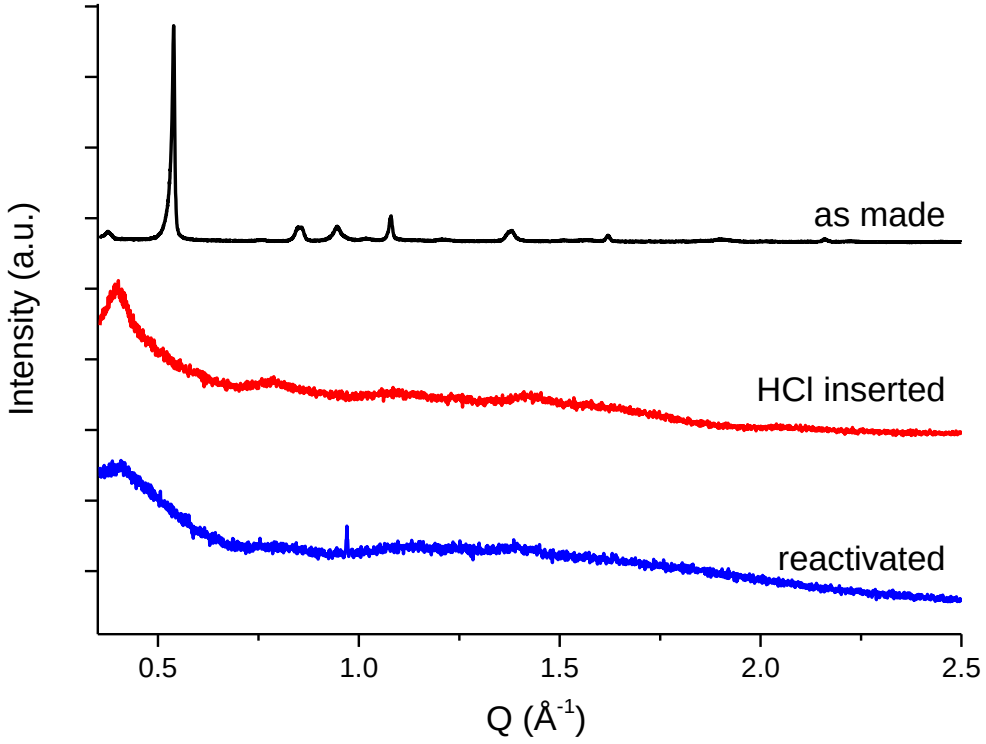

Figure 5.23

PXRD pattern of V-PMOF (black) V-PMOF-HCl (red) and V-PMOF following the removal of HCl at 165°C at 10^{-2} mbar.

Formic acid loading was subsequently attempted on the V-PMOF. As seen in Figure 5.24, PXRD of the formic acid loaded sample revealed that the material retains its crystallinity upon acid loading with no amorphous region, in concurrence with the analogous Al-PMOF material. As mentioned previously, this may indicate an ordered arrangement of formic acid in the pores, or perhaps be a result of reduced X-ray scattering power of the constituent atoms of formic acid, and hence a weaker impact on the diffraction pattern. No additional peaks are observed in the diffraction pattern following formic acid loading.

UV-visible spectroscopy performed on V-PMOF-FA (Figure 5.25) reveals a broad, low-intensity Soret band at 435 nm and four Q bands at 514 nm, 537 nm, 578 nm

and 622 nm. The presence of the four Q band indicates that the porphyrin core remains largely in the free-base form, comparable Al-PMOF-FA discussed in chapter 4.

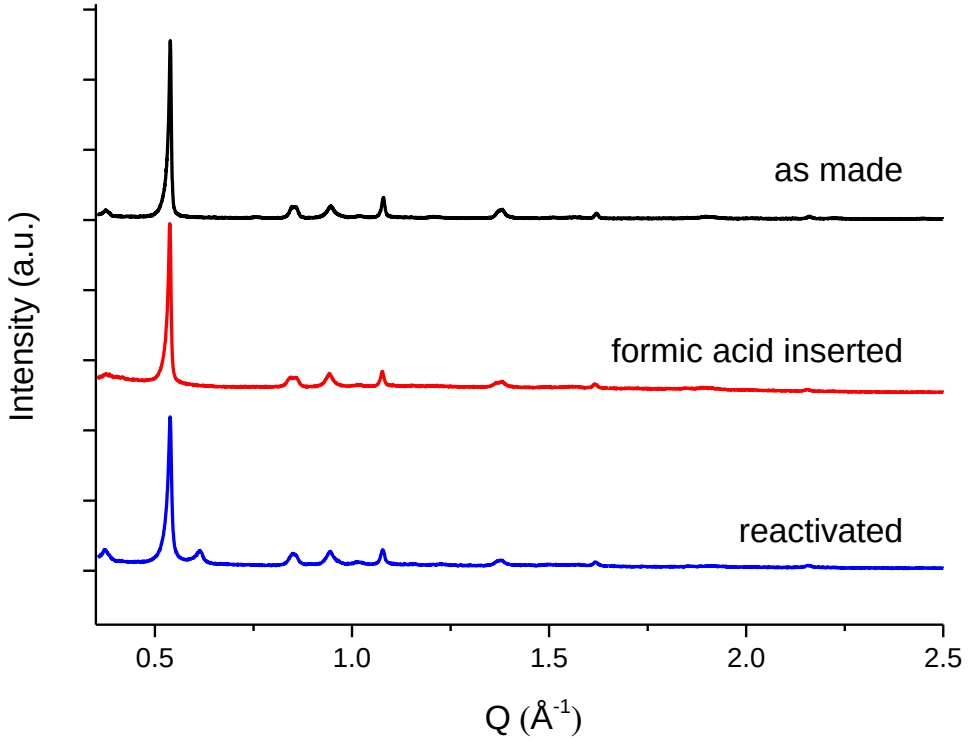

Figure 5.24

PXRD pattern of V-PMOF (black) V-PMOF-FA (red) and V-PMOF following the removal of HCl at 165^{o}C at 10^{-2} mbar

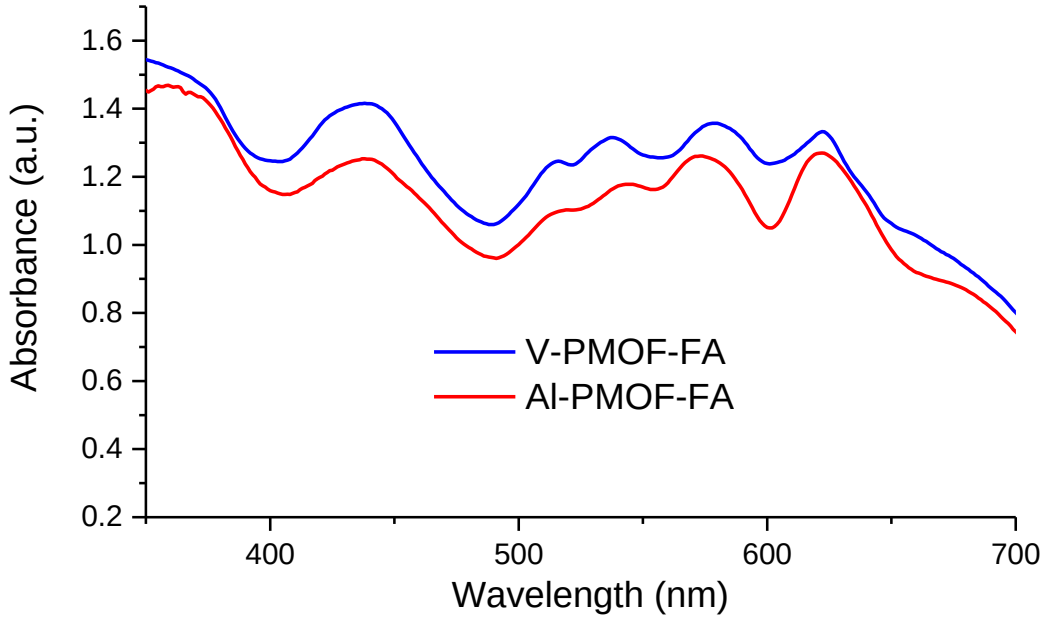

Figure 5.25

UV-Visible spectrum of V-PMOF-FA (blue). UV-Visible spectrum of Al-PMOF-FA (red) shown for comparison.

Nitrogen isotherms were conducted in order to assess if any damage occurs to the pore structure of the material following a cycle of formic acid loading and removal (Figure 5.24). It was discovered that following the initial cycle, a significant decrease in pore volume had occurred, a large decrease from 0.623 cm^3/g to 0.360 cm^3/g, approximately 42% in relation to the free-base material. Subsequent cycling afforded no further appreciable loss in pore volume. This loss is comparable to Al-PMOF-FA, which after loading and reactivation is seen to be lose 39% of its pore volume.

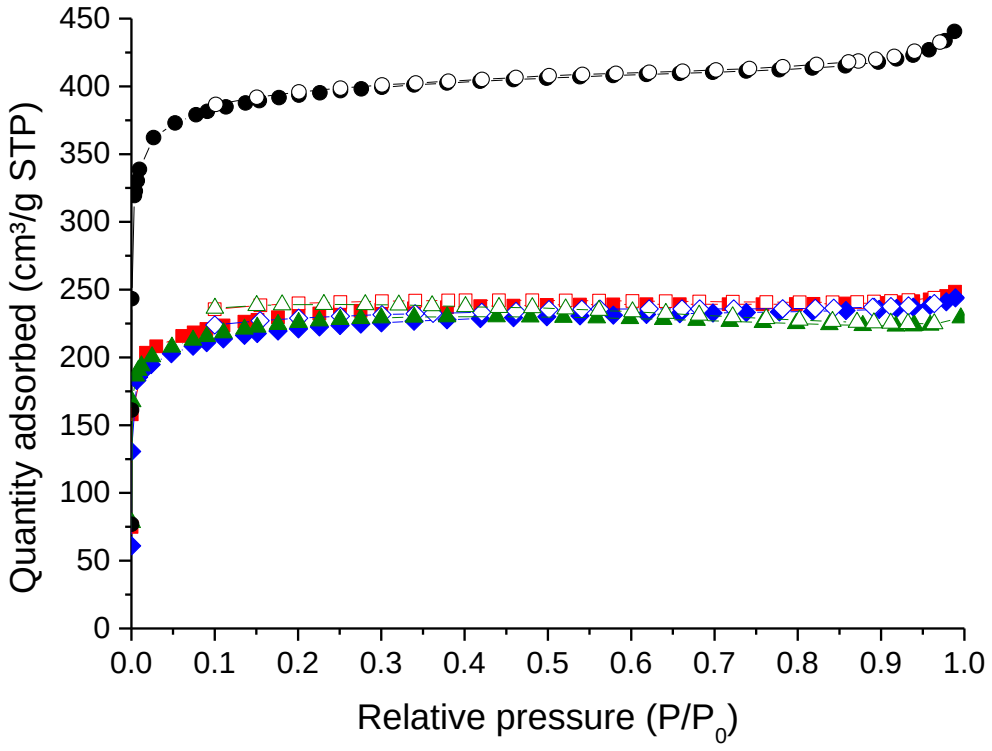

Figure 5.26

Nitrogen isotherms at 77K after cycling formic acid uptake and removal at 165 ^{o}C, 10^{-2} mbar. Fresh, activated V-PMOF is shown in black circles; the first. second and third cycles are shown in red squares, blue diamonds and green triangles, respectively. Adsorption and desorption is denoted by filled and empty symbols.

Thermo-gravimetric analysis was performed on samples before acid loading, and after removal procedures, shown in Figure 5.27. It can be seen following formic acid removal at 165 ^{o}C and 10^{-2} mbar the TGA trace is similar to that before acid loading, with no evidence of free formic acid remaining in the pores. However, it is noted that weight % of inorganic residue is slightly decreased after formic acid loading, suggesting that following the acid loading and removal process some additional organic material is present. It seems the loss of porosity observed after a cycle of acid loading and removal is likely due to formic acid reacting with the MOF, resulting in partial collapse of the framework.

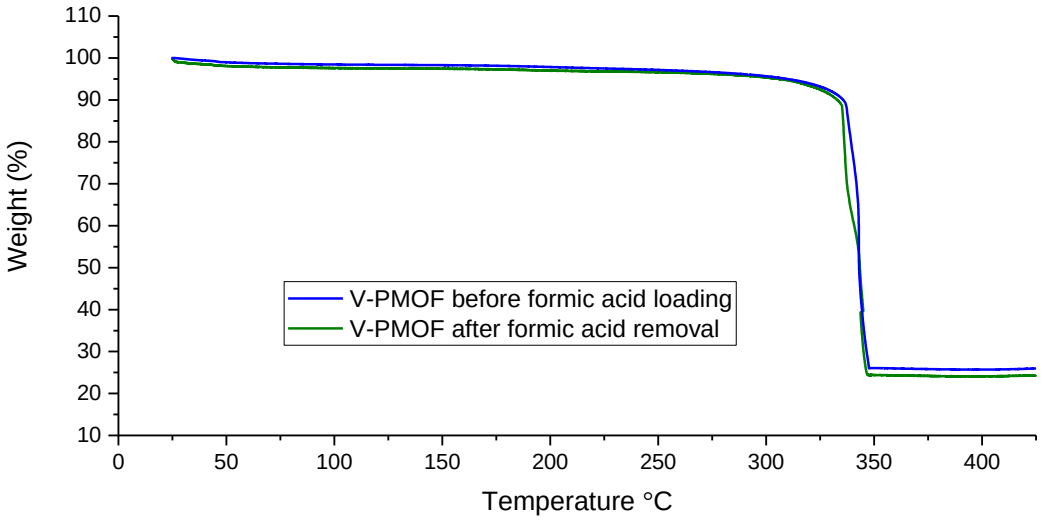

Figure 5.27

TGA of V-PMOF before acid loading (blue), after acid removal at 165 ^{o}C, 10^{-2} mbar (green)

5.4.2 Ammonia breakthrough

A dry flow of ammonia was chosen in order to assess the potential of V-PMOF as an ammonia sorbent (Figure 5.28). Ammonia was detected above 20 ppm after 38.5 minutes of testing, comparing very favourably to the benchmark BPL activated carbon (7 mins), Al-PMOF (14 mins) and even In-PMOF (33 mins). The amount of ammonia adsorbed at breakthrough is calculated to be 0.024 mmol which gives an NH_3:porphyrin ratio of approximately 0.74:1 in the MOF. Considering the similarity in pore volumes and structure of the V-PMOF and Al-PMOF, and that both materials are seen to have free-base porphyrin cores, the difference in breakthrough times is quite prominent. However, it is proposed that the difference may be a consequence of the oxidation states of the metals, Al(III) and V(IV), which results in an oxide bridge between vanadium atoms, in comparison with the hydroxide bridge observed between aluminium atoms. The oxide bridge is likely to form stronger hydrogen

bonds with the influent ammonia than the hydroxide bridge, accounting for the greater uptake of ammonia before breakthrough. Loading with formic acid provides a considerable increase in ammonia uptake, with a V-PMOF-FA uptake time of 81 minutes, resulting in more than an 11-fold increase in performance in comparison with the benchmark BPL carbon.

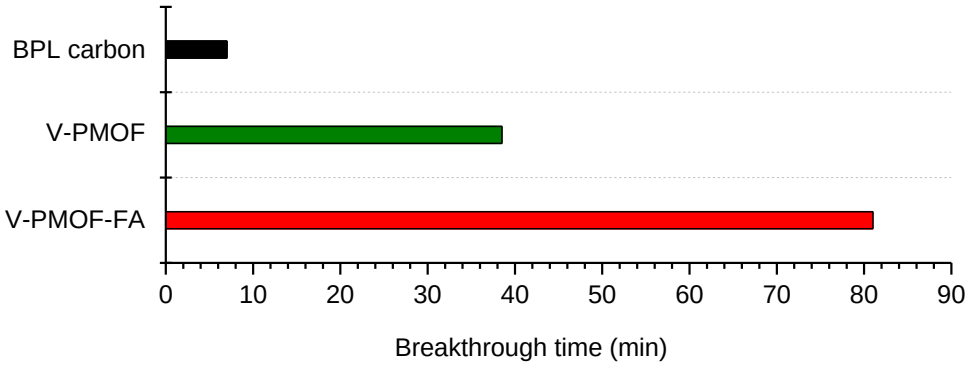

Figure 5.28

Dry (0% RH) breakthrough times for V-PMOF (green) and V-PMOF-FA (red). BPL carbon (black) shown for comparison.

5.4.3 CO_2 and CH_4 uptake

A high pressure (up to 18.5 bar) CO_2 isotherm was conducted to assess the viability of V-PMOF for CO_2 capture at 298 K in comparison with the Al and In analogues. The isotherm is shown in Figure 5.29. V-PMOF is seen to almost reach saturation at 18.5 bar, adsorbing 267 cm^3/g CO_2 (STP), or 52.5 wt%. This value is almost comparable to that measured for In-PMOF (52.7 wt%), but considerably lower than the value measured for Al-PMOF (61.6 wt%).

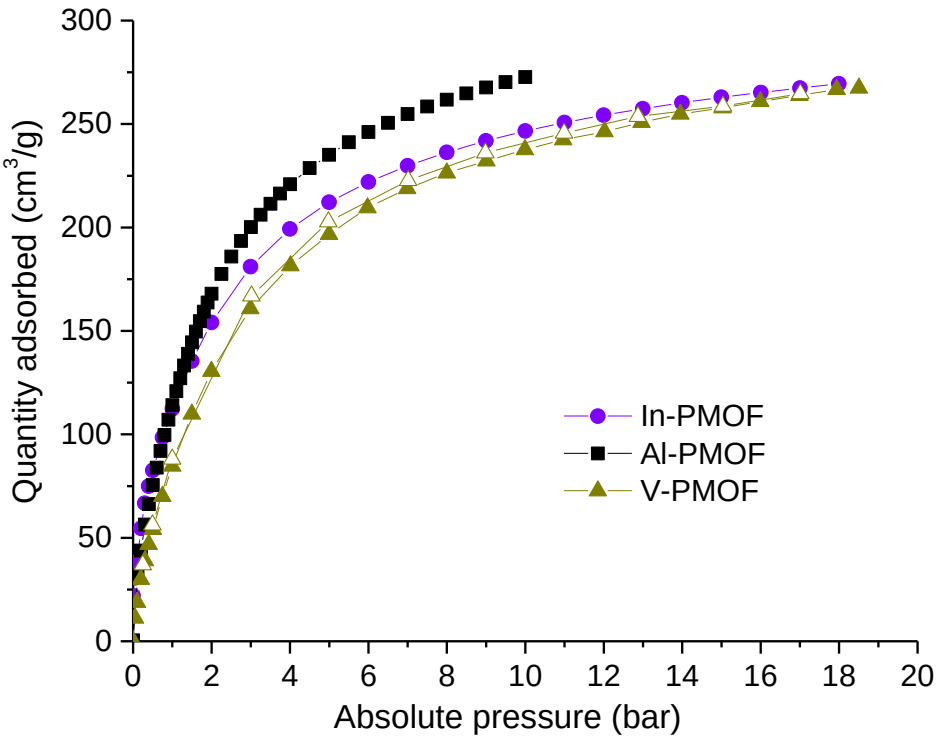

Figure 5.29

High pressure CO_2 adsorption isotherm for V-PMOF carried out at 298 K. In-PMOF (purple circles) and Al-PMOF (black squares) shown for comparison. Adsorption and desorption is denoted by filled and empty symbols, respectively. Al-PMOF isotherm carried out by the group of Prof. Mark Thomas, University of Newcastle

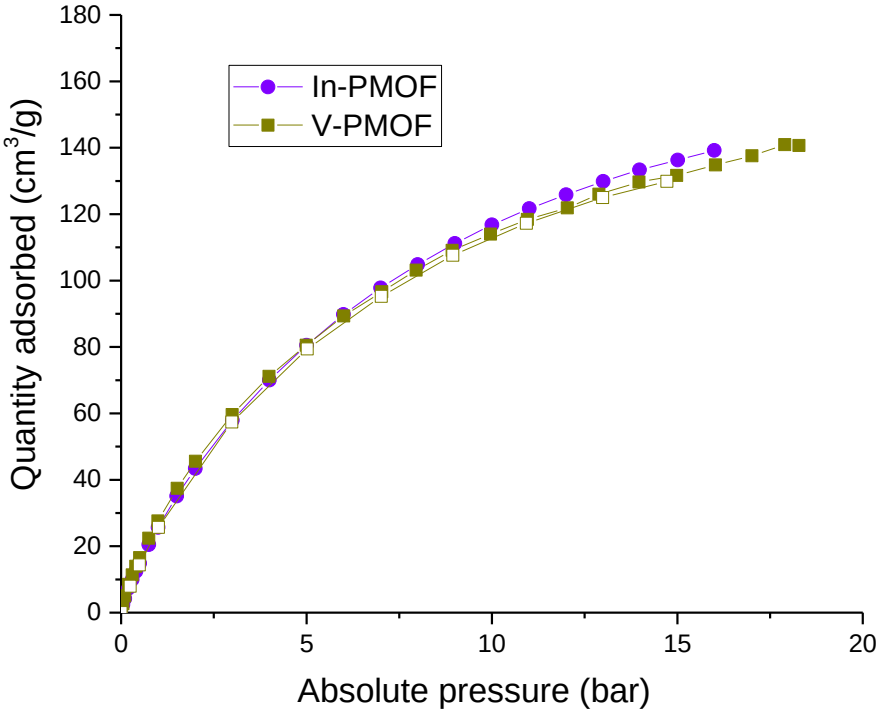

Figure 5.30

High pressure CH_4 adsorption isotherm for V-PMOF (yellow squares) carried out at 298 K. CH_4 adsorption for In-PMOF (purple circles) is shown for comparison. Adsorption and desorption is denoted by filled and empty symbols, respectively.

High pressure (up to 18.5 bar) CH_4 adsorption was conducted to evaluate V-PMOF for natural gas storage at 298K (Figure 5.30). The isotherm does not quite reach saturation at 18.5 bar, however the highest measured value shows that 141 cm^3/g of CH_4 (STP) is adsorbed. As shown, CH_4 uptake is comparable to that of In-PMOF.

Ideal adsorbed solution theory (IAST) was used to calculate the CO_2/CH_4 selectivity of V-PMOF at 298K based on the single-component gas adsorption isotherms using a 1:1 ratio of CO_2/CH_4. The results are shown in Figure 5.31. Selectivity is

calculated to be 5.8 at low pressure (0.1 bar) and 5.6 at higher pressure (10 bar). As with In-PMOF, this selectivity is underwhelming relative to current materials.[21]

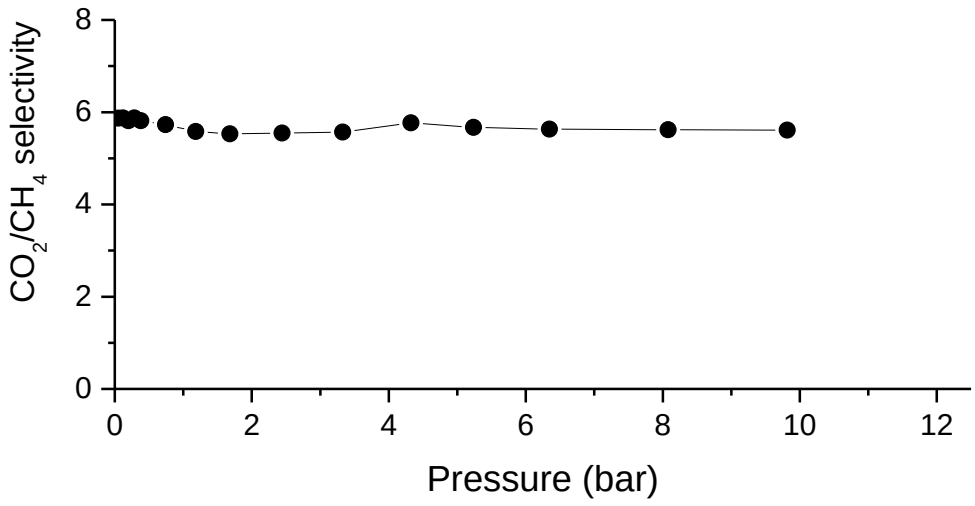

Figure 5.31

CO_2 /CH_4 selectivity of V-PMOF calculated using ideal adsorbed solution theory (IAST)

5.5 Conclusion

In this chapter the synthesis of an indium porphyrin metal organic framework has been optimised and the resulting material has been fully characterised revealing a material isostructural to Al-PMOF, with a larger unit cell and the presence of indium in the porphyrin core. The material showed reasonable performance as an ammonia sorbent, outperforming activated carbon and Al-PMOF. Its increased performance was attributed to the presence of InOH within the porphyrin core, resulting in improved hydrogen bonding with ammonia. Acid loading was attempted, however unfortunately the framework proved entirely unstable to acid.

In-PMOF was assessed for CO_2 and CH_4 capture, with the isosteric heats of adsorption at zero coverage for CO_2 calculated to be a relatively moderate at 29.0 kJ/mol. CO_2/CH_4 separation was determined using the ideal adsorbed solution theory, which showed only modest separation of around 5:1 at low pressures.

A vanadium porphyrin MOF, isostructural to the Al-PMOF and In-PMOF, was synthesised and evaluated as a sorbent for ammonia using micro-breakthrough experiments. The material showed a moderate affinity for ammonia, outperforming its aluminium and indium analogues, and far surpassing BPL activated carbon. The material was shown to be entirely unstable to HCl, however the material was stable to formic acid loading, showing a corresponding increase in ammonia uptake performance. CO_2 and CH_4 isotherms were carried out using V-PMOF, which exhibited comparable behaviour to the isostructural In-PMOF, showing CO_2/CH_4 separation of around 6:1 at both low and high pressures.

5.6 References

1. W. M. Haynes and D. R. Lide, *CRC handbook of chemistry and physics : a ready-reference book of chemical and physical data*, CRC Press, Boca Raton, Fla., 2011.
2. A. Coelho, *Journal*, 2010, DOI: citeulike-article-id:12635012.
3. J. A. Johnson, X. Zhang, T. C. Reeson, Y.-S. Chen and J. Zhang, *J. Am. Chem. Soc.*, 2014, **136**, 15881-15884.
4. W.-Y. Gao, Z. Zhang, L. Cash, L. Wojtas, Y.-S. Chen and S. Ma, *CrystEngComm*, 2013, **15**, 9320-9323.
5. A. Fateeva, P. A. Chater, C. P. Ireland, A. A. Tahir, Y. Z. Khimyak, P. V. Wiper, J. R. Darwent and M. J. Rosseinsky, *Angew. Chem. Int. Ed.*, 2012, **51**, 7440-7444.
6. P. Stephens, *J. Appl. Crystallogr.*, 1999, **32**, 281-289.
7. O. V. Dolomanov, L. J. Bourhis, R. J. Gildea, J. A. K. Howard and H. Puschmann, *J. Appl. Crystallogr.*, 2009, **42**, 339-341.
8. J. M. Thomas and W. J. Thomas, *Principles and Practice of Heterogeneous Catalysis*, Wiley, 1996.
9. R. Sabouni, H. Kazemian and S. Rohani, *Environ Sci Pollut Res*, 2014, **21**, 5427-5449.
10. J. A. Mason, K. Sumida, Z. R. Herm, R. Krishna and J. R. Long, *Energy & Environmental Science*, 2011, **4**, 3030-3040.
11. P. Chowdhury, C. Bikkina and S. Gumma, *J. Phys. Chem. C*, 2009, **113**, 6616-6621.
12. Z. Zhao, Z. Li and Y. S. Lin, *Industrial & Engineering Chemistry Research*, 2009, **48**, 10015-10020.
13. B. Arstad, H. Fjellvåg, K. Kongshaug, O. Swang and R. Blom, *Adsorption*, 2008, **14**, 755-762.
14. A. Ö. Yazaydın, R. Q. Snurr, T.-H. Park, K. Koh, J. Liu, M. D. LeVan, A. I. Benin, P. Jakubczak, M. Lanuza, D. B. Galloway, J. J. Low and R. R. Willis, *J. Am. Chem. Soc.*, 2009, **131**, 18198-18199.

15. H. Furukawa, N. Ko, Y. B. Go, N. Aratani, S. B. Choi, E. Choi, A. Ö. Yazaydin, R. Q. Snurr, M. O'Keeffe, J. Kim and O. M. Yaghi, *Science*, 2010, **329**, 424-428.
16. P. L. Llewellyn, S. Bourrelly, C. Serre, A. Vimont, M. Daturi, L. Hamon, G. De Weireld, J.-S. Chang, D.-Y. Hong, Y. Kyu Hwang, S. Hwa Jhung and G. Férey, *Langmuir*, 2008, **24**, 7245-7250.
17. J. Moellmer, A. Moeller, F. Dreisbach, R. Glaeser and R. Staudt, *Microporous Mesoporous Mater.*, 2011, **138**, 140-148.
18. S. Couck, J. F. M. Denayer, G. V. Baron, T. Rémy, J. Gascon and F. Kapteijn, *J. Am. Chem. Soc.*, 2009, **131**, 6326-6327.
19. P. D. C. Dietzel, V. Besikiotis and R. Blom, *J. Mater. Chem.*, 2009, **19**, 7362-7370.
20. J. A. Mason, M. Veenstra and J. R. Long, *Chem. Sci.*, 2014, **5**, 32-51.
21. Y. Liu, Z. U. Wang and H.-C. Zhou, *Greenhouse Gases: Science and Technology*, 2012, **2**, 239-259.
22. H.-S. Choi and M. P. Suh, *Angew. Chem.*, 2009, **121**, 6997-7001.
23. J. J. Low, A. I. Benin, P. Jakubczak, J. F. Abrahamian, S. A. Faheem and R. R. Willis, *J. Am. Chem. Soc.*, 2009, **131**, 15834-15842.
24. J. E. Huheey, *Inorganic Chemistry: Principles of Structure and Reactivity*, Harper International, 1983.
25. R.D.Madan and S. Prakash, *Modern Inorganic Chemistry*, S Chand & Co Ltd, 1987.
26. I. J. Kang, N. A. Khan, E. Haque and S. H. Jhung, *Chemistry – A European Journal*, 2011, **17**, 6437-6442.

6 Zirconium metal-organic frameworks

6.1 Introduction

In the field of metal organic frameworks, Zr^{4+} based MOFs are well known for their high thermal and chemical stability[1] as well as their high surface areas.[2] Most carboxylate-based zirconium MOFs, with the notable exception of the MIL-140 series,[3] are based on a secondary building unit (SBU) consisting of a zirconium oxide hydroxide structure, $Zr_6O_4(OH)_4$ shown in Figure 6.1, which can coordinate with up to 12 carboxylate groups. This SBU is integral in a MOF series denoted UiO-66-X, whereby UiO stands for Universitetet i Oslo, and X can be a variety of functional groups.[4] The use of modulators (usually carboxylic acids such as formic, acetic or benzoic acid) has greatly progressed the synthesis of these materials. Modulators are thought to work by slowing crystal growth of the MOFs by competing with linker molecules in the binding to the SBU. The use of modulators allows control over crystal size, and provides a synthetic route to many materials that had otherwise proved elusive.

There are examples in the literature of adding amino functionality to MOFs resulting in much increased ammonia uptake.[5] With its high stability, and the ability to functionalise its BDC linkers, it was thought that UiO-66 may provide a good platform to add amino functionality, with the aim of adsorbing ammonia as a result of favourable hydrogen bonding between ammonia and $-NH_2$ groups.

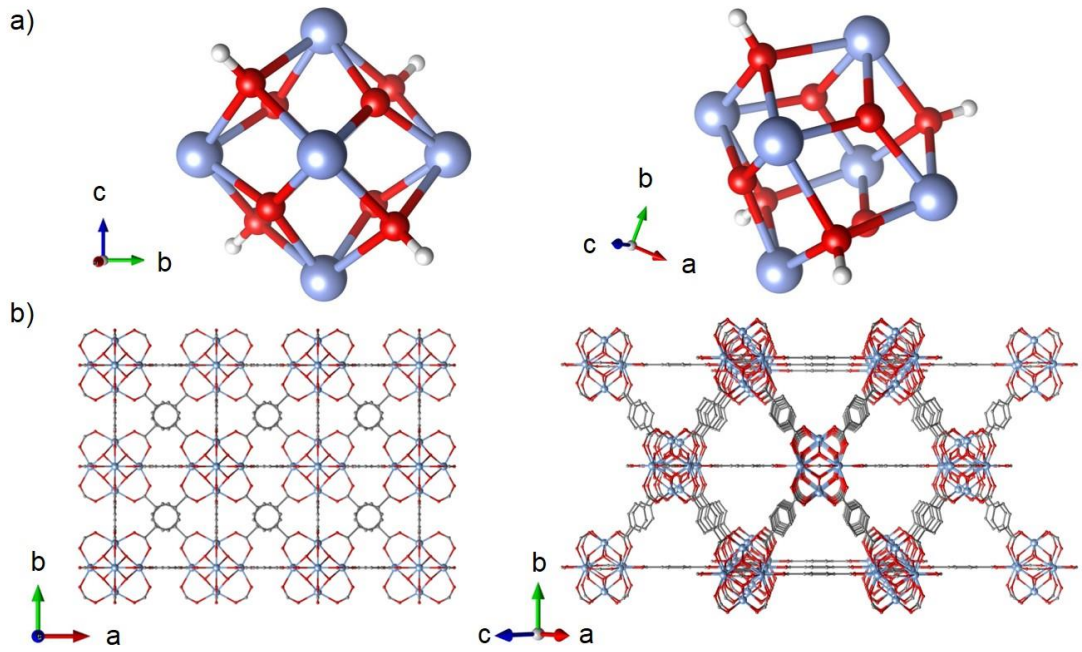

Figure 6.1

UiO-66; zirconium (blue), oxygen (red), carbon (grey), hydrogen (white) a) Inorganic SBU b) Crystal structure of UiO-66. CIF can be found on the open-access Crystallography Open Database at http://www.crystallography.net/cod

6.2 Synthesis

UiO-66 materials were synthesised using a modified method of that used in the work by Schaate et al.[6] All chemicals are from Sigma-Aldrich, used without further purification.

UiO-66

$ZrCl_4$ (0.3 mmol) and benzoic acid (7.5 mmol) were added to DMF (10 mL) in a 40 mL Teflon capped borosilicate glass vial and sonicated for 1 minute to fully dissolve the reagents. Terephthalic acid (0.3 mmol) was added to the reaction mixture and sonicated for 10 seconds. The vial was tightly capped and heated to 120 ^{o}C at a rate

of 10 ^{o}C/min. The vial was kept at 120 ^{o}C for 24 h, then cooled to room temperature at a rate of 2 ^{o}C/min. The precipitate was collected by vacuum filtration, washing with DMF three times (3 x 50 mL) and once with THF (1 x 20 mL). The white solid was then left to dry in air. The MOF was then activated by heating to 120 ^{o}C under reduced pressure (10^{-2} mbar).

UiO-66-NH_2

$ZrCl_4$ (0.3 mmol), benzoic acid (7.5 mmol) and water (1.2 mmol) were added to DMF (10 mL) in a 40 mL Teflon capped borosilicate glass vial and sonicated for 1 minute to fully dissolve the reagents. 2-Aminoterephthalic acid (0.3 mmol) was added to the reaction mixture and sonicated 10 seconds. The vial was tightly capped and heated to 120 ^{o}C at a rate of 10 ^{o}C/min. The vial was kept at 120 ^{o}C for 24 h, then cooled to room temperature at a rate of 2 ^{o}C/min. The precipitate was collected by vacuum filtration, washing with DMF three times (3 x 50 mL) and once with THF (1 x 20 mL). The pale yellow solid was then left to dry in air. The MOF was then activated by heating to 120 ^{o}C under reduced pressure (10^{-2} mbar).

UiO-66-$(NH_2)_2$

$ZrCl_4$ (0.3 mmol), benzoic acid (7.5 mmol) and water (0.6 mmol) were added to DMF (10 mL) in a 40 mL Teflon capped borosilicate glass vial and sonicated for 1 minute to fully dissolve the reagents. 2,5-Diaminoterephthalic acid (0.3 mmol) was added to the reaction mixture and sonicated for 1 min; 2,5-Diaminoterephthalic acid is relatively insoluble in DMF and this serves to dissolve some linker, the vial was tightly capped and heated to 120 ^{o}C at a rate of 10 ^{o}C/min. The vial was kept at 120 ^{o}C for 24 h, then cooled to room temperature at a rate of 2 ^{o}C/min. The precipitate

was collected by centrifugation, mixed with DMF and centrifuged. This process was repeated 5 times (5 x 30 mL DMF) and once with THF (1 x 20 mL). The brown solid was then left to dry in air. The MOF was then activated by heating to 120 ^{o}C under reduced pressure (10^{-2} mbar).

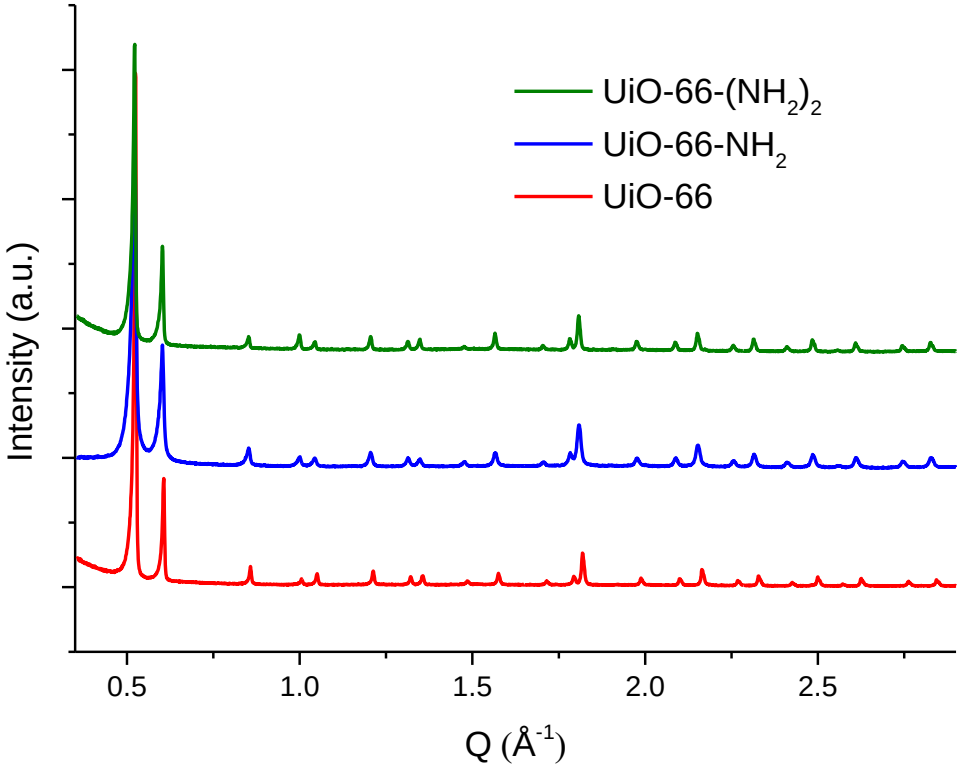

Figure 6.2

PXRD patterns of synthesised UiO-66 (red) UiO-66-NH_2 (blue) and UiO-66-$(NH_2)_2$ (green). All peaks index to the *Fm-3m* space group.

6.3 Dry ammonia breakthrough

Initially, breakthrough experiments were performed on the UiO-66 series using a dry ammonia stream, the breakthrough times are shown in Figure 6.3. Ammonia was detected after 31 minutes of testing, performing considerably better than the

benchmark BPL activated carbon. The amount of ammonia adsorbed at breakthrough is calculated to be 0.019 mmol, a loading of only 1.08 wt%. As UiO-66 has no reactive functionality on its organic linker units, it is thought that the good performance in comparison with activated carbon is a result of free hydroxide groups on the inorganic nodes of the MOF, providing hydrogen bonding sites for the influent ammonia.

The addition of an NH_2 moiety to the linker units of UiO-66 results in an increase of ammonia uptake, with UiO-66-NH_2 yielding breakthrough after 54 minutes. This is equivalent to uptake of 0.033 mmol, or 1.88 wt%. This result was largely expected, with ammonia thought to be hydrogen bonding with the NH_2 moieties throughout the framework.

The addition of a second NH_2 group resulted in an unexpected observation. It was seen that breakthrough time was somewhat decreased in comparison with the mono-amino UiO-66, with breakthrough occurring after 48 minutes. Equating to 0.029 mmol ammonia, or 1.67 wt%, this is still considerably greater uptake than the non-functionalised UiO-66. The decrease in performance in comparison with UiO-66-NH_2 is thought be due to the decreased pore volume of UiO-66-$(NH_2)_2$ indicating that a balance between increased functionality at the cost of reduced porosity is of importance. Indeed, a recent paper[7] which directly compares ammonia breakthrough for UiO-66-OH and UiO-66-$(OH)_2$ also finds the trend that increased functionality does not necessarily result in increased adsorption capacity, with UiO-66-$(OH)_2$ performing less well than the mono-functionalised material.

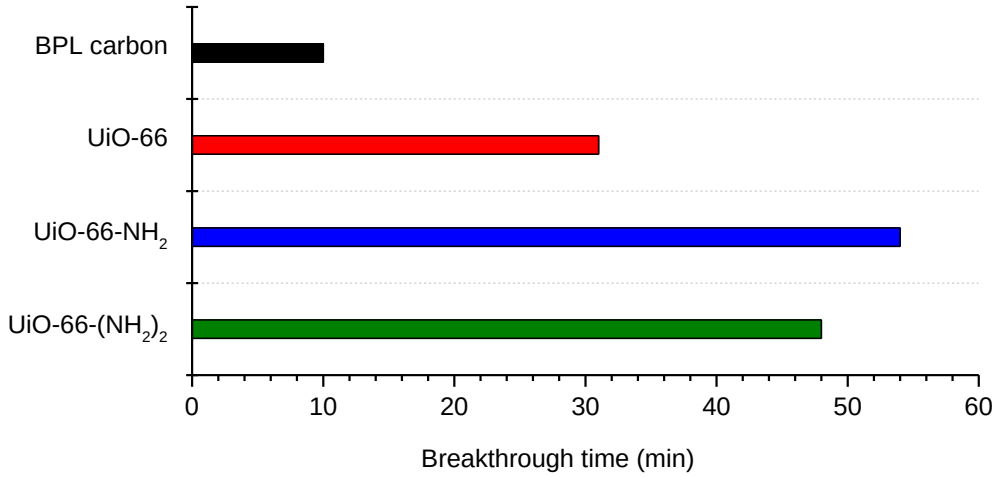

Figure 6.3

Ammonia breakthrough times of UiO-66 (red), UiO-66-NH_2 (blue) and UiO-66-$(NH_2)_2$ (green) in a 0% RH flow of ammonia. BPL activated carbon (black) is shown for comparison.

6.4 Humid breakthrough

Following the good performance observed during dry breakthrough testing, the UiO-66 series of materials were subjected to humid ammonia breakthrough runs, the breakthrough times for which are shown in Figure 6.4. Immediately obvious is the fact that the all materials outperform BPL carbon and that the trend in ammonia uptake now follows the trend of increasing functionality. For UiO-66 ammonia breakthrough occurred after 40.5 minutes in the humid flow, an uptake of 0.025 mmol, 1.41 wt%. As seen for many other materials, the humid ammonia flow affords an increase in uptake in comparison with the dry flow, consistent with the theory that water can form a film in the pores of the MOF which solubilises ammonia.[8]

In contrast with the usual trend, under the humid flow UiO-66-NH_2 showed a decrease in performance in comparison with a dry flow. With an uptake of 0.027 mmol, 1.53 wt%, with ammonia breakthrough after 44 minutes, the material shows a

decrease in uptake of approximately 19%. This behaviour has been observed in the literature[7, 9] whereby competitive adsorption of water is proposed as the reason for decreased uptake in humid flows. Furthermore, UiO-66-$(NH_2)_2$ also shows no increase in performance in the presence of water, with a humid ammonia breakthrough time comparable to that of the dry breakthrough time of 48 minutes.

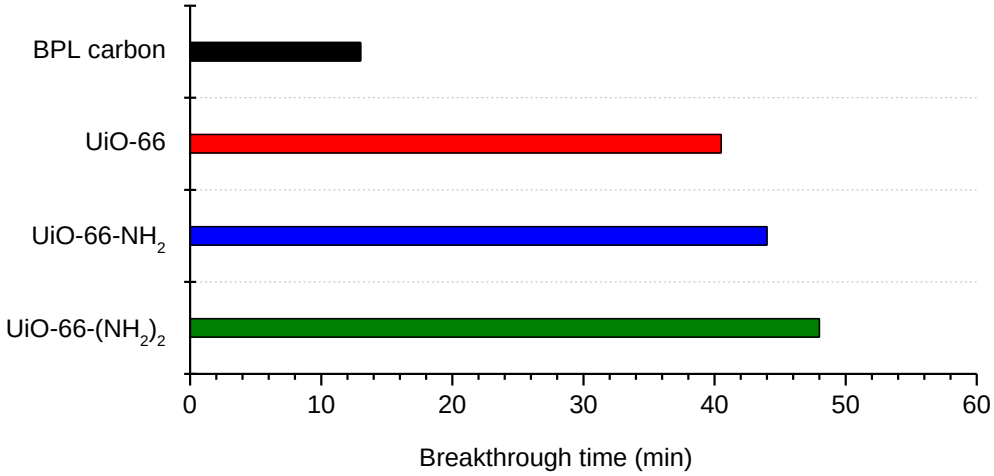

Figure 6.4

Ammonia breakthrough times of UiO-66 (red), UiO-66-NH_2 (blue) and UiO-66-$(NH_2)_2$ (green) in an 80% RH flow of ammonia. BPL activated carbon (black) is shown for comparison.

Table 6.1 Breakthrough times and ammonia uptake of UiO-66 MOFs in dry and humid flows

Material	**RH (%)**	**Breakthrough time (min)**	**NH_3 uptake at breakthrough (wt %)**
UiO-66	0	31	1.08
	80	40.5	1.41
UiO-66-NH_2	0	54	1.88
	80	44	1.53
UiO-66-$(NH_2)_2$	0	48	1.67
	80	48	1.67
BPL carbon	0	7	0.24
	80	13	0.45

In order to help explain these results, the water and nitrogen adsorption isotherms of the UiO-66 series were studied, shown in Figure 6.5 and Figure 6.6, respectively. Nitrogen isotherms all show Type I behaviour, with a decrease in pore volume with the addition of each amino functional group, with UiO-66, UiO-66-NH_2 and UiO-66-$(NH_2)_2$ exhibiting pore volumes of 0.528, 0.417 and 0.309 cm^3/g respectively.

From the water isotherms, it can be seen that overall uptake of water is dominated by pore volume of the materials, with UiO-66 adsorbing 34.1 wt% at 95 % relative humidity, UiO-66-NH_2 adsorbing 30.8 wt% and UiO-66-$(NH_2)_2$ adsorbing 27.0 wt%. At low relative humidities the amino functionality results in greater uptake in the case of UiO-66-NH_2 in comparison with the unmodified UiO-66.

It seems at low RH, the decreased overall capacity of the diamino MOF almost cancels out the effects of the increased functionality, as the isotherms of the diamino and unmodified MOFs are comparable in this region.

The shape of the initial part of a Type V water isotherm is determined by surface chemistry.[10,11] The low RH part of the isotherms indicates that water has the highest affinity for the surface of UiO-66-NH_2, considerably more so than UiO-66-$(NH_2)_2$ and UiO-66. This may indicate that the reason we observe the largest decrease in performance (between dry and humid breakthrough experiments) for UiO-66-NH_2 is because it has a higher affinity for water, and thus competitive adsorption between water and ammonia is much more apparent. Hence any benefit attained from the solubilisation of ammonia in water is apparently outweighed by the quantity of water present. The converse seems to be apparent for UiO-66, and when considering UiO-66-$(NH_2)_2$, the more functionalised surface, but lower overall capacity results in

water uptake which strikes a balance between the benefits attained from the solubilisation of ammonia and competitive adsorption.

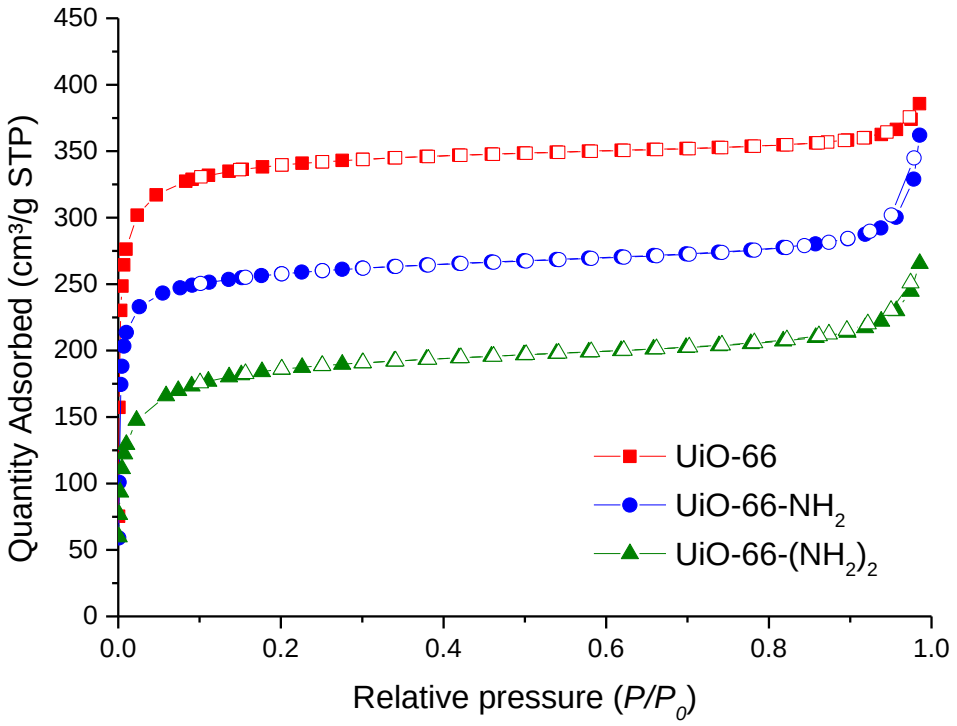

Figure 6.5

Nitrogen isotherms at 77K of UiO-66 (red) UiO-66-NH_2 (blue) and UiO-66-$(NH_2)_2$ (green). Adsorption and desorption is denoted by filled and empty symbols.

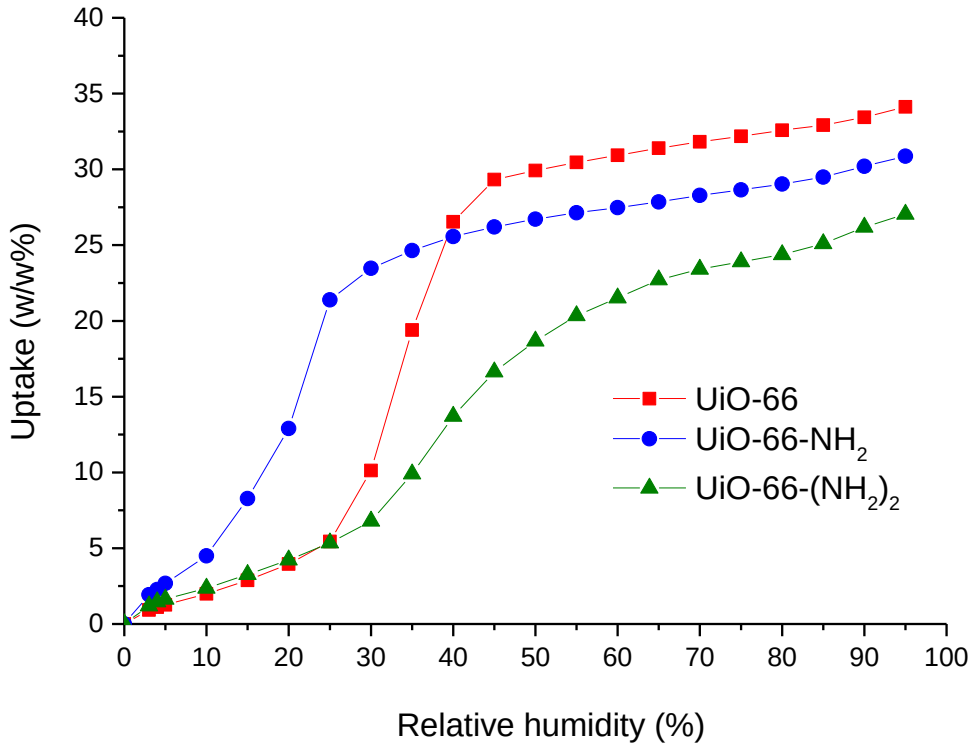

Figure 6.6

Water isotherm at 298 K UiO-66 (red) UiO-66-NH_2 (blue) and UiO-66-$(NH_2)_2$ (green) from 0% RH to 95% RH.

6.5 Acid insertion

Due to the high stability of these zirconium frameworks, and based on previous success with acid insertion in the porphyrin MOFs, it was decided to attempt acid insertion experiments using the aminated UiO-66 series. The same method described in chapter 4 was used for the insertion of HCl into UiO-66-NH_2 and UiO-66-$(NH_2)_2$. Following exposure to HCl, the structure of the frameworks was maintained, as shown by PXRD (Figure 6.7). Furthermore, SEM also revealed no visible difference before and after HCl loading.

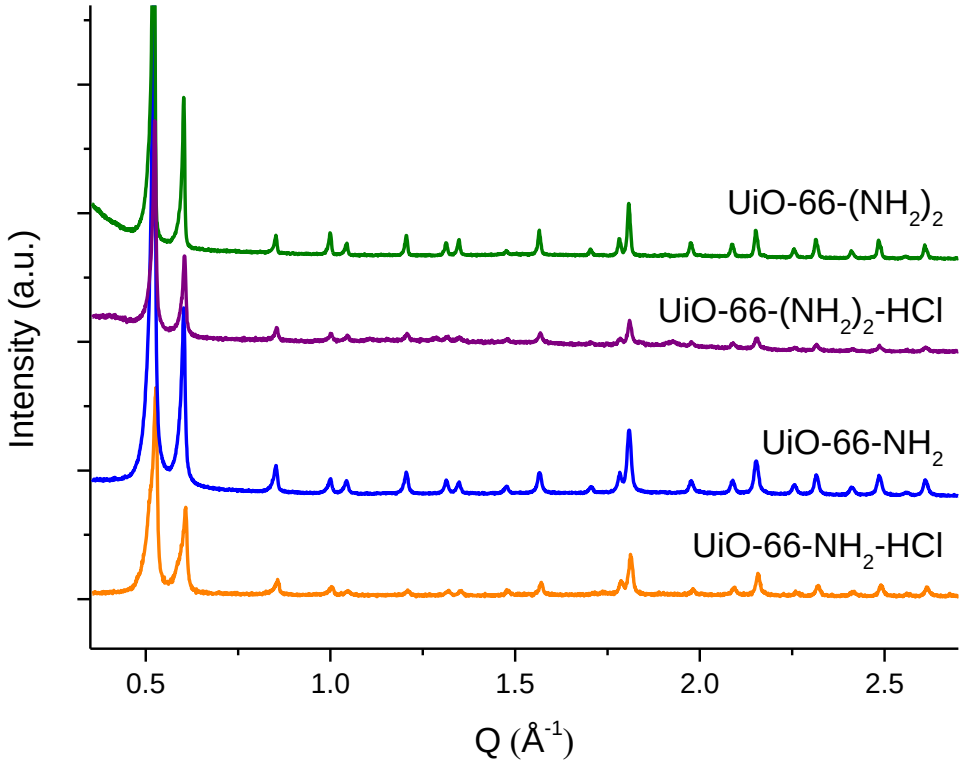

Figure 6.7

PXRD patterns of synthesised UiO-66-NH_2 (blue), UiO-66-NH_2-HCl (orange), UiO-66-$(NH_2)_2$ (green) and UiO-66-$(NH_2)_2$-HCl (purple).

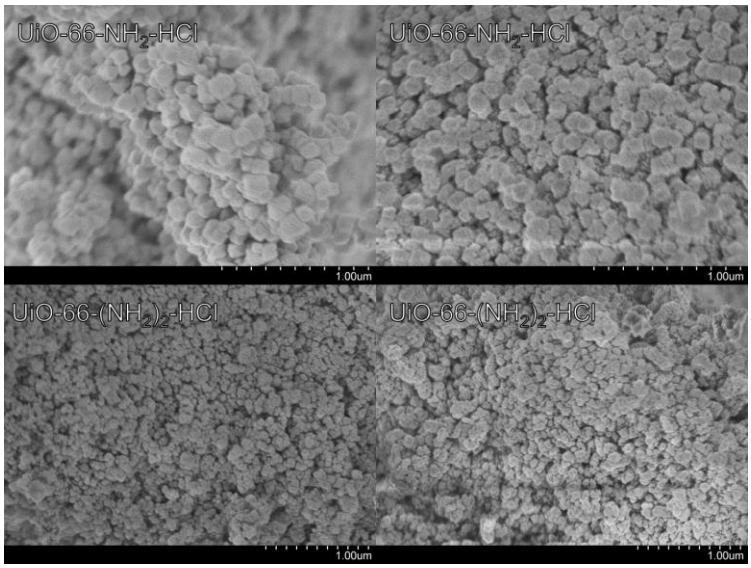

Figure 6.8

SEM images of the aminated UiO-66 MOFs before and after HCl loading

Dry ammonia breakthrough experiments were then performed using UiO-66-NH_2-HCl and UiO-66-$(NH_2)_2$-HCl, the breakthrough times for which are shown in Figure 6.9. Clearly evident is that the loading of HCl into the UiO-66 series has the intended effect of increasing ammonia breakthrough times. UiO-66-NH_2-HCl has adsorbed 0.073 mmol ammonia at breakthrough, which occurred after 121.5 minutes, a loading of 4.22 wt%. The HCl loading affords 2.25-fold increase in performance over the non-loaded MOF.

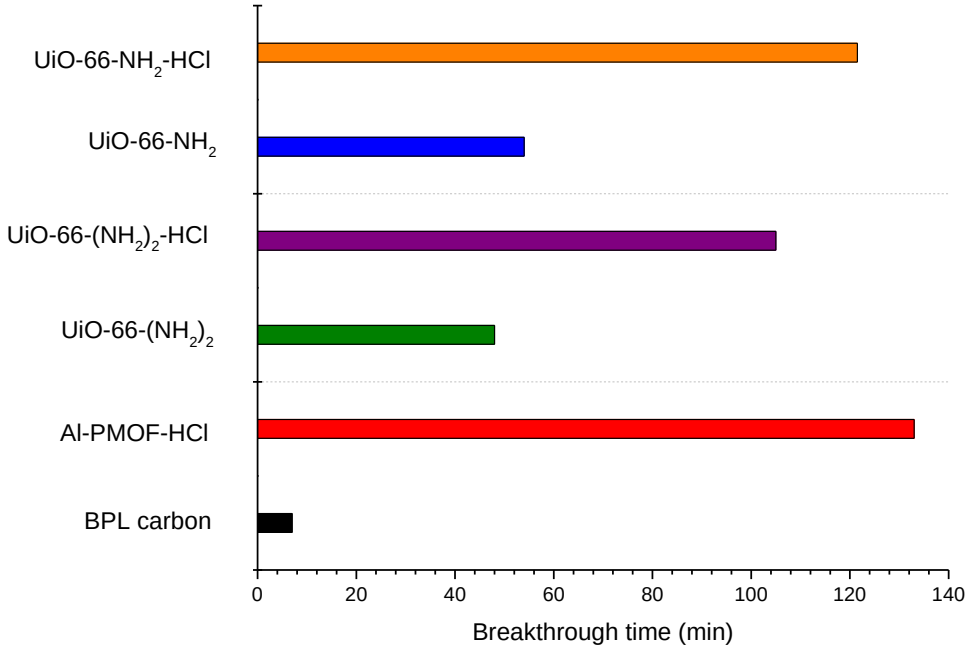

Figure 6.9

Ammonia breakthrough times of, UiO-66-NH_2-HCl (orange), and UiO-66-$(NH_2)_2$-HCl (purple) in a 0% RH flow of ammonia. UiO-66-NH_2 (blue), UiO-66-$(NH_2)_2$ (green), Al-PMOF-HCl (red) and BPL activated carbon (black) are shown for comparison.

Interestingly, following the same trend observed for the non-loaded MOFs, ammonia breakthrough occurs after a shorter time of 105 minutes in the case of UiO-66-$(NH_2)_2$-HCl (0.064 mmol ammonia, 3.65 wt%), which nevertheless equates to a 2.19-fold increase in performance in comparison to the non-loaded MOF. The lesser performance of UiO-66-$(NH_2)_2$-HCl in comparison with UiO-66-NH_2-HCl is thought to be due to the lesser porosity of the framework, as is the case with the non-loaded materials.

Further investigation was necessary regarding the performance of these materials in humid ammonia flows. The aminated materials were tested under a humid flow using a slightly decreased flow rate of 20 ml/min, the breakthrough curves for which are shown below in Figure 6.10. Once again, the materials follow the same trend observed for the non-loaded MOFs with the mono-amino material exhibiting a slightly longer breakthrough time of 104 minutes (0.043 mmol ammonia, 2.41 wt%, and the diamino material exhibiting breakthrough after 95 minutes (0.039 mmol ammonia, 2.13 wt%). It is noted that that the uptake of ammonia under a humid flow is decreased in comparison to the dry flow. This trend is opposite to that seen with the acid-loaded porphyrin materials presented in chapter 4, but it seems evident that under high humidity conditions, water presents competition for the uptake of ammonia.

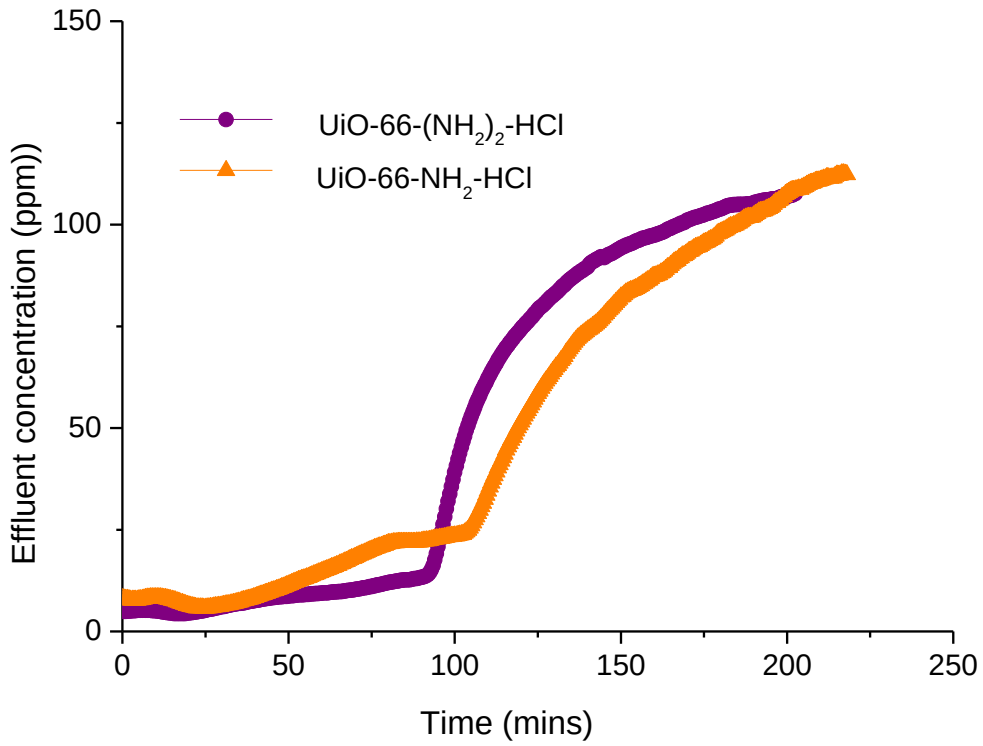

Figure 6.10

Ammonia breakthrough curve for UiO-66-NH_2-HCl (orange), and UiO-66-$(NH_2)_2$-HCl (purple) in a 0% RH flow of ammonia.

PXRD patterns were measured for both UiO-66-NH_2-HCl and UiO-66-$(NH_2)_2$-HCl following exposure to ammonia flow (Figure 6.11 and Figure 6.12, respectively). It was observed that the structure of these materials is maintained after exposure to ammonia, exhibiting this class of materials' remarkable stability. These results contrast to those obtained for Al-PMOF as discussed in chapter 4, whereby PXRD showed an almost complete loss of crystallinity of the sample. It is observed that PXRD patterns of all materials exhibit peaks which can be attributed to ammonium chloride, evidence of the reaction between the HCl stored the pores of the MOF and the influent ammonia. The sharp peaks attributed to ammonium chloride suggest

that, as with Al-PMOF, the ammonium chloride does not form within the pores of these materials.

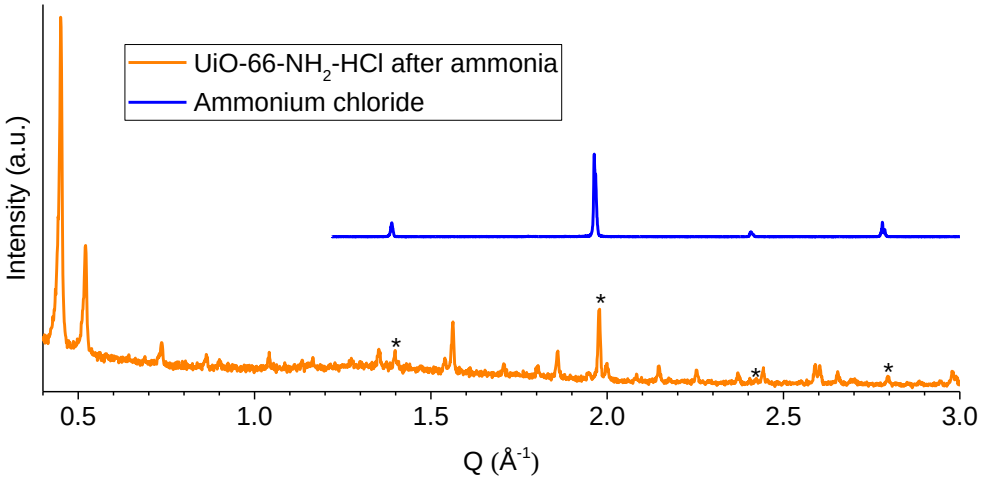

Figure 6.11

PXRD pattern of UiO-66-NH_2-HCl (orange) following exposure to ammonia. PXRD pattern of ammonium chloride (blue) shown for comparison. Starred peaks are attributed to ammonium chloride.

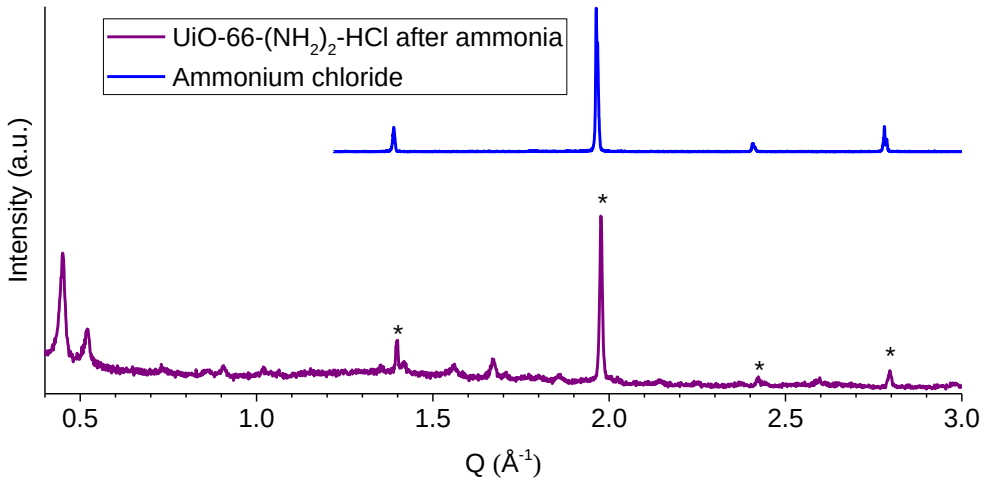

Figure 6.12

PXRD pattern of UiO-66-$(NH_2)_2$-HCl (purple) following exposure to ammonia. PXRD pattern of ammonium chloride (blue) shown for comparison. Starred peaks are attributed to ammonium chloride.

6.6 Conclusion

The amino functionalised UiO-66 series of MOFs were expected to increase ammonia uptake by exploiting the formation of favourable hydrogen bonds. The addition of a single -NH_2 group resulted in a large increase in ammonia uptake in dry conditions, though the addition of a second -NH_2 group, though still outperforming the unfunctionalised material, performed less well than the mono-amino analogue. This result highlighted the importance of porosity of the material, in addition to functionality. The aminated materials showed further deviation from the expected trend when tested in humid flows with no improvement over dry flows, and a decrease in performance in the case of the mono-amino material. This was attributed to competitive uptake of water.

Acid insertion experiments showed that these materials are stable to HCl loading, and the loaded materials exhibit large increases in performance in kinetic breakthrough experiments in comparison with their non-loaded analogues. When testing in humid ammonia flows, the aminated HCl-loaded materials exhibited the same trend as in dry flows, but with overall decreased performance. The HCl-inserted aminated UiO-66 materials exhibited excellent stability to influent ammonia as evidenced by PXRD.

6.7 References

1. M. Kandiah, M. H. Nilsen, S. Usseglio, S. Jakobsen, U. Olsbye, M. Tilset, C. Larabi, E. A. Quadrelli, F. Bonino and K. P. Lillerud, *Chem. Mater.*, 2010, **22**, 6632-6640.
2. T. C. Wang, W. Bury, D. A. Gómez-Gualdrón, N. A. Vermeulen, J. E. Mondloch, P. Deria, K. Zhang, P. Z. Moghadam, A. A. Sarjeant, R. Q. Snurr, J. F. Stoddart, J. T. Hupp and O. K. Farha, *J. Am. Chem. Soc.*, 2015, **137**, 3585-3591.
3. V. Guillerm, F. Ragon, M. Dan-Hardi, T. Devic, M. Vishnuvarthan, B. Campo, A. Vimont, G. Clet, Q. Yang, G. Maurin, G. Ferey, A. Vittadini, S. Gross and C. Serre, *Angewandte Chemie-International Edition*, 2012, **51**, 9267-9271.
4. J. H. Cavka, S. Jakobsen, U. Olsbye, N. Guillou, C. Lamberti, S. Bordiga and K. P. Lillerud, *J. Am. Chem. Soc.*, 2008, **130**, 13850-13851.
5. D. Britt, D. Tranchemontagne and O. M. Yaghi, *Proc. Natl. Acad. Sci. U.S.A.*, 2008, **105**, 11623-11627.
6. A. Schaate, P. Roy, A. Godt, J. Lippke, F. Waltz, M. Wiebcke and P. Behrens, *Chemistry – A European Journal*, 2011, **17**, 6643-6651.
7. H. Jasuja, G. W. Peterson, J. B. Decoste, M. A. Browe and K. S. Walton, *Chem. Eng. Sci.*, 2015, **124**, 118-124.
8. C. Petit, B. Mendoza and T. J. Bandosz, *Langmuir*, 2010, **26**, 15302-15309.
9. T. G. Glover, G. W. Peterson, B. J. Schindler, D. Britt and O. Yaghi, *Chem. Eng. Sci.*, 2011, **66**, 163-170.
10. F. Rouquerol, J. Rouquerol and K. Sing, in *Adsorption by Powders and Porous Solids*, eds. F. Rouquerol, J. Rouquerol and K. Sing, Academic Press, London, 1999, pp. 237-285.
11. S. J. Gregg and K. S. W. Sing, *Adsorption, Surface Area, & Porosity, Second Edition*, Academic Press, 1982.

7 Summary

This work has presented the synthesis and characterisation of water stable metal-organic frameworks and conjugated microporous polymers and their assessment by dynamic micro-breakthrough experiments as sorbents for ammonia.

The porous polymer CMP-1 has been functionalised with both one and two carboxylic acid moieties per monomer. An increase in ammonia uptake by the mono-acid over the unfunctionalised material was seen, however the di-acid polymer showed less ammonia uptake than even the unfunctionalised CMP-1 in dry conditions. Isotherms using N_2, H_2O and MeOH revealed the likelihood of a highly hydrogen bonded polymer network which in effect resulted in a closed di-acid polymer structure, inaccessible to ammonia at 298 K. When a humid flow of ammonia was used the di-acid polymer was seen to outperform its mono-acid and unfunctionalised analogues, with ammonia uptake performance following the trend of increasing acid functionality. This was attributed to the ability of water to disrupt the hydrogen bonding of the network sufficiently to allow ammonia access to the increased density of carboxylic acid groups in the network.

The aluminium porphyrin-based metal-organic framework, Al-PMOF, has been shown to adsorb large quantities of both hydrochloric and formic acids; ion chromatography and thermo-gravimetric analysis revealed 6.1 molecules of HCl and 6.4 molecules of HCOOH are adsorbed per porphyrin linker. The MOF shows outstanding stability towards these guests, evidenced by the ability to cycle the acid loading despite vigorous removal conditions (170^oC at 10^{-2} mbar) and still maintain

porosity. By exploiting the Brønsted acid-Brønsted base interactions, ammonia uptake by these acid-loaded materials was observed to be excellent, with loadings of up to 4.6 and 7.9 wt% in the case of Al-PMOF-HCl in dry and humid conditions, respectively, which equates to 3.8 and 6.8 molecules of ammonia per porphyrin linker unit. The increase in performance in the simulated humidity of environmental conditions is advantageous for useful application.

An indium porphyrin-based MOF has been characterised to reveal a material isostructural to Al-PMOF, with a larger unit cell and the presence of In(III)OH bound within its porphyrin core. The material has been shown to perform well as an ammonia sorbent, outperforming BPL activated carbon and Al-PMOF. Interestingly, the MOF was unstable to the loading of formic and hydrochloric acids, which attributed to the lability of In(III). The material's potential for CO_2 and CH_4 uptake was also assessed, with favourable uptakes of 269 and 139 cm^3/g, respectively, however only moderate selectivity of CO_2 over CH_4. A vanadium porphyrin-based MOF, has been shown exhibit good ammonia uptake, outperforming its isostructural aluminium and indium analogues, and far surpassing BPL activated carbon. The material is seen to be entirely unstable to HCl loading, yet stable to formic acid loading, which yields a corresponding increase in ammonia uptake.

UiO-66 has been functionalised with one and two amino groups per linker. It was observed that the addition of a single -NH_2 group resulted in significant increases in ammonia uptake however the addition of a second -NH_2 group resulted in ammonia uptake between that of the unfunctionalised material mono-amino analogue, highlighting the important balance between porosity and functionality. The addition of moisture to the ammonia flow revealed competitive uptake of water in the case of

the aminated MOFs, with decreased uptake in the case of UiO-66-NH_2 and no change in the overall uptake of UiO-66-$(NH_2)_2$. The materials are shown to be stable to HCl loading, maintaining their crystalline structure, with the resulting materials yielding excellent improvements in ammonia uptake, adsorbing more than 2 times the quantity of ammonia over the non-loaded MOFs.

To conclude, the porous materials studied in this work have displayed potential to be utilised as ammonia sorbents, outperforming activated carbon, the current mainstay in the sorptive protective field. Literature reports of previous work in this area report functionality aimed at interaction with ammonia intrinsic to the material, a rationale that has been used in this work. In addition, the results presented here have demonstrated the ability of highly stable frameworks to be loaded with chemically active material with functionality targeted towards ammonia, which has exhibited large performance increases over materials with targeted intrinsic functionality. As such it seems a viable future route that porous materials may be selected or designed not necessarily based on functionality toward the challenge gas itself, but instead based on functionality to promote its use as a reservoir for a more chemically active material. With the continuous discovery of highly chemically stable porous materials, this approach may offer a means for the synthesis of materials with unprecedented ammonia uptake.

7.1 Summary table

Table 7.1 Ammonia uptake exhibited by the porous materials studied in this work

Material	Ammonia uptake (mmol/g)	
	Dry flow (0% RH)	Humid (80% RH)
Al-PMOF-HCl	2.93	5.00
Al-PMOF-FA	2.43	3.33
UiO-66-NH_2-HCl	2.43	1.43
UiO-66-$(NH_2)_2$-HCl	2.13	1.30
V-PMOF-FA	1.67	-
Al-PMOF-HCl-vac	1.13	-
UiO-66-NH_2	1.10	0.90
UiO-66-$(NH_2)_2$	0.97	0.97
Zn-Al-PMOF	0.88	-
V-PMOF	0.80	-
In-PMOF	0.70	-
UiO-66	0.63	0.83
Co-Al-PMOF	0.49	-
In-PMOF-HCl	0.33	-
Al-PMOF	0.31	0.53
Zn-Carnosine	0.29	-
CMP-1-COOH	0.25	0.40
CMP-1	0.10	0.14
CMP-1-$(COOH)_2$	0.07	0.57
CC3	0.06	-
Ce-(HTCPB)	0.01	-

7.2 Summary graph

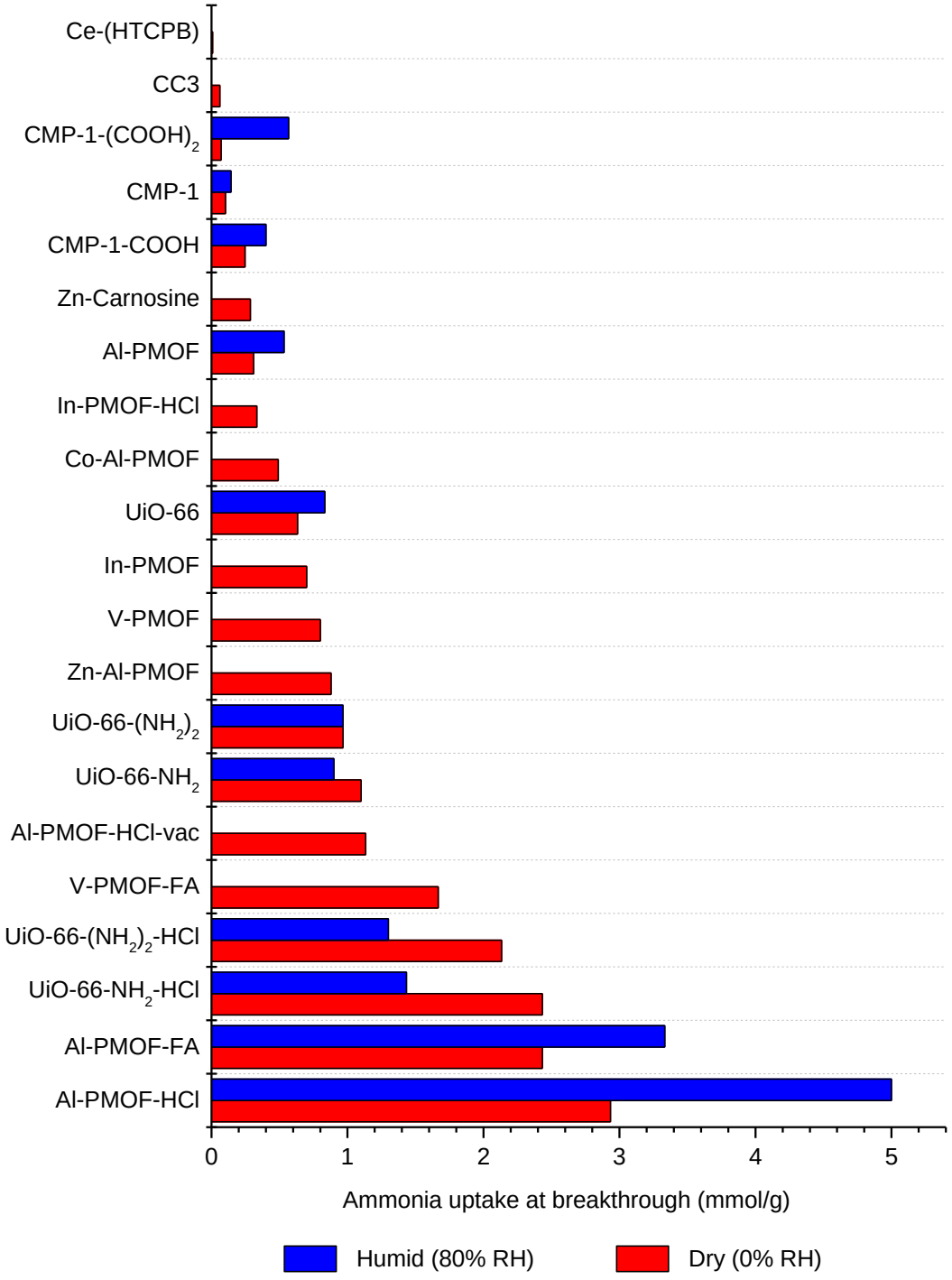

Figure 7.1

Ammonia uptake exhibited by the porous materials studied in this work